FUNCTIONAL MORPHOLOGY OF THE OVIRAPTOROSAURIAN CRANIUM

LUKE E. MEADE

A thesis submitted to the University of Birmingham
for the degree of DOCTOR OF PHILOSOPHY

School of Geography, Earth and Environmental Sciences
College of Life and Environmental Sciences
University of Birmingham

August 2022

Abstract

Oviraptorosaurians were a group of theropod dinosaurs that reached high diversity in the Late Cretaceous (100.5–66 million years ago). Later diverging members evolved a distinctive cranium which was extensively pneumatised, short and tall, and ended in a robust, toothless beak. Their skull has been previously interpreted as adapted for a powerful bite as part of a herbivorous or omnivorous diet. This thesis focusses on testing whether these interpretations of oviraptorosaurian cranial function are accurate. Digital 3D models were created of four key oviraptorosaurian species — early diverging oviraptorosaurian *Incisivosaurus gauthieri*, and later diverging oviraptorid oviraptorosaurians *Citipati osmolskae*, *Conchoraptor gracilis*, and *Khaan mckennai*. Finite element analysis using scaled loads demonstrates oviraptorosaurian cranial shape was stronger (lower stresses) and more efficient (lower total strain energy) compared with other herbivorous theropod crania (*Erlikosaurus* and *Ornithomimus*) and performed similarly well or better compared with large carnivore *Allosaurus*. Digital volumetric reconstructions of jaw adductor musculature quantify elevated bite forces in oviraptorosaurians compared with other herbivorous theropods (349–499 N in *Citipati* down in order of cranial size to 53–83 N in *Incisivosaurus*). Maximum angles of oviraptorosaurian jaw gape were estimated as similar to but more limited than reported estimates for herbivorous theropod *Erlikosaurus* and greatly more limited than carnivorous theropods. When approaches were combined to model muscle driven biting, oviraptorosaurians display greater cranial stress than other theropods indicating that the increased relative force of their jaw adductor musculature outweighs the effect of a comparatively strengthened cranial morphology. Oviraptorid crania may function closer to structural safety limits while feeding due to the influence of other functional or developmental pressures acting on their cranial shape. Nevertheless, it appears Oviraptoridae were adapted for powerful bites as part of a predominately but not necessarily exclusively herbivorous diet, distinct from other herbivorous theropods, while cranial function varied among oviraptorids with different species favouring different positions of biting.

Rendered reconstruction of oviraptorid *Citipati osmolskae* by L. E. Meade

Acknowledgements

Firstly, I want to thank my supervisor Stephan Lautenschlager for his support, inspiration, and guidance throughout my PhD. I am tremendously grateful to Stephan for giving me the opportunity to pursue my interests and for his kindness and generosity along the way — I feel incredibly lucky to have had him as a supervisor. In addition, I thank my co-supervisors Richard Butler and Michael Pittman for the opportunities they have provided, their expertise, insightful discussion, and the other ways they have helped me become a better researcher. Thanks are also due to Jason Hilton, Ivan Sansom, and Kirsty Edgar, for the opportunities and encouragement they have given me through my PhD studies.

The Earth Sciences department is full lovely people that have improved my time as a PhD student, too many to thank individually. I am very grateful to my colleagues and friends in Stephan's research group — Charlotte, Fion, Jordan, and Richard, our Wednesday coffee mornings helped keep some sense of normality throughout Covid and were valuable to me. Thank you to those fellow PhD students in G23 — especially Alastair, Lisa, Iacopo, Bridget, Nicola, Struan, Alice, Kerys, Gemma — those upstairs — JP, Emma H, Jake, Hazel, Matt, Marie — and friends elsewhere in the building — Emma D, Thomas, Andy — for good times at coffee mornings, the allotment (thanks Kate!) parkrun, games nights and DnD, and everything else (not the shark).

This thesis would not have been possible without Amy Balanoff, Stephan Lautenschlager, and Andrew Cuff providing digital datasets. This research was greatly improved thanks to Khishigjav Tsogtbaatar, Jolanta Kobylinska, Vladimir Alifanov, and Xing Xu for allowing me access to specimens in their care. Thanks to Eva Herbst for our discussions on Blender and the work we were able to do.

I thank the Central England NERC Training Alliance (CENTA) for funding my PhD studies and greatly appreciate the help Mica Jones and Ella Young gave me during their

time working with CENTA — you two helped a lot of us.

To my girlfriend and best friend, Doody — the biggest thank you for everything, the support you gave me in the weeks dedicated to this thesis was incredible. You're fab.

Lastly, I am so grateful for the unwavering support my family has shown me while pursuing my career as a palaeontologist — to my parents, Andy and Liz, and to my siblings, Harriet and Matthew, thank you for your belief and enthusiasm.

List of papers

The following papers were published during the course of my doctoral study at the University of Birmingham.

Publications incorporated in this thesis:

MEADE, L. E. and MA, W. 2022. Cranial muscle reconstructions quantify adaptation for high bite forces in Oviraptorosauria. *Scientific Reports*, **12**, 1–15.

HERBST E. C., **MEADE L. E.**, LAUTENSCHLAGER S., FIORITTI N. and SCHEYER T. M. 2022. A toolbox for the retrodeformation and muscle reconstruction of fossil specimens in Blender. *Royal Society Open Science*, **9**, 220519.

Other publications:

BUTLER, R. J., SENNIKOV, A. G., DUNNE, E. M., EZCURRA, M. D., HEDRICK, B. P., MAIDMENT, S. C., **MEADE, L. E.**, RAVEN, T. J. and GOWER, D. J. 2019. Cranial anatomy and taxonomy of the erythrosuchid archosauriform '*Vjushkovia triplicostata*' Huene, 1960, from the Early Triassic of European Russia. *Royal Society Open Science*, **6**, 191289.

MA, W., PITTMAN, M., LAUTENSCHLAGER, S., **MEADE, L. E.** and XU, X. 2020b. Functional morphology of the Oviraptorosaurian and Scansoriopterygid skull. *Bulletin of the American Museum of Natural History*, **440**, 229–249.

MAIDMENT, S. C., SENNIKOV, A. G., EZCURRA, M. D., DUNNE, E.M., GOWER, D. J., HEDRICK, B. P., **MEADE, L. E.**, RAVEN, T. J., PASCHCHENKO, D. I. and BUTLER, R. J. 2020. The postcranial skeleton of the erythrosuchid archosauriform *Garjainia prima* from the Early Triassic of European Russia. *Royal Society Open Science*, **7**, 201089.

EZCURRA, M. D., BUTLER, R. J., MAIDMENT, S. C., SANSOM, I. J., **MEADE, L. E.** and RADLEY, J. D. 2021. A revision of the early neotheropod genus *Sarcosaurus* from the Early Jurassic (Hettangian–Sinemurian) of central England. *Zoological Journal of the Linnean Society*, **191**, 113–149.

MEADE, L. E., PLACKETT, A. R. and HILTON, J. 2021. Reconstructing development of the earliest seed integuments raises a new hypothesis for the evolution of ancestral seed-bearing structures. *New Phytologist*, **229**, 1782–1794.

Contents

List of Figures

List of Tables

1 | Introduction

1.1 The Oviraptorosauria

Oviraptorosauria is a clade of maniraptoran theropod dinosaurs with an increasingly excellent fossil record from the Cretaceous of Asia and North America. The group is currently represented by upwards of 40 genera (Lü *et al.*, 2016; Funston, 2019) which range from chicken-sized forms to the eight metre long, two tonne *Gigantoraptor erlianensis* (Xu *et al.*, 2007) and show perhaps one of the last diversifications of non-avian theropod dinosaurs before the K–Pg boundary (Lü *et al.*, 2017; Funston *et al.*, 2020b). A spectacular fossil record has given detailed insights into their diversity (Lü *et al.*, 2017; Funston *et al.*, 2018; Funston *et al.*, 2021), ecology (Funston *et al.*, 2018; Ma *et al.*, 2020a; 2020b), feathered integument (Ji *et al.*, 1998; Xu *et al.*, 2010), ontogeny (Lü *et al.*, 2013a; Funston *et al.*, 2019; Wei *et al.*, 2022), and reproduction (Sato *et al.*, 2005; Wiemann *et al.*, 2017) and nesting (Norell *et al.*, 1994; 1995a; Dong and Currie, 1996; Clark *et al.*, 1999; Varricchio *et al.*, 2008; Norell *et al.*, 2018; Yang *et al.*, 2019; Yang and Sander, 2022) — the group has become famous for their preserved eggs and examples of brooding, from which circumstances they also derive their name (Osborn, 1924; Barbold, 1976a; 1976b).

The cranium of oviraptorosaurians is particularly distinctive among theropod dinosaurs (Fig. 1.1). Later diverging oviraptorosaurians (from what we know from oviraptorid crania) are characterised by highly modified, pneumatic crania (Fig. 1.1B–E) (Kundrát and Janáček, 2007) that are short and tall, sometimes elaborately crested

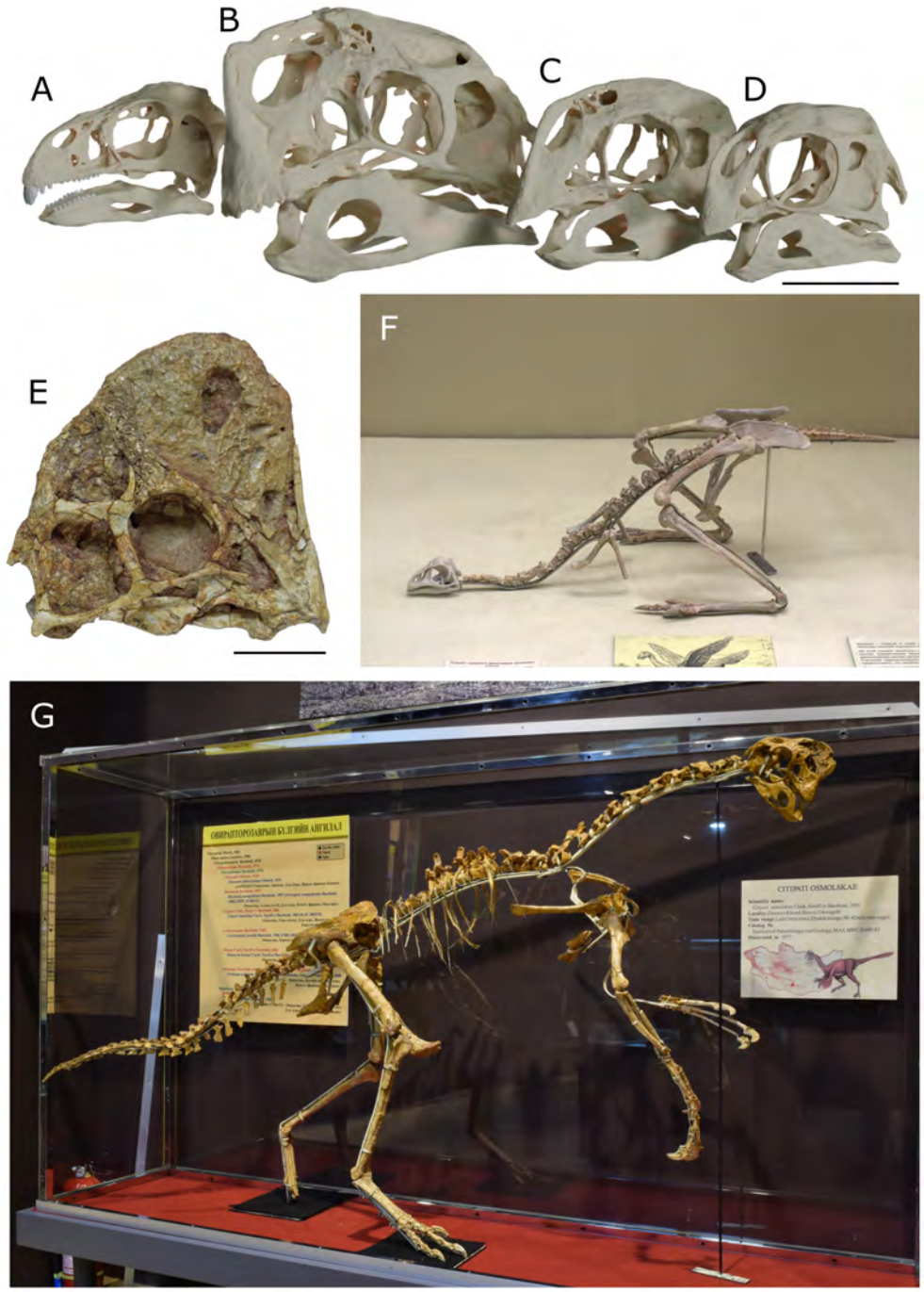

Figure 1.1: Digital skull models of (A) early diverging oviraptorosaurian *Incisivosaurus gauthieri*, and oviraptorid oviraptorosaurians (B) *Citipati osmolskae*, (C) *Khaan mckennai*, and (D) *Conchoraptor gracilis* with 5 cm scale bar. (E) Cranium of high crested oviraptorid *Rinchenia mongoliensis* MPC-D 100/32a, scale bar 5 cm. (F) Skeleton of *Avimimus portentosus* with reconstructed skull on display at Orlov Museum of Paleontology, Moscow. (G) Mounted skeleton of MPC-D 100/42, an oviraptorid from the Zamyn Khondt locality of the Djadokhta Formation, likely *Citipati* sp., on display at Hunnu Mall, Ulaanbaatar. Digital models and photographs were created by the author.

(Fig. 1.1E) (Barsbold, 1986; 1988; Lü *et al.*, 2017; Funston *et al.*, 2018) and end in a toothless beak. The cranium is borne on a relatively long neck (Fig. 1.1G) (Sues, 1997; Lü, 2003) and the rest of their body plan is characterised by elongate hindlimbs (Currie and Russell, 1988; Rhodes *et al.*, 2020) and grasping forelimbs with recurved claws (Fig. 1.1G) (Senter and Parrish, 2005; Funston *et al.*, 2020b), along with tails that are more bird-like than other theropods, being shorter and containing fewer vertebra (Persons *et al.*, 2013), and terminating in an apical pygostyle in some taxa (Barsbold *et al.*, 2000a; 2000b) (Fig. 1.1F,G).

The ecosystem role, diet, and cranial function of Late Cretaceous oviraptorosaurians has remained uncertain, largely due to this peculiar cranial morphology. However, they may have been one of the few non-avian theropod groups that pursued herbivory to a significant extent (Zanno and Makovicky, 2011).

1.2 Phylogenetic position and groupings

Their beaked, superficially bird-like crania, combined with extensive cranial and vertebral pneumatisation (Barsbold *et al.*, 1990), evidence of pennaceous feathering (Ji *et al.*, 1998), pygostyles (Barsbold *et al.*, 2000a; 2000b), and other features led Oviraptorosauria to be considered a basal, flightless avalian clade when its current main internal classifications were first set out (Maryańska *et al.*, 2002; Osmólska *et al.*, 2004), perhaps secondarily flightless (Maryańska *et al.*, 2002). This affinity with birds has since been challenged, and Oviraptorosauria has frequently been recovered as the sister clade of Paraves (Senter *et al.*, 2012; Turner *et al.*, 2012; Brusatte *et al.*, 2014; Xu *et al.*, 2015; Lefèvre *et al.*, 2017), together forming the clade Pennaraptora (Fig. 1.2) (Brusatte *et al.*, 2014; Foth *et al.*, 2014; Xu *et al.*, 2017; Pittman *et al.*, 2020). The closest relatives of Pennaraptora are frequently found to be either therizinosaurians (Senter *et al.*, 2012; Turner *et al.*, 2012; Xu *et al.*, 2015) or alvarezsauroids (Senter, 2007; Zanno, 2010).

The earliest diverging oviraptorosaurians such as *Incisivosaurus gauthieri* (Fig.

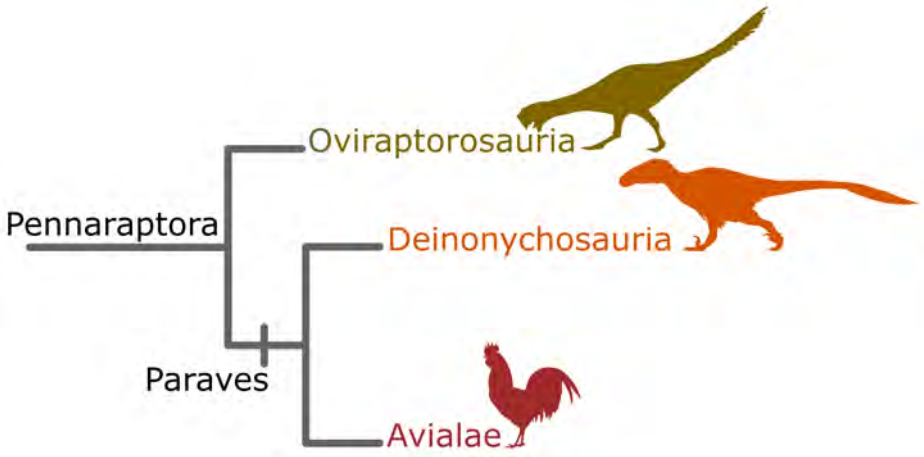

Figure 1.2: Simplified cladogram showing relationship of Oviraptorosauria to the rest of the Pennaraptora (see Pittman *et al.*, 2020). Silhouettes from phylopic.org, with thanks to J. Headden and S. Hartman, representing *Heyuannia yanshini* for Oviraptorosauria, *Utahraptor ostrommaysi* for Deinonychosauria, and *Gallus gallus domesticus* for Avialae.

1.1A) (Xu *et al.*, 2002) and the caudipterids (Ji *et al.*, 1998; Zhou and Wang, 2000) were small bodied (<1 m), still bore teeth, and are typically from the Yixian Formation of Liaoning, China (Barremian–Aptian; 125.9 Ma, Chang *et al.*, 2017). Following these, the group becomes toothless and more highly modified, with the Avimimidae (Fig. 1.1F) (Kurzanov, 1981; Funston *et al.*, 2016; Tsuihiji *et al.*, 2017)) diverging before two sister groups that comprise the majority of oviraptorosaurian diversity: the families Caenagnathidae and Oviraptoridae (together forming the Caenagnathoidea) (Fig. 1.3).

Relationships within each family are less well constrained due to missing data from taxa diagnosed from very incomplete material (Lü and Zhang, 2005; Zanno and Sampson, 2005; Sullivan *et al.*, 2011; Longrich *et al.*, 2013; Yu *et al.*, 2018), particularly among Caenagnathidae (Longrich *et al.*, 2013, Funston and Currie, 2016). Caenagnathids are typically represented by fragmentary remains, predominantly from North America (Longrich *et al.*, 2013), and even in the taxa with most skeletal material represented, the cranium is poorly known. Oviraptorids, in contrast, are represented by increasingly diverse and excellent fossil specimens that may display a high degree of completeness (Clark *et al.*, 2001; Lü *et al.*, 2016; Lü *et al.*, 2017; Funston *et al.*,

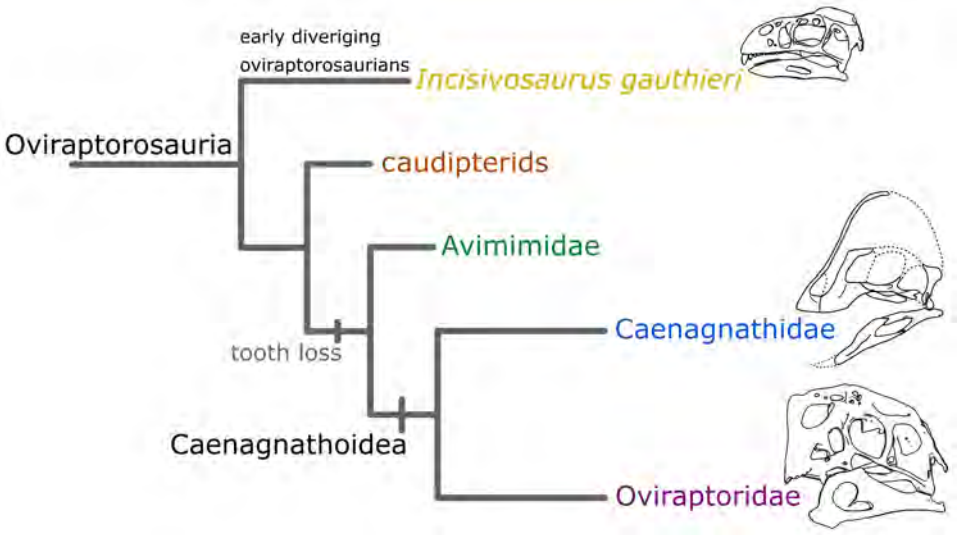

Figure 1.3: Simplified cladogram showing key groups within Oviraptorosauria (see Lü *et al.*, 2017; Yu *et al.*, 2018; Funston *et al.*, 2020b). Skull outline representing Caenagnathidae is *Anzu wyliei*, adapted from Lamanna *et al.* (2014), with missing material represented by dashed lines. Skull outline representing Oviraptoridae is *Citipati osmolskae*, based on the retrodeformed model from this study; likewise for *Incisivosaurus gauthieri*.

2020b). This thesis will therefore focus more on the Oviraptoridae due to the availability of well-preserved crania.

1.3 History of the "egg thief lizards"

The first species to be named, that would later be included among Oviraptorosauria (as a caenagnathid), was *Chirostenotes pergracilis* (Gilmore, 1924) from the Dinosaur Park Formation of Alberta, Canada. The species was described from the partial articulated remains of both hands. The description of the eponymous *Oviraptor philoceratops* (Osborn, 1924) followed later the same year. Osborn (1924) acknowledges that the generic and specific names (*Oviraptor* — "egg seizer"; *philoceratops* — "fondness for ceratopsian eggs") may be entirely misleading as to the feeding habits of the taxon. The names were a result of the holotype skull being discovered lying over a clutch of dinosaur eggs, the animal supposed to have been overtaken by a sandstorm while ransacking the nest. Osborn (1924) concluded succinctly that *O. philoceratops* was

herbivorous or omnivorous.

The characterisation of oviraptorosaurians as egg thieves received some traction in popular culture and has been discussed subsequently (Currie *et al.*, 1993). From the posterior of the oviraptorid primary palate projects a ventral tooth-like process consisting of the maxillae and vomer. This projection was mentioned by Currie *et al.* (1993) as reminiscent of extant oophagous snakes, the specialised pointed vertebral hypapophyses of which are adapted to puncture swallowed eggs (Gans and Oshima, 1952).

However, Norell *et al.* (1994) published the discovery of embryonic oviraptorid specimens and identified the eggs associated with the *Oviraptor* type specimen as the same morphotype. They suggested the animal had not died while feeding on the eggs but had instead perished while incubating or protecting them. Subsequent discoveries of oviraptorid remains in brooding positions guarding similar nests further vindicates the group (Norell *et al.*, 1995a; Dong and Currie, 1996; Clark *et al.*, 1999; Fanti *et al.*, 2012).

It is unlikely eggs were a large enough part of the diet of all oviraptorosaurians to influence their cranial functional morphology. Eggs may have been a potential but infrequent food stuff as part of a generalist omnivorous diet, but it would be incorrect to think of Oviraptorosauria any more as 'egg-eaters' than modern ravens or badgers (Hounsome and Delahay, 2005; Coates *et al.*, 2008).

1.4 Palaeoecology and diet

Apart from a few examples in early diverging species (gastroliths linked with herbivory in *Caudipteryx zoui*, Ji *et al.*, 1998; Wings and Sander, 2006), there is no substantial direct evidence of diet in oviraptorosaurians. Norell *et al.* (1994) reported two baby troodontid skulls found associated with eggshell fragments amid the eggs and body fossil of a brooding oviraptorid but speculated they could be predating or parasitising the nest, if not the remains of food. Fragmented lizard remains near the stomach cavity

are reported in the *Oviraptor philoceratops* holotype (AMNH 6517, Norell *et al.*, 1995b), perhaps its final meal.

In discussing the skulls and diets of later diverging oviraptorosaurians – the caenagnathids and oviraptorids – focus on the mandible is possible with both groups but largely limited to just the oviraptorids for the cranium. Crania are absent or highly fragmentary for all of Caenagnathidae but based on maxillae and the mandibles of some caenagnathids (Sternberg, 1940; Cracraft, 1971; Currie *et al.*, 1993; Sues, 1997; Funston and Currie, 2014; Lamanna *et al.*, 2014) the snout was probably moderately elongate, unlike the deep shortened rostrum of oviraptorids. Some of the most complete caenagnathid cranial remains are those of *Anzu wyliei* (Lamanna *et al.*, 2014) from the Hell Creek Formation (Maastrictian) — premaxilla fragments indicate a cranium with a tall crest and longer rostrum than oviraptorids.

Morphological differences between the mandibles of caenagnathids and oviraptorids suggest broadly different feeding styles and diets between the two groups (Longrich *et al.*, 2010; 2013; Funston and Currie, 2016; Ma *et al.*, 2017; 2020b). Interpretations of caenagnathid diets are typically more predatory (Funston and Currie, 2016) or forms of herbivory focussing on plant materials softer than those eaten by oviraptorids (Longrich *et al.*, 2013). These ideas derive from caenagnathid mandibles being more slender, and without the depth and robust symphysis of those in oviraptorids, providing caenagnathids a lower mechanical advantage to the jaw for a quicker but weaker bite (Ma *et al.*, 2020b). The anterior tip of the mandibles of some caenagnathids is more recurved and pointed compared with oviraptorids, perhaps advantageous in slashing meat (Funston and Currie, 2016) and prey capture. Exceptions exist such as the massive early diverging caenagnathid *Gigantoraptor*, in which the mandible takes a deeper more oviraptorid-like shape (Xu *et al.*, 2007; Ma *et al.*, 2017).

Crania in oviraptorids are diverse and well-preserved. Though filled with pneumatic air spaces, topped by thin, sometimes delicately ornamented skull roofs, and bearing reduced rod-like jugals and quadratojugal bones, the oviraptorid cranium is

frequently interpreted as strong and adapted for a powerful bite (Barsbold, 1976a; Funston *et al.*, 2018; Ma *et al.*, 2020b). This interpretation stems from the premaxillae and palate which appear robust. Furthermore, the cranium, particularly the rostrum, is shortened which increases the mechanical advantage of their jaws and deepened dorsoventrally as a supposed adaptation for strength. This is to the extent that some species have crania that are as tall or taller than they are long due to dome-shape skull roofs (*Oksoko avarsan*, Funston *et al.*, 2020b) or tall crests (*Rinchenia mongoliensis*, Funston *et al.*, 2018; *Corythoraptor jacobsi*, Lü *et al.*, 2017) (Fig. 1.1E).

The apparent strength of the cranium has been used to suggest specialist crushing durophagous diets focussing on molluscs, (Barsbold, 1976a). This would be a very specialist diet, especially considering the diversity of oviraptorid species and the fact many derive from arid or semi-arid depositional environments more so than fluvial deposits (Longrich *et al.*, 2010; 2013; Funston *et al.*, 2018).

Most interpretations now focus on some form of herbivorous diet (Smith, 1992). However, many interpretations still contextualise this alongside the supposed strength of the oviraptorid cranium and bite, with authors suggesting this could be adaptive to procure and process a wide range of foodstuffs such as seeds, nuts, fruits, stems, and bark (Zanno and Makovicky, 2011; Longrich *et al.*, 2013; Lü *et al.*, 2013b, Funston and Currie, 2014; Funston and Currie, 2016; Ma *et al.*, 2017; Funston *et al.*, 2018; Ma *et al.*, 2020b), similar to modern parrots (Benavidez *et al.*, 2018), or to shear tough xerophytic vegetation adapted for environments with scarce water (Longrich *et al.*, 2010). It is difficult to speculate on the topic of specialist herbivorous diets as very little is known of the flora in their environment (Fastovsky *et al.*, 1997; Longrich *et al.*, 2010). Oviraptorid mandibles (more than their crania) also bear striking resemblance to those of the extinct, herbivorous dicynodont synapsids (Cracraft, 1971; Osmolska, 1976; Elzanowski, 1999), with their short, deep profile, lack of teeth, and robust dentary symphysis.

To what extent oviraptorids blurred the boundary between herbivory and omnivory (as is frequently the case in extant vertebrates) is uncertain and likely varies by

species (Zanno and Makovicky, 2011).

1.5 Aims and thesis outline

The assertion that the oviraptorid cranium, despite being pneumatic and airy, is adapted for strength and a powerful bite has been put forward by many studies but not objectively tested or quantified. Previous investigation into the functional morphology of the skull of Oviraptoridae and Caenagnathidae has focussed on the mandible, using 2D and 3D finite element analysis to examine performance (Funston and Currie, 2014; Ma *et al.*, 2022), or assessing metrics like mechanical advantage in the jaws (Sakamoto, 2010; Ma *et al.*, 2020a; 2020b). The crania, which are some of the most highly modified and aberrant among Dinosauria, have not yet been studied with the depth and digital methods applied to other dinosaur groups (e.g. Rayfield, 2001; Rayfield *et al.*, 2007; Young *et al.*, 2012; Button *et al.*, 2014; 2016; Cuff *et al.*, 2015; Lautenschlager *et al.*, 2016; Gignac and Erickson, 2017; Taylor *et al.*, 2017; Cost *et al.*, 2020).

In this thesis, I present a detailed investigation of the cranial functional morphology in oviraptorosaurians, particularly focussing on Oviraptoridae (due to a lack of preserved crania in Caenagnathidae) and the early diverging *Incisivosaurus*, in comparison to other theropod dinosaurs.

The overarching aims of this thesis are to:

- Determine if and how the oviraptorosaurian cranium is relatively stronger than crania of other theropod dinosaurs (especially those with inferred herbivorous diets).
- Quantify if oviraptorosaurian crania are adapted to generate comparatively powerful bite force compared to herbivorous theropods.
- Understand how the above aspects of oviraptorosaurian cranial functional morphology link with diet and diversity of functional ecology.

I focus on using digital methods predicated on high quality 3D models of oviraptorosaurian crania accurately restored to in-life condition. I use finite element analysis (FEA) to assess comparative structural strength and performance via suitable metrics (e.g. von Mises stress, total strain energy). I investigate cranial musculature using digital volumetric reconstruction.

Chapter 2 focuses on methodology and the specimens this thesis is chiefly based on. I briefly give background on the techniques used in this work — the application of finite element analysis (FEA) in palaeontology and the reconstruction of soft tissues in fossil taxa — before setting out best practises for the digital retrodeformation of fossil specimens and detailed accounts of the procedures I used to create retrodeformed 3D models of the crania (and mandibles) for the four oviraptorosaurians that are the focus of this thesis.

Chapter 3 presents a direct structural comparison of the oviraptorid cranial morphology with that of other theropods in terms of strength and efficiency through a non-physiological bending test. I test the hypothesis that the peculiar shape of the oviraptorid cranium is an adaptation to better resist bending forces (as may be experienced as the reaction force from a powerful bite) compared with theropod dinosaurs of more conventional cranial morphology.

Chapter 4 presents digital 3D reconstructions of oviraptorosaurian jaw adductor musculature. I test the hypothesis that cranial shortening and expansion of muscle space increases bite forces relatively in Oviraptoridae compared with other herbivorous theropods. I describe and compare oviraptorosaurian jaw adductor muscle anatomy, estimate bite forces in four oviraptorosaurians, compare these with other herbivorous theropod taxa, and assess how the reconstructed jaw adductor muscle anatomy may have constrained the maximal angle of gape in oviraptorosaurian species.

Chapter 5 presents additional FEA scenarios addressing questions of functional morphology, feeding, and diet. I integrate results from the previous two chapters to test the hypothesis that the relative strength of the oviraptorid cranium is great

enough to resist their relatively powerful jaw adductor muscle forces. I also test the effect of accessory feeding scenarios driven by neck musculature on cranial performance, and the influence a keratinous beak covering has on cranial performance in Oviraptoridae.

2 | Methods and specimens

Section 2.1.3 *Digital restoration and retrodeformation of fossil specimens* and Figure 2.2 of this chapter are adapted from part of my contribution to the following publication in *Royal Society Open Science*. My contribution involved developing the skeletal retrodeformation methods, writing the related section of the manuscript, and creating the accompanying figure.

Herbst, E. C., **Meade, L. E.**, Lautenschlager, S., Fioritti, N. and Scheyer, T. M. 2022. A toolbox for the retrodeformation and muscle reconstruction of fossil specimens in Blender. *Royal Society Open Science*, **9**, 220519.

Section 2.2 *Specimen information and associated retrodeformation procedure* is lightly adapted from Supplementary Information 1 of the following publication in *Scientific Reports*; Figures 2.3-2.10 are new. CT-scanned datasets were provided by A. Balanoff. My co-author W. Ma provided the photogrammetric model of the *Incisivosaurus gauthieri* (IVPP V 13326) mandible. I created the retrodeformed skull models and wrote the text of this section. Both authors approved its published version.

Meade, L. E. and Ma, W. 2022. Cranial muscle reconstructions quantify adaptation for high bite forces in Oviraptorosauria. *Scientific Reports*, **12**, 3010.

2.1 Digital methods

2.1.1 *Finite element analysis in palaeobiology*

Finite element analysis (FEA) can be used to predict deformation in a structure under loading (Zienkiewicz *et al.*, 2005). The method simplifies a complex object into a finite number of small, geometrically simple elements which are connected at shared nodes. This makes it possible to quickly but accurately approximate displacement throughout the structure in reaction to loading and depending on its shape, boundary conditions, and material properties, and give related data such as discrete stress or strain values at elements/nodes (Richmond *et al.*, 2005).

Stress (σ) is defined as force per unit area (Nm^{-2}). Strain (ε) is the deformation from an applied load and defined as a change in length divided by original length ($\Delta l/l$). The first of two properties of importance in defining the mechanical performance of a material are principally the Young's modulus (E, the modulus of elasticity), the ability of a material to withstand stretching/deformation in length when under lengthwise tension or compression, given by the ratio of tensile stress (σ) to tensile strain (ε):

$$E = \sigma/\varepsilon$$

The second property is the Poisson's ratio (ν) which is the negative of the ratio between transverse strain (ε_t) and longitudinal strain (ε_l) in the elastic loading direction, i.e. the ratio of the change in width of a material to the change in length as a result of strain:

$$\nu = -\varepsilon_t/\varepsilon_l$$

It is impossible to measure the original material properties of fossilised bone. Studies have used substitute material properties from modern bones of similar histo-

logical structure (e.g. bovine haversian bone; Rayfield, 2001; Button *et al.*, 2016), or from taxa comprising an extant phylogenetic bracket to an extinct species in question (e.g. using crocodilian or avian bone values for non-avian dinosaurs; Lautenschlager *et al.*, 2016). The unknown material properties of extinct forms, simplification of the FE model materials to be isotropic, and other uncertain parameters mean the absolute magnitudes of stress/strain in FEA of fossil taxa cannot be relied upon. Nevertheless, FE models appear to reliably reproduce patterns of stress and strain (Rayfield, 2007; Bright and Rayfield, 2011), and FEA parameters can be set up to assess relative differences in these metrics between fossil forms — for example, scaling models (or input loads) to control for differences in size — or exploring hypothetical morphologies to better understand actual functional morphology.

This is possible as metrics like stress and strain can be biologically relevant measures of performance (Richmond *et al.*, 2005; Rayfield, 2007). Mechanical function is closely linked with the adaptation of skeletal morphologies (Roesler, 1987). Through evolutionary shape change and mechanisms of mechanical adaptation such as bone remodelling (Wolff, 1892; Huiskes *et al.*, 2000; Ruff *et al.*, 2006), the shape of bones is adapted to function energetically efficiently and minimise the chance for structural failure (with the caveat of phylogenetic, ontogenetic, and physical constraints) within a biological system. Thus, as stress and strain are useful indicators of how close a structure is to failure or severe deformation, stress and strain magnitude and distribution can provide information on how well adapted the structure is to different types of loading (Dumont *et al.*, 2005; Rayfield, 2007; Dumont *et al.*, 2009).

The metric of von Mises stress in particular is a good predictor of failure through ductile fracture (Nalla *et al.*, 2003), the model of fracture that applies to failure in bones (most biological materials have some elastic properties; Dumont *et al.*, 2009). Total strain energy, a measure of the energy expended to deform a structure with a given volume, may also be useful in assessing function (Dumont *et al.*, 2009; Tseng and Flynn, 2018). More work efficient structures will store less strain energy and are at

an advantage if selection for energy saving is relevant to a system (likely one of many processes guiding the evolution of a structure).

Through using FEA to assess how fossil structures differently perform (in terms of strength and energy efficiency), we can meaningfully assess hypotheses of ecological function.

2.1.2 *Reconstruction of musculature in extinct taxa*

Bias for harder and more mineralised tissues to fossilise leads to soft tissues being under-represented in the fossil record and poorly understood in many extinct species (Lautenschlager, 2016a). This can create problems when addressing phylogenetic, functional, and ecological questions concerning fossil taxa. Much effort has focussed on reconstructing muscles in extinct tetrapods, particularly cranial musculature (Lautenschlager, 2013), as this has a key function in how an organism interacts with its environment, chiefly its ability to procure and process food. Metrics like bite force (and jaw mechanical advantage) are correlated with dietary ecology (Sakamoto, 2022), and feeding behaviour is closely linked to patterns of macroevolutionary change and co-evolutionary processes (Barrett and Rayfield, 2006).

Efforts to reconstruct the jaw adductor musculature of fossil tetrapods has progressed from identification of lines of action (Adams, 1919; Haas, 1955; Ewer, 1965) and origin–insertion sites (Barghusen, 1973; King, 1981; Holliday, 2009), and the use of skull measurements as a proxy for muscle forces (Thomason, 1991; Wroe *et al.*, 2005), towards physical (e.g. clay; Rayfield, 2001; Mazetta *et al.*, 2009) and digital modelling (Lautenschlager, 2013; Lautenschlager, 2016a; Herbst *et al.*, 2022) and Bayesian phylogenetic predictive methods (Sakamoto, 2022). These tend to be based on assessing an extant phylogenetic bracket (the condition in the closest related living clades) and osteological clues (e.g. muscle scars) to reconstruct the positioning of muscles in fossil specimens to different degrees of inference (Holliday and Witmer, 2007; Holliday, 2009; Gignac and Erickson, 2016). For 3D reconstructions, these in-

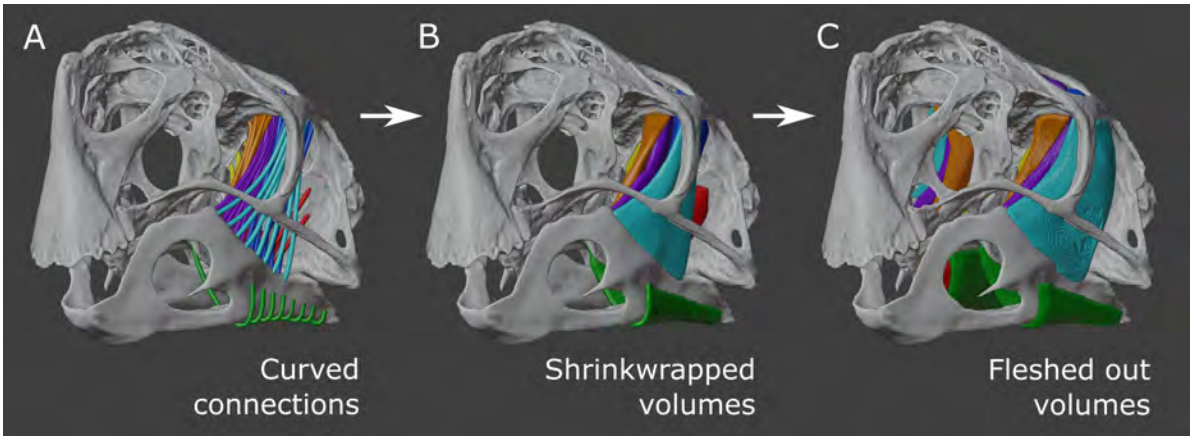

Figure 2.1: Stages of fleshing out a digital reconstruction of jaw adductor musculature in the oviraptorid *Citipati osmolskae*. Muscle origin–insertion paths connected with simple curves (A). Convex hull shrinkwrapped around sets of curved connections (B). Convex hulls grown into volumes filling available space (C).

terpretations can then be digitally "fleshed out" to fill available space within the cranium/jaw with muscular bodies (Lautenschlager, 2013; Gignac and Erickson, 2017) (Fig. 2.1A–C).

Ultimately, this allows for the physiological cross-sectional area of muscles to be measured, which is proportional to their ability to generate contractile force, and typically estimated at 0.3 Nmm^{-2} (Thomason, 1991; Wroe, 2005; Lautenschlager, 2013). However, unknown muscle parameters (chiefly pennation angle and length of muscle fibres; Bates and Falkingham, 2018; though see Lieber, 2022) may require additional correction factors (Thomason, 1991; Wroe et al, 2005; Lautenschlager, 2013) and introduce a degree of uncertainty on top of that from the anatomical reconstruction of muscle arrangement. Such uncertainty in modelling has been demonstrated in mammal crania (Broyde *et al.*, 2021; Bates *et al.*, 2021). Nevertheless, more restrictive cranial architecture in archosaurs, with both an upper and lower temporal bar, may limit the scope for reconstructive inaccuracy in groups such as dinosaurs.

Reconstructed muscle force vectors can feed into further digital functional analyses like FEA (Rayfield, 2001; Rayfield, 2007; Dumont *et al.*, 2009), multibody dynamic analyses (MDA; Bates and Falkingham, 2012; Snively *et al.*, 2013; Lautenschlager *et al.*, 2016; Lautenschlager *et al.*, 2018; Lautenschlager, 2020), and spe-

cialised analyses such as assessing musculo-skeletal constraints on gape (Lautenschlager, 2015; Meade and Ma, 2022). A progression of the method from Lautenschlager (2013) is used in Chapter 4 of this work to reconstruct jaw adductor musculature in oviraptorosaurians and described therein. Muscle force estimates are further used to inform FEA in Chapter 5.

2.1.3 *Digital restoration and retrodeformation of fossil specimens*

The use of 3D data to study fossil material is currently an increasingly popular and dynamic field of research including biomechanical, finite element, and geometric morphometric analyses exploring taxonomic and ecological questions, all predicated on digital 3D models (Cunningham *et al.*, 2014). Techniques to convert fossils into 3D models such as photogrammetry, surface scanning, CT-scanning and other techniques have become common in palaeontological studies (Mallison, 2011; Falkingham, 2012; Cunningham *et al.*, 2014; Díez Díaz *et al.*, 2021). Unfortunately, fossil specimens are often distorted, disarticulated, and/or possess cracks. It is often important to correct morphological distortions, returning them to an "in-vivo" condition before analyses are possible (Molnar *et al.*, 2012; Tschopp *et al.*, 2013; Button *et al.*, 2014; Cuff and Rayfield, 2015; Lautenschlager, 2016b). Such processes have been termed "restoration", for the reassembly or correction of cracks, breaks, and missing elements in fossil specimens, and "retrodeformation", for the correction of more plastic shape distortions (Lautenschlager, 2016b). Many studies have not made a strict distinction between the two terms, and this work will generally employ the latter term, "retrodeformation", to refer to the process of digitally fixing fossils generally. In palaeontological studies, Blender has been most frequently used for rendering high-quality images as it is a powerful ray-tracing software package. Fairly few publications have taken advantage of the power of Blender for mesh creation, manipulation, positioning, and analysing range of motion (Garwood and Dunlop, 2014; Rahman and Lautenschlager, 2016b; Lautenschlager, 2017; Miedema *et al.*, 2020; Herbst *et al.*, 2021; Richards *et al.*, 2021; Meade

and Ma, 2022; DeVries *et al.*, 2022). This study found Blender to be the most effective software package of retrodeformation of the fossil material, with impressive capabilities for rendering attractive figures, performing functional analyses (i.e. the gape analyses of Chapter 4), all while being free and frequently updated. Blender could perform all necessary retrodeformation techniques (i.e. those detailed in Lautenschlager, 2016b) including, but not limited to, correction of cracks, breaks and missing sections, translation and rotation of disarticulated elements, mirroring of material, correction of shear and plastic modes of deformation, and constructing composite models from multiple specimens (see Fig. 2.2).

General guidelines for accuracy were followed for all specimens and are documented here as follows, and all work was performed by a single worker (the author): Working in orthographic view kept objects the same size and proportions regardless of the distance between the viewport camera and the object, allowing for more objective assessment of shape and the use of reference images. Reference images of undeformed specimens, closely related species, or useful schematics were used wherever possible to guide creating material from scratch or editing and preserve objectivity and accuracy. For work in Blender, these were added as objects where they can be resized, rotated, and translated as needed within the window view space. Positioning objects in alignment with the main axes allowed effective use of preset orthographic viewpoints along each axis and for constraining mesh edits and sculpting along certain axes, increasing control and accuracy. Correct model alignment also allowed for easy mirroring of elements, where material was preserved on only one side. On this topic, procedure followed here considered the most objective source for material to replace missing areas is from another symmetrical side/area of the specimen, followed by other specimens of the same species, then closely related specimens. Symmetry within biological structures or other indicators (such as orbit shape being roughly circular; Arbour and Currie, 2012); Cuff and Rayfield, 2015) were considered as objective evidence of deformation. Such justification was assessed for every edit on the geometry of a speci-

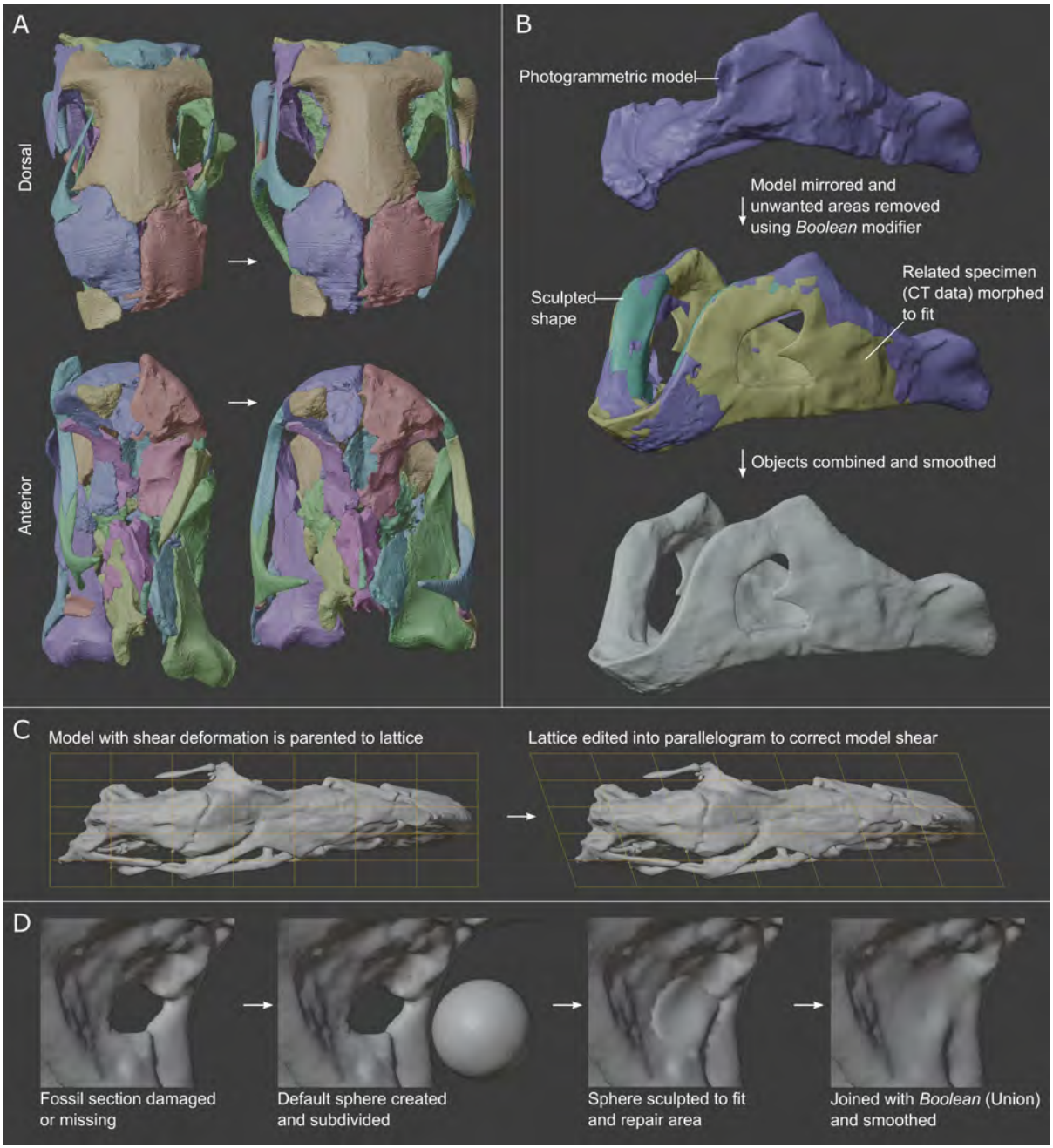

Figure 2.2: Examples of retrodeformation processes in Blender. Elements were correctly repositioned as separate objects (A). Combination and smoothing of photogrammetric, CT, and sculpted models to produce a single mesh (B). Lattice modifier used to correct model shear (C). Sculpting a sphere to reconstruct a missing part of the fossil, followed by a Boolean union modifier to join the meshes (D).

men. Care was taken with multiple remeshing/smoothing as these deteriorated surface details of specimens.

A more comprehensive guide to the retrodeformation of fossil material (focussing on Blender) is given in Herbst *et al.* (2022), greatly derived from the lessons learned in fixing the specimens presented in this chapter. Information on each specimen that was retrodeformed from CT-scanned data to form the basis of this thesis is now given and figured.

2.2 Specimen information and associated retrodeformation procedure

The four oviraptorosaurian skull models described and figured here form the basis of the data for this PhD thesis. They were provided by A. Balanoff in the form of CT-scan image sets (as described below) and fortunately represent both early diverging oviraptorosaurians (*Incisivosaurus*), and later diverging oviraptorid oviraptorosaurians of varying skull morphotypes (the more ornamented *Citipati* and the decreasingly ornamented *Khaan* and *Conchoraptor*). Many additional potential specimens I visited were highly incomplete, damaged, or largely reconstructed, and the creation of high-quality 3D models from CT-data (necessary for internal morphology in pneumatic oviraptorid crania) even from well preserved specimens is very time consuming. Any efforts towards this were further obfuscated by the COVID-19 pandemic which made organising the scanning of additional specimens logistically unfeasible in the time frame of the project.

Institutional abbreviations: **IVPP**: Institute of Vertebrate Paleontology and Paleoanthropology, Chinese Academy of Sciences, Beijing, China; **MPC**: Mongolian Palaeontological Centre, Ulaanbaatar, Mongolia; **PIN**: Paleontological Institute, Russian Academy of Sciences, Moscow, Russia; **STM**: Shandong Tianyu Museum of Nature, Pingyi, China; **ZPAL**: Institute of Paleobiology, Polish Academy of Sciences, Warsaw, Poland.

2.2.1 *Incisivosaurus gauthieri IVPP V 13326*

Provenance

The specimen was collected from the Lujiatun Unit of the lowermost Yixian Formation, near the Luijitun village of Beipiao City, Liaoning, China. These strata date to the Early Cretaceous (Barremian–Aptian; 125.9 Ma in Chang *et al.*, 2017; older than 128 Ma in Swisher *et al.*, 2002). The specimen comprises a cranium, anterior mandibles, a postdentary mandible fragment figured by Xu *et al.* (2002) but potentially lost (Balanoff *et al.*, 2009), and a partial cervical vertebra.

CT-Scanning

IVPP V 13326 was scanned at Stony Brook University medical scanning facility in 2004. The cranium was scanned along the coronal axis (parameters unknown) yielding 404 DICOM of 512 x 512 pixel resolution. Slice spacing is 0.31 mm, and x-, y-resolution is 0.188 mm. The CT-dataset was initially used by Balanoff *et al.* (2009) for cranial and endocranial descriptions of *I. gauthieri* (endocranial cast subsequently used in Balanoff *et al.*, 2013; Balanoff *et al.*, 2014; Balanoff *et al.*, 2016; Balanoff *et al.*, 2018).

Condition and taphonomic damage

The cranium is nearly complete on the right side and very incomplete on the left (Fig. 2.3D). Much of the cranial interior is still enclosed in matrix as removal would endanger the specimen (Balanoff *et al.*, 2009). The cranial elements and teeth present are relatively well preserved and undistorted; however, there are numerous cracks, breaks, and holes present in elements. The first two teeth are present on both sides. Posteriorly, teeth are generally present on at least one side. Displacement of individual elements and fragments is typically minor and mostly confined to slight movement on the sagittal plane. Much of the right jugal-quadratojugal bar has been extensively physically reconstructed, showing little detail of its original morphology. There is a promi-

nent break through the middle of the braincase and adductor chamber, separating the posteriormost quarter of the skull, visible roughly following the frontal–parietal contact on the skull roof. The plane of the break runs anterodorsally to posteroventrally. The cranium is sheared approximately 15° with the left side displaced anteriorly relative to the right. This is most clearly seen in the shape of the braincase, the relative positions of the lacrimals, postorbitals, and the frontal–parietal contact (and associated break) (Fig. 2.3E). The cranium has been laterally compressed (Balanoff *et al.*, 2009) (Fig. 2.3A,B,E,F). The posterior half is especially slender and the foramen magnum is tall and thin. It seems reasonable that lateral compression of the skull caused both the braincase to collapse in on itself and the strap-like and thin postorbital–squamosal and jugal–quadratojugal connections, and the plate-like quadrate–pterygoid flange to collapse medially, pivoting inwards posterior to where they are better supported mediolaterally in the orbital region by the skull roof via the frontal (Fig. 2.3E) and the palate via the ectopterygoid (Fig. 2.3F).

The mandible of IVPP V 13326 (not CT-scanned) is preserved partially in two pieces; an anterior section comprising both rami extending posteriorly to just beyond the termination of the mandibular fenestra and a posterior piece representing the right articular surface and retroarticular process (unable to be located; potentially lost).

Cranial retrodeformation procedure

The IVPP V 13326 CT-dataset is the oldest and lowest resolution dataset used in this study. The images, though relatively low resolution, show good contrast between bone, teeth, and matrix, along with presumed neurovascular spaces in the premaxilla and braincase. The fossil bone and tooth material was segmented in Avizo Lite (version 9.3.0). Pulp cavities inside the teeth were also segmented. A large number of elements required mirroring from the more complete right side to the left and/or repositioning. Individual elements/fragments were segmented and assigned into their own label fields. As the purpose was restoration (rather than osteological description) this

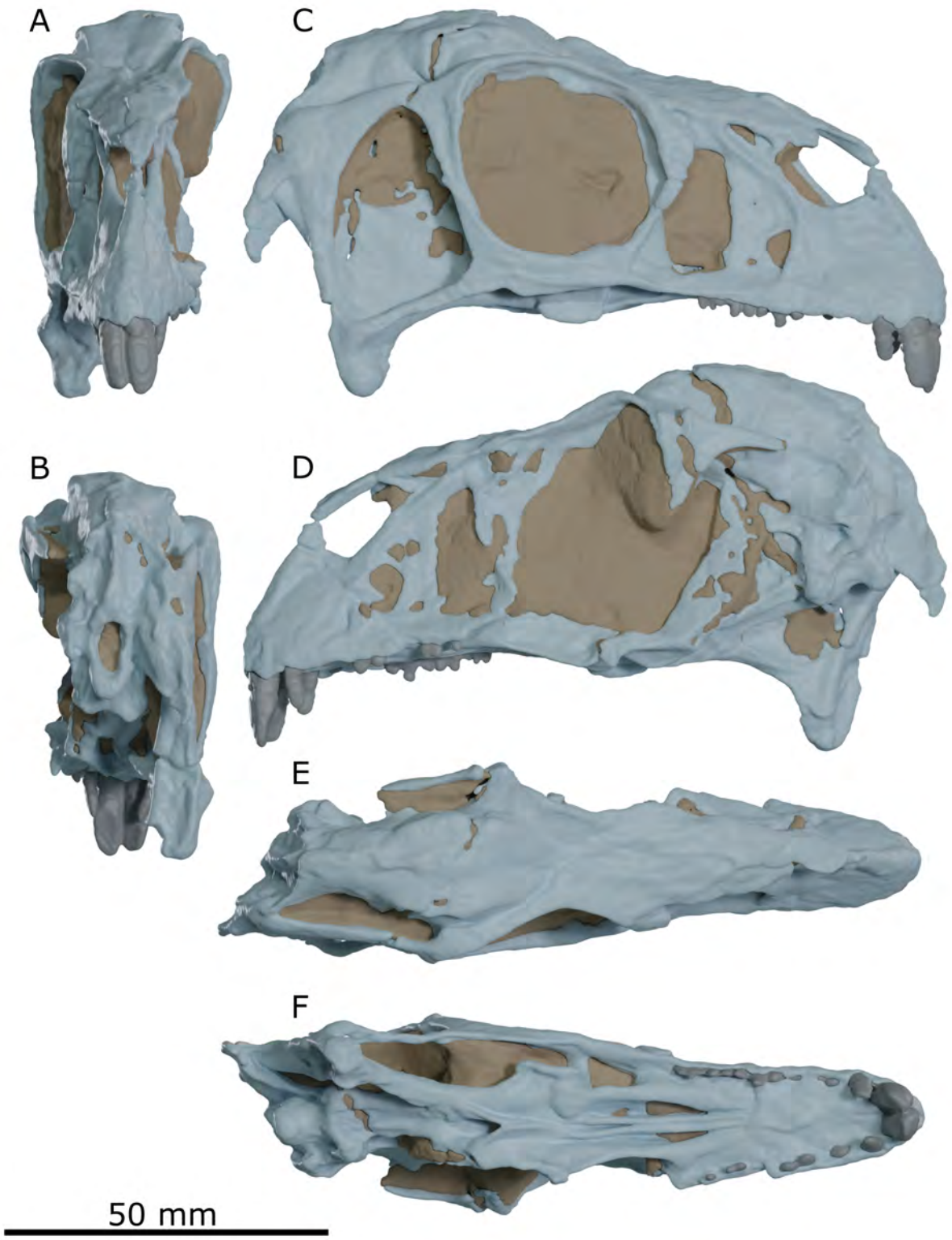

Figure 2.3: *Incisivosaurus gauthieri* (IVPP V 13326) cranium before retrodeformation, rendered to show fossil material (blue-grey) and matrix (brown), in anterior (A), posterior (B), right lateral (C), left lateral (D), dorsal (E), and ventral (F) views. Note the much more complete right side, shear displacing the left side anteriorly, and likely compression most affecting the posterior third of the cranium.

was loosely focussed on individual bones, but more focussed on identifying 'retrodeformational units' that required repositioning/mirroring work.

To correct the deformational shear, all label fields were subjected to the Avizo 'Shear' module (setting 15 degrees); the CT-dataset was already aligned for this to work correctly. Label fields of those units that required mirroring were duplicated and the relevant axis reversed. Surface meshes generated from the label fields were then repositioned in the project window using the transform editor to restore the cranium as far as possible. Repositioning of cranial elements was done in relation to a base that consisted of the most complete part of the skull in which elements were correctly articulated. This consisted of the left premaxilla, right premaxilla (lower bigger part), right maxilla, right nasal (without nares fragment), left lacrimal, left jugal, left palatine, vomer, left pterygoid (+epipterygoid), left quadrate (lower bigger part), left quadratojugal (lower bigger part), parabasisphenoid, left postorbital, both frontals (and including parts of the orbitosphenoids and laterosphenoids), and all segmented teeth, including internal replacements.

Initially, another complex of respectively correctly positioned bones was repositioned onto this base. These were the posterior bones of the skull, comprising much of the braincase and adductor chamber, slightly displaced from the main base of skull bones by the prominent anterodorsal–posteroventral break. These comprised both parietals, supraoccipital, the lateral braincase elements of both sides, basioccipital, left quadrate (upper smaller part), left quadratojugal (upper smaller part), and left squamosal. The only other repositioned elements that were not mirror images of those from the more complete right side were a smaller upper part of the left premaxilla (?upper part of maxillary process) and a fragment forming the dorsal margin of the nares.

Those bones required to be mirrored, due to absence on the left side, were mirrored from the right and correctly positioned in the following units:

- A unit comprising the mirrored right quadrate (bigger lower part), right quadratojugal (bigger lower part), right pterygoid (including epipterygoid), right ectoptery-

goid, and the right palatine (left not used so the unit fit correctly as detailed below).

- A unit comprising the mirrored right squamosal, right quadrate (smaller upper part), right quadratojugal (smaller upper part).
- Mirrored right jugal.
- Mirrored posterior of the right parietal and right paroccipital process.
- Mirrored right portion of the parabasisphenoid to complete its missing left side.
- Mirrored teeth from right side, not present on left, to complete left tooth row.

Though all of the left palatine, all of the left nasal, much of left maxilla (though in two parts), much of the left postorbital, the medial half of left lacrimal, and anterior half of left pterygoid+epipterygoid, are actually preserved on the left side, fitting these bones to correctly contact their neighbours once their missing neighbours had been mirrored from the right side proved problematic, especially where forming complex contacts such as in the palate. These bones listed were therefore not used in the assembled model. Instead, mirrored duplicates of the right palatine, right nasal, right maxilla, right lacrimal, and right pterygoid+epipterygoid (which were all more complete anyway) were used and improved overall model quality (Fig. 2.4C).

The medial half of the articular surface of the quadrate was still missing (absent from the right quadrate and its mirrored element). To model the geometry of this small missing area without being too speculative, the corresponding region was scaled and added to the assembled *Incisivosaurus* skull from the quadrate of a photogrammetric 3D model of *Avimimus* specimen PIN 3907/3 (model produced in Agisoft Photoscan (version 1.3.4) using 107 photos from a Nikon D3300 DSLR camera with a 50 mm lens). This seemed reasonable as the two species are early diverging oviraptorosaurians and have a similar quadrate morphology. It is also a very small region, likely of little importance in muscle reconstruction or finite element analyses (FEA), and essentially an aesthetic addition.

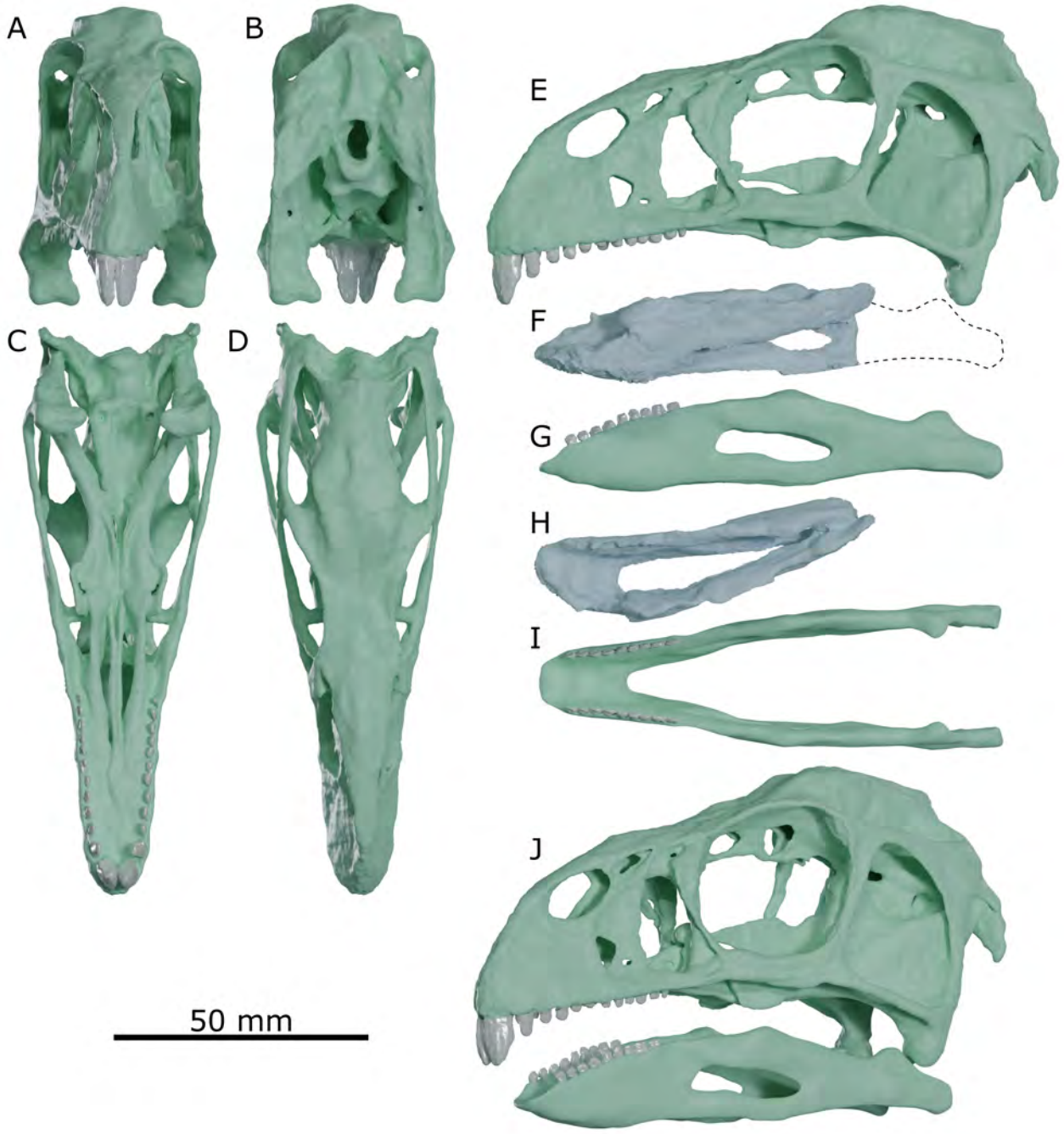

Figure 2.4: *Incisivosaurus gauthieri* (IVPP V 13326) cranium (A–E) after retrodeformation and mandible (F–I) before and after retrodeformation. Cranium shown in anterior (A), posterior (B), ventral (C), dorsal (D), and left lateral (E) views. Mandible shown in left lateral view (F) as a photogrammetric model (grey) with drawn outline of missing (described but lost) posterior fragment, followed by left lateral view of retrodeformed mandible (G). Photogrammetric model of mandible (H) and retrodeformed model (I) also shown in dorsal view. An oblique view of the retrodeformed cranium and mandible when articulated is also given (J).

The repositioned component surfaces of the cranium were scanned back to label fields using the 'Scan to Volume' Avizo module and combined back into one label field using the 'Relabel' module. Cracks, breaks, and smaller missing areas were then corrected with the 'paintbrush' tool and interpolation using the segmentation editor (see Lautenschlager, 2016b). During this step, some additional minor asymmetry was corrected in the premaxilla with the paint tool, the incisor-like teeth were repositioned with a slight rotation to make them more symmetrical (including their pulp cavities), minor asymmetry in the dorsal arch of the nares was corrected, and teeth 3 and 4 were slightly elongated to more resemble other examples of *Incisivosaurus* (STM22-6, previously assigned to *Similicaudipteryx*, now *I. gauthieri* (Xu, 2020).

The unsheared and restored skull, though now complete and usable for further analyses, is still likely deformed mediolaterally – the model is remarkably slender. Balanoff *et al.* (2009) remarked the endocranial cast of the skull to be extremely mediolaterally compressed, and the foramen magnum to be tall and slender. Other closely related early diverging oviraptorosaurians (such as *Avimimus portentosus* and *A. nemegtensis*; Funston *et al.*, 2018) possess very circular foramina magna, as do related theropods of similar size such as dromaeosaurids. To reduce the amount of mediolateral compression in the *Incisivosaurus* model with some degree of objectivity, the Avizo model surface was imported into Blender (version 2.90.0) and the postorbital region we identified as most prone to compression (see Condition and taphonomic damage section) was expanded laterally using a 'Lattice' deform modifier until the foramen magnum was of a similar height:width ratio (11:10) as *Avimimus portentosus* PIN 3907/3 (Fig. 2.4B), also an early diverging oviraptorosaurian. At this stage, the jugal–quadratojugal bar (which in IVPP V 13326 is physically restored with matrix and cement) was also straightened out as it bends to be medially convex, likely erroneously obfuscating space for musculature (Fig. 2.4C). This final retrodeformed model was imported back into Avizo and, through the 'Scan to Volume' module, used to replace the posterior morphology of the model that was segmented into different materials (bone,

teeth, pulp) so the model would be divided into these different materials for use in future FEA study.

Mandibular retrodeformation procedure

A 3D model of the anterior mandible piece of IVPP V 13326 was created through photogrammetry; 115 photos taken with a Nikon D7200 DSLR camera were processed in Agisoft PhotoScan (version 1.0.4.1847). The posterior piece was created in Blender (version 2.90.0) using box modelling (see Rahman and Lautenschlager, 2016), guided by images of the piece figured by Xu *et al.* (2002), as this piece was not observed in person and may be lost.

In Blender, the relatively undeformed dentary symphysis (Fig. 2.4H) was positioned in the correct position for a closed jaw in relation to the cranium. The less complete left ramus of the mandible was removed and the right ramus was retrodeformed to follow the margin of the retrodeformed skull's premaxilla, maxilla, and jugal, manipulating the mesh mediolaterally with the 'Elastic Deform' brush in Blender's 'Sculpt Mode'. The adjusted ramus was then mirrored to the left side (Fig. 2.4I). The box modelled posterior piece was also mirrored from right to left (Fig. 2.4G,I). The retrodeformed anterior section of the mandible and the two rear pieces, once positioned correctly with regard to each other and the cranium, were exported as PLY files and imported into Avizo.

These surfaces were converted to a single label field with the 'Scan to Volume' module and the missing sections between front and rear were interpolated in the segmentation editor. Minor holes and imperfections in the photogrammetric model were reconstructed with the "paintbrush" tool. Nine dentary teeth were created as a separate material in this label field in the correct places based on where the photogrammetric model showed their presence/sockets. The exact internal size of the teeth (the extent of their roots) couldn't be ascertained as the photogrammetric model doesn't include internal detail, so the rearmost nine teeth in the upper jaw were mirrored dorsoventrally

and inserted into the dentary as a reasonable approximation (Fig. 2.4G,I).

Finally, the complete mandible model was transferred from Avizo to Blender and widened in the same way the cranium's mediolateral compression was corrected, using a 'Lattice' deform modifier (Fig. 2.4I).

2.2.2 *Citipati osmolskae MPC-D 100/798*

Provenance

MPC-D 100/798 was discovered at the Ukhaa Tolgod locality of the Djadokhta Formation of Mongolia (Clark *et al.*, 2001; Clark *et al.*, 2002). The Djadokhta Formation dates to the Campanian, Late Cretaceous (Dashzeveg *et al.*, 2005; Dingus *et al.*, 2008; Hasegawa *et al.*, 2009). The specimen comprises a nearly complete skeleton and is the holotype for *C. osmolskae*. MPC-D 100/798 was first described by Clark *et al.* (2001) in a rapid communication focussing almost solely on the cranium and mandible. *Khaan mckennai* was first described in the same publication.

CT-Scanning

The mandible, hyoid, stapes, and scleral ossicles were removed from the cranium 'block' prior to CT-scanning in 1997 for Clark *et al.* (2002). The CT-dataset used in this study includes only the cranium of MPC-D 100/798 and was generated at the University of Texas High-Resolution X-ray CT Facility for A. Balanoff in 2010. Scan parameters were 250 kV and 2.8 mA, yielding 371 JPG images of 1024 x 1024 pixel resolution. Slice spacing is 0.25 mm and x-,y-resolution is 0.196 mm. This dataset was used in a number of studies into palaeoneurology, and cranial and brain shape evolution (Balanoff *et al.*, 2013; Balanoff *et al.*, 2014; Balanoff *et al.*, 2016; Balanoff *et al.*, 2018).

Condition and taphonomic damage

The MPC-D 100/978 cranium is remarkably well preserved. All cranial elements are present; it was the first oviraptorosaurian cranium described preserving the stapes and epipterygoid bones (Clarke *et al.*, 2001). Few cranial bones show obvious taphonomic damage. Areas of matrix are left unprepared within the endocranial and pneumatic spaces and support the delicate jugal–quadratojugal bars, parasphenoid process, epipterygoids, paroccipital processes, and the interfenestral bars of the maxilla within the accessory antorbital fenestrae.

Breaks/holes are minor and present in: the left quadratojugal; left frontal just anterior to the supratemporal fenestra; the right frontal just anterior to the supratemporal fenestra and just anterior to the contact with the right postorbital; the middle of the ventral surface of the right pterygoid; and in the anterior of the ventral surface of the left pterygoid (Fig. 2.5). Fragments are missing from the dorsal margin of the right orbit, the articular surface of the left quadrate, and from the left paroccipital process (Fig. 2.5B,E,F). There is a loose contact between the right postorbital and frontal (Fig. 2.5E). A small nook in the left jugal near the posteroventral corner of the orbit is identified as a possible pathology by Clark *et al.* (2002) (Fig. 2.5C). The posterior half of the cranium has a slight left/right shear most visible in the relative positions of the supratemporal fenestrae, quadrates, and paroccipital processes – positioned relatively anteriorly on the left, posteriorly on the right (Fig. 2.5E).

Cranial retrodeformation procedure

The CT-dataset shows poor contrast in some areas between fossil and matrix, primarily around the parabasisphenoid, interior of the beak, and within pneumatic areas (where no internal bony struts can be seen). Bone material was segmented from the remaining matrix in Avizo Lite (version 9.3.0), additionally guided by notes and photographs from physically examined oviraptorosaurian specimens. Small cracks, break, holes, and loose contacts were corrected through interpolation in the Avizo segmentation editor

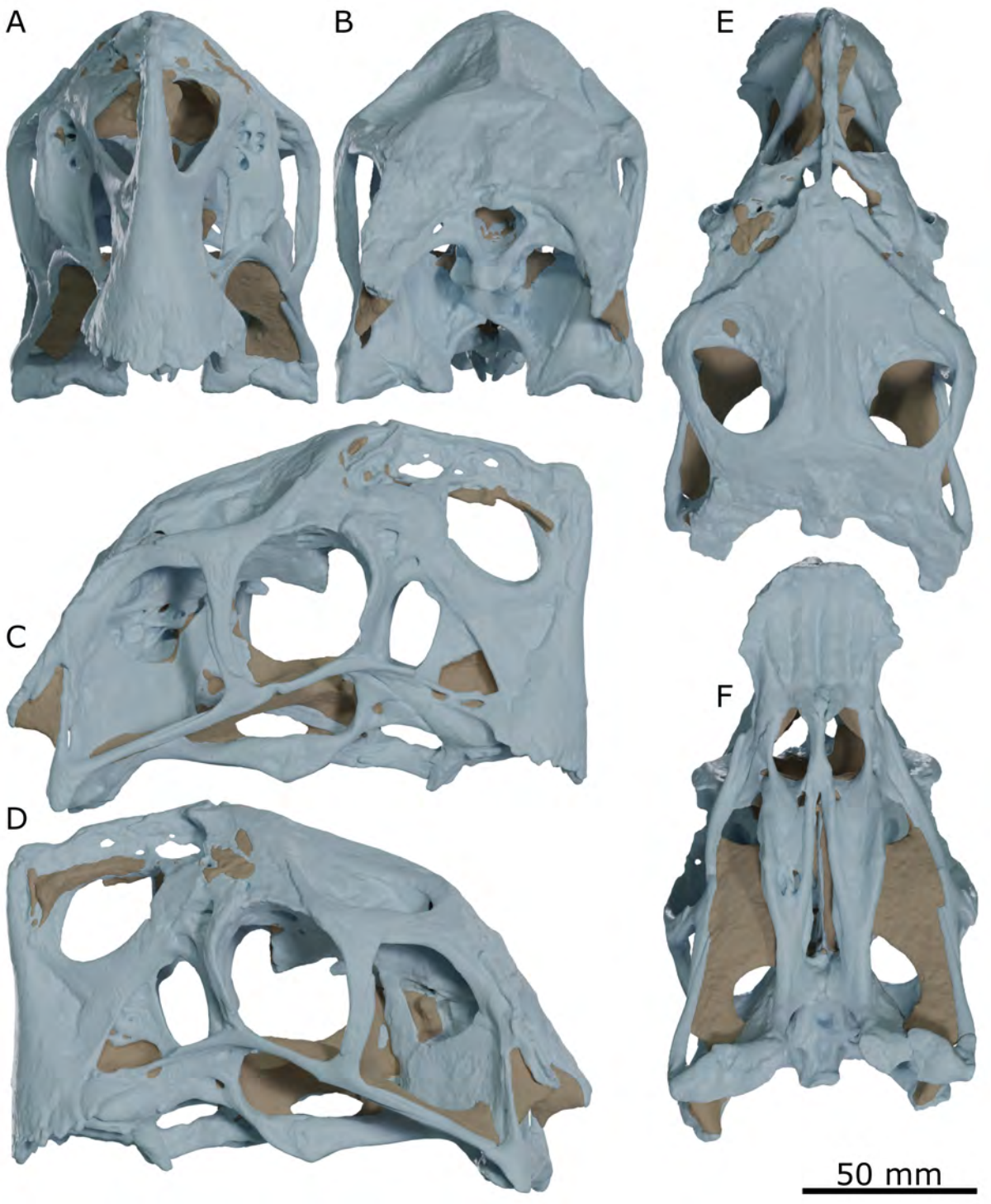

Figure 2.5: *Citipati osmolskae* (MPC-D 100/798) cranium before retrodeformation, rendered to show fossil material (blue-grey) and matrix (brown), in anterior (A), posterior (B), right lateral (C), left lateral (D), dorsal (E), and ventral (F) views. Note the shear deformation visible in the dorsal, ventral and posterior views.

(see Lautenschlager, 2016b). The larger missing fragments of the right orbit and left quadrate and paraoccipital process were corrected with mirroring: the label field file was duplicated and relevant mirroring axis flipped in the crop editor so a mirror image selection could be made in the segmentation editor and transferred directly into the main model. The matrix-filled pneumatic areas of the left nasal were too delicate and complex to be distinguished in CT, so the corresponding structure of the right (more thoroughly physically prepared) was also mirrored to replace them (Fig. 2.6A,D).

Final correction of the minor asymmetry (left/right shear in posterior half) was initially performed in Landmark, but it became clear Blender offered better results. Using Blender's 'Lattice' modifier to adjust each side of the posterior half of the cranium, symmetry was restored to the positions of the paroccipital processes, supratemporal fenestrae, and postorbital bars (Fig. 2.6).

Mandibular retrodeformation procedure

The mandible of *Citipati osmolskae* specimen MPC-D 100/798 is not included in the CT-dataset and was unable to be studied in person due to the COVID-19 pandemic. The mandible of the Dzamyn Khondt, oviraptorid MPC-D 100/42 (previously misidentified as *Oviraptor philoceratops*, likely *Citipati* sp.; Clark *et al.*, 2002) had been studied in person and modelled photogrammetrically, so was modified to be used as a stand-in. The photogrammetric model was constructed in Agisoft Photoscan (version 1.3.4) and comprised 2 chunks (of 61 and 37 photos) from a Nikon D3300 DSLR camera with a 50mm lens.

The morphology of the MPC-D 100/42 mandible is similar to that of MPC-D100/978 but mediolaterally thinner and of a slightly different geometry in lateral view. The photogrammetric model of the MPC-D 100/42 mandible was exported to Blender and the 'Lattice' deform modifier was used to slightly alter its shape and scale to closely match reference images of the MPC-D 100/978 mandible. The result articulated and fit convincingly with the retrodeformed cranium (Fig. 2.6F). We are confident in using

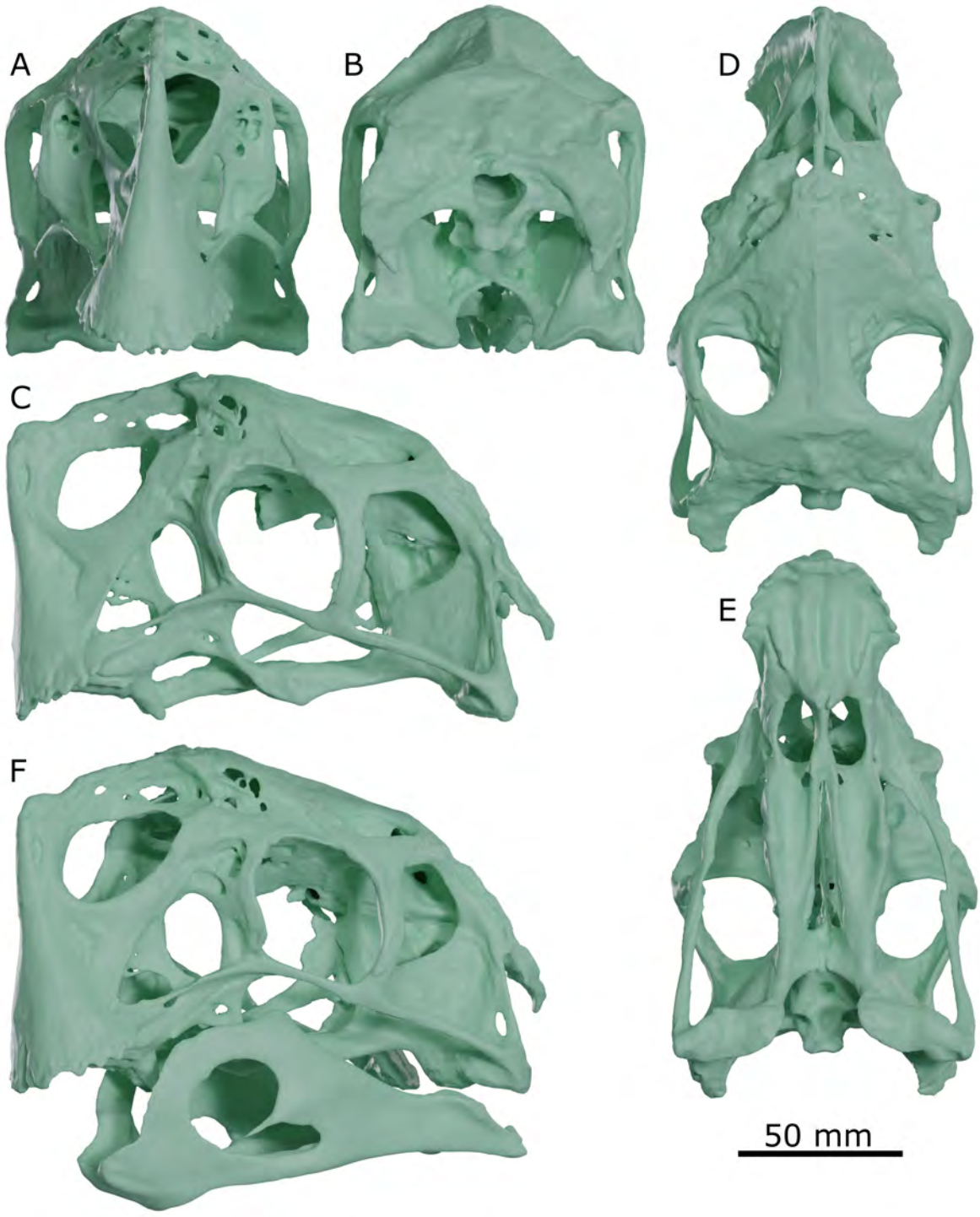

Figure 2.6: *Citipati osmolskae* (MPC-D 100/798) cranium and mandible after retrodeformation. Cranium shown in anterior (A), posterior (B), left lateral (C), dorsal (D), and ventral (E) views, and with mandible in position in oblique view (F).

this altered mandible as a stand-in due to its many similarities with the *C. osmolskae* holotype mandible, the opportunities we had to study its bony morphology in person (muscle attachments sites), and the fact the cranium is the more important component in our method as the bony constraint of muscle size.

2.2.3 *Khaan mckennai MPC-D 100/973*

Provenance

MPC-D 100/973 was discovered at the Ukhaa Tolgod locality of the Djadokhta Formation of Mongolia (Clark *et al.*, 2001; Balanoff and Norell, 2012), of Campanian, Late Cretaceous age (Dashzeveg *et al.*, 2005; Dingus *et al.*, 2008; Hasegawa *et al.*, 2009). MPC-D 100/973 is one of three nearly complete skeletons referred to *K. mckennai* (along with MPC-D 100/1002) by Clark *et al.* (2001) when the species was first described and MPC-D 100/1127 designated the holotype. MPC-D 100/973 differs from MPC-D 100/1002 and MPC-D 100/1127 as its cranium and mandible have been freed from the rest of its skeleton (permitting CT-scanning). The other two specimens are borne intact on large sandstone slabs. Additional information on the provenance and preparation of MPC-D 100/973 can be found in Balanoff and Norell (2012).

CT-Scanning

MPC-D 100/973 was scanned at the University of Texas High-Resolution X-ray CT Facility for A. Balanoff in 2009. The specimen comprising cranium, mandible, hyoids, and an axial vertebra was scanned along the coronal axis in two passes and the slices were reassembled digitally. Scan parameters were 210 kV, 0.14 mA, yielding 912 JPG images of 1024 x 1024 pixel resolution. Slice spacing is 0.1637 mm and x-, y-resolution is 0.076 mm. The CT-dataset was initially used by Balanoff and Norell (2012) for osteological description of *K. mckennai* (endocranial cast subsequently used in Balanoff *et al.*, 2013; Balanoff *et al.*, 2014; Balanoff *et al.*, 2016; Balanoff *et al.*, 2018).

Condition and taphonomic damage

The scanned portion of MPC-D 100/973 containing the cranium and mandible (and hyoids and a cervical vertebra) is heavily matrix-bound – the fossil material is very fragmentary (Fig. 2.7). It preserves essentially all cranial bones in articulation, though many are damaged, deformed, and/or slightly out of position. Most notably, the premaxilla–nasal arch is missing, as are significant portions of the maxillae, pterygoids, palatines, parabasisphenoid, and epipterygoids (Fig. 2.7C,D). The skull roof is heavily fragmented and crushed, obfuscating the pneumatic areas within (Fig. 2.7E). The cranium (and likely also mandible) is dorsoventrally compressed compared to MPC-D 100/1127 and MPC-D 100/1002 (Balanoff and Norell, 2012). This is most noticeable in the shape of the orbit and foramen magnum (Fig. 2.7B), and the lack of a rounded skull roof (Fig. 2.7D). Much of the dorsoventral compression appears to be associated with breaks in the nasal processes of the premaxilla, lacrimal bones, postorbital bars, parabasisphenoid and quadrates. The roof and posterior of the skull may have tilted ventrally, rotating around the break in the lacrimals, with the nasal processes of the premaxilla breaking anteriorly as the postorbital bars fractured and the quadrates (and associated elements) cracked posteriorly (Fig. 2.7C,D).

The mandible is complete apart from minor cracks and small missing areas (in the surangulars and angulars) and displacement of some of the medial elements (left splenial and angular) (Fig. 2.7C,D,F). It is articulated with the cranium but displaced posteriorly, exacerbating an overbite. It has likely been dorsoventrally compressed similarly to the cranium (Fig. 2.7C,D).

Cranial retrodeformation procedure

Relatively poor contrast between fossil and matrix, and the heavily damaged and fragmented thin cranial bone, make this CT-dataset the most challenging of the four to work with. Individual cranial bones were not segmented, instead, elements or fragments that required repositioning/mirroring work were segmented as ‘retrodeformational units’ in

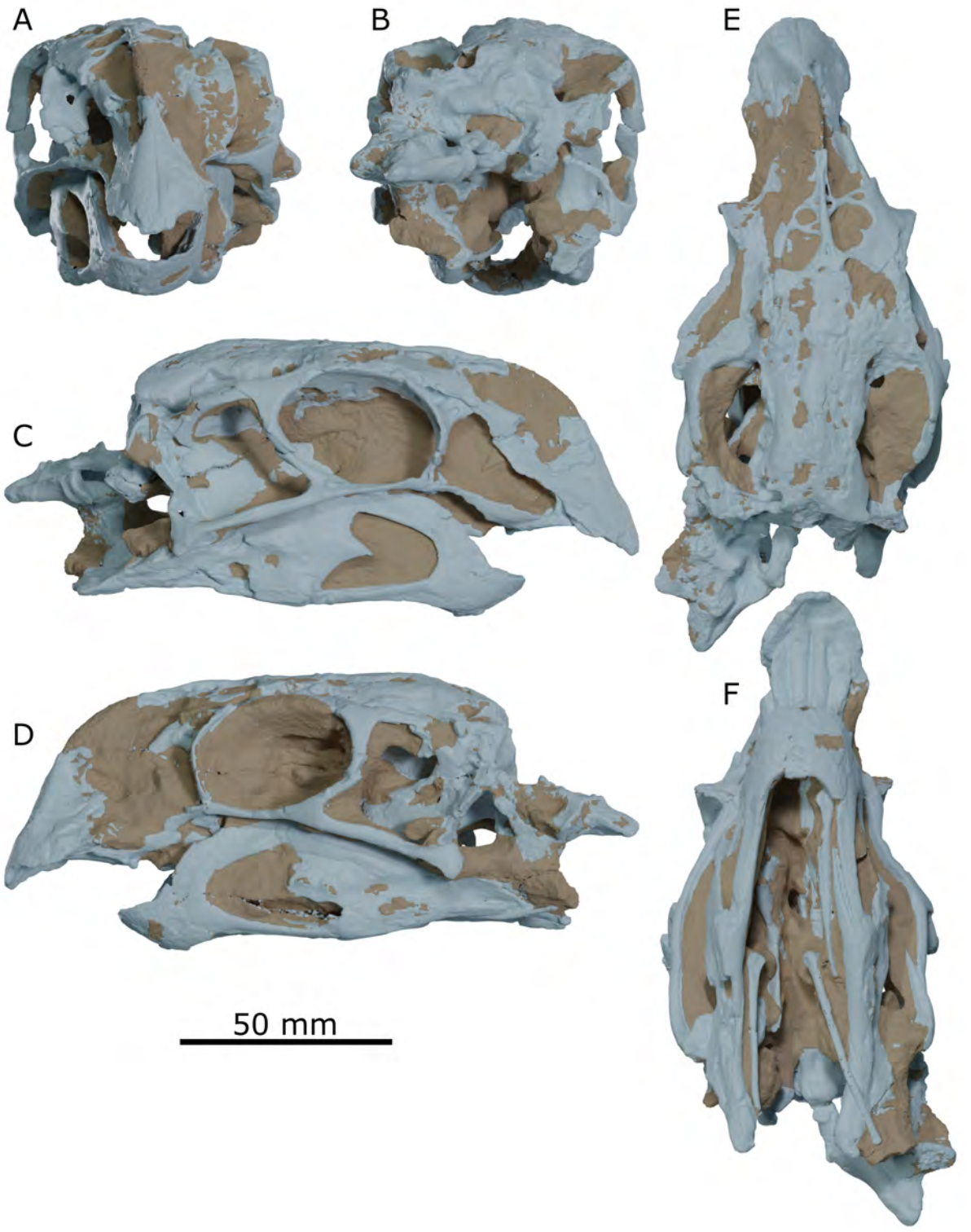

Figure 2.7: *Khaan mckennai* (MPC-D 100/973) cranium and mandible before retrodeformation, rendered to show fossil material (blue-grey) and matrix (brown), in anterior (A), posterior (B), right lateral (C), left lateral (D), dorsal (E), and ventral (F) views. Note the dorsoventral compression of the cranium visible in how the bones of the orbit have collapsed.

Avizo Lite (version 9.3.0). The largest of the units, comprising the most complete and articulated series elements, included the posterior nasals, the frontals, parietals and majority of the braincase, the latero- and orbitosphenoids, the occipital region dorsal to the foramen magnum, the medial part of the exoccipitals and their contribution to the paroccipital processes, the dorsal part of the squamosals and postorbitals (the supratemporal bar), the dorsal part of the lacrimals, and the dorsal part of the nasal process of the premaxilla. This series of elements was used as a base onto which the other displaced elements were repositioned (Fig. 2.8).

The only other articulated unit comprised mostly ventral elements including the rest of the premaxilla, the maxillae, right jugal, right quadratojugal, the parasphenoid rostrum, vomer, left ectopterygoid, left palatine, and left pterygoid. All other repositioned units were individual cranial elements or fragments thereof. These included four parts of the left jugal, two parts of the left postorbital (jugal process), the left quadratojugal, two parts of the right postorbital, the left quadrate (upper part missing), the right quadrate (upper part missing), part of the right quadrate flange, two fragments of the right paroccipital process, and the basioccipital and lower part of the braincase immediately within the foramen magnum. Additionally, mirrored duplicates of the left ectopterygoid, left palatine, and left pterygoid were created to replace their missing right counterparts (Fig. 2.8D).

Surfaces meshes were generated from separate label fields for each unit that required repositioning. The surface meshes were then repositioned in the Avizo project window using the transform editor to restore the cranium as far as possible, before the surfaces were scanned to volumes and relabelled back into a single label field.

The cranium still had a number of significantly missing areas. The missing regions of the occiput, paroccipital processes, quadrate flanges and squamosals were replaced through a mix of interpolation using the Avizo paint tool and deforming elements from these regions taken from *Conchoraptor gracilis* specimen MPC-D 100/3006, which is closely related, using the Avizo transform editor (Fig. 2.8B).

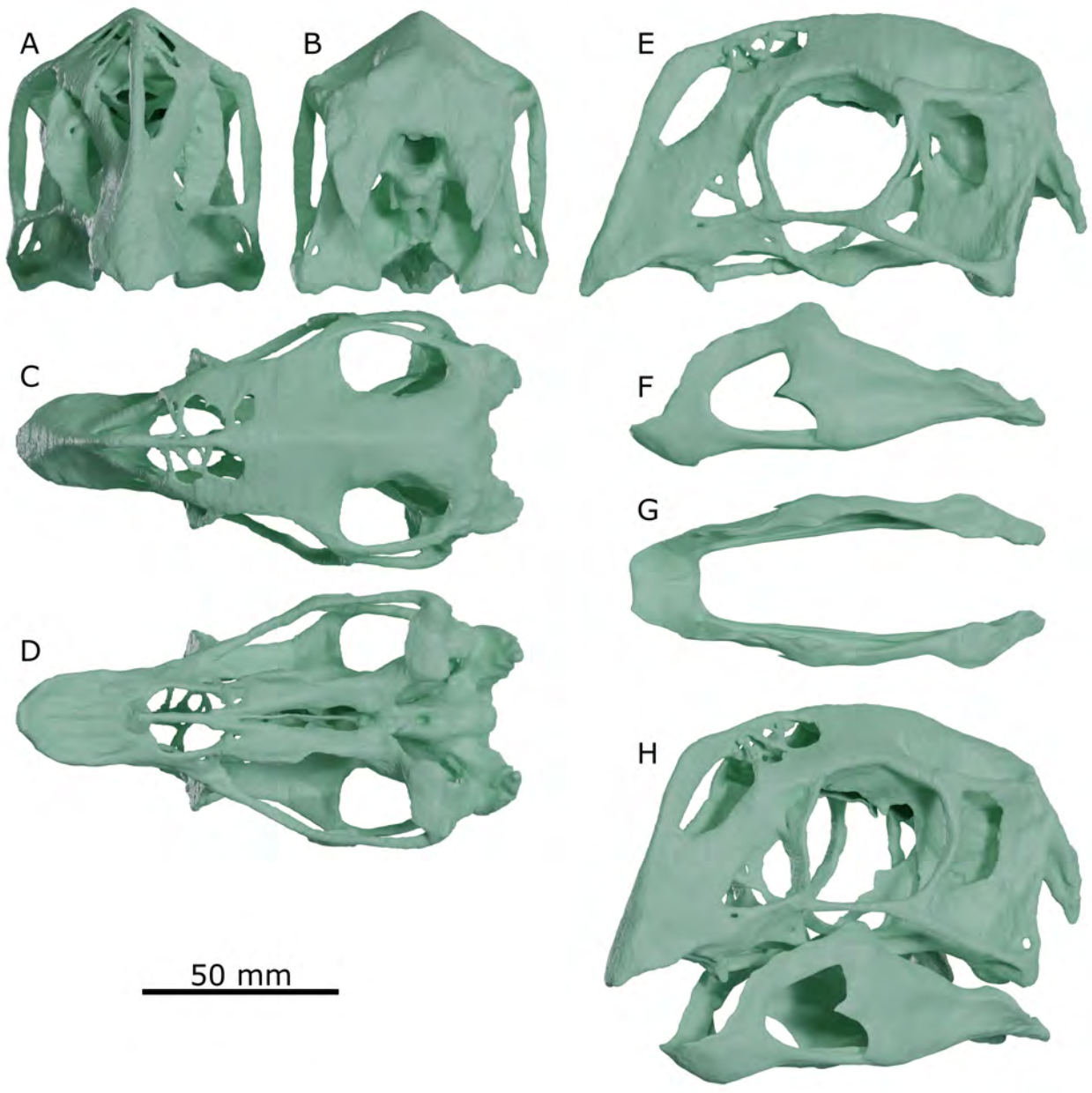

Figure 2.8: *Khaan mckennai* (MPC-D 100/973) cranium (A–E) and mandible (F, G) after retrodeformation. Cranium shown in anterior (A), posterior (B), dorsal (C), ventral (D), and left lateral (E) views. Mandible shown in left lateral (F) and dorsal (G) views, and articulated in position with the cranium in oblique view (H).

These elements were scanned to volumes so the 3D information could be manipulated and made to fit in the segmentation editor. Similarly, more minor parts of the vomer, epipterygoids, and basisphenoid (Fig. 2.8E), were taken from *Citipati osmolskae* MPC-D 100/798, and edited to replace missing regions – as these elements were not well preserved in *C. gracilis* MPC-D 100/3006 either. The missing parts of the nasal process of the premaxilla were created using the 'paintbrush' tool and interpolation (Fig. 2.8E).

A surface was generated of the now essentially complete cranium and exported from Avizo into Blender as, though the repositioning of elements had somewhat increased the height of the dorsoventrally compressed cranium, the cranium was still not of a similar height:length ratio as MPC-D 100/1127 and MPC-D 100/1002 (Balanoff and Norell, 2012), likely indicating the effect of some more plastic deformation in addition to the now corrected displacement of elements. This was corrected in two steps.

The height:width measurements of the orbit of the almost retrodeformed MPC-D 100/973 were compared to MPC-D 100/1127 and MPC-D 100/1002; an increase in cranial height of 1.16x was required. This was achieved by transforming the retrodeformation in Blender, correcting the orbit proportions. Subsequently, the cranial roof was still slightly too flat, reducing overall cranial height, when compared to reference images of MPC-D 100/1127 and MPC-D 100/1002. This compression of the dorsal pneumatic cavities within the skull roof of MPC-D 100/973 was corrected by dragging the dorsal surface of the frontals and parietals higher, until the pneumatic space within was increased (Fig. 2.8E). This completed the retrodeformed geometry of the MPC-D 100/973 cranium, giving it a morphology much more similar to the other *K. mckennai* specimens.

Mandibular retrodeformation procedure

The CT-dataset of *Khaan mckennai* MPC-D 100/973 was the only CT-dataset studied substantially including a mandible, which was nearly complete. The retrodeformation of the mandible was fairly straightforward and mostly done in Avizo. The elements of the mandible were easier to segment separately than the cranial elements of this dataset, as they were more loosely articulated and closer to the specimen's surface. The more complete right splenial was mirrored to replace the left, as were parts of the surface of the right articular. This was done by duplicating the label field, flipping its axes in the crop editor, and then selecting the relevant element/area in the segmentation editor, changing back to the unmirrored original label field where the selection could be moved/added in. The left angular was repositioned slightly, also in the segmentation editor. Minor areas of the surface of other bones were mirrored and cracks and breaks filled using the 'paintbrush' tool and interpolation in Avizo's segmentation editor (Fig. 2.8F–H).

A surface was created and exported to Blender, where the 'Lattice' deform modifier was used to correct minor asymmetry. The height of the mandible was also increased by the same correction factor as the cranium (1.16x) as the influence of plastic deformation in the form of dorsoventral compression was likely to be similar (Fig. 2.8F.

2.2.4 *Conchoraptor gracilis MPC-D 100/3006 and ZPAL MgD-1/95 composite*

MPC-D 100/3006

Provenance

MPC-D 100/3006 is from the Khulsan locality of the Baruungoyot Formation, Mongolia (Funston *et al.*, 2018). The Baruungoyot Formation dates to upper Campanian–lower Maastrichtian age, overlying the Djadokhta Formation (Gradziński and Jerzykiewicz, 1974a, 1974b; Fanti *et al.*, 2012). The specimen comprises the posterior half of the

cranium and a small posterior section of the left mandibular ramus, along with assorted postcranial material (Balanoff, 2011; Balanoff *et al.*, 2014).

CT-Scanning

MPC-D 100/3006 was CT-scanned at Ohio University for A. Balanoff, yielding 995 DICOM images of 698 x 460 pixel resolution. The voxels are cubic with a resolution of 0.092 mm. The CT-dataset was initially used for endocranial description of *C. gracilis* (Balanoff *et al.*, 2014; endocranial cast also used in Balanoff *et al.*, 2013, Balanoff *et al.*, 2016, and Balanoff *et al.*, 2018).

Condition and taphonomic damage

The cranium (posterior half) is internally bound by matrix, supporting disarticulated elements (Fig. 2.9G). The mandibular fragment is unconnected (Fig. 2.9K). Missing anterior elements include the nasals, majority of the lacrimals, maxillae, premaxillae, vomer, palatines, and the anterior of the ectopterygoids and pterygoids (Fig. 2.9K,L). All elements of the posterior half of the cranium are preserved (apart from areas of the epipterygoids and parabasisphenoid) but many are fractured into two or three pieces and/or disarticulated (Fig. 2.9H,J,K,L). This appears caused by a mediolateral compression that has fractured, displaced, rotated, and overlapped elements rather than deforming them plastically. This may be linked to the suggestion of Balanoff *et al.* (2014) that IGM 100/3006 was not fully mature skeletally as its braincase sutures are not completely fused.

The MPC-D 100/3006 specimen (and CT-scan) also includes a small posterior fragment of the left mandibular ramus and retroarticular process (Fig. 2.9K).

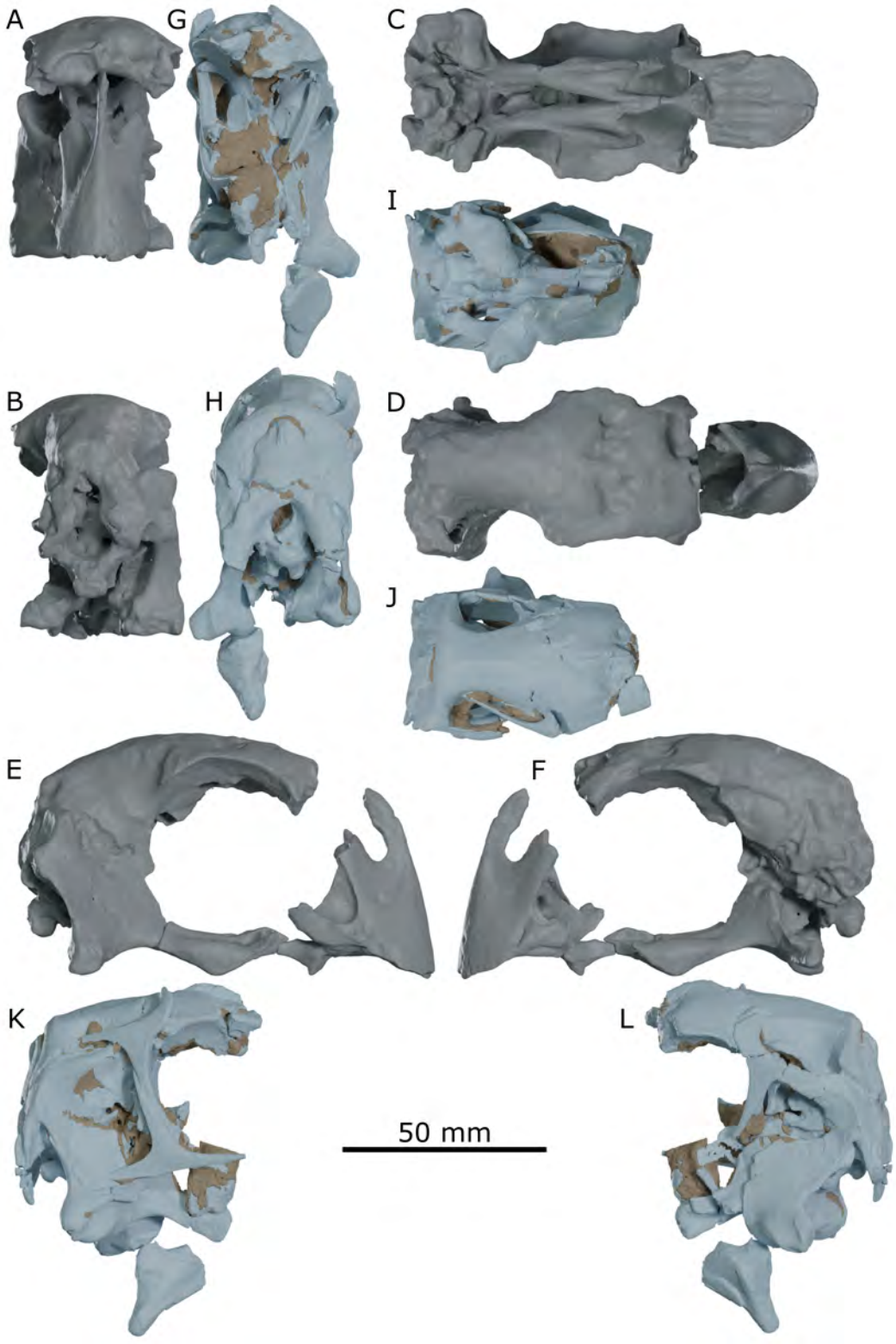

Figure 2.9: *Conchoraptor gracilis* (MPC-D 100/3006 (A–F) and ZPAL MgD-I/95 (G–L)) cranial parts before retrodeformation, rendered to show fossil material (blue-grey) and matrix (brown) segmented from CT-data, and photogrammetric models (of ZPAL MgD-I/95) in grey. Specimens are shown in anterior (A, G), posterior (B, H), ventral (C, I), dorsal (D, J), right lateral (E, K), and left lateral (F, L) views. Note the slightly smaller relative size of the ZPAL MgD-I/95 specimen (G–L).

ZPAL MgD-I/95

Provenance

ZPAL Mg-D I/95 is from the Hermiin Tsav locality of the Baruungoyot Formation, Mongolia (Kundrát, 2007; Kundrát and Janáček, 2007), of upper Campanian–lower Maastrichtian age (Gradziński and Jerzykiewicz, 1974a; 1974b; Fanti *et al.*, 2012). The specimen comprises a nearly complete cranium and mandible (Osmólska, 1976).

Photogrammetry

The cranium is separated into four sections: the braincase and the right epipterygoid, squamosal, and quadrate; the premaxillae, maxillae, and anterior vomer; the right pterygoid, posterior vomer, and ectopterygoid; and the left pterygoid, ectopterygoid, and quadrate. Each section was photographed using a Nikon D3300 DSLR camera with a 50mm lens, borne on a tripod and triggered remotely, either moving the camera or the specimen itself. Photogrammetric models were generated in Agisoft Photoscan (version 1.3.4) by processing 'chunks' representing the specimen photographed positioned in different orientations which were then aligned and merged:

The braincase section was photographed by moving the camera. Three separate chunks were processed comprising 58, 58, and 54 photos. The premaxilla section was photographed by moving the camera. Three chunks of 45, 41, and 39 photos were processed. The right pterygoid section was photographed keeping the camera static, rotating the specimen on a turntable. Two chunks of 36 and 34 photos were processed. The left pterygoid section was also photographed using a turntable. Two chunks of 38 and 37 photos were processed.

Condition and taphonomic damage

The cranium of ZPAL Mg-D I/95 was figured whole by Osmólska (1976) but is now in four parts (as described above). The overall morphology of the cranium is undistorted

(Fig. 2.9E,F). It is missing parts of the maxillary and nasal processes of the premaxillae, lateral areas of the maxillae, the regions surrounding the choanae (Fig. 2.9C,E,F). It notably lacks the majority of the lacrimals and the elements of the temporal, postorbital, and jugal arches (Fig. 2.9E,F). The posterior of the parietals, supraoccipital, and most of the basicranium are also missing, and the left lateral wall of the braincase is heavily damaged (Kundrát, 2007; Kundrát and Janáček, 2007) (Fig. 2.9B,F). Numerous other areas are damaged in minor ways, such as pitting in the cranial roof (though this may in fact be the damaged remnants of pneumatic fenestrae in the frontals; Funston, 2019) (Fig. 2.9D). Minor areas of matrix are left within the premaxillae, maxillae, and in and around the braincase (Fig. 2.9B,E,F).

The mandible comprises the left dentary, disarticulated left splenial, and much of the right postdentary ramus (mostly the surangular and articular, the angular is essentially absent) (Fig. 2.10F). The left dentary and right postdentary elements are held together by matrix in the correct relative position (Fig. 2.10G).

Composite model

Cranial retrodeformation procedure

The MPC-D 100/3006 CT-dataset offers the greatest detail of the four used in this study. All elements (and fragments thereof) could be segmented separately in Avizo Lite (version 9.3.0) with relative confidence – useful as the main focus of retrodeforming this specimen was repositioning individual elements and fragments. Surfaces were generated for each separately segmented cranial element and exported to Blender where they were repositioned to articulate as properly as possible (see Fig. 2.2A).

Mirrored duplicates were made of the right jugal, anterior of the right pterygoid, the two parts of the right quadratojugal, and left ventrolateral surface of the basisphenoid (where pterygoids connect), to fill in for where these elements were missing on the other side (Fig. 2.10D). The right squamosal and right laterosphenoid were also mirrored, though they had counterparts on the left, as this resulted in a better overall

skull articulation (there may have been some plastic deformation on their left counterparts). Similarly, minor edits using the 'Elastic Deform' brush in 'Sculpt Mode' were made on thinner areas of the squamosals and quadrate flanges to improve bone articulation. This resulted in an essentially completely retrodeformed posterior half of the skull, with only minor gaps between elements in places. Nevertheless, MPC-D 100/3006 does not preserve any elements rostral to the frontals, jugals, and pterygoids.

These elements of *C. gracilis* were sourced from specimen ZPAL MgD-1/95, which was studied in person and modelled photogrammetrically. The 3D models of ZPAL MgD-1/95 were imported into Blender and positioned to articulate and overlay the retrodeformed MPC-D 100/3006 in the correct position. Measurements of ZPAL MgD-1/95 from Balanoff *et al.* (2014) suggest this specimen is very similar in size to MPC-D 100/3006. Observations presented here suggest it is slightly bigger, especially considering the damage to the occipital region of ZPAL MgD-1/95, and the supposed status of MPC-D 100/3006 as a sub-adult (Balanoff *et al*., 2014). The retrodeformed MPC-D 100/3006 was scaled up 1.149x to articulate correctly with ZPAL MgD-1/95 (Fig. 2.10E).

The composite specimen still lacked some material, chiefly much of the lacrimals, the anterior jugals, the ectopterygoids, palatines, vomer, and small details of the maxilla. These elements were imported into Blender from the 3D retrodeformed model of *Khaan* specimen MPC-D 100/973, and correctly positioned and modified with the 'Elastic Deform' brush in 'Sculpt Mode' to function as a replacement (Fig. 2.10E).

With the elements from MPC-D 100/3006, ZPAL MgD-1/95, and the modified *Khaan* retrodeformation all occupying the correct positions in Blender, all were exported separately back to Avizo. They were converted to label fields with the same reference field so they were occupying the same relative positions — active selections in the segmentation editor could therefore be directly transferred between the label fields. In this way, a final complete composite was created in the segmentation editor

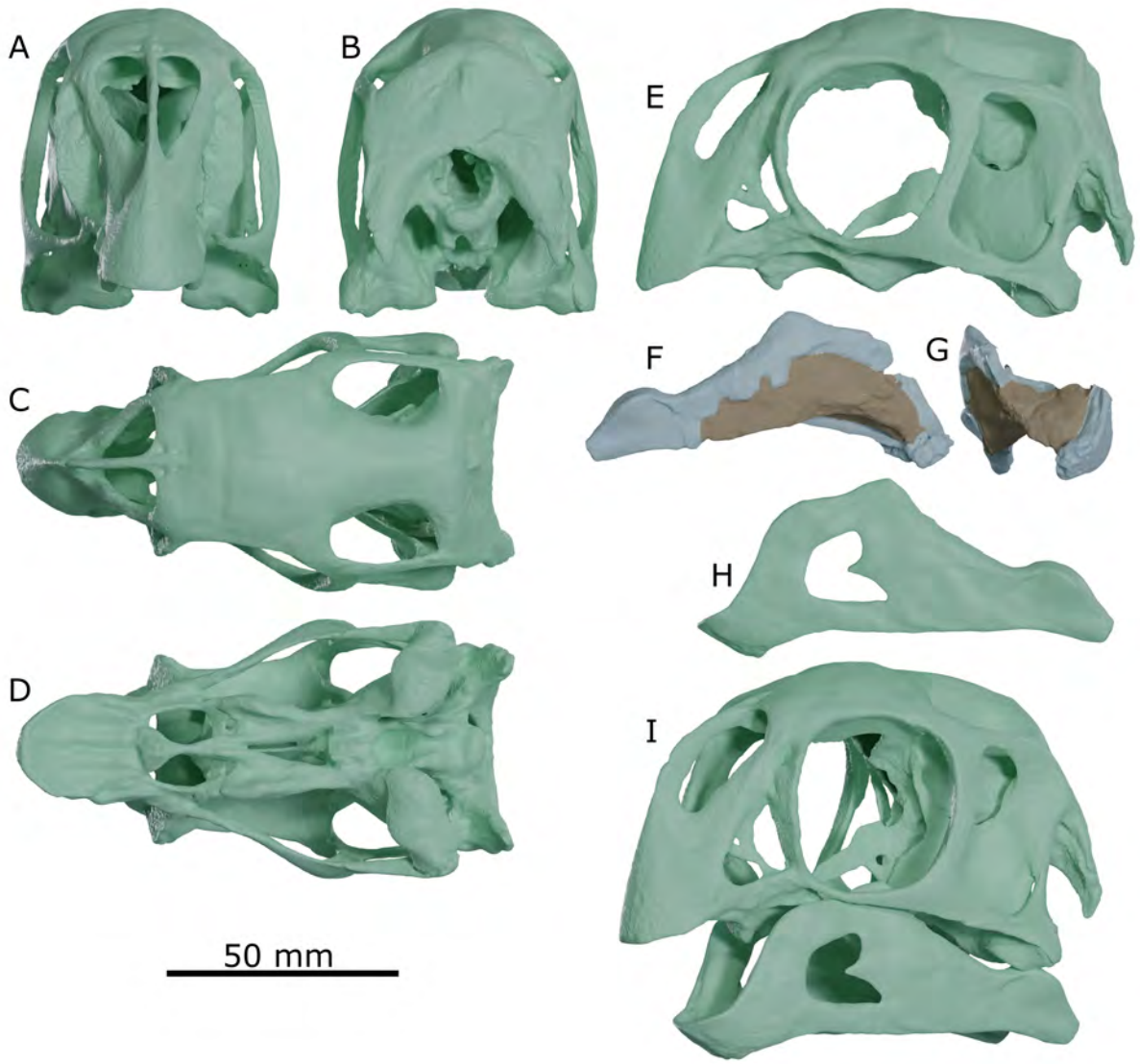

Figure 2.10: *Conchoraptor gracilis* composite cranium and mandible model after retrodeformation and mandible of ZPAL MgD-I/95 before retrodeformation. Composite cranium shown in anterior (A), posterior (B), dorsal (C), ventral (D), and left lateral (E) views. Photogrammetric model of damaged ZPAL MgD-I/95 mandible shown in right lateral (F) and anterior (G) views, roughly coloured to show bone (blue-grey) and matrix (brown). Retrodeformed mandible shown in left lateral view (H) and in articulation with the cranial model in oblique view (I).

adding necessary sections from ZPAL MgD-1/95 and the modified *Khaan* elements to the main articulated section of MPC-D 100/3006; any minor missing sections or loose element connections were corrected using the Avizo 'paintbrush' segmentation tool and interpolation, or the Avizo selection grow function (Lautenschlager, 2016b). Minor asymmetries in the orientation of the quadrates and paroccipital processes of this final model were corrected in Blender using the 'Lattice' deform modifier.

This final retrodeformed specimen gives a very similar cranial length to that given by Osmólska (1976) for the intact ZPAL Mg-D I/95 (Fig. 2.10).

Mandibular retrodeformation procedure

The mandible fragment from ZPAL MgD-1/95 includes the anteriormost part of the dentary and a disarticulated left splenial of the left mandibular ramus, and the dorsal parts of the length of the surangular with a fairly complete articular region of the right mandibular ramus. The fragment was digitised with photogrammetry, using the same camera set-up as the ZPAL MgD-1/95 cranial material. The model was constructed from 31 photos in Agisoft Photoscan (version 1.3.4).

The fragment was overlaid with a mirrored duplicate and the matrix was removed to give a good overall morphology of the mandible. 3D material from the mandible of *Khaan* was deformed to the shape of the *Conchoraptor* mandible, using a 'Lattice' modifier, to fit the missing lateral areas of the surangular and angular, and fill in for the medial mandibular morphology, giving the rami a realistic thickness (Fig. 2.10H,I). Some sculpted shapes were used to complete any final gaps. These various components were combined with a Boolean (Union) modifier and the overall retrodeformed shape matched reference images of other *Conchoraptor* specimens (MPC-D 100/20 and MPC-D NatGeo.2018.036a) and fit the retrodeformed skull. The model also closely resembled a number of specimens identified as *Conchoraptor gracilis* among the collections of the MPC that have been recovered from poachers and not yet assigned specimen numbers.

3 | Strength and comparative performance of the oviraptorid cranium in response to bending

My contribution to this chapter involved leading all parts of the research, including data collection, analysis, interpretation of results, as well production of the manuscript, figures, and tables. Feedback was given on interpretation of results and drafts of the manuscript by S. Lautenschlager, R. Butler, and M. Pittman.

3.1 Introduction

The cranium of oviraptorid oviraptorosaurians has a unique morphology among Dinosauria and is the most aberrant part of their skeleton (Smith, 1992; Osmólska *et al.*, 2004; Ma *et al.*, 2020b). This is the consequence of a suite of contrasting features. Their crania depart from a 'standard' tetanuran theropod architecture with expanded pneumatic spaces (Clark *et al.*, 2002; Kundrát and Janáček, 2007; Balanoff and Norell, 2012), a delicate often ornamented skull roof (Barsbold, 1988; Osmólska *et al.*, 2004; Lü *et al.*, 2004; Lü *et al.*, 2016; Lü *et al.*, 2017; Funston *et al.*, 2020b), thin rod-like jugals and quadratojugals (Clark *et al.*, 2002, Lü *et al.*, 2015; Wang and Hu, 2017), and large orbits (Kundrát and Janáček, 2007) that make the cranium lightweight and open. However, where other theropods crania are dominated by a longer rostrum (often most of the cranial length) with significant contribution from the maxillae, the rostrum

in oviraptorids is shortened (to approximately a third or quarter of the cranium) and dominated by more massive premaxillae. In addition, the robust toothless premaxilla and palate, and expanded space for musculature suggest adaptation towards high bite forces in Oviraptoridae (Barsbold, 1977; 1986; Currie *et al.*, 1993; Ma *et al.*, 2020b). The question remains if and how these features of the highly modified oviraptorid cranium integrate into a structure that is adapted to support powerful jaws.

If the distinctive morphology of the oviraptorid cranium is an adaptation towards producing high bite forces, we would predict the cranial structure will be better able to resist bending forces and experience lower mechanical stresses when compared to theropods of a more conventional skull shape. Oviraptorid crania likely differ from other theropod dinosaurs in their response to the biomechanical challenge of handling stresses from biting. This chapter presents a structural comparison of cranial performance in oviraptorid oviraptorosaurians *Citipati osmolskae* (Clark *et al.*, 2001), *Khaan mckennai* (Clark *et al.*, 2001), and *Conchoraptor gracilis* (Barsbold, 1986); these species were selected for the reasons described in Chapter 2.

Their cranial performance is compared with that of early diverging oviraptorosaurian, *Incisivosaurus gauthieri*, the earliest diverging member of Oviraptorosauria from the Early Cretaceous of China, which has a cranial morphology that is intermediate between typical non-oviraptorosaurian tetanuran theropods and the more unorthodox oviraptorids (Xu *et al.*, 2002; Balanoff *et al.*, 2009). *Incisivosaurus* still has premaxillary and maxillary teeth (including odd elongate incisor-like front teeth). Heightening and shortening of the oviraptorid cranium makes the orbit appear relatively large, and a degree of rostral shortening (the premaxilla and maxilla contribute roughly equally to form half the cranial length) gives *Incisivosaurus* a relatively large orbit, but the cranium is not dorsoventrally expanded. *Incisivosaurus* has a more typical theropod jugal shape (Xu *et al.*, 2002; Balanoff *et al.*, 2009; Sullivan and Xu, 2017), not the rod-like form of the oviraptorids (Clark *et al.*, 2002, Lü *et al.*, 2015). The bones of its skull roof are pneumatised but to a lesser extent than in Oviraptoridae (Kundrát and Janáček,

2007; Balanoff *et al.*, 2009).

These four oviraptorosaurians are also compared with carnivorous and herbivorous theropods of a more 'standard' cranial morphology: *Allosaurus fragilis* (Marsh, 1877), *Erlikosaurus andrewsi* (Barsbold and Perle, 1980), and *Ornithomimus edmontonicus* (Sternberg, 1933). *Erlikosaurus* and *Ornithomimus* present an interesting comparison to the oviraptorids as they also represent theropod groups – Therizinosauroidea and Ornithomimosauria – that have adapted towards herbivory (Zanno and Makovicky, 2011; Ma *et al.*, 2021) and are partially (*Erlikosaurus*) or fully (*Ornithomimus*) edentulous (Sternberg, 1933; Lautenschlager, 2013; Cuff and Rayfield, 2015).

Finite element analyses (FEA) of 3D models of the crania of these species can assess cranial strength and efficiency in response to bending forces, comparing cranial functional performance (Ross, 2005; Rayfield, 2007; Dumont *et al.*, 2009). The hypothesis tested here is that oviraptorid cranial morphology, adapted as part of a system to produce powerful sustained bite forces, will be stronger and more efficient in response to bending compared with the earlier diverging oviraptorosaurian *Incisivosaurus* and other non-oviraptorosaurian theropods.

This study focuses on directly comparing strength and efficiency using scaled applied loads, a non-physiological strength test independent of muscular and behavioural differences, to assess and directly compare the general performance of different cranial shapes. Similar approaches have previously been used to examine cranial function in other dinosaur groups (Rayfield, 2011; Button *et al.*, 2014; Button *et al.*, 2016; Lautenschlager *et al.*, 2016). The use of physiologically derived loads in FEA (from cranial muscle reconstructions) is presented in Chapter 5, focussing more on how each species may have performed in different feeding scenarios and questions of comparative functional ecology.

3.2 Methods

Avizo Lite (version 9.3.0) was used to generate 3D surfaces of retrodeformed oviraptorosaurian cranial models (see Chapter 2 for retrodeformational procedure) using 'unconditional smoothing 3'; this smoothing setting balanced producing meshes with a clean geometry with minimal loss of information in delicate structures of the model. Using the Avizo simplification editor, cranial models were simplified to <400,000 triangular faces, a number high enough to provide a density of tetrahedral elements great enough for sufficiently detailed FEA results (Bright and Rayfield, 2011) but without excessive file size (for faster analytical speed and easier data processing). Cranial meshes were checked to be manifold and cleaned in the Avizo mesh editor, correcting intersecting faces, face orientations, and triangles with large aspect ratios and small dihedral angles. Table 3.1 gives the final face counts of the retrodeformed 3D cranial models used in the FEA.

Solid mesh models were created in Hypermesh (version 13.0.110), converting the cranial surface meshes to a structure of four-noded tetrahedral elements (tet4). The number of tet4 elements in each model is given in Table 3.1. Cranial models of *Allosaurus* and *Erlikosaurus* were supplied by S. Lautenschlager as Hypermesh files that had been used in previously published FEA studies (Lautenschlager *et al.*, 2013; Lautenschlager *et al.*, 2016; Rahman and Lautenschlager, 2017; Montefeltro *et al.*, 2020). The *Ornithomimus* model was supplied by A. Cuff, which had also been used in previously published FEA and muscle reconstruction studies (Cuff and Rayfield, 2015; Bestwick *et al.*, 2021). Experimentally derived material properties were assigned in Hypermesh to the bone and teeth (for dentulous crania) components of each cranial model based on extant alligator mandibles (E = 20.49 GPa, υ = 0.40) (Zapata *et al.*, 2010; Lautenschlager *et al.*, 2013) and extant crocodile teeth (E = 60.40 GPa, υ = 0.31) (Creech, 2004; Reichel, 2010; Lautenschlager *et al.*, 2013). These were considered isotropic and homogenous.

Table 3.1: Surface and volumetric measurements of retrodeformed cranial models used for FEA and information on their mesh geometries.

Cranial model (Genus)	Surface area (mm^2)	Volume (mm^3)	Face count	Tetramesh elements	Force applied (N)
Incisivosaurus	23185	21500	382551	1879557	100.0
Citipati	83100	137631	394540	1830266	358.4
Khaan	39037	52092	381842	2002012	168.4
Conchoraptor	35336	45904	380980	2024584	152.4
Allosaurus	804496	6213307	354322	1764510	3469.9
Erlikosaurus	124014	203474	391888	915853	534.9
Ornithomimus	77949	103010	399370	1642940	336.2

The cranial models were constrained at four points on the articular surface of each quadrate (to represent the stability of the jaw joint during biting) and three points on the occipital condyle (to represent bony/muscular support of the cranium). This scenario appeared to best model the stability of the cranium without over-constraining the structure. Constraints on the quadrates alone produced excessively high stresses throughout the pterygoid and pterygoid ramus of the quadrate, obfuscating the distribution of stress patterns in other structures of the skull. Constraints on the paroccipital processes in addition to the quadrates and occipital condyle (additionally modelling the stability of postcranial musculature on the cranium during biting) gave very similar results to only constraining the quadrates and occipital condyle but increased stresses in the parietals and paroccipital processes themselves. The results of sensitivity testing these different constraint scenarios are presented in Appendix A.

For this comparative bending test, extrinsic loads were applied perpendicular to the palate. These forces were scaled to the cranial model surface area (stress scales with area; Dumont *et al.*, 2009), up from an arbitrary but realistic force of 100N on the smallest cranium, *Incisivosaurus*, ensuring all models experienced the same relative load. Table 3.1 summarises the cranial surface area and loads applied in each model. This scenario removed the effect of size in comparing cranial strength and efficiency and made this test independent of differences in the force vectors and proportional strengths of jaw adductor muscles, focussing purely on how well different

cranial morphologies function in response to bending. In each scenario, forces were applied bilaterally to the anterior tip of the beak (or front teeth), the lateral edge of the midpoint of the beak (or middle of tooth row), and posterior extent of the palate: the distinctive 'tooth-like' projection of the maxillae and vomer in the oviraptorids; the rear teeth in the others (shown in Fig. 3.1). The effect of applying the load unilaterally (to the left side) was also assessed.

Results are compared qualitatively through visual comparison of contour plots of von Mises stress and quantitatively by mean and peak stress values and total strain energy. However, artificially high values of stress can result in artefacts from small element size and using point loads and constraints (Dumont *et al.*, 2009; Marcé-Nogué *et al.*, 2016). To account for this and make peak stress a useful metric, the top 5% of values were excluded when comparing values of peak stress (and in the calculation of mean values) from exported reports of the von Mises stress value at every element node for each FEA scenario, a solution similar to other FEA studies (see Walmsley *et al.*, 2013; Marcé-Nogué *et al.*, 2016; Tseng and Flynn, 2018). Appendix A shows the 95% values and the calculated means and medians (from both 95% and 100% of data) produce a very similar pattern but are dissimilar to the to 100% values, justifying this approach. Contour plots showing stress distribution are figured using the Viridis colour scheme to enhance interpretation and accessibility (Lautenschlager, 2021).

An additional correction factor was applied to values of total strain energy from the FEA models for them to be comparable, as strain energy scales with volume not area. This was based on equation (5) from Dumont *et al.* (2009). In order to compare to the total strain energy (U) in model 'A', strain energy in model 'B' can be scaled using the ratio of the loads (F) squared and the cube root of the volumes (V) ratio according to the following formula:

$$U_{B'} = \left(\frac{V_B}{V_A}\right)^{1/3} \left(\frac{F_A}{F_B}\right)^2 U_B$$

This value of total strain energy ($U_{B'}$) can be directly compared to the value computed for model A.

Models were imported into Abaqus (version 6.14) for FEA solving and visualisation.

3.3 Results

Table 3.2 gives values of von Mises stress and total strain energy for each cranium under the different loading scenarios of this comparative bending test. Figure 3.1 and 3.2 show contour plots of von Mises stress in FEA of the oviraptorids under bilateral and unilateral loading respectively; Figure 3.3 and 3.4 show contour plots of the other theropods under bilateral and unilateral loading. Summaries of stress values in each cranial FEA are plotted in Figure 3.5 (bilateral loading) and Figure 3.6 (unilateral loading). Differences between bilateral and unilateral loading in this test were relatively minor and are compared using mean von Mises stress in Figure 3.7.

Stress decreases in all models as force is applied more posteriorly, closer to the model constraints (Fig. 3.1–3.7). This is the effect of the force being identical in each scenario, rather than increasing in magnitude as bite force likely would when moving closer to the jaw joint (more mechanical advantage). This effect is greatest therefore in *Allosaurus*, *Erlikosaurus*, and *Ornithomimus*, compared with the oviraptorosaurians, which are characterised by shortened cranial rostra.

Differences between bilateral and unilateral loading are minor in the anterior loading scenario (Fig. 3.7). The mid-palate loading scenario displays the greatest differences with stress increased in all taxa when unilaterally loaded. *Citipati* stands out with a larger increase than other oviraptorosaurians, the result of a relatively wider palate. Posteriorly, stress is also slightly increased by loading unilaterally, though this is only noticeable in crania where the loads were posteriorly applied to both or one side of a tooth row rather than a single tooth-like projection in the back of the palate (the three oviraptorids).

Table 3.2: Comparative von Mises stress and total strain energy results from the analyses modelling bilateral and unilateral bite reaction forces (scaled to relative cranial surface area) on cranial models of oviraptorid oviraptorosaurians *Conchoraptor*, *Khaan*, *Citipati*, along with early diverging oviraptorosaurian *Incisivosaurus*, and *Allosaurus*, *Erlikosaurus*, and *Ornithomimus* – theropods with more conventional skull morphology. * The top 5% of values are excluded in each dataset to account for artificially high stress values from point loads and nodal constraints. †Total strain energy values reported have undergone an additional correction factor as strain energy scales with volume rather than surface area (Dumont *et al*., 2009).

	Bilateral loading			Unilateral loading		
	Mean element stress* (MPa)	Peak element stress* (MPa)	Total strain energy† (mJ)	Mean element stress* (MPa)	Peak element stress* (MPa)	Total strain energy† (mJ)
Conchoraptor						
Anterior	2.56	8.05	13.6	2.58	8.08	14.0
Mid-palate	2.19	7.13	10.2	2.37	7.70	11.4
Posterior	1.82	6.39	7.67	1.82	6.40	8.07
Khaan						
Anterior	3.27	10.0	17.5	3.28	10.1	18.0
Mid-palate	2.81	8.81	13.3	2.99	9.43	14.6
Posterior	2.53	8.19	10.8	2.54	8.20	11.3
Citipati						
Anterior	3.67	13.1	22.2	3.73	13.2	22.7
Mid-palate	3.35	11.8	18.0	3.78	12.6	20.4
Posterior	2.81	10.2	12.9	2.81	10.2	13.4
Incisivosaurus						
Anterior	3.88	11.8	21.5	3.87	11.8	21.6
Mid-palate	3.04	9.98	14.6	3.14	10.5	15.7
Posterior	2.78	9.10	11.6	2.92	9.73	13.2
Allosaurus						
Anterior	3.11	11.8	30.5	3.17	11.9	31.0
Mid-palate	2.31	8.83	16.3	2.51	9.41	17.9
Posterior	1.29	5.65	6.26	1.49	6.35	7.85
Erlikosaurus						
Anterior	7.87	23.4	48.3	7.92	24.3	50.6
Mid-palate	5.36	17.3	25.3	5.70	18.9	29.0
Posterior	4.76	15.8	17.4	5.05	17.9	24.3
Ornithomimus						
Anterior	7.86	23.3	49.9	7.91	24.6	52.6
Mid-palate	5.44	17.2	26.6	5.78	19.8	32.8
Posterior	4.67	18.7	29.2	5.15	21.5	41.2

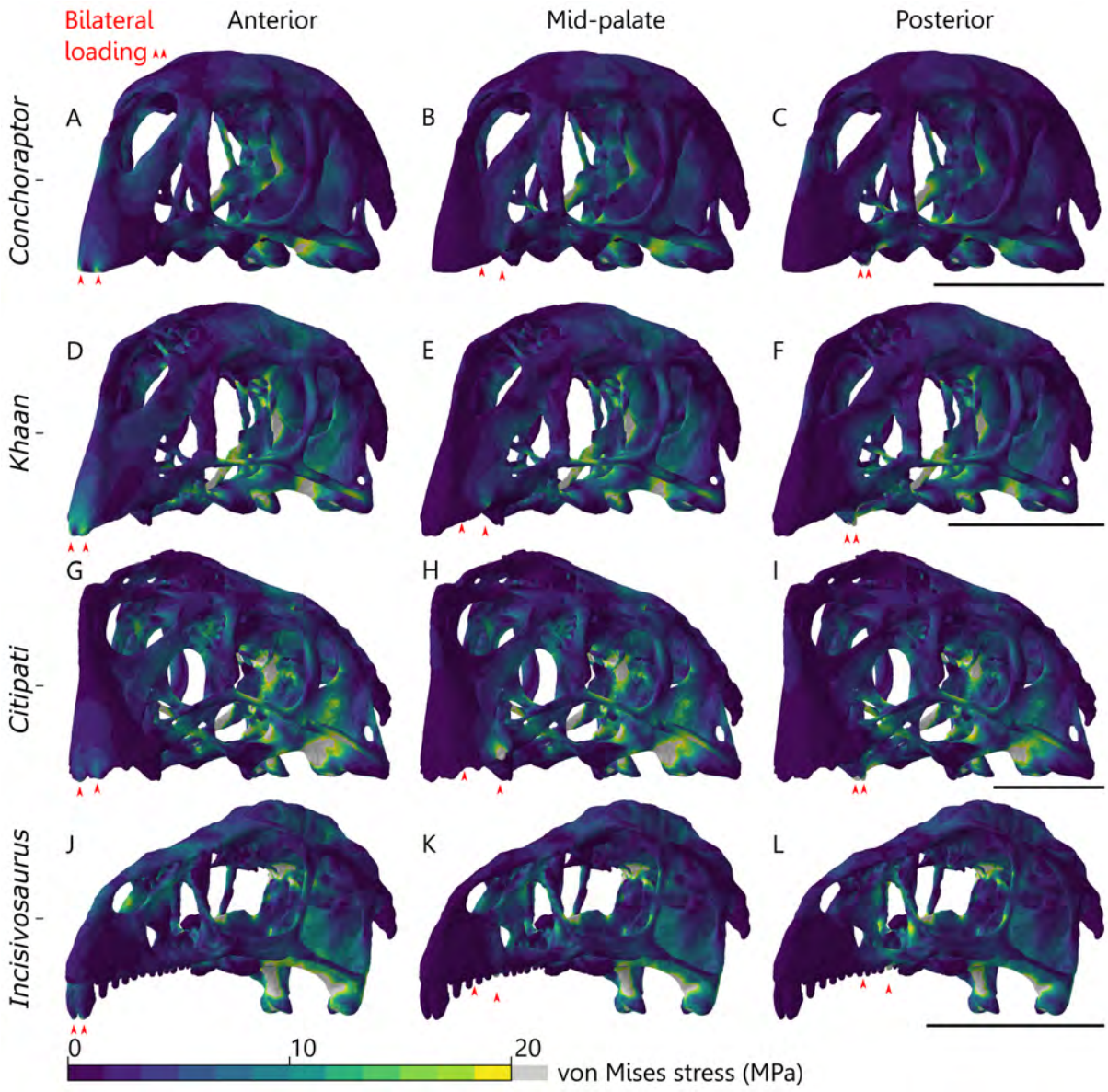

Figure 3.1: Von Mises stress (MPa) contour plots from FEA of bilaterally applied forces on cranial models of oviraptorosaurians *Conchoraptor* (A–C), *Khaan* (D–F), *Citipati* (G–I), *Incisivosaurus* (J–L). Applied forces (shown by small red arrows) scaled so ratio of cranial surface area:force applied was identical in all. Forces applied to anterior of the beak/teeth (A, D, G, J), the middle tooth/lateral edge of beak (B, E, H, K), or the posterior teeth/ tooth-like projection on oviraptorid palate (C, F, I, L). All scale bars on the right are 50 mm.

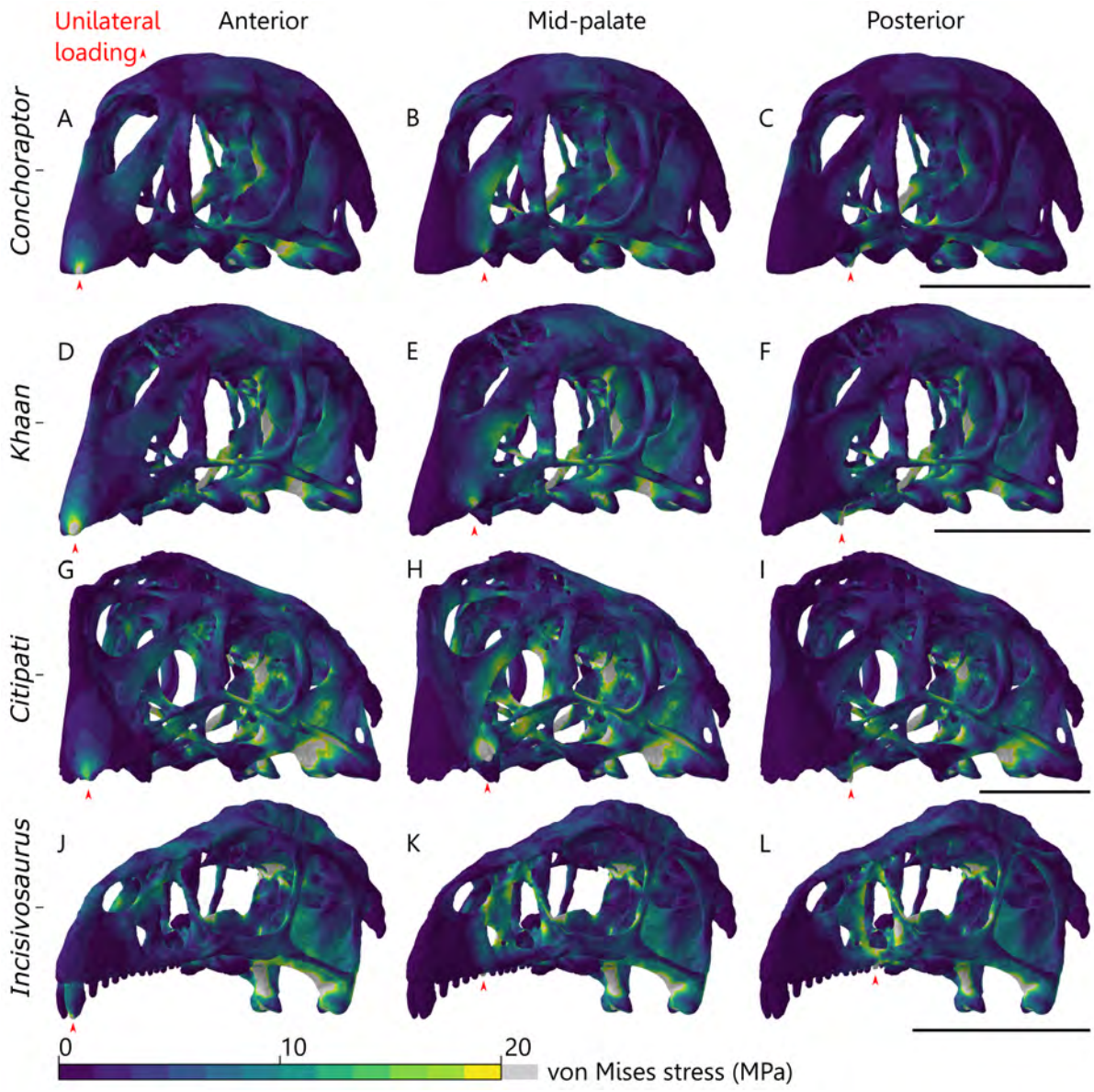

Figure 3.2: Von Mises stress (MPa) contour plots from FEA of unilaterally applied forces on cranial models of oviraptorosaurians *Conchoraptor* (A–C), *Khaan* (D–F), *Citipati* (G–I), *Incisivosaurus* (J–L). Applied forces (shown by small red arrow) scaled so ratio of cranial surface area:force applied was identical in all. Forces applied to anterior of the beak/teeth (A, D, G, J), the middle tooth/lateral edge of beak (B, E, H, K), or the posterior teeth/ tooth-like projection on oviraptorid palate (C, F, I, L). All scale bars on the right are 50 mm.

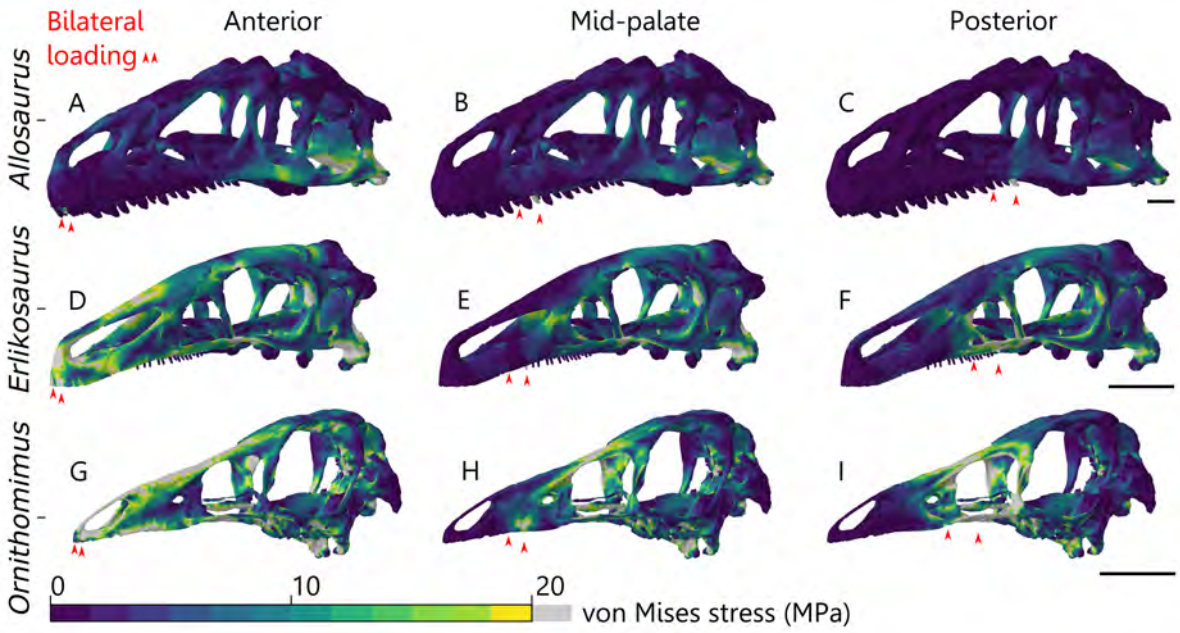

Figure 3.3: Von Mises stress (MPa) contour plots from FEA of bilaterally applied forces on cranial models of *Allosaurus* (A–C), *Erlikosaurus* (D–F), and *Ornithomimus* (G–I). Applied forces (shown by small red arrows) scaled so ratio of cranial surface area:force applied was identical in all. All scale bars on the right are 50 mm.

The four oviraptorosaurian crania generally display lower stress magnitudes than *Erlikosaurus* and *Ornithomimus*. Of the oviraptorosaurians, stress is consistently lowest in *Conchoraptor*, followed by *Khaan* (Fig. 3.5 and 3.6). *Allosaurus* experiences mean stress similar to that of the oviraptorids, between the values of *Conchoraptor* and *Khaan* under anterior and mid-palate loading, but experiences the lowest mean von Mises stress of all species under posterior loading. Mean and peak stress are consistently slightly higher in *Citipati* and *Incisivosaurus*, compared with the other two oviraptorosaurians, but which of these is greater depends on bite position. Mean and peak stress are consistently highest in the herbivorous theropods *Erlikosaurus* and *Ornithomimus*, which show almost identical stress magnitudes apart from under posterior loading.

Under anterior loading, all four oviraptorosaurians experience similar mean and peak von Mises stress to *Allosaurus*. The oviraptorosaurians experience much lower mean and peak stress than *Erlikosaurus* and *Ornithomimus*, herbivorous theropods

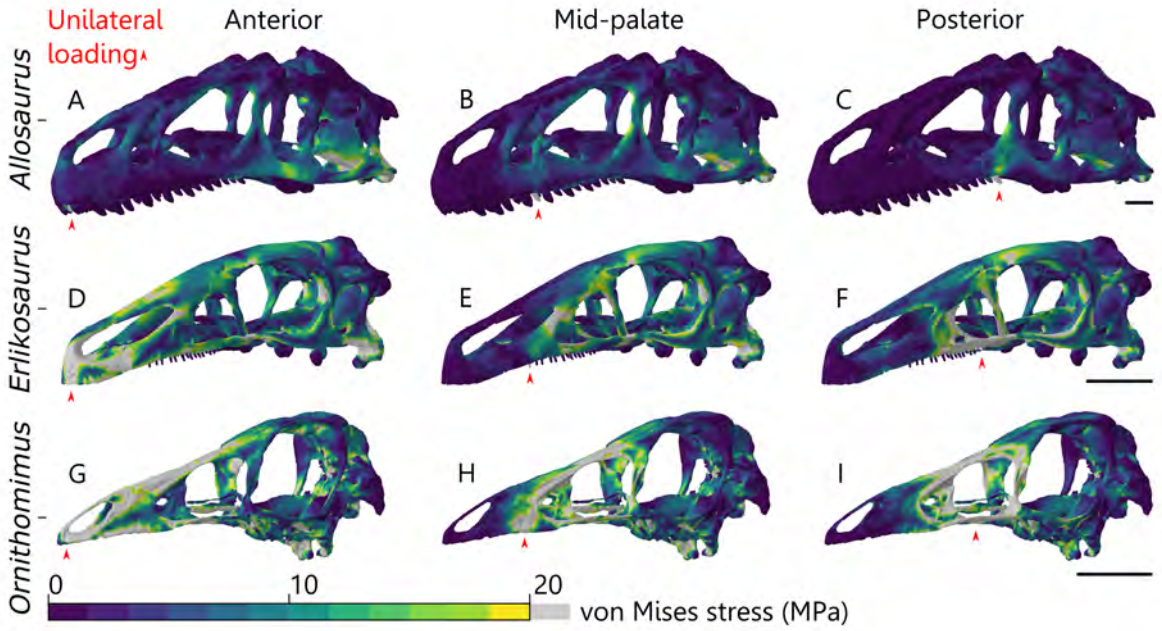

Figure 3.4: Von Mises stress (MPa) contour plots from FEA of unilaterally applied forces on cranial models of *Allosaurus* (A–C), *Erlikosaurus* (D–F), and *Ornithomimus* (G–I). Applied forces (shown by small red arrow) scaled so ratio of cranial surface area:force applied was identical in all. All scale bars on the right are 50 mm.

of a more conventional cranial morphology. The early diverging *Incisivosaurus* displays the highest mean stress out of the oviraptorosaurians in this anterior scenario, but the oviraptorid oviraptorosaurian *Citipati* displays higher peak stress.

Under mid-palate loading, mean and peak von Mises stress are still higher in *Erlikosaurus* and *Ornithomimus* than in the oviraptorosaurians, but to a lesser degree (Fig. 3.5 and 3.6). Mean stress in *Allosaurus* remains only marginally higher than that of *Conchoraptor* (the lowest) with peak stress showing more of a difference. In contrast to the anterior scenario, under mid-palate loading *Citipati* experiences both the highest mean and peak stress of any oviraptorosaurian (higher than the early diverging *Incisivosaurus*). When the mid-palate of *Citipati* is loaded unilaterally, it uniquely experiences higher mean stress than under the anterior scenario (Fig. 3.7 and Table 3.2).

Under posterior loading, *Ornithomimus* cranium shows the highest peak stress, though *Erlikosaurus* has a higher mean stress under bilateral posterior loading (Fig.

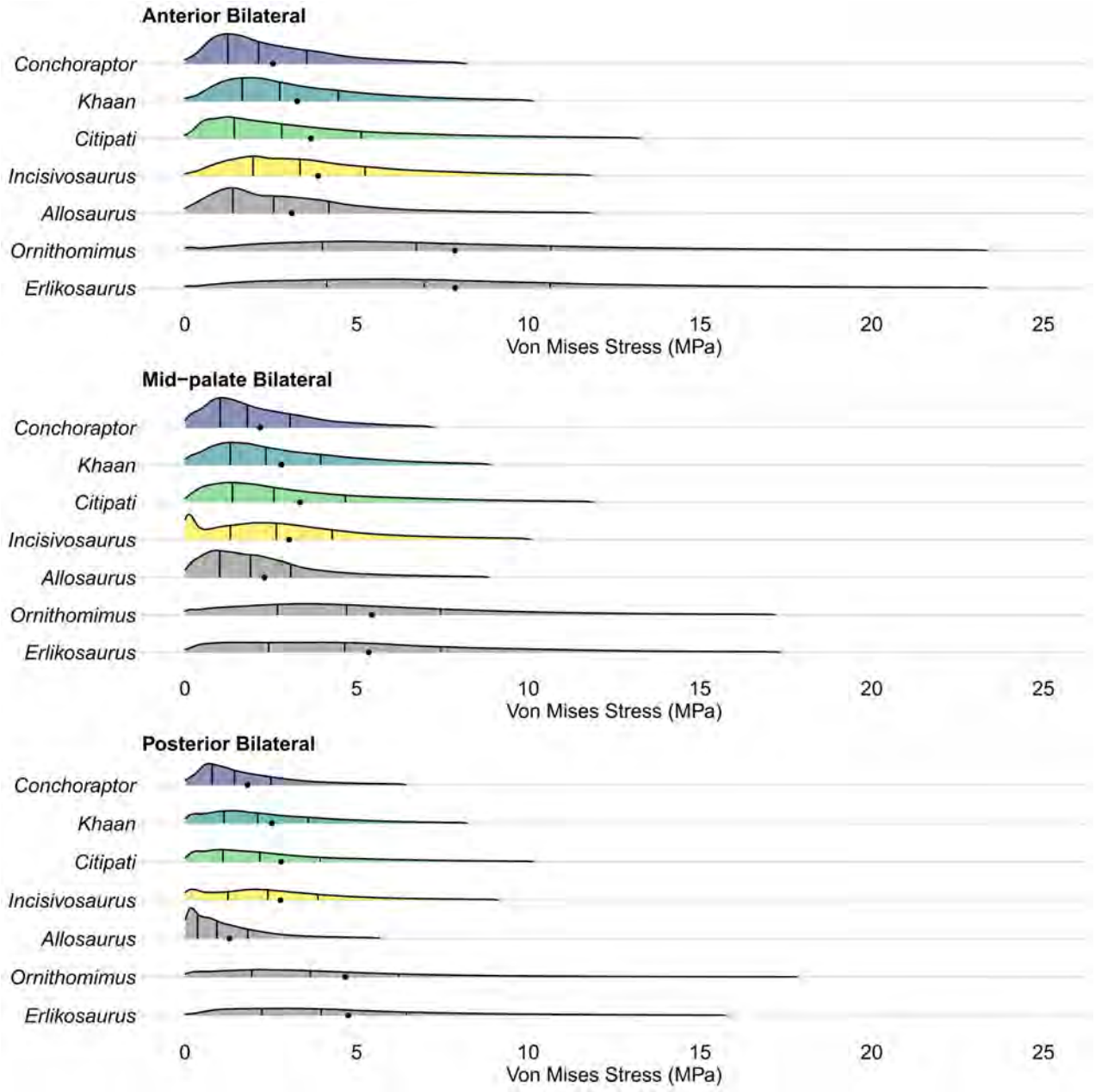

Figure 3.5: Density plots of element von Mises stress (MPa) from FEA of bilaterally applied palatal forces on cranial models of the oviraptorosaurians (coloured) *Incisivosaurus*, *Citipati*, *Khaan*, and *Conchoraptor*, along with non-oviraptorosaurian tetanuran theropods (grey) *Allosaurus* and *Erlikosaurus*, and *Ornithomimus*. The points represent the mean. Vertical bars represent the first quartile, median, and third quartile. Three different positions on the palate were tested with applied forces scaled so the ratio of cranial surface area:force applied was identical in each species.

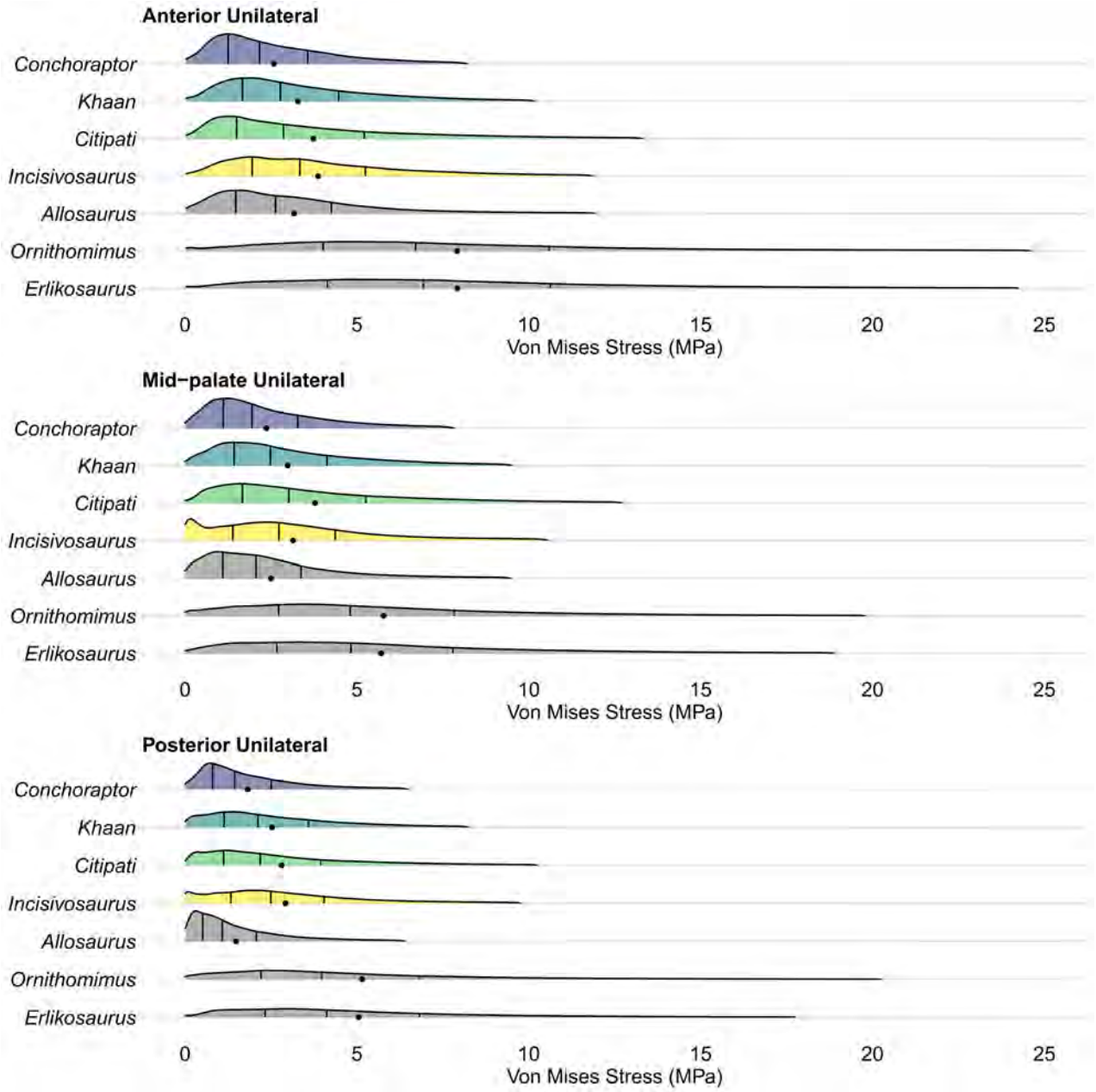

Figure 3.6: Density plots of element von Mises stress (MPa) from FEA of unilaterally applied palatal forces on cranial models of the oviraptorosaurians (coloured) *Incisivosaurus*, *Citipati*, *Khaan*, and *Conchoraptor*, along with non-oviraptorosaurian tetanuran theropods (grey) *Allosaurus*, *Erlikosaurus*, and *Ornithomimus*. The points represent the mean. Vertical bars represent the first quartile, median, and third quartile. Three different positions on the palate were tested with applied forces scaled so the ratio of cranial surface area:force applied was identical in each species.

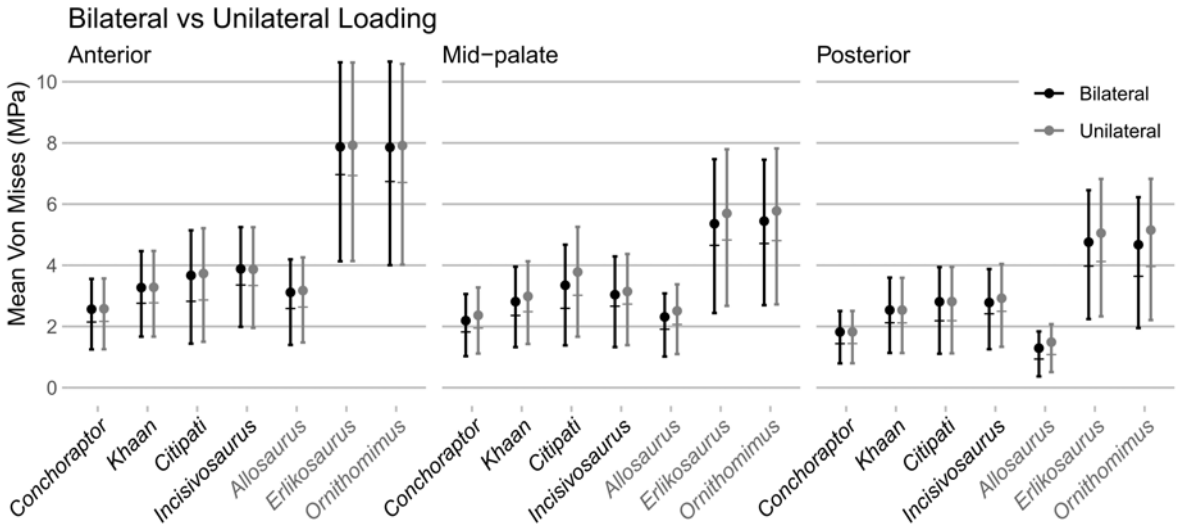

Figure 3.7: Mean values and whiskers showing first quartile, median, and third quartile of von Mises stress (MPa) from FEA of bilaterally and unilaterally applied palatal forces on cranial models of oviraptorosaurians *Incisivosaurus*, *Citipati*, *Khaan*, and *Conchoraptor*, along with *Allosaurus*, *Erlikosaurus*, and *Ornithomimus*.

3.5 and 3.6). *Ornithomimus* is unique in having higher peak stress under posterior loading, compared to mid-palate loading. Cranial stress in *Allosaurus* is decreased substantially and it displays the lowest peak and mean von Mises stress under both bilateral and unilateral posterior loading. Cranial stress in the oviraptorosaurians is only slightly decreased compared to mid-palate loading. Mean and peak stress in *Citipati* is slightly higher than that of *Incisivosaurus*, but to a very small degree.

The oviraptorosaurian crania are characterised by patterns of stress highest around the quadrate's anterior contact with the pterygoid (Fig. 3.1). This area of higher stress is much more elongated along the ventral surface of the pterygoid in *Incisivosaurus* (Fig. 3.1J–L). The thin epipterygoid and parasphenoid rostrum in all four oviraptorosaurians also experience high stresses (Fig. 3.1) but these bones are very thin and may have been poorly ossified or more flexibly connected to the rest of the cranium than is modelled in this FEA. More unique to the oviraptorids, smaller hotspots exist on the pterygoid just anterior of its contact with the epipterygoid, along the anterior of the jugal, and the posterior of the quadratojugal – the jugal and quadratojugal are much thinner and rod-like in the oviraptorids (Fig. 3.1A–I), compared to a

more typically theropod jugal morphology in *Incisivosaurus* (Fig. 3.1J–L).

The nasals and nasal process of the premaxilla are significantly less stressed in the oviraptorids (Fig. 3.1A–I), compared with *Incisivosaurus* (Fig. 3.1J–L) where the whole skull roof is more broadly stressed and to a slightly greater magnitude. The oviraptorosaurians generally experience very low stress in the premaxilla, maxilla, nasal, and over across the cranial roof.

The other three theropods also experience stress hotspots in the quadrate and pterygoid but in *Erlikosaurus* and *Ornithomimus* this is to a greater extent than in the oviraptorosaurians (Fig. 3.3 and 3.4). In addition, the connecting quadratojugal and jugal are greatly more stressed (Fig. 3.3 and 3.4). The cranial roof, lacrimal, and postorbital all experience relatively higher stress than those of the oviraptorosaurians. Under anterior loading, the premaxilla and nasal are also more stressed, especially in *Erlikosaurus* and *Ornithomimus* (Fig. 3.3D–I), than in the oviraptorosaurians. These stresses in the nasal (and maxilla) are especially severe in *Ornithomimus*, and present in all bite positions (Fig. 3.3 and 3.4G–I).

For a cranium reminiscent of the morphology of other theropods, compared to oviraptorids, the early diverging oviraptorosaurian *Incisivosaurus* shows very little stress on the jugal and quadratojugal (Fig. 3.1J–L). All three non-oviraptorosaurian theropods show higher stresses on both bones in all bite positions (Fig. 3.3 and 3.4), whereas *Incisivosaurus* shows very little stress on the jugal/quadratojugal in any scenario (Fig. 3.1J–L). In general, patterns of cranial stress in *Incisivosaurus* more resemble those of the oviraptorids, compared with the other theropods, implying similar adaptations that characterise the structural response of the oviraptorid cranial morphology.

However, positioning loading more posteriorly increases stress in the lacrimal of *Incisivosaurus* more so than in the oviraptorids (Fig. 3.1L). *Incisivosaurus* generally has more extensive areas of higher stress ventrally on the quadrate/pterygoid, slightly greater stress magnitudes more broadly over the skull roof. Under anterior loading

specifically, there is greater stress in the nasal arch, but lower stress in the premaxilla than in the oviraptorids (Fig. 3.1J). This is likely linked to *Incisivosaurus* possessing teeth, modelled separately to bone in the FEA. Loading the prominent incisor-like teeth of *Incisivosaurus* does not produce any aberrant stress patterns (Fig. 3.1J) suggesting they would not be unsuitable for feeding.

Total strain energy is lower in the oviraptorosaurian crania than the other theropods under anterior loading. Under mid-palate loading, the total strain energy of *Allosaurus* falls below that of *Citipati*, which is consistently the highest value among the oviraptorosaurians. Under posterior loading, *Allosaurus* has the lowest total strain energy of any taxon. This may result from the rear of *Allosaurus* toothrow, nearly under the lacrimal, being relatively more posterior than in the oviraptorids, whose shortened rostrum confines the entire hard palate to a smaller but more anteriorly located region. Total strain energy in *Erlikosaurus* and *Ornithomimus* remains much higher than the other taxa in all loading positions. *Ornithomimus*, the taxon with highest total strain energy throughout, is the only taxon to have a higher total strain energy under posterior loading compared with mid-palate loading.

3.4 Discussion

This structural comparison of the oviraptorid cranium with other theropods of more conventional cranial morphology supports the hypothesis that Oviraptoridae developed a stronger and more energetically efficient cranial morphology. Their crania achieve this despite extensive pneumatic spaces and a heavily reduced jugal–quadratojugal bar morphology. This may have been linked with feeding strategies that relied on powerful sustained biting. In combination with a strengthened cranium, a high degree of relative strength in the form of the oviraptorid mandible, in comparison with other non-avialan coelurosaurian theropods, has been demonstrated through FEA by Ma *et al.* (2021).

In this bending test, the shortening of the cranium in oviraptorids allows stress to be more readily transmitted through robust posterior processes of the premaxilla

below the nares, lessening stress in the nasals and frontals dorsal to the antorbital fenestra. The contour plots indicate that stress is also effectively channelled ventrally from the rostrum, via the modified longitudinally directed connection of the pterygoid and ectopterygoid with the maxilla (Elzanowski, 1999; Maryańska *et al.*, 2002), and via the short stout vomer, into the pterygoids which are robust. Stress is channelled more relatively posteriorly, essentially posterior to the orbital region, and overall stress is reduced by the development of robust palatal bones, compared to more conventional theropod cranial morphology. The effect of this is that the most pneumatic areas of the cranium (such as areas of the nasal, and frontal containing large air spaces) experience very low stress.

Interestingly, considering its peculiar intermediate morphology (Xu *et al.*, 2002), the cranium of the early diverging oviraptorosaurian *Incisivosaurus* is characterised by stress patterns in response to bending that more closely resemble oviraptorid oviraptorosaurians than other toothed theropod dinosaurs. This chapter helps identify that the cranium of *Incisivosaurus* already has several of the functional adaptations that characterise the cranial response to bending forces in the oviraptorids. Enlargement of the orbit, and the beginnings of a shortened skull and reinforced palate, funnel stress away from the jugal–quadratojugal bar to other areas, giving general stress patterns much more similar to the oviraptorids. It appears the more typically massive theropod-like jugal in early diverging oviraptorosaurians such as *Incisivosaurus* is not a structural limiting factor in cranial function, and in a position to be adaptively reduced towards the more minimal morphology of the oviraptorids.

Citipati differs from the other two oviraptorids tested. In this bending test its cranium appears weaker, experiencing higher cranial stress than other oviraptorids under loading, and sometimes even higher than the earlier diverging *Incisivosaurus*. This is especially the case when force is applied unilaterally to the edge of the mid-palate. Its beak is relatively wider than the other oviraptorids, positioning unilateral force relatively further from the midline of the cranium. This increase in stress shows

as notably greater stress magnitudes in the otherwise minimally stressed nasal bones; the most stressed the nasals become in any of the scenarios for the oviraptorids (Fig. 3.2E).

This chapter did not model a keratinous beak covering in any taxon. A keratinous rhamphotheca has been shown to reduce cranial stress when biting, though typically only beneath the area covered (Lautenschlager *et al.*, 2013). My results find the premaxilla and maxilla are not highly stressed in the oviraptorids compared to posterior cranial areas. This suggests their cranial morphology is at a stage where stress reduction is not a main driving factor in the evolution of their beak shape. Contrastingly in *Erlikosaurus* and *Ornithomimus*, a keratinous rhamphotheca would reduce stress in some of the most highly stressed areas during anterior loading (see also Lautenschlager *et al.*, 2013; Lautenschlager *et al.*, 2016; Bestwick *et al.*, 2021).

Zanno and Makovicky (2011) noted development of heterodonty is characteristic of dinosaur taxa spanning a trophic shift and/or being likely omnivorous/herbivorous. Interestingly, conical/incisiform teeth are associated with areas of subsequent tooth loss in several herbivorous lineages (Zanno and Makovicky, 2011). Specialised tooth types and arrangements such as the loss of pronounced replacement waves and gaps between teeth (a more continuous cutting surface) may function as analogous to a beak as plant material is adopted into the diet, a precursor to later evolution of a rhamphotheca (Zanno and Makovicky, 2011).

The premaxillary teeth in *Incisivosaurus* may function like the tip of a beak with more uniform close lanceolate maxillary teeth like the lateral cutting margins of a beak. The incisor-like front of *Incisivosaurus* teeth bear prominent wear facets (Xu *et al.*, 2002; Balanoff *et al.*, 2009), so were clearly an important tool for food processing or otherwise interacting with its environment. The cranium of *Incisivosaurus* also includes replacement teeth for its front pair of premaxillary teeth (Balanoff *et al.*, 2009). While development of a rhamphotheca in *Erlikosaurus* has an obvious function in strengthening a highly stressed area of the cranium (Lautenschlager *et al.*, 2013), it may be the

case that the development of a rhamphotheca in oviraptorosaurians was linked with an adaptive pressure towards having a feeding apparatus that was more continuously replaced in terms of wear (and potentially self-sharpening) to function more reliably and consistently. In this way they would function in an analogous way to the beaks of modern parrots which can be entirely replaced in a few months (Fecchio *et al.*, 2010). The influence on cranial stress of a modelled keratinous covering to the oviraptorid beak will be tested in Chapter 5.

3.5 Conclusion

Oviraptorosaurians tested using finite element analysis with scaled loading had stronger and more energetically efficient crania in resisting bending forces compared to herbivorous theropods of more conventional cranial morphology and broadly matched the relative cranial strength of the large, carnivorous *Allosaurus* (which has been considered overengineered; Rayfield, 2001). The FEA contour plots here indicate the cranial morphology of oviraptorids is adapted to channel stresses away from thin and pneumatic areas; the posterior processes of its premaxillae and its palate experience stresses rather than the nasals and cranial roof. The cranium of the early diverging oviraptorosaurian *Incisivosaurus* performed more similarly to those of the oviraptorids compared with other theropods, and in some cases was stronger (than *Citipati*). The oviraptorosaurian premaxilla and nasal showed very low stress, suggesting stress reduction was not an important functional factor of their keratinous rhamphotheca – this will be tested directly in Chapter 5. This finding contrasts with the beaks of therizinosaurian and ornithomimosaurian taxa such as *Erlikosaurus* and *Ornithomimus* that also underwent dietary shifts away from carnivory (Zanno and Makovicky, 2011).

4 | Cranial muscle reconstructions quantify adaptation for high bite forces in Oviraptorosauria

This chapter is a lightly modified version of the following paper published in *Scientific Reports*. I generated the muscle reconstructions, performed the gape analysis, prepared figures and wrote the first draft of the manuscript. Both authors analysed the data, revised the manuscript, and approved its published version.

Meade, L. E. and Ma, W. 2022. Cranial muscle reconstructions quantify adaptation for high bite forces in Oviraptorosauria. *Scientific Reports*, **12**, 3010.

4.1 Introduction

Oviraptorosaurians are pennaraptoran theropods that include some of the most specialised, aberrant dinosaurs, with the later diverging members splitting into two major clades—Oviraptoridae and Caenagnathidae (Pittman *et al.*, 2020; Funston *et al.*, 2020). The skull morphology of oviraptorid oviraptorosaurians appears to be adapted towards producing a powerful sustained bite (Barsbold, 1986; Lü *et al.*, 2013b; Funston *et al.*, 2017; Ma *et al.*, 2020b). Though their crania are heavily pneumatised, they are short and tall, have expanded spaces for jaw musculature, and are equipped with a deep mandible and a robust palate terminating in a toothless beak. This anatomy has been speculated as consistent with forms of durophagy (i.e. egg eating, molluscivory;

Barsbold, 1986; Currie *et al.*, 1993) but there is a strong case for the Oviraptoridae being primarily herbivorous (Smith, 1992, Longrich *et al.*, 2010; Zanno and Makovicky, 2011; Lü *et al.*, 2013b; Funston *et al.*, 2018; Ma *et al.*, 2020b) numbering them among a very few herbivorous theropod groups (with ornithomimosaurs and therizinosaurs; Zanno and Makovicky, 2011). We quantitatively assess the functional capabilities of the oviraptorosaurian skull using digital techniques, focussing on their jaw adductor myology, to better understand their jaw function and possible dietary niche.

Digital muscle reconstructions have previously been used to estimate bite forces and make comparisons of jaw adductor muscle anatomy in ornithomimids and therizinosaurs (Lautenschlager, 2013; Cuff and Rayfield, 2015), and among other herbivorous dinosaurs (e.g. *Psittacosaurus*, Taylor *et al.*, 2017; sauropods such as *Camarasaurus*, *Plateosaurus*, and *Diplodocus*, Button *et al.*, 2014; Button *et al.*, 2016). In this study, we use computed tomographic (CT) and photogrammetric datasets representing the crania of *Citipati osmolskae*, *Khaan mckennai*, and *Conchoraptor gracilis*, oviraptorid oviraptorosaurians from the Late Cretaceous (Campanian) of Mongolia (Osmólska, 1976; Clark *et al.*, 2001; Clark *et al.*, 2002; Kundrát, 2007; Kundrát and Janáček, 2007; Funston *et al.*, 2018). We also study the earliest diverging oviraptorosaurian *Incisivosaurus gauthieri*, from the Early Cretaceous of China (Barremian) (Xu *et al.*, 2002). *Incisivosaurus* is one of the very few oviraptorosaurians with teeth (along with caudipterids), which bear wear facets that are a strong indicator of herbivory (Xu *et al.*, 2002). We use the CT and photogrammetric data to create retrodeformed 3D models of these species' crania and mandibles. Based on the retrodeformed 3D models, we reconstruct oviraptorosaurian jaw adductor musculature and use the reconstructions to estimate bite forces. Additionally, we assess how the reconstructed jaw adductor muscle anatomy may have constrained the maximal angle of gape in each species (Lautenschlager, 2015).

This set of four 3D skull models and myological reconstructions allows us to compare bite forces, jaw adductor muscle anatomy, and jaw function between the

earliest diverging oviraptorosaurian and later diverging oviraptorids, and between oviraptorosaurians and other herbivorous theropods. Our results are of interest for the question of if and how diet changed with cranial function over the course of oviraptorid evolution.

4.2 Methods

4.2.1 *Digitisation and retrodeformation of specimens*

CT scans of the crania of *Incisivosaurus* (IVPP V13326), *Citipati* (MPC-D 100/798), *Khaan* (MPC-D 100/973; also including mandible), and *Conchoraptor* (MPC-D 100/3006) were provided by A. M. Balanoff (see Balanoff *et al.*, 2009; Balanoff and Norell, 2012; Balanoff *et al.*, 2013; Balanoff *et al.*, 2014; Balanoff *et al.*, 2016; Balanoff *et al.*, 2018). Photogrammetry was used to digitise mandibular material from *Incisivosaurus* (IVPP V13326), *Citipati* sp. (MPC-D 100/42) and additional partial cranial and mandibular material of *Conchoraptor* (ZPAL Mg-D I/95). CT scanning parameters, photogrammetric methods, and additional information on specimen provenance are summarised in Chapter 2. CT datasets were segmented in Avizo Lite (version 9.3.0). Digital retrodeformation of the crania and mandibles was based on Lautenschlager (2016b) and was performed in Avizo Lite, Blender (version 2.9.0), and Landmark, restoring taphonomic damage as objectively as possible. This involved interpolation of material over cracks and breaks, repositioning of disarticulated and fragmented elements, replacement of missing elements by mirroring or modification from related species, and the correction of plastic deformation such as compression and shear. Full information on retrodeformational procedure by specimen is also given in Chapter 2.

4.2.2 *Volumetric muscle reconstruction*

The origin and insertion sites of eight cranial muscles were identified based on skull morphology, studies of related theropod groups, and extant analogues (Holliday, 2009).

The methodology for 3D reconstruction of cranial myology was derived from Lautenschlager (2013). The skull geometry of oviraptorosaurians, particularly their large orbit (and likely large eyeball), indicates the origin–insertion path of many cranial muscles cannot be straight and is obfuscated by other structures and each other. We therefore deviated slightly from Lautenschlager (2013) and others (Cuff and Rayfield, 2015; Button *et al.*, 2016) in our method by connecting identified origin and insertion sites with simple curves rather than straight cylinders/rods; this also allowed easier modelling of the wrapping of the *m. pterygoideus ventralis*. Bundles of eight Bezier curves were created in Blender between origin and insertion sites of each muscle, following their likely path and avoiding intersections with bone and other muscles. A spherical mesh was created centrally in the orbit and scaled until it contacted the orbit; it was then scaled to 95% of this size (leaving a small presumed space for other tissues and muscles; the eyeball would not contact surrounding bone) to form a basic eyeball that the muscle paths were not allowed to intersect. A default Blender 'UV sphere' mesh was subdivided ('subdivision surface' modifier; subdivisions 2) and shrinkwrapped ('shrinkwrap' modifier) around each bundle of curves to form a convex hull. These simple volumes were smoothed and remeshed. Minor areas of overlap occurred between convex hulls in crowded regions where multiple muscles met their origin/insertion sites. Rather than removing overlaps in Blender (i.e. using additional editing or Boolean modifiers), the Blender muscle volumes were imported into Avizo to flesh them out in the same way as Lautenschlager (2013) and others (Cuff and Rayfield, 2015; Button *et al.*, 2016) and overlapping volumes were resolved by allocating half the overlap to each muscle, or making corrections where a muscle volume was erroneously encroaching on another's defined origin/insertion site. The basic muscle volumes were expanded equally in the Avizo segmentation editor ('grow selection') until they touched each other and were constrained by osteology, reaching their limits. These were then smoothed in Avizo's segmentation editor to form the final reconstructions. Muscle force estimates were calculated following the dry skull method (Thomason, 1991). Values for muscle

cross-sectional areas (CSA) were calculated by dividing muscle volume (given by Avizo surface area and volume module) by its length (obtained by Avizo measurement module). The CSA of each muscle was multiplied by an assumed isometric muscle stress value of 0.3 N/mm^2 (Weijs and Hillen, 1985; Thomason, 1991; Wroe *et al.*, 2005).

$$Fmus = CSA \times \sigma$$

Calculated muscle force values were multiplied by a correction factor of 1.5 following Thomason (1991) to account for underestimation due to factors such as muscle pennation not being accounted for. Muscle forces and derived bite forces are reported in this study with this correction factor; Appendix B also gives full sets of values without the correction factor. To calculate the resultant vertical force vectors acting at muscle attachments points on the mandible, muscle forces were multiplied by the cosines of the insertion angles of muscles, measured (Avizo measurement module) in the sagittal (α) and coronal (β) planes on the 3D reconstruction.

$$Fres = Fmus \times cos\alpha \times cos\beta$$

Contribution toward bite force from each muscle was estimated at three points on the palate of each species: the anterior tip of the beak/teeth; the middle level of the palate/toothrow; the tooth-like projection in the posterior of the oviraptorid palate/the posteriormost teeth, to assess a complete range of positions anteroposteriorly that may be contacting food. Estimates of bite force were calculated by rearranging the relationship between outlever length (distance from bite point to jaw joint) and the inlever length (distance from insertion point of muscle to jaw joint). Bite forces calculated for each side of the mandible were summed for the final total bite force estimates.

$$Fbite = (Fres \times Linlever) \div Loutlever$$

We assume all jaw adductor muscles participated equally and fully during contraction.

4.2.3 *Musculoskeletal constraints on gape angle*

The retrodeformed cranium and mandible models were imported into Blender for muscle-constrained gape analysis following Lautenschlager (2015). The separate cranium and mandible components were connected using an armature (of two bone elements) with a centre of rotation at the jaw joint. Blender's keyframe animation tool was used to animate and model a jaw opening cycle in which one frame represented 0.5°. The jaw adductor muscles were modelled as two simple cylinders connecting the anteriormost and posteriormost extent of the muscle's origin and insertion sites. Curved connections between muscle origin and insertion (as used for the basis of our anatomical muscle reconstruction) were not modelled for this analysis; they only minimally affected estimates of optimal and maximum gape angle and their stretch during jaw opening was too uncertain to model objectively. The cylinders were connected to the armature, allowing them to extend as the mandible rotated. A python script (adapted from that of Lautenschlager, 2015) was used to measure the strain of each muscle cylinder throughout the modelled jaw opening cycle and export the values to a text file.

Muscles comprise a structure of overlapping filament cross-bridges and inherently have a strain range over which maximal tetanic contraction can be achieved (optimal tension up to 130% of resting length) and a maximum tension limit (170% of resting length; Nigg and Herzog, 2007; Sherwood *et al.*, 2012). This structural constraint was used by Lautenschlager (2015) to estimate the gape angle at which the limit of optimal tension is reached and the maximum limit of gape that might occur for muscle tension to still be possible. The optimal and maximum limits of gape were therefore estimated once a muscle cylinder reached 130% and 170% resting length respectively. The script and Blender setup could be set to terminate the cycle when a muscle cylinder reached a determined strain ratio between its stretched and relaxed

state and render this terminal step in the jaw opening cycle.

The resting gape must lie at a small open angle, given the length–tension relationship of muscles, in order to generate necessary force during biting (Nigg and Herzog, 2007; Porro *et al.*, 2011). Lautenschlager (2015) tested theropod skulls at resting gape angles of 3° and 6°, concluding these to approach realistic values. The oviraptorosaurian models here were tested from a resting gape of 5°; this was the degree of gape at which the 3D anatomical reconstruction of the jaw muscles was done.

4.3 Results

4.3.1 *Cranial myology*

The muscular origin and insertion sites interpreted in the cranium and mandible of each species are identified in Figure 4.1; the 3D reconstructed jaw adductor muscles are shown in Figure 4.2 (*Incisivosaurus* and *Citipati*) and Figure 4.3 (*Khaan* and *Conchoraptor*).

m. adductor mandibulae externus medialis (mAMEM)

The origin site of the mAMEM is less clear than others of the mAME group (Holliday, 2009) and we reconstruct it, as others have done, in the posterior portion of the supratemporal fossa (Lautenschlager *et al.*, 2013; Cuff and Rayfield, 2015; Button *et al.*, 2016) where it is constrained anterolaterally and anteromedially by the positions of mAMES and mAMEP (Fig. 4.1). This region comprises parts of the squamosal and parietal in all four taxa and is generally vertical, concave, and featureless in all apart from *Citipati*. In this taxon, within the supratemporal fossa, the squamosals and parietals are flattened and orientated to form a deep and concave platform directly perpendicular to the line of action of this muscle (Fig. 4.1E). The extent and direction of the mAMEM body are somewhat constrained in all taxa by the anterior, dorsal, and

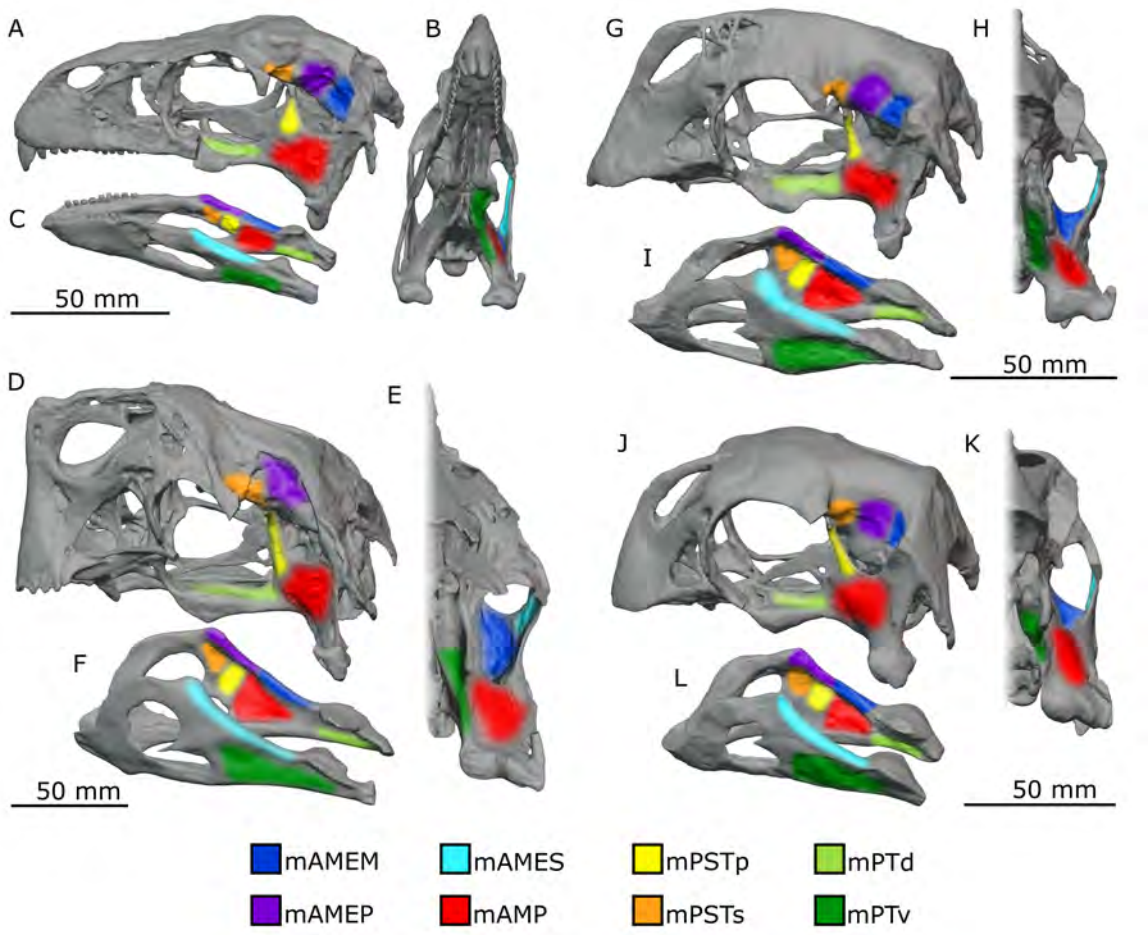

Figure 4.1: Locations of reconstructed jaw adductor muscle origin and insertion sites for *Incisivosaurus gauthieri* (A–C), *Citipati osmolskae* (D–F), *Khaan mckennai* (G–I), and *Conchoraptor gracilis* (J–L). Crania are shown in dorsolateral view (A,D,G,J) with temporal and postorbital bars removed to better show medial regions within supratemporal fenestra. The left sides of the crania are shown in anteroventral view (B,E,H,K) with lower temporal and postorbital bars removed to better show posterior and lateral regions within supratemporal fenestra. Mandibles shown in dorsolateral view (C,F,I,L), lateral muscle insertions sites are shown on the left rami, medial insertion sites on the right rami. Scale bars 50 mm. Muscle abbreviations given in results section.

posterior edges of the squamosal, quadrate flange, and epipterygoid respectively.

The insertion sites are typically unclear (Holliday, 2009; Lautenschlager *et al.*, 2013). The surangular dorsomedially forms a shelf that overhangs the adductor fossa in *Citipati*, *Khaan*, and *Conchoraptor* (potentially taphonomically exaggerated in the latter two). Insertion onto the dorsomedial and posterior margin of the coronoid eminence (along with insertion of the mAMEP onto the eminence) has been suggested

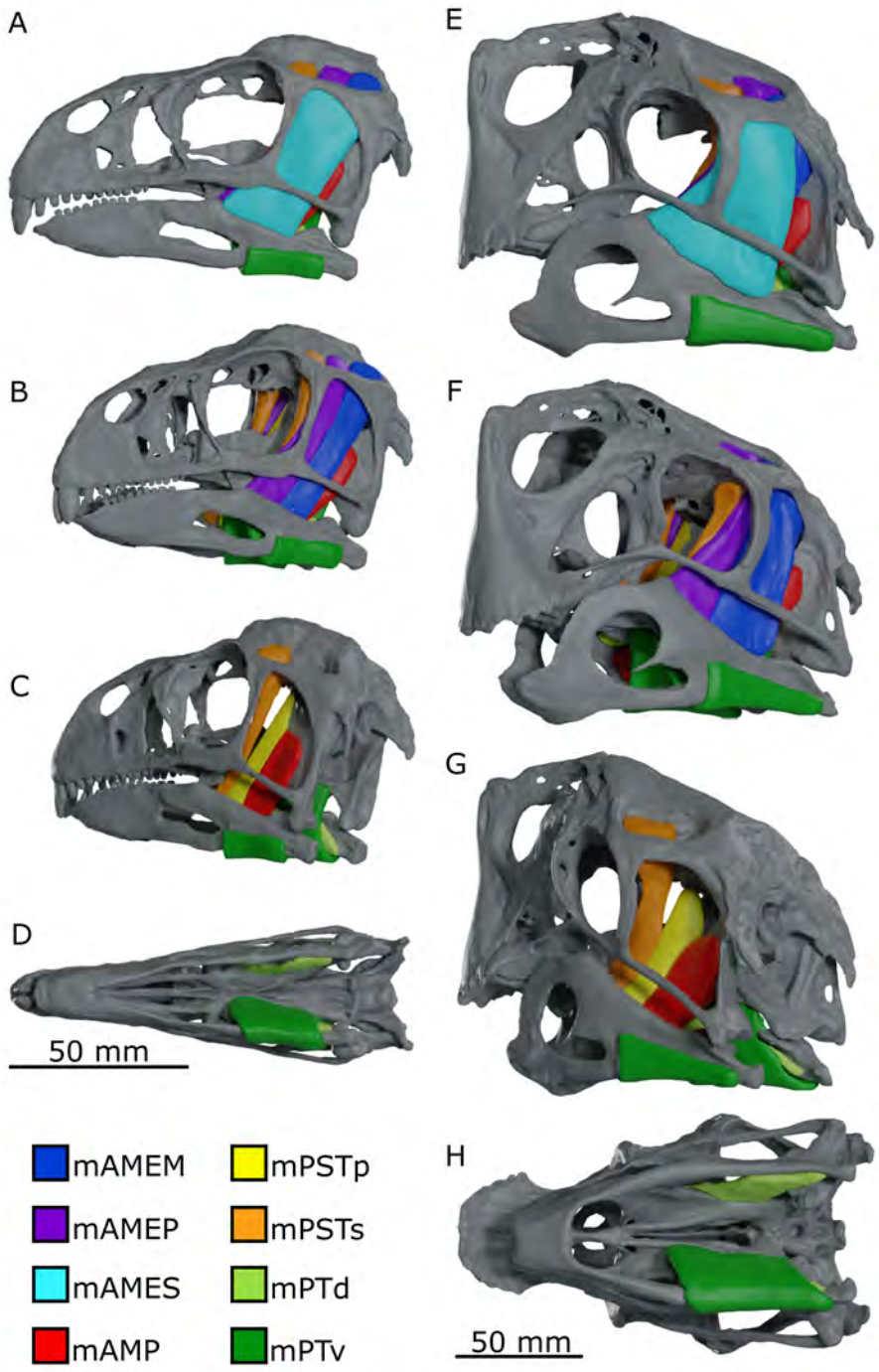

Figure 4.2: Reconstructed jaw adductor musculature of *Incisivosaurus gauthieri* (A–D) and *Citipati osmolskae* (E–H) shown complete in lateral view (A,E), anterolateral view with mAMES removed (B,F), posterolateral view with mAME complex removed (C,G), and ventral view (D,H) with only the mPT muscles (mPTv removed on left). Scale bars 50 mm, legend colour coded to identify individual muscles. Muscle abbreviations given in results section

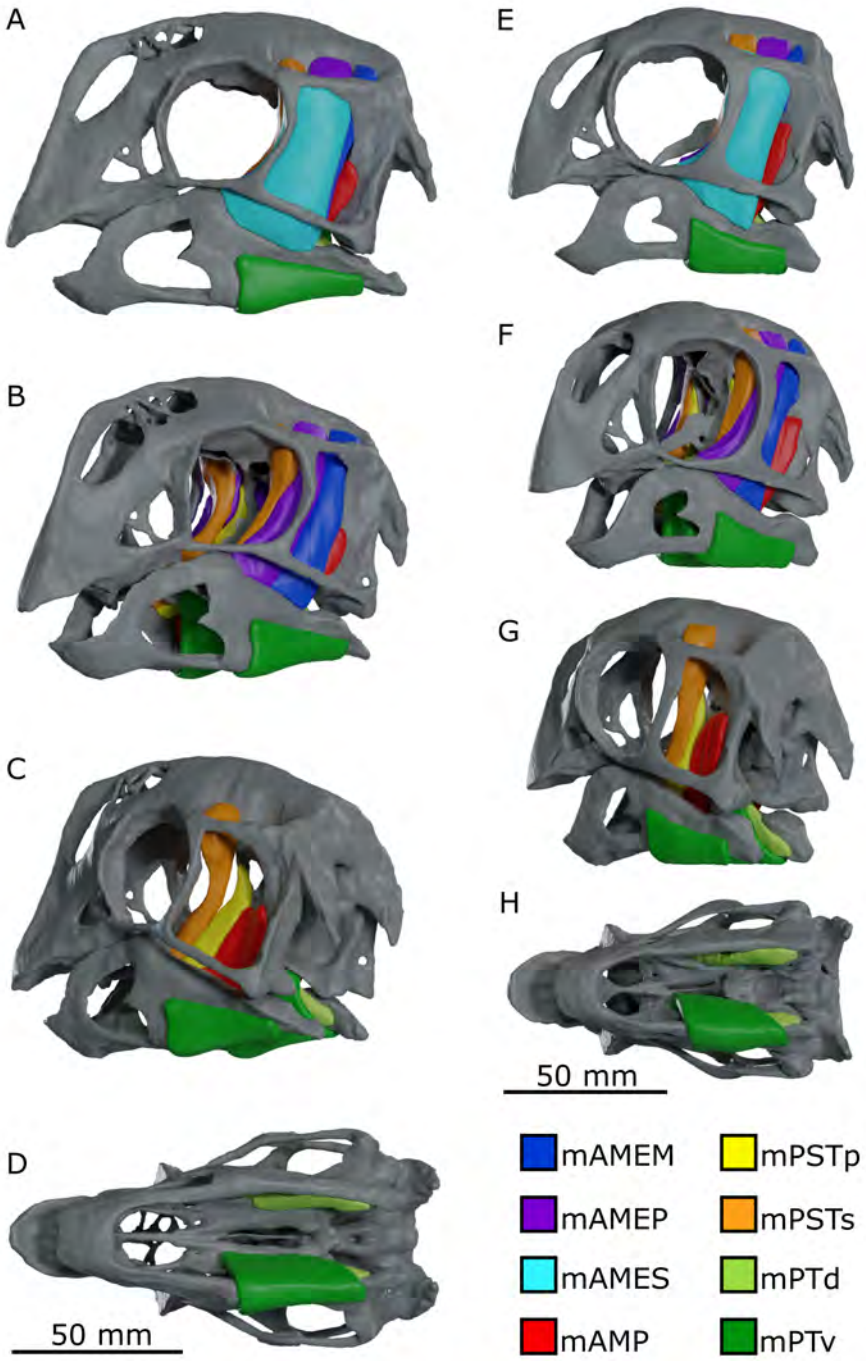

Figure 4.3: Reconstructed jaw adductor musculature of *Khaan mckennai* (A–D) and *Conchoraptor gracilis* (E–H) shown complete in lateral view (A,E), anterolateral view with mAMES removed (B,F), posterolateral view with mAME complex removed (C,G), and ventral view (D,H) with only the mPT muscles (mPTv removed on left). Scale bars 50 mm, legend colour coded to identify individual muscles. Muscle abbreviations given in results section.

for the mAMEM (Holliday, 2009; Lautenschlager *et al.*, 2013; Cuff and Rayfield, 2015; Ma *et al.*, 2017), but the palatal morphology (especially in the oviraptorids) restricts space around the coronoid eminence so that we do not reconstruct both the mAMEM and mAMEP as inserting in this area. Instead, we reconstruct the mAMEM as inserting on the shelf-like upper part of the surangular's dorsomedial surface, posterior to the more anterior insertion of the mAMEP, allocating roughly half of the available surface to each (Fig. 4.1C,F,I,L). This insertion surface is unclear and largely reconstructed in *Incisivosaurus* where there is a less well-defined slight convexity on the upper part of the medial surangular surface (Fig. 4.1C). This area of the retrodeformed mandible model for *Conchoraptor* uses material from *Khaan* and the two are thus similar (Fig. 4.1I,L).

It is possible the mAMEM and mAMEP merged along their path or did indeed both insert in relation to the coronoid eminence (Nabavizadeh, 2020b) but ultimately this would not change reconstructed bite force results significantly.

m. adductor mandibulae externus profundus (mAMEP)

The mAMEP generally has a medial and/or anteromedial origin within the supratemporal fenestra. A vertical crest, similar to that interpreted as the anterior border of the origination site in *Carcharodontosaurus* and *Daspletosaurus* (Holliday, 2009), *Allosaurus* (Rayfield, 2001), *Corythosaurus* (Ostrom, 1961), and *Erlikosaurus* (Lautenschlager *et al.*, 2013), is also identified in *Citipati* (Clark *et al.*, 2002) (Fig. 4.1D). We interpret it as the boundary between the mAMEP and mPSTs origins. A small sharp prominence, perhaps similar, is present on the lateral surface of the braincase in *Incisivosaurus* (Fig. 4.1a). The surface is more featureless in *Khaan* and *Conchoraptor* (Fig. 4.1G,J), so the anterior limit of the mAMEP origin is constrained by the origin area of the mPSTs (in turn based on the extent and position of the laterosphenoid).

In *Citipati*, a pneumatic opening in the posterolateral wall of the parietal (visible at the posterior of the mAMEP origin in Fig. 4.1D), underneath where the squamosal

contacts the parietal to form the posteromedial margins of the supratemporal fenestra, seems to limit the mAMEP origin posteriorly, dividing it from the mAMEM. A similar opening is not as large or obvious in the other taxa, but similar limits to the origination sites are constrained by the geometry of the supratemporal fenestra. The dorsal extent of the origin is also clear in *Citipati* where a sharp lateral edge, running from the frontal–parietal contact posterolaterally to form the posterior boundary of the supratemporal fossa, separates the dorsal surface of the parietals from their lateral surfaces that contribute to the supratemporal fossa (Fig. 4.1D). This edge may function for muscle attachment similarly as suggested for a parietal ridge in the oviraptorid *Oksoko* (Funston *et al.*, 2020b).

We reconstruct the mAMEP inserting more anteriorly than mAMEM on the mandible (Fig. 4.1C,F,I,L), including around the apex of the coronoid elevation itself, along with the mAMES, specifically on the dorsomedial surface of coronoid prominence (Holliday, 2009; Nabavizadeh, 2020b).

m. adductor mandibulae externus superficialis (mAMES)

In all taxa, the mAMES can be reliably hypothesised to originate on the supratemporal bar (Holliday, 2009) (Fig. 4.1B,E,H,K). In oviraptorosaurs, this is formed by the postorbital and squamosal. The supratemporal bars in all taxa are mediolaterally flattened, with the medial surface directed slightly ventromedially, more so in *Citipati* than the others (Fig. 4.1E). The postorbital bars are concave along almost the entire medial surface in *Citipati*. In the other taxa, only the squamosal contribution is concave, with the postorbital ramus being flat or perhaps weakly convex in *Khaan* (Fig. 4.1H). There are no clear osteological signs of the extent of the mAMES origin site so we restrict it to the medial surfaces of the supratemporal bar. The ventral surface is narrow (as the bars are mediolaterally thin) and the medial surface is slightly orientated in the correct muscle direction in all taxa. The mAMES is reconstructed as originating along the full extent of this medial surface with its anterior and posterior limits constrained by the

origins of the mPSTs and mAMEM respectively.

The main body of the jugal has a trough-like gently concave medial surface in all taxa (especially so in *Conchoraptor* where the postorbital process of the jugal also has confluent concavity on its posteromedial surface). It appears like its form would neatly wrap over the exterior of the mAMES as it bulged outwards laterally and followed it anteroventrally on its origin–insertion path.

The mAMES likely inserts onto the dorsolateral edge and lateral surface of the surangular (Holliday, 2009; Nabavizadeh, 2020b), on a shelf running from the coronoid process to the articular (Fig. 4.1C,F,I,L). This shelf is more strongly defined in the later diverging taxa, especially *Citipati* (Fig. 4.1F) and *Khaan* (Fig. 4.1I). The mandibles of the oviraptorids bear apically triangular coronoid eminences, which are anteriorly displaced compared to those of other herbivorous dinosaurs. This has been hypothesized to increase mechanical advantage and attachment area for the temporal musculature as an adaptation for a stronger crushing bite (Barsbold, 1977; Smith, 1992; Ma *et al.*, 2017). The anteriorly displaced coronoid eminence in oviraptorids has been hypothesized to indicate a more anteriorly extending mAMES (as suggested for some ornithischians; Nabavizadeh, 2020a; 2020b). The mAMES is reconstructed thus here. The insertion site is constrained ventrally by the reconstructed extent of the mPTv insertion site, and dorsomedially by the insertions of the mAMEM and mAMEP, which insert onto the dorsomedial surface of the surangular.

m. pseudotemporalis superficialis (mPSTs)

In all four taxa, the mPSTs originates on the anterior and/or anteromedial wall of the supratemporal fenestra. In *Citipati*, the area is formed predominantly by the capitate process of the laterosphenoid and the posterior portions of the frontal (Fig. 4.1D). This surface is concave and rugose. The lateral surface of the laterosphenoid is also rugose, indicating a muscle attachment (Clark *et al.*, 2002). The site is bounded laterally by the postorbital, and two ridges may constrain the origin site of the mPSTs (Clark

et al., 2002): a sharp ridge runs posteromedially from the capitate process of the laterosphenoid to the epipterygoid contact, forming the ventral boundary, and a vertical ridge on the medial wall of the supratemporal fossa constrains the origin posteromedially, demarking it from the mAMEM. A triangular anterodorsal–posteroventral sloping surface (where a clear frontoparietal fossa has been lost in derived oviraptorids) extends to the dorsotemporal fossa. The anterodorsal extent of the mPSTs origin site on this surface is unclear. The frontoparietal fossa has been argued as a vascular space in dinosaurs rather than a site of muscle attachment (Holliday *et al.*, 2020), and we place the mPSTs similarly (Holliday *et al.*, 2020; Fig. 7 therein), extending into this sloping triangular space but not wholly filling it. We do not reconstruct any attachment of the mPSTs extending onto the frontal processes of the postorbitals.

In *Khaan*, the origin site is less well preserved (Fig. 4.1G). The mPSTs origin is placed in a similar position to *Citipati* and may extend slightly onto the lateral surface of parietals which contribute to the area. Similarly, in *Conchoraptor* (Fig. 4.1J), there is more of a contribution of the parietal to the anterior wall of supratemporal fenestra, but very little or no contribution of the frontal. In *Conchoraptor*, the whole origin site is more anteromedially positioned, and exhibits a large smooth exposure of the laterosphenoid. There are no obvious scars or ridges in the above-mentioned area of *Khaan* and *Conchoraptor*. In *Incisivosaurus*, the anterior corner of the supratemporal fossa is narrow and the mPSTs is more anteromedially positioned (Fig. 4.1A). The origin site likely comprises the laterosphenoid and small parts of the frontal and parietal.

The insertion of the mPSTs is likely related to the medial aspect of the coronoid elevation and parts of the medial adductor chamber (Nabavizadeh, 2020b). As the medial regions of the coronoid elevation are occupied by the mAMEP in our reconstruction we position the mPSTs, as the deepest temporal muscle, inserting into the anterior portion of the medial mandibular fossa (Holliday, 2009) and its anterodorsal rim (Fig. 4.1C,F,I,L).

m. pseudotemporalis profundus (mPSTp)

The mPSTp likely attached to the epipterygoid when present in dinosaurs (Holliday, 2009). When first described in detail, the epipterygoid of *C. osmolskae* (Fig. 4.1D) was noted as the largest of any known theropod, with a unique strongly twisted body and dorsal tip hosting robust muscle scars (Clark *et al*., 2002). We therefore locate the mPSTp origin site on the epipterygoid of each taxon with confidence and reconstruct its origin along the length of the epipterygoid, which is present in all four taxa (though partially reconstructed in *Khaan* and *Conchoraptor*) (Fig. 4.1G,J).

The insertion site is problematic but based on extant taxa the muscle likely inserted along the medial surface of the coronoid process or surangular (Holliday, 2009). As the coronoid process is occupied by the insertions of the mAMES and mAMEP, we position the insertion of the mPSTp dorsomedially on the surangular, occupying the dorsal rim of the mandibular adductor fossa, the position being largely constrained dorsally by the insertions of the mAMEM and mAMEP (Fig. 4.1C,F,I,L).

m. pterygoideus dorsalis (mPTd)

The origin site of the mPTd is reconstructed as the linear dorsal surface of the pterygoid in all oviraptorids where a longitudinal concavity runs anteriorly along their length anterior of the pterygoid flange (*Khaan* has a convex dorsal surface but the origin site is modelled similarly (Fig. 4.1H), and possibly the anteriormost dorsolateral surface of the pterygoid flange. The site is limited anteriorly and anterolaterally by the palatines and ectopterygoids, onto which no attachment was modelled as they are relatively small and delicate. In *Incisivosaurus*, the anterior extent of the origin site is constrained by the level of the jugal ramus of the ectopterygoid anterolaterally and the main body of the ectopterygoid laterally to around a longitudinal concavity on the dorsal surface of the pterygoid (Fig. 4.1A)—there seems very little/no origination on the palatine.

The mandibular insertion of the mPTd is commonly regarded to be onto the medial surface of the articular and retroarticular process (Holliday, 2009). We recon-

struct the mPTd in this position (Fig. 4.1C,F,I,L), inserting in the narrow medial surface of the posterior aspect of the mandibular ramus, under the medial facet of the articular glenoid and posteriorly onto the medial surface of the retroarticular process.

m. pterygoideus ventralis (mPTv)

The mPTv is well constrained through phylogenetic bracketing and we reconstruct it in the oviraptorids as originating along the ventral surface of the pterygoid, probably also extending onto the ventral aspect of the pterygoid flange (Holliday, 2009) and posteriorly terminating before the contact with the quadrate. The anterior of the origin is reconstructed as the level of the ectopterygoid contact, with the site entering the longitudinal ventral concavity that is anteriorly confluent with the choanae. In *Citipati*, the pterygoid flange is noted as reduced compared to typically carnivorous theropods, maintaining a roughly consistent width throughout its length (Fig. 4.1E), as suggested by Clark *et al.* (2002) to indicate a relatively small m. pterygoideus. However, the main pterygoid body of oviraptorids is relatively elongate. This may be an adaptation to open space for an expanded mAME group to insert onto the mandible, whilst maintaining volume of the mPT. The pterygoids of *Incisivosaurus* are also elongate and reduced in width (Fig. 4.1B), though not as extreme as in the derived oviraptorids (Balanoff *et al.*, 2009). The origin of the mPTv on the pterygoid ventral surface is interpreted as running from the posteroventral margin anteriorly into a trough medial to the ectopterygoid, and lateral of a ventral flange termed the accessory ventral flange by Xu *et al.* (2002), terminating anteriorly before the palatine contact.

In all taxa, the mPTv wraps around the ventral surface of the mandibular rami and inserts on the broad section of the lateral surface of the mandible (Fig. 4.1C,F,I,L), predominantly comprising the angular.

4.3.2 *Bite force estimates*

Measurements of the final volumetric muscle reconstructions are given in Table 4.1 along with the calculated muscle contraction force, resultant force acting on the mandible, and relative contribution of each muscle. The oviraptorid oviraptorosaurians show greater muscle volumes compared to the earlier diverging *Incisivosaurus*. This is confirmed by greater muscle CSA values relative to cranial surface area in *Citipati* (1.80×10^{-2}), *Khaan* (1.77×10^{-2}), and *Conchoraptor* (1.37×10^{-2}), compared to *Incisivosaurus* (1.21×10^{-2}). Table 4.2 shows the inlever and outlever measurements used to calculate bite force resulting from each cranial muscle (and their relative contribution) and the total estimated bite force in each species, for three different bite positions. These range from 349–499 N in *Citipati* down in order of cranial size to 53–83 N in *Incisivosaurus*. Complete calculations and values for Tables 4.1 and 4.2 along with measurements for the cranial models are documented in Appendix B.

The condition of the oviraptorid oviraptorosaurian skull is characterised by an increased volume for jaw adductor musculature and increased mechanical advantage resulting from anteroposterior shortening, compared with the more conventional theropod skull geometry of the earlier diverging *Incisivosaurus*. Estimated bite forces conserve a greater proportion of the resultant force applied to the mandible (Fbite/Fres) in the oviraptorids compared with *Incisivosaurus*. This results from greater mechanical advantage in the oviraptorids' jaw for all bite positions, though the difference relative to *Incisivosaurus* is greatest anteriorly (see Table 4.3) These two factors result in their comparatively stronger estimated bite forces, an increase of 17–84% greater (depending on species and bite position; see Table 4.2) than would be predicted by scaling by cranial surface area. The increased relative bite force of the oviraptorids is not a result of more beneficial muscle insertion angles; there is no clear difference in the ratio of resultant muscle force acting on the mandible to the actual muscle force produced (Fres/Fmus) between *Incisivosaurus* (0.894) and the three later diverging taxa (*Citipati*, 0.856; *Khaan*, 0.851; *Conchoraptor*, 0.899).

Table 4.1: Geometric measurements of reconstructed muscles and estimated contraction force (*Fmus = (volume / length) × 0.3 N/mm^2 × 1.5* (Thomason, 1991; Wroe *et al.*, 2005)). Insertion angles of muscles measured in the sagittal (α) and coronal (β) planes used to calculate resultant vertical force acting on mandible (*Fres = Fmus × cosα × cosβ*). Muscle volume, length, and insertion angles are average values for a single side; Fmus and Fres are the total of both sides on the mandible.

Muscle	Volume (mm^3)	Length (mm)	Fmus (N)	Contribution (%)	α	β	Fres (N)	Contribution (%)
Incisivosaurus								
AMEM	1492.1	43.4	30.9	12.3	27.6	4.4	27.3	12.2
AMEP	1393.8	44.4	28.2	11.2	30.0	4.2	24.4	10.9
AMES	2242.3	41.7	48.4	19.2	24.2	1.5	44.1	19.6
AMP	671.5	21.9	27.7	11.0	27.4	2.1	24.6	10.9
PSTp	379.0	31.1	11.0	4.4	26.6	5.3	9.8	4.4
PSTs	698.1	45.7	13.7	5.5	19.4	1.5	13.0	5.8
PTd	589.3	29.8	17.8	7.1	44.4	11.8	12.5	5.5
PTv	1695.8	20.7	73.7	29.3	13.3	15.6	69.1	30.8
Sum	9161.7		251.5				224.7	
Citipati								
AMEM	16130.0	69.2	209.9	15.6	23.8	4.0	191.6	16.6
AMEP	10122.5	59.9	152.1	11.3	32.4	8.4	127.1	11.0
AMES	19580.5	58.7	300.2	22.2	16.3	6.8	286.2	24.8
AMP	7221.5	43.8	148.4	11.0	44.7	14.7	102.1	8.8
PSTp	4876.0	50.9	86.2	6.4	33.6	27.2	63.8	5.5
PSTs	6962.5	64.9	96.6	7.2	25.9	5.9	86.5	7.5
PTd	3638.5	42.2	77.6	5.7	37.5	13.3	59.9	5.2
PTv	10858.0	35.1	278.8	20.7	19.0	25.1	238.8	20.7
Sum	79389.5		1349.9				1155.9	
Khaan								
AMEM	4032.0	48.5	74.9	12.1	28.9	1.2	65.6	12.4
AMEP	4398.0	45.8	86.5	13.9	35.5	7.1	69.9	13.2
AMES	6371.5	46.3	123.9	20.0	17.7	9.3	116.4	22.0
AMP	1782.5	27.5	58.3	9.4	40.4	7.7	44.0	8.3
PSTp	1440.0	34.8	37.2	6.0	39.5	22.5	26.6	5.0
PSTs	2260.5	49.3	41.3	6.7	27.0	2.7	36.8	7.0
PTd	1679.5	30.4	49.7	8.0	47.2	12.7	33.0	6.2
PTv	3900.0	23.6	148.9	24.0	14.9	19.2	135.8	25.7
Sum	25864.0		620.7				528.0	
Conchoraptor								
AMEM	2141.5	46.9	41.1	9.4	26.9	2.0	36.6	9.3
AMEP	2950.5	44.5	59.7	13.7	33.4	7.0	49.5	12.7
AMES	4071.0	46.1	79.6	18.3	18.8	6.6	74.8	19.1
AMP	1573.0	27.9	50.8	11.7	24.9	1.6	46.0	11.8
PSTp	786.0	31.1	22.7	5.2	17.1	9.8	21.4	5.5
PSTs	1678.5	47.5	31.8	7.3	22.6	4.1	29.3	7.5
PTd	1096.5	34.2	28.8	6.6	38.6	8.0	22.3	5.7
PTv	3528.0	26.4	120.3	27.7	14.0	17.9	111.1	28.4
Sum	17825.0		434.9				391.1	

Table 4.2: Bite force estimates (newtons) for each species, calculated (*Fbite = (Fres × Linlever) ÷ Loutlever*) for three points on their primary palate: the anterior tip of the beak/teeth; the middle level of the palate/ toothrow; the tooth-like projection in the posterior of the oviraptorid palate/the posteriormost teeth. Percentages in brackets reported next to the bite force estimates for the oviraptorid taxa show how much greater these estimates are compared to values that would be predicted by scaling up the bite force estimates of *Incisivosaurus* by cranial surface area.

	Anterior			Mid-palate			Posterior			
	Inlever	Outlever	Fbite (N)	Inlever	Outlever	Fbite (N)	Inlever	Outlever	Fbite (N)	Contribution (%)
Incisivosaurus										
AMEM	19.8	90.4	6.0	19.8	71.6	7.5	19.8	58.1	9.3	11.3
AMEP	30.3	90.4	8.2	30.3	71.6	10.3	30.3	58.1	12.7	15.4
AMES	23.4	90.4	11.4	23.4	71.6	14.4	23.4	58.1	17.8	21.6
AMP	19.9	90.4	5.4	19.9	71.6	6.8	19.9	58.1	8.4	10.2
PSTp	26.0	90.4	2.8	26.0	71.6	3.6	26.0	58.1	4.4	5.3
PSTs	31.5	90.4	4.5	31.5	71.6	5.7	31.5	58.1	7.0	8.5
PTd	9.4	90.4	1.3	9.4	71.6	1.6	9.4	58.1	2.0	2.5
PTv	17.6	90.4	13.5	17.6	71.6	17.0	17.6	58.1	20.9	25.4
Sum			53.0			67.0			82.5	
Citipati										
AMEM	37.1	142.0	47.1	37.1	122.0	54.9	37.1	99.4	67.4	13.5
AMEP	61.9	142.0	54.2	61.9	122.0	63.1	61.9	99.4	77.5	15.5
AMES	48.0	142.0	94.4	48.0	122.0	109.9	48.0	99.4	134.9	27.0
AMP	47.2	142.0	33.1	47.2	122.0	38.5	47.2	99.4	47.2	9.5
PSTp	56.8	142.0	25.2	56.8	122.0	29.3	56.8	99.4	36.0	7.2
PSTs	66.7	142.0	39.7	66.7	122.0	46.2	66.7	99.4	56.7	11.4
PTd	18.1	142.0	7.3	18.1	122.0	8.5	18.1	99.4	10.5	2.1
PTv	30.6	142.0	48.2	30.6	122.0	56.1	30.6	99.4	68.8	13.8
Sum			349.3			406.5			499.0	
			(84%)			(69%)			(69%)	
Khaan										
AMEM	18.6	103.6	11.8	18.6	88.7	13.7	18.6	72.0	16.9	8.6
AMEP	34.3	103.6	23.2	34.3	88.7	27.0	34.3	72.0	33.3	16.9
AMES	27.4	103.6	30.8	27.4	88.7	36.0	27.4	72.0	44.3	22.4
AMP	26.1	103.6	11.1	26.1	88.7	12.9	26.1	72.0	15.9	8.1
PSTp	36.5	103.6	9.4	36.5	88.7	10.9	36.5	72.0	13.5	6.8
PSTs	41.4	103.6	14.7	41.4	88.7	17.1	41.4	72.0	21.1	10.7
PTd	13.4	103.6	4.3	13.4	88.7	5.0	13.4	72.0	6.1	3.1
PTv	24.7	103.6	32.3	24.7	88.7	37.7	24.7	72.0	46.5	23.5
Sum			137.3			160.4			197.6	
			(54%)			(42%)			(42%)	
Conchoraptor										
AMEM	16.8	85.8	7.2	16.8	76.9	8.0	16.8	58.3	10.6	6.7
AMEP	29.8	85.8	17.2	29.8	76.9	19.2	29.8	58.3	25.3	16.1
AMES	24.7	85.8	21.5	24.7	76.9	24.0	24.7	58.3	31.6	20.2
AMP	21.1	85.8	11.3	21.1	76.9	12.6	21.1	58.3	16.6	10.6
PSTp	26.5	85.8	6.6	26.5	76.9	7.4	26.5	58.3	9.7	6.2
PSTs	31.6	85.8	10.8	31.6	76.9	12.0	31.6	58.3	15.9	10.1
PTd	13.6	85.8	3.5	13.6	76.9	4.0	13.6	58.3	5.2	3.3
PTv	22.1	85.8	28.6	22.1	76.9	31.9	22.1	58.3	42.0	26.8
Sum			106.7			119.0			157.0	
			(32%)			(17%)			(25%)	

Table 4.3: Mechanical advantage values for the three different positions of the bite force estimates.

	Mechanical advantage		
	Anterior	Mid-palate	Posterior
Incisivosaurus	0.236	0.298	0.367
Citipati	0.302	0.352	0.432
Khaan	0.260	0.304	0.374
Conchoraptor	0.273	0.304	0.401

The relative contribution of the different cranial muscles to bite force is broadly similar in each species (Fig. 4.4). The mPTv is typically the largest component, followed closely by the mAMES, then the rest of the mAME complex. *Citipati* differs from the others with a relatively stronger mAMES and mAMEM, and a relatively low value for the mPTv. The width of the *Citipati* cranium and mandible make the mPTv less vertically orientated and the reconstruction of the mPTv (in all taxa) is less well constrained by bone and other muscle volumes—its volume could be underestimated in all models. No clear difference emerges between *Incisivosaurus* and the later diverging oviraptorids in the relative contributions of cranial muscles to bite, apart from a slightly relatively weaker mPSTp and mPSTs—reconstructed muscles are proportionally similar but relatively larger in the oviraptorids. The bite force estimates of the four oviraptorosaurians (including *Incisivosaurus*) are significantly greater than estimates (from similar digital methods) made for other putatively herbivorous theropods of much larger body mass (Fig. 4.5) both relatively and absolutely.

4.3.3 *Gape analysis*

The early diverging oviraptorosaurian *Incisivosaurus* showed the highest estimates of optimal (25.0°) and maximum gape limit (49.5°) compared with the oviraptorid oviraptorosaurians, though not by much; estimates for gape limit in *Khaan* were lowest (20.5° and 40.0°), marginally less than *Citipati* (21.0° and 41.0°). Values for *Conchoraptor* (23.0° and 46.0°) lie between *Incisivosaurus* and the others. Figure 4.6 shows these estimates along with charts of the muscle cylinder strains that they are derived from.

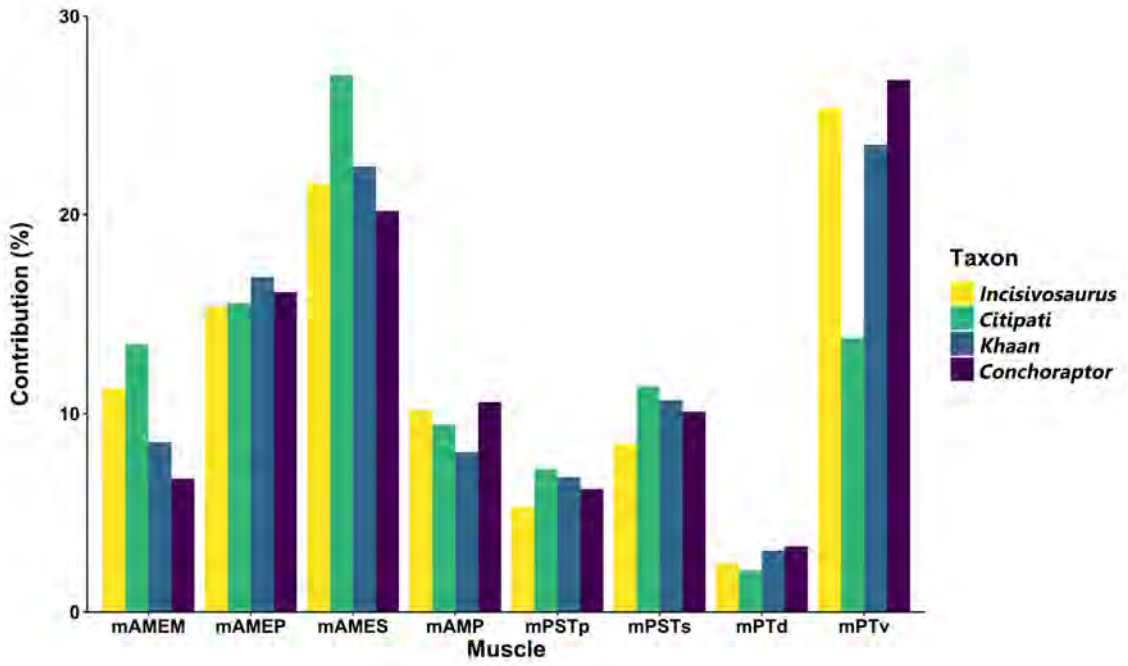

Figure 4.4: The relative contribution of each cranial muscle to total estimated bite force by species. Note that the condition of *Citipati* appears the most dissimilar to all others in its comparatively stronger mAMEM, mAMES and weaker mPTv

The anteriormost cylinder representing the mPTv constrains optimal and maximum gape in all but *Citipati*, in which it is constrained by the anteriormost regions of the mAMES. In this taxon the postorbital half of the skull is particularly low, sloping posteriorly, and the relatively low upper temporal bar directs the strong mAMES ventromedially to a prominent coronoid process of the surangular of the mandible. This leads to a shorter resting length for this muscle, causing its extension during jaw opening to exceed our tension limits just before the mPTv (which is the next most extended). The mAMEM is also relatively more extended in *Citipati*. The other three species are more similar in relative muscular strain, reinforcing the finding that relative muscle strength and arrangement in *Citipati* has more differences compared with other oviraptorids, than between some oviraptorids (*Khaan* and *Conchoraptor*) and earlier diverging oviraptorosaurians (*Incisivosaurus*).

Acting antagonistically to the jaw closing muscles is the m. depressor mandibulae (mDM), primarily responsible for jaw depression (opening). It originates from around

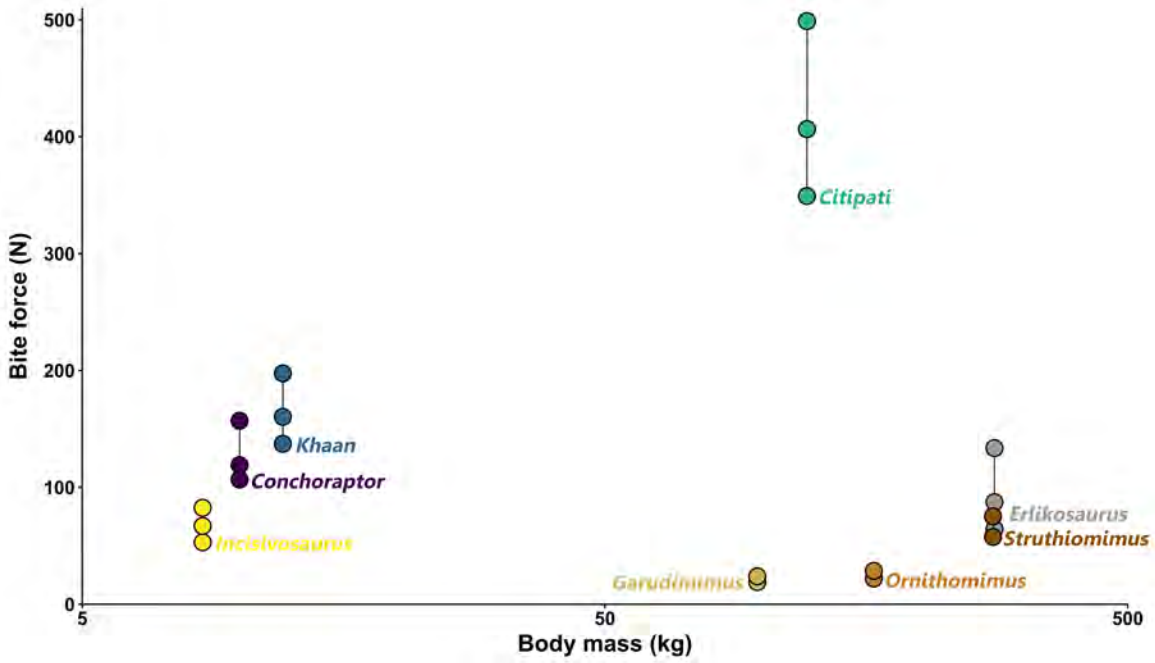

Figure 4.5: Comparison of the estimated bite forces in multiple positions of *Incisivosaurus* and three oviraptorid oviraptorosaurians with other likely herbivorous theropod taxa that have had estimates made using similar digital volumetric methods (Lautenschlager, 2013; Cuff and Rayfield, 2015) show the oviraptorosaurians (oviraptorids especially) are capable of much stronger bite forces both relative to body mass and absolutely. Body mass values from Zanno and Makovicky (2013).

the paroccipital processes of the cranium, inserting onto the dorsal aspect of the retroarticular process of the mandible (Holliday, 2009, Nabavizadeh, 2020b). During the gape analysis, we checked mDM length change (from a shorter state at the maximum and optimal estimated gape angles to an elongated state at the 5° resting jaw angle) was not unrealistic. Strain values of the mDM were all calculated to be below the maximum strain limit (1.7) we modelled for the jaw adductors. From its shortest (maximum gape limit) the mDM in *Incisivosaurus* was extended by a factor of 1.08 at the estimated optimal gape limit and 1.20 the 5° resting jaw angle, *Citipati* reached 1.11 and 1.33 respectively, *Khaan* reached 1.16 and 1.48, and *Conchoraptor* reached 1.19 and 1.67.

The oviraptorosaurians show estimated gape limits much lower than those of carnivorous theropods tested by Lautenschlager (2015), more like herbivorous thero-

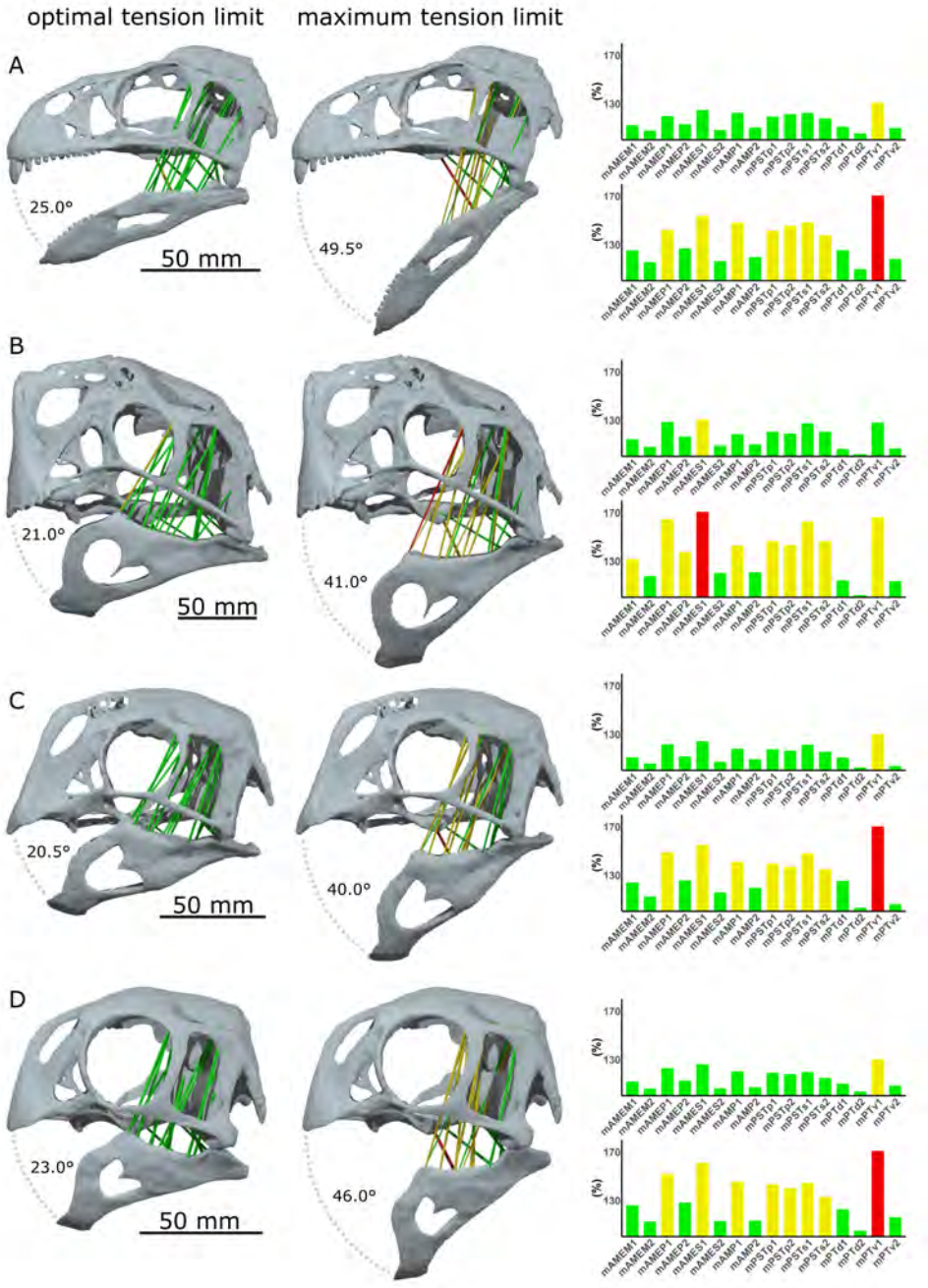

Figure 4.6: Estimates of the gape angle limit of optimal tension and the maximum limit of gape for muscle tension in *Incisivosaurus gauthieri* (A), *Citipati osmolskae* (B), *Khaan mckennai* (C), and *Conchoraptor gracilis* (D) from a muscle resting length at a gape angle of 5°. Bar charts show the strain factors of individual modelled muscle cylinders at optimal and maximum tension limit; anteriormost muscle cylinders suffixed '1', posteriormost suffixed '2'. Muscle cylinders (and corresponding bars) are colour coded yellow and red when exceeding 130% and 170% of resting length respectively, otherwise green. Note that the anterior mPTv constrains gape in all species apart from *Citipati* which is constrained by the anterior mAMES. Scale bars 50 mm. Muscle abbreviations given in results section.

pod *Erlikosaurus* (optimal tension limit 24.0°; maximum tension limit 49.0°; resting gape of 6°). It is noted that herbivorous species exhibit lower gape angles than carnivorous species (Herring and Herring, 1974; Lautenschlager, 2015), and thus our estimates of gape angle may be further support for a herbivorous diet among oviraptorosaurians (when considered against other theropods). Lautenschlager (2015) notes that experimental results document gape angle in modern birds can reach angles up to around 40°. The maximum gape angles estimated for these oviraptorosaurians are similar to experimental results of gape angle in birds among passerines and Galliformes, which can reach around 40° (Zusi, 1967; Lederer, 1975; Hoese and Westneat, 1996; Bout and Zweers, 2001) (though this can be greater in parrots, Carril *et al.*, 2015)—a functional similarity between the crania of birds and oviraptorids which, beyond superficial beaked appearance, are quite dissimilar.

4.4 Discussion

This study is the first attempt at quantifying oviraptorosaurian bite forces. Our estimates show the Oviraptoridae were capable of producing greatly stronger bite forces than other herbivorous theropods, and those of *Incisivosaurus* were roughly equal to ornithomimids of body mass roughly 33 times its size. These results suggest that oviraptorid oviraptorosaurians (and to a lesser extent earlier diverging oviraptorosaurians such as *Incisivosaurus*) significantly differed in cranial function from other herbivorous theropod groups of both similar and larger size, potentially feeding on very different foodstuffs. Oviraptorids shared an environment with both ornithomimosaurs and therizinosaurs, and other additional herbivorous dinosaurs such as ankylosaurs, hadrosaurs, and sauropods (Funston *et al.*, 2018). The strong bite forces estimated here could have allowed oviraptorids to acquire and process tougher plant material than ornithomimosaurs and therizinosaurs. Herbivores of greatly larger body mass and forms with adaptations towards complex jaw mechanisms or gut processing capabilities (i.e. sauropods, hadrosaurs) could likely also cope with tough vegetation, but

oviraptorids may have been able to focus on entirely different food sources purely from the difference in their relative size (focussing on small tough items ignored by larger forms) and height stratification of material (focussing low to the ground). Their jaw strength would also feasibly allow them to handle small prey, to supplement a mostly herbivorous diet, and generally broaden the range of possible food items as a useful tool for both food procurement and initial processing. This adaptability could have given them a competitive advantage among the potentially sparse vegetation of their semi-arid environment (Funston *et al.*, 2018).

Suggesting specific food sources is difficult as plant fossils are rare from the formations associated with the oviraptorids studied here (Jeryzkiewicz *et al.*, 2021). A key dietary focus of oviraptorids may have been small tough stems, nuts or seeds, similar to modern parrots (Benavidez *et al.*, 2018). It is also, however, impossible to satisfactorily compare the two groups as parrot bite forces and body mass differ from those estimated for oviraptorosaurians by an order of magnitude (Carril *et al.*, 2015). High bite forces also do not necessitate dietary specialism (i.e. such specificity as molluscivory)—instead, they widen the range of possible food sources with oviraptorosaurians potentially being effective generalists or specialists depending on the environment. The result that *Incisivosaurus* has the lowest jaw mechanical advantage, relative bite force, and highest gape angle may suggest it more retained some plesiomorphic dietary adaptation to omnivory/non-herbivorous foodstuffs. Our gape analysis suggests jaw clearance may limit potential prey items to around 6 cm in maximum transverse dimensions.

The orbits are large in all four oviraptorosaurian species but the shortened crania and more anteriorly positioned coronoid eminence of the mandibles in the oviraptorids result in direct muscle paths between origin and insertion intersecting the presumed space for the eyeball. The muscular reconstructions presented here, with the mAMEP, mAMES, and mPSTs required to curve anteriorly around the presumed ocular space, are reminiscent of a similar muscular condition in parrots (Hofer, 1950;

Carril *et al.*, 2015). We reject any parrot-like muscular attachments onto the jugal parrots (Hofer, 1950; Carril *et al.*, 2015) as hypothesised in some non-avian dinosaurs (Holliday, 2009) and assessed in the also superficially parrot-like *Psittacosaurus* (Taylor *et al.*, 2017); the jugals are very thin and delicate in oviraptorids.

Differences in bite force between *Incisivosaurus* and the oviraptorids are chiefly due to different cranial geometries and available space for musculature, rather than changes in muscular arrangement. The steady increase of bite force estimate with size in oviraptorosaurians in this study (shown in Fig. 4.6) arises from a fairly consistent muscular arrangement in our reconstructions, though there are some differences. The only consistent difference of *Incisivosaurus* compared to the oviraptorids is a relatively slightly weaker mPSTp and mPSTs. The most different in muscle arrangement is *Citipati*, in which the mAMEM and mAMES are relatively stronger than the other oviraptorids and *Incisivosaurus*. The increased relative contribution of these muscles to bite force in *Citipati* is a result of its morphologically distinctive wide, anterodorsal–posteroventrally sloping occiput. This places the supratemporal fenestra more anteriorly and forms a platform for the mAMEM to be larger and better directed, more efficiently orientating both the mAMEM and mAMES to insert on a relatively larger coronoid process. This is combined with a wider adductor chamber allowing relatively larger musculature, especially expansion of the mAMES which originates from a more robust and concave supratemporal bar with a large amount of space to fill between this origin and its broad insertion on the mandible. *Citipati* shows the largest increase in bite force (relative to cranial surface area, see Table 4.2) compared with the early diverging *Incisivosaurus* out of the three oviraptorids, and therefore the greatest estimated bite force due to its larger body mass. The increased size and efficiency of the muscles within the adductor chamber in *Citipati*, especially the mAMEM and mAMES, results in the comparatively lower contribution of the mPTv to bite force, with the mPTv also positioned less vertically. However, the extent of the mPTv is more difficult to reconstruct as it is less surrounded by bony constraints both medially and laterally

around the mandible and is only in substantial contact with the volume of the mPTd. The mPTv volume was reconstructed by growing the basic shrinkwrapped volume to a similar degree as the other muscle volumes were able to be expanded before they were constrained by adjacent muscles, without making the mPTv substantially thicker than its origin area. This resulted in a realistic volume that we estimate as relative strong but could feasibly have been even larger in size.

Oviraptorids (and caenagnathids) have a craniomandibular joint which would have allowed anteroposterior sliding (Holliday, 2009; Ma *et al.*, 2017; Ma *et al.*, 2020b; Nabavizadeh, 2020b). For anteroposterior movement of the mandible to take place, the origin and insertion of the jaw adductor muscles must be off a vertical line (Funston and Currie, 2014; Nabavizadeh, 2020b). Most adductor muscles (mAME and mPST groups) have a posterodorsal line of action. The condition in *Citipati* differs from the other oviraptorids as the mAME group, which contributes the most to bite force, is more vertically orientated and the only muscles positioned off the vertical in an opposing anterodorsal line, the mPT group, are relatively much weaker than the other oviraptorids. This positions the mAME less for palinal motion of the jaw and the mPT would produce a weaker returning forward motion, potentially indicating *Citipati* had a stronger vertical crushing bite with less emphasis on anteroposterior grinding jaw movement. In addition to body size, this could hint at an element of niche partitioning resulting from jaw function between *Citipati* and co-occurring oviraptorids like *Khaan*.

No crania of the other key group within Oviraptorosauria, the Caenagnathidae, are well enough preserved to undertake the same kind of digital myological and biomechanical analyses possible for the species studied here. Essentially no material representing the muscle origin sites identified in this study has been described for caenagnathids but there is a good availability of mandibular specimens (Funston and Currie, 2014; 2016; Lamanna *et al.*, 2014; Ma *et al.*, 2017; Funston *et al.*, 2020a). Caenagnathid mandibles are typically elongate and slender compared to oviraptorid mandibles. The surangular and angular of caenagnathids are less tall and surround

a large external mandibular fenestra which is less anteriorly positioned, providing relatively less available space for musculature to insert. Any coronoid eminence is low or absent, presumably reducing the mechanical advantage of the mAME and mPST muscle groups in a condition contrary to the dorsally projecting coronoid eminence of the oviraptorids which increases mechanical advantage. Nevertheless, the jaw adductor musculature of the caenagnathids mandible likely inserted onto similar positions (Nabavizadeh, 2020b; Figure 4L of Holliday, 2009) as oviraptorids. The recognition of a lateral flange on the dentary of *Anzu* and *Gigantoraptor* (Lamanna *et al.*, 2014) has been compared with a similar feature interpreted as an adductor insertion site in dicynodonts (King *et al.*, 1989) (which have mandibles similar to oviraptorosaurians, capable of anteroposterior sliding movement) but a similar attachment site laterally onto the dentary of caenagnathids would position the mAMES insertion much more anteriorly than that reconstructed here in oviraptorids, likely unrealistically forward relative to the orbit and adductor chamber.

The diet of caenagnathids has been suggested to be more carnivorous than oviraptorids (Zanno and Makovicky, 2011; Funston and Currie, 2016; Ma *et al.*, 2020a; 2020b). Several caenagnathids mandibles show a sharp, upturned tip and the lower mechanical advantage of their jaws would result in a weaker but quicker jaw opening/closure compared to oviraptorids, a possible adaption for catching mobile prey of a small body size as part of a carnivorous or omnivorous diet (Zanno and Makovicky, 2011; Funston and Currie, 2016; Ma *et al.*, 2020b). Herbivory focussing on softer plant material than that consumed by oviraptorids (Longrich *et al.*, 2013) has also been suggested, though caenagnathids appear to lack features positively adapted towards herbivory. However, exceptions such as the huge *Gigantoraptor*, the mandible of which appears short and deep as in those of oviraptorids (the cranium is unknown) (Ma *et al.*, 2017), imply a mix of feeding styles and niche partitioning within Caenagnathidae, with adaption among some caenagnathids towards high bite forces as in Oviraptoridae. Lack of material makes clear statements difficult.

It is worth noting that oviraptorid dinosaurs were toothless and likely possessed keratinous beaks. The morphology of rhamphothecae would affect our estimates of bite force, changing bite position and mechanical advantage. The premaxilla and dentary shape of Oviraptoridae is variable and beak shapes within the group are also likely to have varied. However, it is uncertain how closely the rhamphotheca would have followed underlying bone and reconstruction of this covering's morphology is problematic.

4.5 Conclusion

Muscular reconstructions show oviraptorosaurian dinosaurs were capable of producing relatively strong bite forces, potentially being predominantly herbivorous generalists or specialists depending on the environment. Cranial shortening and expansion of muscle space in oviraptorids increased bite force compared with early diverging oviraptorosaurians, but muscular arrangement remained fairly conservative, differing more within Oviraptoridae itself (*Citipati* differed more from its fellow oviraptorids in the relative contribution of different muscles to bite force than did *Incisivosaurus*).

Our results suggest herbivorous theropods (including oviraptorids) were niche partitioned by both body size, but also clearly by cranial function. Bite forces vary greatly more between oviraptorids and therizinosaurs (and ornithomimosaurs) than do estimated gape limits, and thus were likely the more important niche partitioning component of cranial function.

These results will serve as an ideal stepping off point for further investigation into the cranial functional morphology of oviraptorosaurians, using the retrodeformed specimens and reconstructed muscle force vectors to inform finite element analyses to compare patterns of stress and strain. This is explored in the following chapter and reveals more information about the specific ways oviraptorosaurian crania were adapted to utilise their relatively strong bite.

5 | Diversity of cranial function in Oviraptorosauria as revealed by biomechanical analyses

My contribution to this chapter involved leading all parts of the research, including data collection, analysis, interpretation of results, as well production of the manuscript, figures, and tables. Feedback was given on interpretation of results and drafts of the manuscript by S. Lautenschlager.

5.1 Introduction

The study presented in Chapter 3 has indicated that the cranial shape of Oviraptoridae was a structure better adapted to resist bending forces when compared with crania from other theropod dinosaurs of varying dietary guilds. Chapter 4 has shown that cranial shortening and expanded space for musculature also suggests oviraptorids had the ability to produce much greater bite force for their body size, compared with other theropods suggested to be herbivorous (Meade and Ma, 2022). This chapter explores further how they may have been using their powerful jaws and the influence of their strengthened jaw adductor musculature on their crania by using finite element analysis (FEA) in combination with the jaw muscle force estimates calculated in Chapter 4 (Meade and Ma, 2022).

Well-informed FEA scenarios using appropriate material properties, functional

loading conditions, and accurate and detailed 3D meshes can replicate stress-strain patterns resulting in bone from loading (Rayfield, 2007; Bright and Rayfield, 2011). Operating under the framework that skeletal morphologies are adapted through evolutionary shape change and bone remodelling (Wolff, 1892; Huiskes *et al.*, 2000; Ruff *et al.*, 2006) towards energetic efficiency and strength in mechanical function, we can use FEA to test hypotheses of function and compare functional morphology between species (Richmond *et al.*, 2005; Dumont *et al.*, 2009). Feeding and diet in fossil taxa have been explored by using FEA to model feeding forces on crania in a wide variety of tetrapod groups (Rayfield, 2007). This has proved a useful method for comparing palaeoecology, particularly in investigating and comparing feeding in extinct herbivorous dinosaur groups (Button *et al.*, 2014, 2016; Lautenschlager *et al.*, 2016; Taylor *et al.*, 2017) and other herbivorous archosaurs (Bestwick *et al.*, 2021).

As discussed in Chapter 2 (Section 2.1.1.), simplifications are a necessity of modelling functional scenarios using FEA (Rayfield, 2007; Herbst *et al.*, 2022). For example, modelling of bone sutures and the chondrocranium, and variation in bone material properties – including anisotropy and modelling of both cortical and trabecular bone – can affect FEA results (Herbst *et al.*, 2022). Exact material properties of bone in extinct taxa are unknown and we cannot use FEA to reliably predict absolute stress-strain values (Rayfield, 2007; Bright and Rayfield, 2011). Instead, comparative approaches can be taken with phylogenetically closely related taxa which can be presumed to vary less in bony material properties and structure to test hypotheses of function on relevant parts of their skeleton.

Here, I test the hypothesis that the oviraptorid cranium will be able to resist the stresses produced by comparatively strengthened adductor musculature, and experience at least similar stress magnitudes as other theropod taxa undergoing muscle driven bites. The loading scenarios of Chapter 3 were important from a perspective of cranial architecture, revealing the comparative strength of the oviraptorid cranium (in response to bending) and how their crania funnel stresses away from their most deli-

cate areas, further evidencing their unique cranial functional morphology was adapted for high bite forces. However, the tests were limited in ecological relevance. This chapter will present FEA scenarios modelling muscle driven bites in three oviraptorid species: *Conchoraptor*, *Citipati*, and *Khaan*. The early diverging oviraptorosaurian, *Incisivosaurus*, is also tested, and all four oviraptorosaurians are compared with the carnivorous theropod *Allosaurus*, and herbivorous theropods *Erlikosaurus* and *Ornithomimus*, each of which has a more conventional theropod cranial shape. The other theropods the oviraptorosaurians are compared were limited to non-avian theropods. This kept the comparison free of additional adaptations encountered in groups like birds in which a substantial degree of cranial kinesis or bone adaptation for other functions (bone reduction for flight) might impair a comparative akinetic approach using identical material properties.

The FEA scenarios modelling different bite positions aim to reveal how differing muscle arrangements and strengths interact with the different theropod cranial shapes to determine how the species studied may have actually used their jaws. Differing performance between bite positions may give clues towards comparative functional ecology in Oviraptoridae. Comparatively lower stresses from a posteriorly positioned/palatal bite point may support the kind of crushing bite linked with durophagy (Barsbold, 1976a; Currie *et al.*, 1993). Lower stresses at anteriorly positioned/rostral bite points may more suggest leaf eating (Smith, 1992) or a parrot-like 'nipping' bite (Funston *et al.*, 2018; Ma *et al.*, 2020b). Equal performance across a range of bite points may indicate more generalist function/diet.

In addition to intrinsic muscle driven biting scenarios, I test several extrinsic loading scenarios simulating head movements related to feeding that would have been driven by postcranial musculature (similar to Lautenschlager *et al.*, 2013; McCurry *et al.*, 2015; and Montefeltro *et al.*, 2020). These were designed to assess how the oviraptorosaurian cranium responds to bending forces more beyond the sagittal plane, in a similar directly comparative way to the bending tests in Chapter 3 using loads

scaled to cranial surface area.

Comparisons will be drawn between each species' cranium by qualitatively comparing contour plots of von Mises stress, quantitatively comparing mean and peak von Mises stress, and total strain energy, and through a holistic comparison of the range of cranial deformation they experience from this array of biting and extrinsic scenarios. The expectation is that species with more specialist cranial function may be adapted to limit deformation in fewer scenarios and those feeding in a more varied or generalist way will experience a lesser range of deformations.

Finally, the influence of a keratinous rhamphotheca covering the beak on the strength and performance of the oviraptorid cranium is tested and its effects are compared with other similar studies (*Erlikosaurus*, Lautenschlager *et al.*, 2013; *Ornithomimus*, Bestwick *et al.*, 2021). I assess if its stress-reducing effect is as limited as in these other studies, and how much its effect may have influenced cranial morphological evolution in oviraptorids.

5.2 Methods

The FE scenarios were created in Hypermesh and use the same models as described in Chapters 3 (see Table 3.1 therein) and 4. The same material properties were used as in Chapter 3 (bone: extant alligator mandibles (E = 20.49 GPa, υ = 0.40; Zapata *et al.*, 2010; Lautenschlager *et al.*, 2013); teeth: crocodile teeth (E = 60.40 GPa, υ = 0.31; Creech, 2004; Reichel, 2010; Lautenschlager *et al.*, 2013). Four nodes on each quadrate articular surface and three nodes on the posterior of the occipital condyle were constrained in all directions. One or two nodes (to model unilateral and bilateral biting respectively) were constrained on the anterior, middle, or posterior of the palate in the vertical (Z) axis (same locations as in the bending test of Chapter 3). The effect of constraining different axes at the bite points was sensitivity tested and is presented in Appendix C (Fig. C.1). Force vectors were applied for each cranial muscle modelled in Chapter 4 (Meade and Ma, 2022), divided across eight nodes on their origin site

totalling the estimated contraction force of each muscle on each side.

A number of further scenarios using extrinsic loading were created to model a head-pull, head-shake, and a head-twist motion (similar to Montefeltro *et al.*, 2020) to additionally test the performance of the crania in ways that may be relevant to feeding, driven by postcranial musculature. The pull scenario comprised two anteriorly directed loads on the lingual surface of the beak tip/front teeth. The shake scenario comprised two loads directed right laterally, one on the medial edge of the right mid-palate tooth/beak rim and one on the opposite lateral edge of the left. The twist scenario comprised a dorsally directed load on the bottom of the right mid-palate tooth/beak rim, and another load ventrally directed at a node corresponding to the region of the premaxilla/maxilla directly above the same point on the opposite side. Models were constrained at the quadrate and occipital condyle for these extrinsic scenarios. Extrinsic loads for pulling, shaking, and twisting scenarios were based on loads from Chapter 3, similarly scaled to cranial surface area but halved in value, as this produced mean von Mises stresses in the pull, shake, and twist scenarios of similar magnitude to the muscle driven intrinsic bite FEA scenarios. This was important so as not to have either the intrinsic or extrinsic scenarios dominating when the deformations from each scenario were compared using principal component analysis.

Additionally, cranial models assessing the influence of a keratinous rhamphotheca covering the beak of the oviraptorids on the distribution and magnitude of stress in their crania were also tested using material properties from bird beaks (E = 1.04 GPa, υ = 0.40) (Chen *et al.*, 2008; Lautenschlager *et al.*, 2013). Keratinous rhamphotheca were constructed for *Citipati*, *Conchoraptor*, and *Khaan* with a thickness scaled to their cranial lengths (keratin thickness in *Citipati* was 2 mm; *Conchoraptor* 1.1 mm; *Khaan* 1.5 mm). These models were primarily tested with bilateral and unilateral muscle driven bites at the anterior and mid-palate (as the posterior bite position would not be covered by the keratin sheath). The effect of a different, longer rhamphotheca morphology was tested for those oviraptorids with a pointed premaxilla (*Conchorap-*

tor and *Khaan*) and the influence of the rhamphotheca on the pull, shake, and twist scenarios was also tested but these will be presented in Appendix C (Fig C.2 and C.3).

The FE models were imported into Abaqus for solving. Contour plots showing stress distribution are figured using the Viridis colour scheme to enhance interpretation and accessibility (Lautenschlager, 2021). When comparing resulting von Mises stress quantitatively through assessing peak stress and calculating means from exported reports of the von Mises stress values at every element node for each FEA scenario, the top 5% of nodal stress values were excluded to account for artificially high stress values from point loads and nodal constraints, similarly to as described in Chapter 3 (see also Walmsley *et al.*, 2013; Marcé-Nogué *et al.*, 2016; Tseng and Flynn, 2018; Montefeltro *et al.*, 2020).

Cranial models of the resulting deformation (increased by a factor of 25 for all models) from the anterior, mid-palate, and posterior muscle driven bites (bilateral and unilateral), the pulling, shaking, and twisting scenarios (using extrinsic loads scaled to cranial surface area), along with an undeformed cranial model, were exported for each species (total of 10 per taxon). A comparison of the variance in deformation each taxon experienced between the different FEA scenarios was then conducted. A Python script imported each deformed cranial model mesh (and the original undeformed mesh for comparison) into Blender (version 2.79), uniformly scaled them based on their longest dimension (length in all cases), and shrinkwrapped a subdivided spherical mesh around their shape (Manning, 2021). The positions of the faces of this sphere mesh, once shrinkwrapped, could be used as landmark coordinates to represent the different deformed cranial model shapes they covered, exporting a set of coordinates for each of the 70 cranial models.

This coordinate data was then subjected to a Procrustes superimposition in PAST (Hammer *et al.*, 2001). Using this Procrustes transformed data, the variance in deformation within each taxon was plotted in PAST using principal component analysis (PCA). This visualised which taxa were represented by a greater spread of deformation

resulting from the different FEA scenarios. The range of deformations within each taxon may indicate how well their cranial functional morphology is adapted to limit deformation across multiple scenarios (or not) — the relative positions of the different taxa on the PCA plot space has little function meaning.

5.3 Results

5.3.1 *Muscle-driven bites*

All oviraptorids show consistent stress hotspots across all bite positions in the supratemporal bar and squamosal, palatine, region of quadrate–pterygoid contact, and the anterior half of vomer (Fig. 5.1). There are noticeable hotspots at the bite points on the premaxilla in the anterior and mid-palate scenarios, exacerbated by the nature of a single node being constrained; the main body of the premaxilla shows very little stress. The oviraptorids show some degree of stress in the processes of the premaxilla above the antorbital fenestrae. There is also some stress consistently in the anteroventral parts of the braincase, near and including the epipterygoids, and in the thin parasphenoid rostrum of all oviraptorosaurians (including *Incisivosaurus*) — though this structure may not have been well ossified.

The bottom of the lacrimal in the mid-palate unilateral and posterior bilateral and unilateral biting scenarios in *Conchoraptor* and *Khaan* shows a similar stress hotspot (Fig. 5.1C–F and 5.2B,C,E,F) (likely from parts of this region being reconstructed from *Khaan* in the *Conchoraptor* retrodeformation). The nasal process of the premaxilla generally shows very little stress in the oviraptorids, only to a small degree in *Conchoraptor* under anterior and posterior biting (Fig. 5.1A,C). The parietals vary in stress among the oviraptorids; low in *Conchoraptor*, medium in *Khaan*, higher in *Citipati*, and consistent across bite point scenarios. The maxillae show fairly high stress in all bite points for *Citipati* (Fig. 5.1G–I), unlike other oviraptorids. This is the area where stress is especially exaggerated by unilateral mid-palate bites in *Conchoraptor* (Fig.

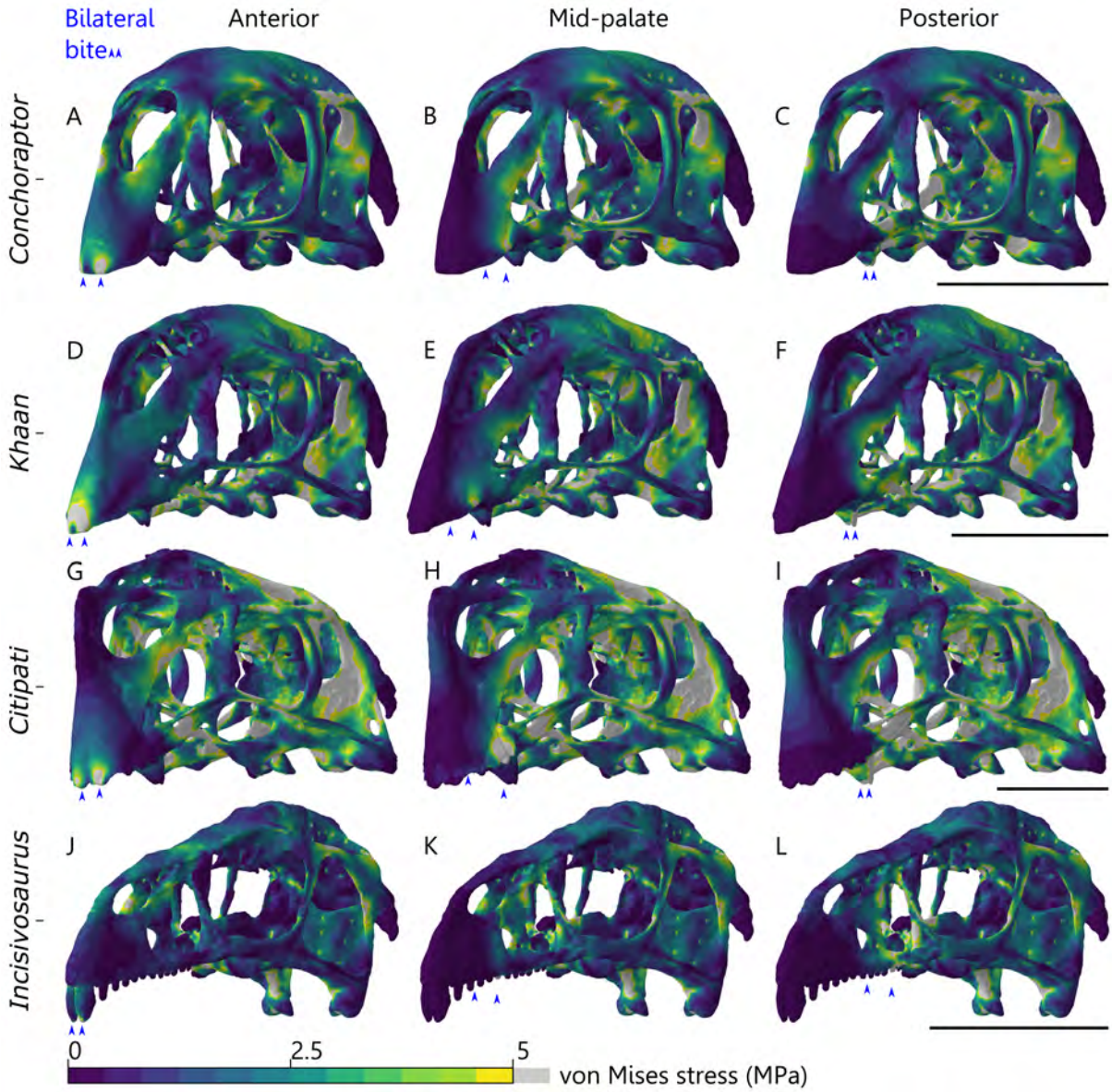

Figure 5.1: Von Mises stress (MPa) contour plots from FEA using bilateral bite point constraints and intrinsic muscle forces in cranial models of oviraptorosaurians *Conchoraptor* (A–C), *Khaan* (D–F), *Citipati* (G–I), and *Incisivosaurus* (J–L). Constraints at bite points shown by small blue arrows at the anterior of the beak/teeth (A, D, G, J), the middle tooth/lateral edge of beak (B, E, H, K), or the posterior teeth/ tooth-like projection on oviraptorid palate (C, F, I, L). All scale bars on the right are 50 mm.

5.2B) and especially *Citipati* (Fig. 5.2H), with essentially the entire region surrounding the antorbital fenestrae experiencing high stresses. The unilateral mid-palate bite is also the only scenario where an oviraptorid, *Citipati*, shows high stresses in the nasal (Fig. 5.2H) (and the contribution of the premaxilla to the nares).

Stress is noticeably lower in *Incisivosaurus* (Fig. 5.1J–L) compared with the oviraptorids but is likewise characterised by stress around the supratemporal bar and squamosal, and the region of the pterygoid–quadrate contact. The nasals and lacrimals show some degree of stress in anterior biting (Fig. 5.1J), while in mid-palate and posterior biting stress is more present on the interfenestral bar of the maxilla, the lacrimal, and the postorbital bar (Fig. 5.1K,L). Unilateral biting chiefly exaggerates stresses in the interfenestral bar of maxilla and the lacrimal in the mid-palate and posterior scenarios (Fig. 5.2K,L), but only by a small amount. Unlike the oviraptorids, the more robust jugal consistently shows low stress. When constrained at the prominent front teeth for an anterior bite, the teeth show fairly low stress (Fig. 5.1J and 5.2J). The premaxillae show negligible stress in all bite scenarios.

Allosaurus shows consistent stress at the lacrimal, quadrate, pterygoid, small regions of squamosal and parietal, palatine, jugal, and postorbital bar (Fig.5.3A–C). Anterior biting also stresses the premaxilla and nasal around the anterior and dorsal edge of the nares (Fig. 5.3A). Anterior and mid-palate biting stresses the maxilla near its contact with the nasals at the dorsal edge of the antorbital fenestra (Fig. 5.3A,B). Posterior biting creates an especially large stress concentration on lacrimal (Fig. 5.3C). Stress increases between bilateral and unilateral scenarios are most noticeable in the mid-palate bite, with increased stress surrounding all areas of the antorbital fenestra (Fig. 5.4B).

Erlikosaurus shows consistent stress in the quadrate, supratemporal bar, parietal, jugal, and maxilla (Fig. 5.3D–F). Anterior biting particularly also stresses the premaxilla and nasal (Fig. 5.3D). Unilateral biting gives slightly more intense stress values in the premaxilla in anterior biting (Fig. 5.4D), and in the maxilla with mid-palate and

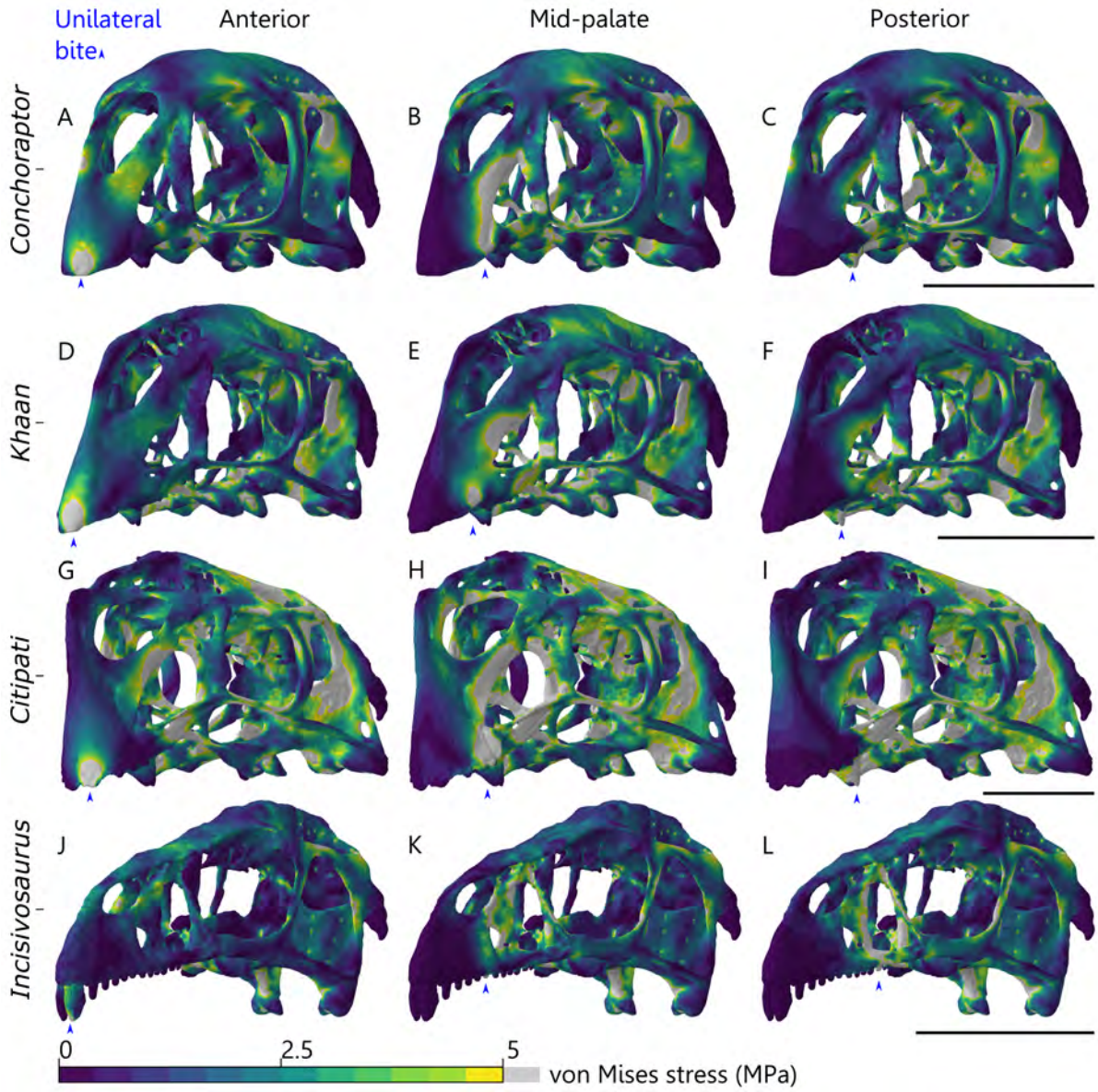

Figure 5.2: Von Mises stress (MPa) contour plots from FEA using a unilateral bite point constraint and intrinsic muscle forces in cranial models of oviraptorosaurians *Conchoraptor* (A–C), *Khaan* (D–F), *Citipati* (G–I), and *Incisivosaurus* (J–L). Constraints at bite points shown by a small blue arrow at the anterior of the beak/teeth (A, D, G, J), the middle tooth/lateral edge of beak (B, E, H, K), or the posterior teeth/ tooth-like projection on oviraptorid palate (C, F, I, L). All scale bars on the right are 50 mm.

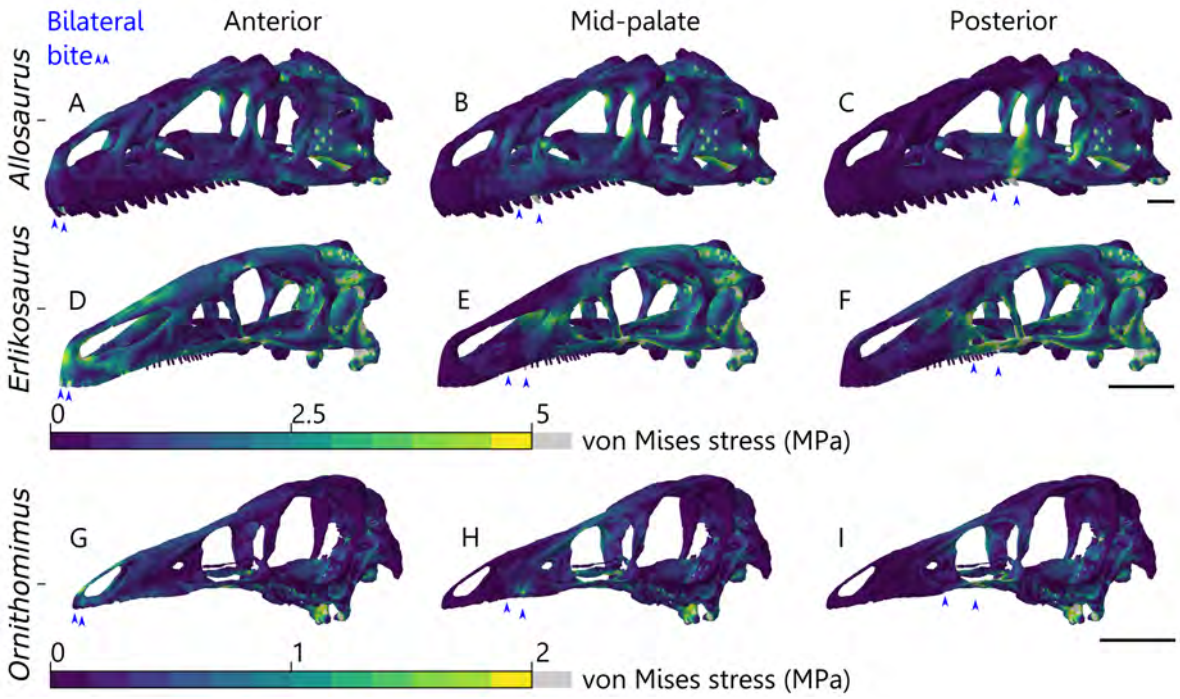

Figure 5.3: Von Mises stress (MPa) contour plots from FEA of bilaterally bite point constraints and intrinsic muscle forces in cranial models of *Allosaurus* (A–C), *Erlikosaurus* (D–F), and *Ornithomimus* (G–I). Constraints at bite points shown by small blue arrows. Note *Ornithomimus* is figured at a different stress scale magnitude due to much lower stresses resulting from weaker jaw adductor muscle forces. All scale bars on the right are 50 mm.

posterior bites (Fig. 5.4E,F). Stresses in *Ornithomimus* are much lower than the other species, due to tiny jaw adductor muscle forces, hence is figured at a different stress scale magnitude (Fig. 5.3 and 5.4). Areas of higher stress are localised to the quadrate in all scenarios (Fig. 5.3G–I), the bite point and nasal arch in anterior bites (Fig. 5.3G), and the region surrounding the antorbital fenestra in mid-palate and posterior bites (Fig. 5.3H,I). There are only minor differences between stresses from bilateral and unilateral biting.

The oviraptorid oviraptorosaurians generally experience greater mean and peak von Mises stress and total strain energy in all bite positions compared to the other theropods (Fig. 5.5) (Table. 5.1). Mean stress is consistently greatest in *Citipati* and then *Khaan*. The oviraptorid with the lowest mean stress is *Conchoraptor* which is fairly equal to that of *Erlikosaurus* (though peak stress and total strain energy are gen-

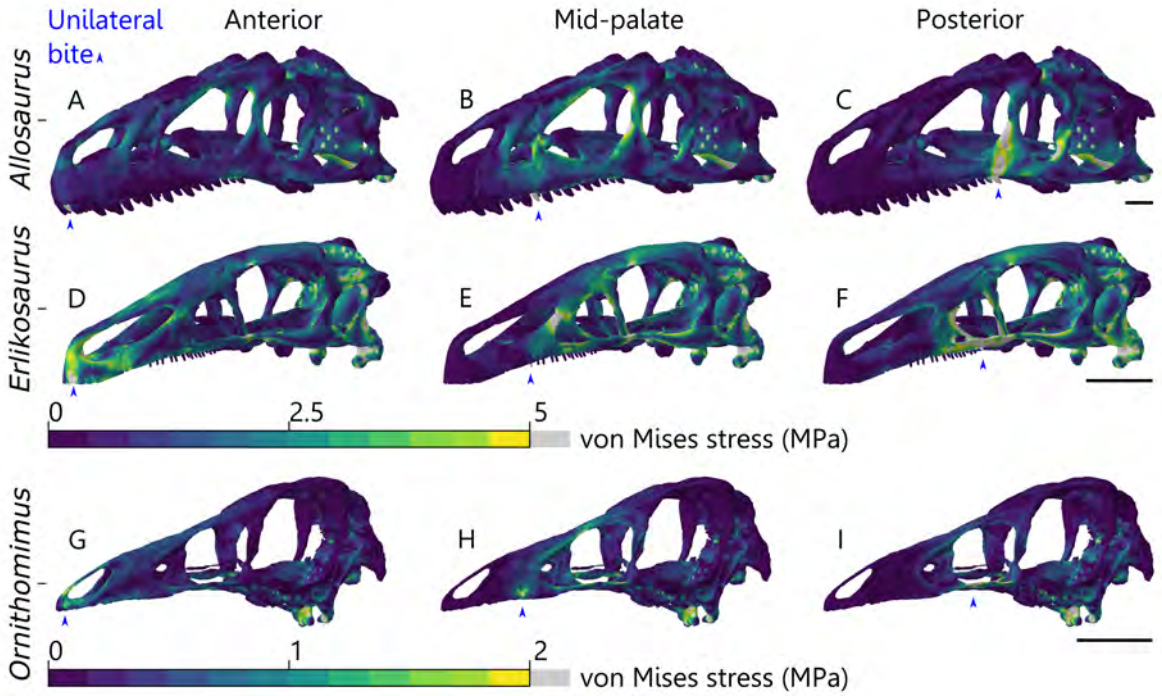

Figure 5.4: Von Mises stress (MPa) contour plots from FEA of a unilateral bite point constraint and intrinsic muscle forces in cranial models of *Allosaurus* (A–C), *Erlikosaurus* (D–F), and *Ornithomimus* (G–I). Constraints at bite points shown by a small blue arrow. Note *Ornithomimus* is figured at a different stress scale magnitude due to much lower stresses resulting from weaker jaw adductor muscle forces. All scale bars on the right are 50 mm.

erally higher in *Conchoraptor*); both experience greater mean von Mises stress under biting than early diverging oviraptorosaurian *Incisivosaurus*. *Allosaurus* experiences the second lowest mean stress while *Ornithomimus* is notably the least, the result of comparatively very weak musculature.

Allosaurus is the only species to have notably less stress in the posterior bites compared with the other locations. *Citipati* is unique in that the posterior bite point produced noticeably greater mean stress than the other bite points. Mean stress tends to be slightly greater in unilateral biting scenarios compared with bilateral, though this is mostly noticeable in mid-palate bites and more of an effect in the oviraptorids compared with *Incisivosaurus* and the other theropods. The greatest difference between a bilateral and unilateral bites occurs with the *Citipati* mid-palate bite position, where unilateral biting causes a much-increased value of mean stress.

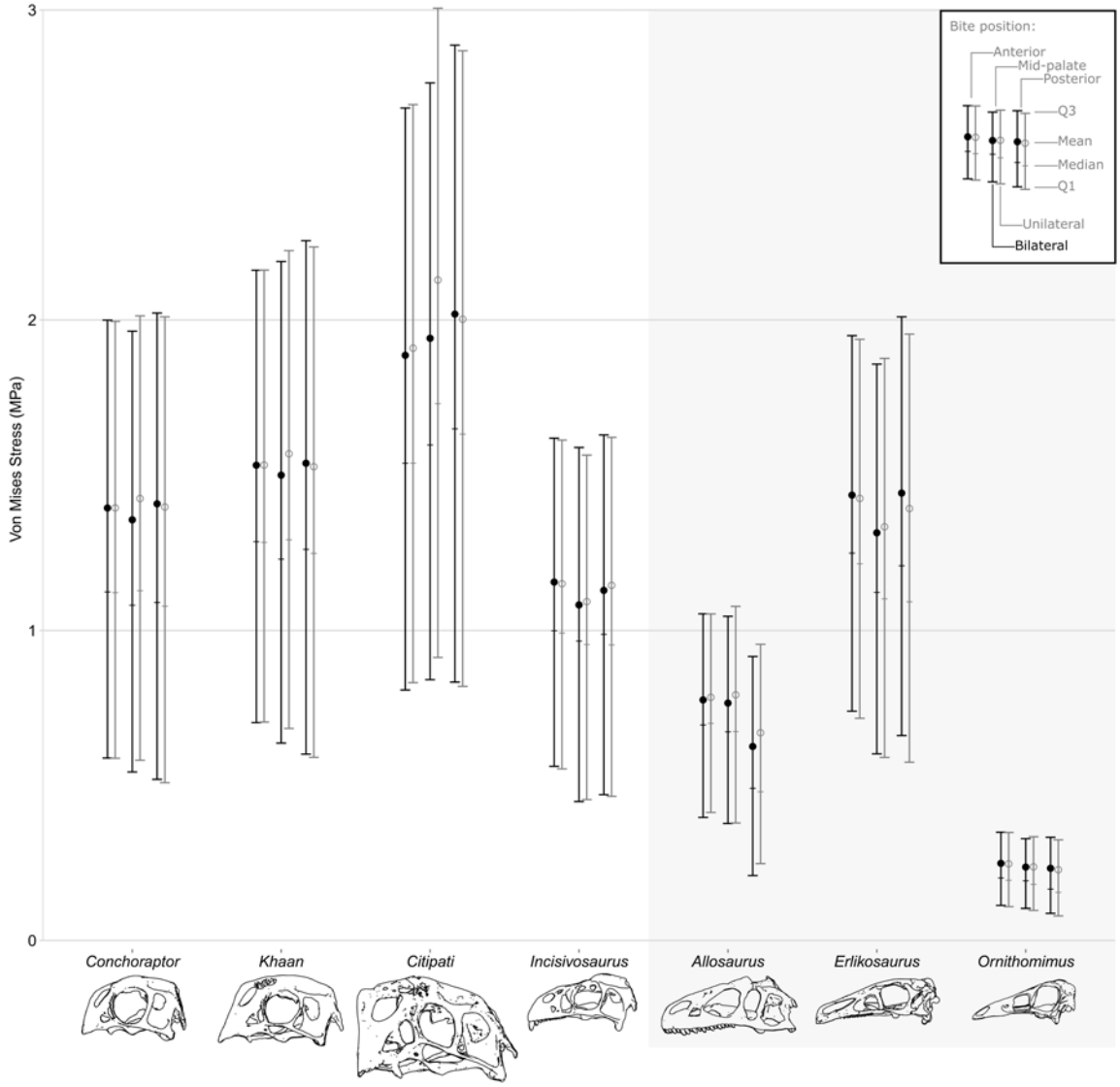

Figure 5.5: Mean values (points) and whiskers showing first quartile, median, and third quartile of von Mises stress (MPa) from FEA of three bilateral and unilateral biting positions using intrinsic muscle forces on cranial models of oviraptorosaurians (white background) *Conchoraptor*, *Khaan*, *Citipati*, and *Incisivosaurus*, along with other theropod dinosaurs (grey background) *Allosaurus*, *Erlikosaurus*, and *Ornithomimus*. Note the greater mean stress in the oviraptorosaurians, especially in *Citipati*, and the great difference between bilateral and unilateral stress response in the *Citipati* mid-palate bite. The top 5% of values were excluded in each dataset to account for artificially high stress values from point loads and nodal constraints. Outlines of oviraptorosaurian crania are the same relative scale; other theropods are not.

Table 5.1: Comparative von Mises stress and total strain energy results from the analyses modelling bilateral and unilateral muscle driven bites and three extrinsic scenarios modelling neck muscle driven feeding movement in cranial models of oviraptorid oviraptorosaurians *Conchoraptor*, *Khaan*, *Citipati*, along with early diverging oviraptorosaurian *Incisivosaurus*, and *Allosaurus*, *Erlikosaurus*, and *Ornithomimus* – theropods with more conventional skull morphology. * The top 5% of values are excluded in each dataset to account for artificially high stress values from point loads and nodal constraints. †Total strain energy values reported have undergone an additional correction factor as strain energy scales with volume rather than surface area (Dumont *et al.*, 2009).

	Bilateral bite			Unilateral bite				Extrinsic loading		
	Mean element stress* (MPa)	Peak element stress* (MPa)	Total strain energy† (mJ)	Mean element stress* (MPa)	Peak element stress* (MPa)	Total strain energy† (mJ)		Mean element stress* (MPa)	Peak element stress* (MPa)	Total strain energy† (mJ)
Conchoraptor										
Anterior	1.39	4.39	2.10	1.39	4.43	2.20	Pull	0.39	1.92	0.85
Mid-palate	1.36	4.41	2.18	1.42	4.91	2.55	Shake	1.80	6.43	3.82
Posterior	1.41	4.85	2.70	1.40	4.86	2.87	Twist	0.51	2.01	0.34
Khaan										
Anterior	1.53	4.54	3.43	1.53	4.58	3.54	Pull	0.34	1.79	0.43
Mid-palate	1.50	4.50	3.39	1.57	4.88	3.85	Shake	1.77	6.21	4.87
Posterior	1.54	4.90	3.98	1.53	4.91	4.16	Twist	0.43	1.49	0.32
Citipati										
Anterior	1.89	5.92	4.00	1.91	6.02	4.20	Pull	0.35	1.67	0.28
Mid-palate	1.94	6.03	4.31	2.13	6.82	5.66	Shake	1.83	6.68	4.52
Posterior	2.02	6.47	4.93	2.00	6.46	5.28	Twist	0.62	2.04	0.44
Incisivosaurus										
Anterior	1.16	3.26	1.61	1.15	3.27	1.62	Pull	0.69	2.65	0.70
Mid-palate	1.08	3.29	1.63	1.09	3.55	1.83	Shake	2.10	8.52	9.10
Posterior	1.13	3.55	1.87	1.15	3.90	2.21	Twist	0.46	1.75	0.36
Allosaurus										
Anterior	0.78	2.33	1.28	0.78	3.35	1.31	Pull	0.51	2.15	0.79
Mid-palate	0.77	2.34	1.26	0.79	2.56	1.43	Shake	1.63	6.27	9.79
Posterior	0.63	2.26	1.18	0.67	2.63	1.60	Twist	0.50	1.53	0.47
Erlikosaurus										
Anterior	1.430	4.20	1.58	1.42	4.29	1.63	Pull	1.00	3.96	0.89
Mid-palate	1.31	4.08	1.42	1.33	4.32	1.56	Shake	3.51	12.4	10.1
Posterior	1.44	4.60	1.73	1.39	4.89	1.99	Twist	0.86	3.61	0.82
Ornithomimus										
Anterior	0.25	0.78	0.07	0.25	0.80	0.07	Pull	0.95	4.34	1.34
Mid-palate	0.24	0.78	0.06	0.24	0.83	0.07	Shake	3.36	13.0	14.3
Posterior	0.23	0.88	0.08	0.23	0.90	0.09	Twist	1.04	5.18	1.63

5.3.2 *Extrinsic head-pull, head-shake, and head-twist loading*

Under the head-pull scenario, oviraptorosaurians experience stress chiefly in the vomer, palatine, pterygoids and jugal (Fig. 5.6A–D). *Incisivosaurus* differs from the oviraptorid

oviraptorosaurians by having more stress at the site of the applied pulling loads (the prominent front teeth, compared with the edentulous premaxilla of the oviraptorids) and a more stressed premaxilla and nasal (Fig. 5.6D).

Allosaurus is also stressed at the teeth, palatines, pterygoids, and jugals during pull, but also stressed at the ectopterygoids and quadratojugals (Fig. 5.6M). *Erlikosaurus* experiences stress across all ventral cranial elements, especially premaxilla, maxilla, jugals, palatines, and quadratojugals, and noticeable stress in the nasals (Fig. 5.6N). *Ornithomimus* shows the greatest stresses, evidence its low stresses from the bite scenarios are the result of weak jaw adductor musculature and not adaptation towards cranial stress resistance. These are most concentrated on the premaxilla, maxilla, vomer, palatines, jugals and quadratojugals of *Ornithomimus* (Fig. 5.6O), along with dorsal stresses around the nares and nasal.

In the head-shaking scenario, which generally causes higher stresses than the other two extrinsic scenarios, the oviraptorids are typically most stressed at the pterygoid, jugal, quadratojugal, palatine, vomer, and the anteroventral areas of the braincase (Fig. 5.6E–G). Areas of the premaxilla dorsal to the antorbital fenestra are also highly stressed but less so in *Citipati* (Fig. 5.6G). The postorbital bar is more stressed in *Khaan* (Fig. 5.6F) than in *Conchoraptor* or *Citipati*. *Incisivosaurus* has stress distributions similar to the oviraptorids but greater magnitudes in the squamosal and lacrimal, and less on the vomer (Fig. 5.6H).

The non-oviraptorosaurian taxa are mostly stressed at the maxilla, jugal, vomer, palatine, quadratojugal, and pterygoid (Fig. 5.6P–R). The skull roof is much more stressed in *Erlikosaurus* and *Ornithomimus* (Fig. 5.6Q,R) than *Allosaurus* (Fig. 5.6P) and the oviraptorosaurians (Fig. 5.6E–H); both *Erlikosaurus* and *Ornithomimus* experience high stresses over much of skull roof and the lacrimal (Fig. 5.6Q,R).

With the head-twisting scenario, the oviraptorids typically show elevated stress at the contribution of the premaxilla to the dorsal edge of the antorbital fenestra and near the contacts of the lacrimal, jugal and maxilla (Fig. 5.6I–K). *Citipati* and *Khaan*

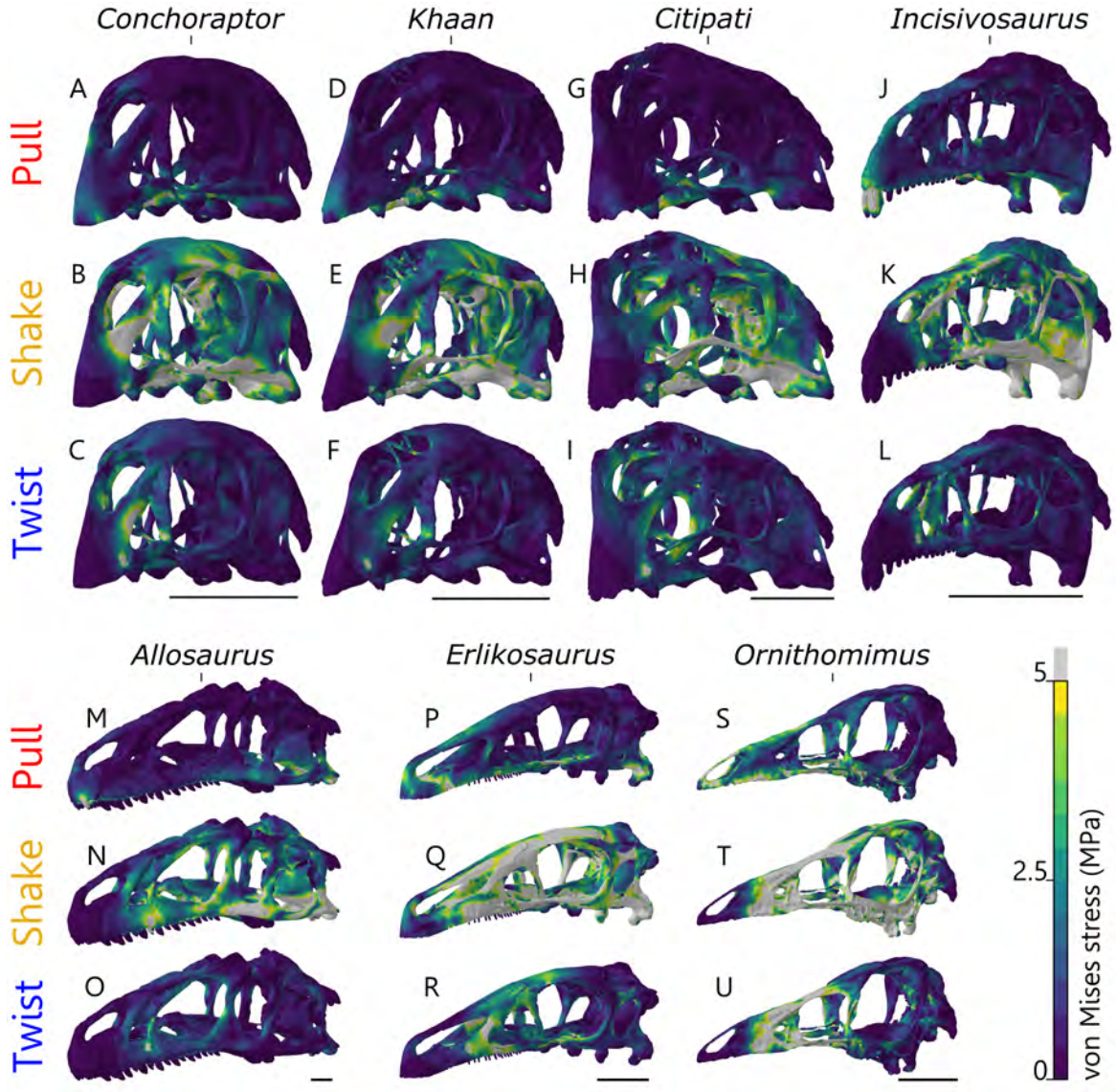

Figure 5.6: Von Mises stress (MPa) contour plots from FEA modelling head pull-back (A–D, M–O), head shaking (E–H, P–R), and head twisting (I–L, S–U) feeding scenarios using extrinsic applied loads (scaled to cranial surface area) on cranial models of oviraptorosaurians *Conchoraptor* (A,E,I), *Khaan* (B,F,J), *Citipati* (C,G,K), and *Incisivosaurus* (D,H,L), along with other theropod dinosaurs *Allosaurus* (M,P,S), *Erlikosaurus* (N,Q,T), and *Ornithomimus* (O,R,U). All scale bars are 50 mm.

(Fig. 5.6J,K) also show some stresses at the delicate bony struts of their nasals. *Incisivosaurus* is similar to oviraptorids, but also with slightly elevated stress on the postorbital bar (Fig. 5.6L).

In *Allosaurus*, the twisting load appears to slightly elevate stress in the maxilla and lacrimal (Fig. 5.6S). *Erlikosaurus* also mainly experiences stress in the maxilla and lacrimal but also the jugal, nasal, frontal, and supratemporal bar (Fig. 5.6T). *Ornithomimus* exhibits clearly increased stress around the entire region of the antorbital fenestra, and some posteriorly around the braincase (Fig. 5.6U).

Oviraptorid oviraptorosaurians perform well in the head-pull scenario and to a slightly lesser extent in the twist-scenario (reversed in *Incisivosaurus*), generally displaying a lower mean stress in one or both scenarios compared with the other theropods (Fig. 5.7). Pull is the lower of these two scenarios in the oviraptorids and *Ornithomimus*, twist is the lower in *Incisivosaurus* and *Erlikosaurus*; the two are even in *Allosaurus*. The lowest values for the pull and shake scenarios are found in *Conchoraptor* and *Khaan*. All three oviraptorids, *Citipati* and *Khaan* especially, have very low mean and peak stress with the pull scenario (Fig. 5.7) (Table. 5.1). Values for pull and shake in *Incisivosaurus* are generally intermediate between the oviraptorids and the other theropods (Fig. 5.7) and it performs second best in the twisting scenario. The shake scenario produces by far the greatest mean von Mises stress of any of the extrinsic scenarios in every species; it is lowest in *Allosaurus*, but only marginally greater in the four oviraptorosaurians, and notably greater in *Ornithomimus*, followed by *Erlikosaurus* (Fig. 5.7).

5.3.3 *Deformation comparison and rhamphotheca stress reduction*

The geometric range of deformation produced by the different FEAs for each of the oviraptorosaurian taxa is typically greater than in each of the non-oviraptorosaurian theropods (Fig. 5.8). *Citipati* displays the largest range of deformation as shown in the PCA, the range of deformation in *Conchoraptor* is lesser, and deformations in *Khaan*

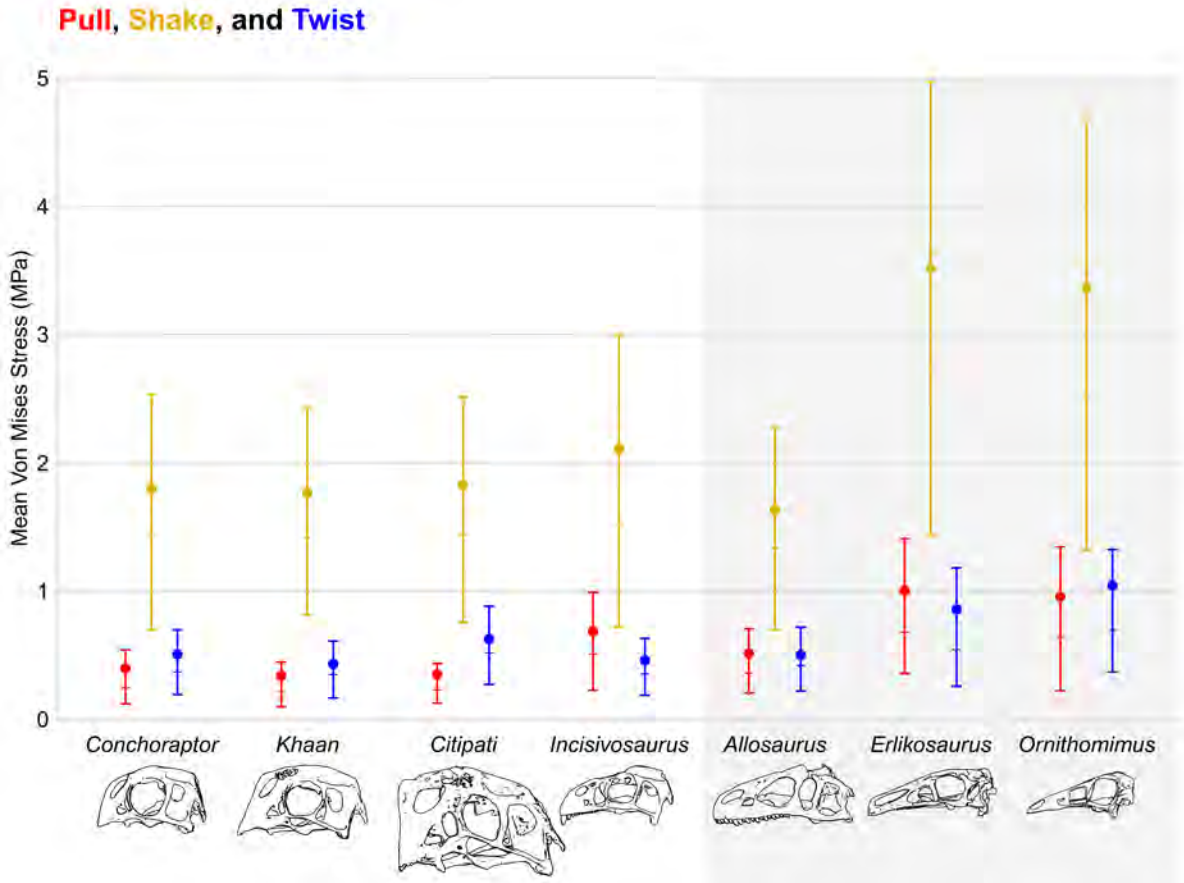

Figure 5.7: Mean values (points) and whiskers showing first quartile, median, and third quartile of von Mises stress (MPa) from FEA modelling head pull-back (red), head shaking (yellow), and head twisting (blue) feeding scenarios using extrinsic applied loads (scaled to cranial surface area) on cranial models of oviraptorosaurians (white background) *Conchoraptor*, *Khaan*, *Citipati*, and *Incisivosaurus*, along with other theropod dinosaurs (grey background) *Allosaurus*, *Erlikosaurus*, and *Ornithomimus*. The top 5% of values were excluded in each dataset to account for artificially high stress values from point loads and nodal constraints. Outlines of oviraptorosaurian crania are the same relative scale; other theropods are not.

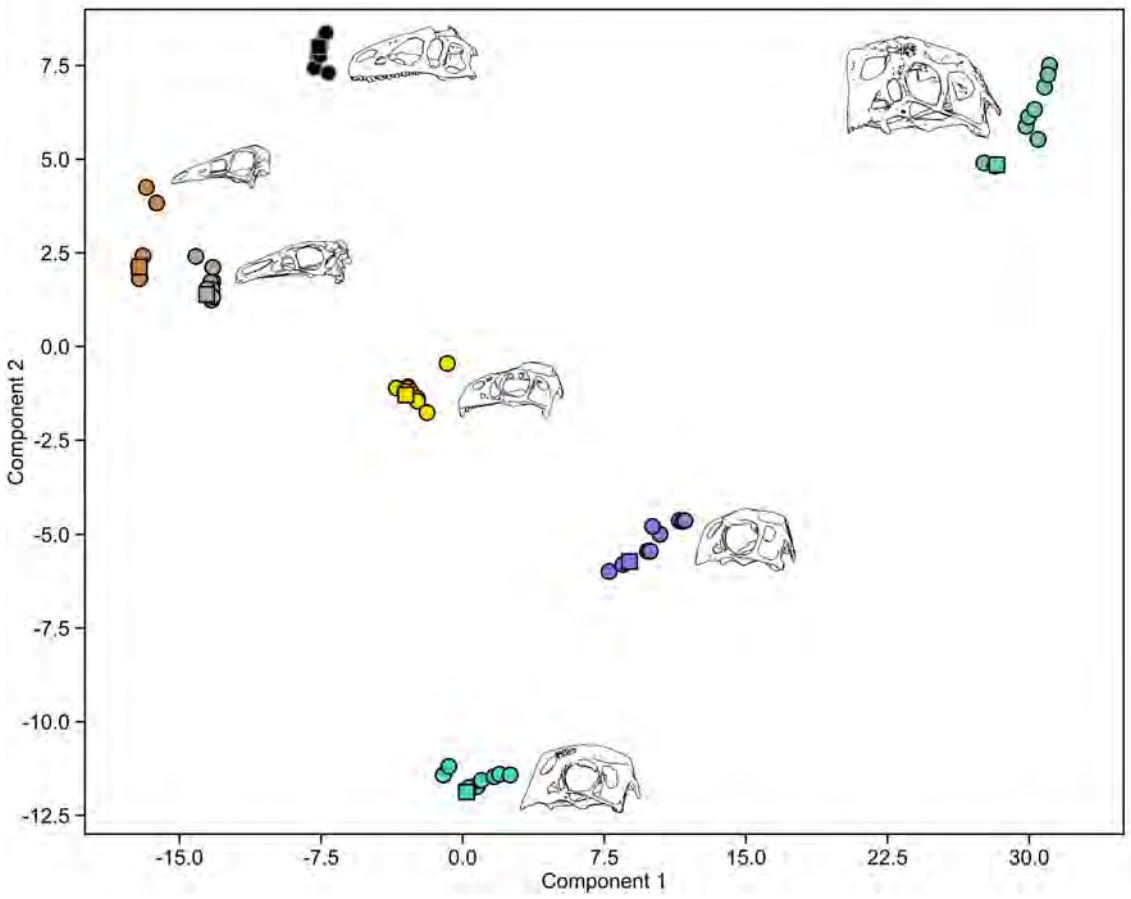

Figure 5.8: Principal component plot showing the range of deformation seen in FEA scenarios on cranial models of oviraptorosaurians *Conchoraptor* (purple), *Khaan* (blue), *Citipati* (green), *Incisivosaurus* (yellow), and other theropods *Allosaurus* (black), *Erlikosaurus* (grey), and *Ornithomimus* (brown). The FEA scenarios plotted comprise anterior, mid-palate, and posterior muscle driven bites (bilateral and unilateral), the pulling, shaking, and twisting scenarios (using extrinsic loads scaled to cranial surface area), along with an undeformed cranial model (plotted with a square), for a total of ten points per species. The position of taxa in relation to each other on the PCA has little functional importance, only the degree of variance between the points representing each taxon. *Citipati* exhibits the largest range of deformations. Principal component 1 explains 75.5% variance, principal component 2 explains 13.4% variance. Outlines of oviraptorosaurian crania are the same relative scale; other theropods are not.

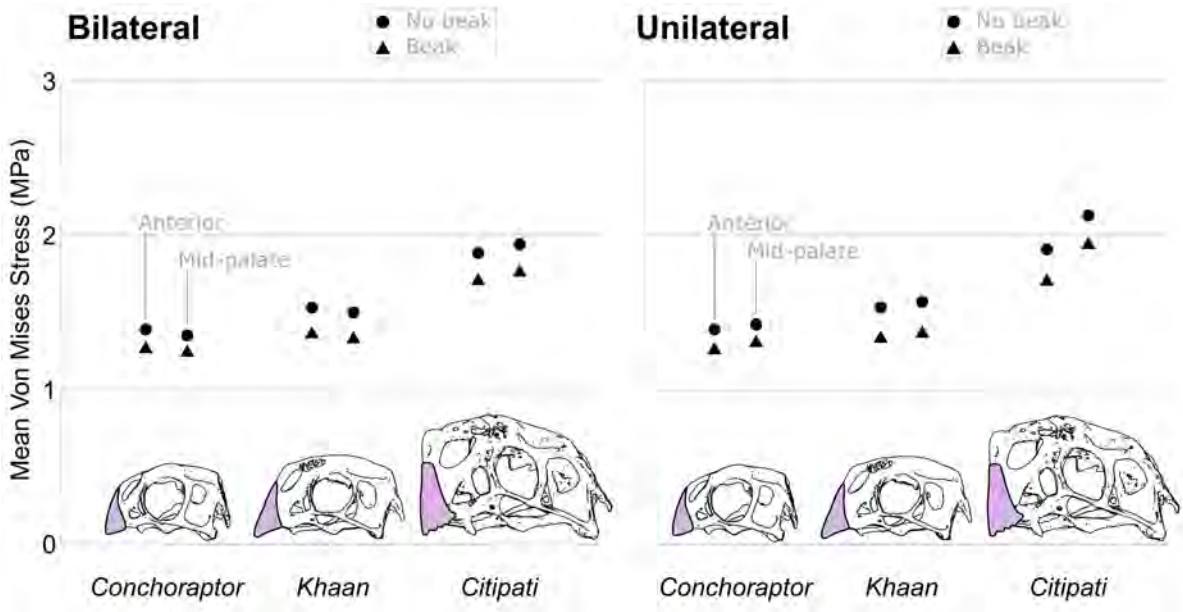

Figure 5.9: The difference in mean values of von Mises stress (MPa) in cranial models of *Conchoraptor*, *Khaan*, and *Citipati* which either did not (circle point) or did (triangle point) include a keratinous rhamphotheca to the beak in FEA using bilateral (left graph) and unilateral (right graph) bite point constraints and intrinsic muscle forces. Note the small and consistent decrease in mean stress in all scenarios as the keratinous covering only decreased stress in its immediate proximity in the cranium. The top 5% of values were excluded in each dataset to account for artificially high stress values from point loads and nodal constraints. Outlines of crania are the same relative scale and show the extent of the reconstructed rhamphotheca.

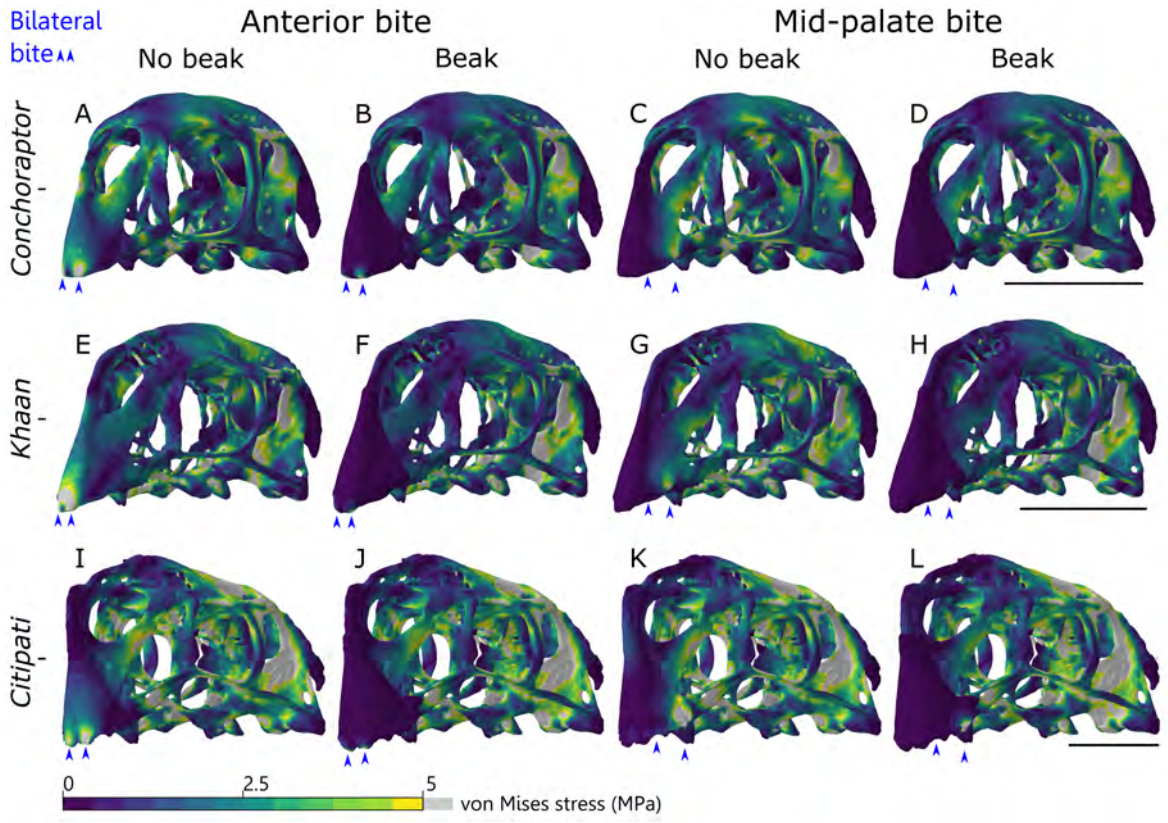

Figure 5.10: Von Mises stress (MPa) contour plots from FEA using bilateral bite point constraints and intrinsic muscle forces in cranial models of oviraptorosaurians *Conchoraptor* (A–D), *Khaan* (E–H), and *Citipati* (I–L) modelled without (A,C,E,G,I,K) and with (B,D,F,H,J,L) a keratinous rhamphotheca covering the beak. Constraints at bite points shown by small blue arrows at the anterior of the beak (A,B,E,F,I,J) and the lateral edge of beak (C,D,G,H,K,L). All scale bars on the right are 50 mm.

and *Incisivosaurus* show a similar degree of spread, less than the other two oviraptorosaurians. The taxa showing the smallest ranges in deformation are *Erlikosaurus* and *Allosaurus*. *Ornithomimus* has a variance of deformation of a similar degree to that of *Conchoraptor*. The position of taxa in relation to each other on the PCA has little functional importance, only the variance among the points representing each taxon, derived from the different FEA scenarios.

A modelled keratinous rhamphotheca covering part of the premaxilla in *Conchoraptor*, *Khaan*, and *Citipati* was shown to consistently reduce mean von Mises stress in bilateral and unilateral bites at the anterior and middle of the palate (Fig. 5.9). However, this reduction appears to result from stress reduction only directly beneath the area covered by the rhamphotheca, and in some minor degree to areas immediately posterior to it (no further posterior than the middle of the orbit), chiefly in the premaxilla and lacrimal (Fig. 5.10). It appears stress in the posterior of the cranium could be slightly increased in the squamosal by the presence of the rhamphotheca (Fig. 10G–H,K–L) in *Khaan* and *Citipati*, an effect that is more pronounced when a rhampotheca is modelled in unilateral biting scenarios (see Appendix C, Fig. C.4).

Results of including the rhamphotheca were similar between bilateral and unilateral biting, and with the pull, shake and twist scenario. Only the von Mises stress contour plots from the anterior bilateral biting scenario are figured here (Fig. 5.10), the others in Appendix C (Fig. C.3 and C.4).

5.4 Discussion

The fact that oviraptorosaurian taxa in this study modelling biting display greater cranial stress than the other theropods indicates that, despite the increased relative strength of the oviraptorid cranial morphology (as shown in Chapter 3), it is not enough to compensate entirely for the greatly increased relative force of their jaw adductor musculature (Chapter 4; Meade and Ma, 2022). This interesting result raises questions as to how, if accurate, this could be adaptive. It may be that functional or developmental pressure

towards their unusual pneumatic cranial shape, while maintaining the musculature for powerful biting, is strong enough that their cranium functions closer to structural safety limits compared with other theropods.

Adaptations towards pneumaticity and reducing cranial mass may be related to the long neck of later diverging oviraptorosaurians. This would obviously not be an identical dynamic to the mass reduction of sauropod skulls in combination with their lengthened necks (Taylor *et al.*, 2009). Instead, a balance between keeping a lightweight skull alongside adaptation towards cranial strengthening may have been necessary for the overall body plan of later diverging oviraptorosaurians with regards to locomotion and cursoriality. Keeping their dorsoventrally expanded crania light would aid with stabilising the structure on their relatively long necks while running at high speeds. Elongate arctometatarsalian hindlimbs have been interpretated as an adaptation for cursoriality and speed for predator avoidance (oviraptorosaurians shared an environment with carnivorous dromaeosaurids, troodontids, and tyrannosaurs) in avimimid (Funston *et al.*, 2018) and caenagnathid oviraptorosaurians, and pursuing small prey (more so in Caenagathidae; Snively *et al.*, 2004; Funston *et al.*, 2015; Funston *et al.*, 2018; but see Rhodes *et al.*, (2020) for alternate wading interpretation). Limbs may be proportionally shorter in oviraptorids (Xu *et al.*, 2013), but they have nevertheless been reconstructed as having robust caudofemoral musculature (Persons *et al.*, 2013) and likely were also fast moving (Christiansen, 1999; Christiansen and Bonde, 2002; Osmólska *et al.*, 2004; Persons *et al.*, 2013).

Oviraptoridae retain a large circular orbit which, among the morphological diversity of orbit shape in Mesozoic archosaurs, is particularly weak (Lautenschlager, 2022). Circular orbits are common in herbivores, but it is feasible that the increased bite forces of oviraptorids may have triggered adaptation towards a different orbit shape, similar to some carnivorous taxa (Lautenschlager, 2022), that provided extra cranial stress resistance (see the elliptical shape of the *Allosaurus* orbit; Fig. 5.3). This is not the case, so visual acuity or some other factor related to vision may have been a very

important part of their cranial function.

Despite higher mean stresses in the oviraptorosaurians from the muscle driven bites (for the muscle strength reasons discussed above), mean stress in the oviraptorosaurians (and then oviraptorids especially) were generally lower than the other theropods in the extrinsic loading scenarios (which were scaled to surface area, not derived from their comparatively strengthened jaw adductor musculature). This reiterates the findings of Chapter 3 and expands on them suggesting that even in these other scenarios (particularly head-pull) their crania are adapted towards greater strength than herbivorous theropod crania, and to a similar or greater relative degree as the cranium of carnivorous *Allosaurus*, which has been previously assessed as overengineered (Rayfield, 2001).

The loading of the muscle driven FEA scenario is based on estimates assuming full contraction simultaneously of each jaw adductor muscle (Lautenschlager, 2013; Cuff and Rayfield, 2015; Meade and Ma, 2022). The results of the oviraptorids experiencing the highest cranial stress during biting are in the context of this assumption. This is likely a simplification of the feeding dynamic in oviraptorids (and the other theropods) but such simplifications are necessary in FEA models (Herbst *et al.*, 2022). Additionally, the comparative method of using identical material properties for bone in all FEAs and treating materials as isotropic and homogenous does not entertain the possibility that the internal structure of oviraptorid cranial bone had some adaptation for additional strength not seen in other groups that in reality would help to buffer cranial stress. Sutures were also not modelled, which have been shown to relieve strain locally (Moazen *et al.*, 2009) but at the expense of elevated strain in other regions of the skull. To accurately model sutures into all the FEA here would have been time consuming and limited how directly comparative the models were.

The oviraptorosaurians were deliberately not compared using FEA with superficially similar avian taxa (such as parrots) as these show substantial cranial kinesis that is important to their cranial function during feeding (Carril *et al.*, 2015). Results

from FEA on bird crania modelled akinetically may not therefore be representative nor a useful comparison for the extinct oviraptorosaurian taxa. Properties of cranial kinesis have been discussed within the oviraptorid cranium, but mobility like that seen in birds appears impossible in the crania of oviraptorosaurians (Maryańska and Osmólska, 1997). Nevertheless, several movable units were suggested by Barsbold (1977) but seem highly unlikely. A more restricted moveable articulation between the quadrate and quadratojugal was suggested by Lü in *Heyuannia huangi* (Lü, 2003) and *Nemegtomaia huangi* (Lü *et al.*, 2004; Lü *et al.*, 2005). This would however require the quadrate to be mobile, which is contrary to interpretations that the otic capitulum is immovably fixed to the braincase wall and in tight extensive contact with the squamosal (Maryańska and Osmólska, 1997; Osmólska *et al.*, 2002; Hendrickx *et al.*, 2015). Also, the quadratojugal appears in tight elongate contact rostrally with the jugal (Clark *et al.*, 2002), and its contact with the quadrate is either fused or strengthened by a deep quadratojugal cotyla on the quadrate and large quadrate condyle on the quadratojugal, and thus likely immovable in oviraptorids (Maryańska and Osmólska, 1997). Holliday and Witmer (2008) interpret the quadrate of most nonavian Maniraptoriformes (including oviraptorosaurians) as slightly kinetically competent (with synovial basal and otic joints and protractor muscles), yet not kinetic because they lacked permissive kinematic linkages.

The increase in stress in a posterior biting position relative to the other locations in *Citipati* may suggest it was not adapted for crushing food with the posterior of its palate. Though possessing the strongest bite forces of the oviraptorosaurians studied here, both relatively and absolutely, it may have applied its powerful jaws towards more anteriorly focussed functions with its wide premaxilla. The uniquely large discrepancy between the mid-palate bilateral and unilateral bites in *Citipati* indicates its cranial morphology was especially poorly adapted for uneven biting in this region and symmetrical application of bite force was likely important to its cranial function. This may indicate a need for controlled biting of static foodstuffs and may suggest the

capture of moving/struggling prey was particularly unlikely/uncommon in *Citipati*. This is also demonstrated by its higher stresses under the extrinsic twisting scenario compared with the other oviraptorids.

Results of bites and extrinsic scenarios suggest *Citipati* was doing something very different to the other oviraptorids and was perhaps more specialist. *Citipati* demonstrating the greatest variety of deformations over the scenarios tested (Fig. 5.8) also suggests its cranial function was specialised rather than adapted to varied loading. Specialisation for a 'cropping' bite at front of beak, which is blunter than other oviraptorids of this study, which would limit potential for instability and asymmetry in bite. In the context of this, the result of the Chapter 4 muscle reconstructions, that suggested *Citipati* muscle architecture was potentially more adapted for a vertical bite with less emphasis on anteroposterior grinding jaw movement, can be clarified that this adaptation for a strong vertical bite was not for 'crushing' purposes, but anteriorly 'cropping' functions. There remains uncertainty about the actual functional margin of the *Citipati* jaws and how they occluded as the rhamphotheca shape is unknown.

It is worth noting that the palatal surface of the premaxillae and maxillae in all oviraptorids (and also *Avimimus portentosus* and the caenagnathid *Chirostenotes pergracilis*) support four longitudinal parasagittal ridges (Barsbold, 1986; Kurzanov, 1981; Maryanska and Osmólska, 1997; Sues, 1997; Elzanowski, 1999; Clark *et al.*, 2001; Balanoff *et al.*, 2012). The function of these structures is unknown but may indicate similarities in the soft tissue covering the region or that this topographic complexity in some way assisted with durophagous feeding behaviours or palinal feeding movements of the mandible. No similar ridges are present on the *Incisivosaurus* palate (Balanoff *et al.*, 2009).

The bony oral margin of the *Citipati* cranium may indicate a wider faceted beak that may have been an effective tool for 'nipping/cropping' tough plant matter. A specialist herbivorous diet in *Citipati* would have differed from other herbivorous theropod groups. Macronarian sauropods like *Camarasaurus* are likewise characterised by mor-

phofunctional evolution towards robust crania, shortened snouts, and relatively powerful anterior bites, but Button and Zanno (2020) found no significant evidence of convergence between sauropods and oviraptorids generally, only a slight overlap in their cranial biomechanical morphospace; *Citipati* was further away from Sauropodomorpha than *Incisivosaurus* and *Conchoraptor* which placed nearby (Button and Zanno, 2020). *Erlikosaurus*, too, was found to be adapted to feeding at the jaw tip (Lautenschlager *et al.*, 2013) but in a way that may have more harnessed neck musculature to compensate for lacking jaw adductor muscle power. *Citipati* did not lack jaw adductor muscle power but has one of the best adapted cranial morphologies tested for the head-pulling scenario; combined with its adaptations for a powerful front-beak bite, stripping or peeling of plant material is a possible functional interpretation. As also mentioned in Chapter 4, herbivorous feeding in oviraptorids would have greatly differed from other co-occurring dinosaur groups with more adaption to oral processing of plant matter, such as ceratopsians and hadrosaurs which possessed dental batteries (Zanno and Mackovicky, 2011).

The other oviraptorids appear more suited towards crushing bites (if the peculiar tooth-like projection of the maxillae and vomer could have been used for this) and a more generalised cranial function and diet; they perform equally well at all bite points of their palate. *Conchoraptor* and *Khaan* cranial function may have been very similar. The two experience a very similar result in terms of mean von Mises stress in all the bite and extrinsic scenarios (Fig. 5.5 and 5.7) and place fairly similarly in the coordinate plot of general cranial deformation. They are of similar size and they may have pursued similar diets but occurred in a different time and place — *Khaan* and *Citipati* are from the Djadokhta Formation (Clark *et al.*, 2001; Campanian age, Dashzeveg *et al.*, 2005; Dingus *et al.*, 2008; Hasegawa *et al.*, 2009); *Conchoraptor* is from the slightly younger Nemegt Formation (Funston *et al.*, 2018; upper Campanian–lower Maastrichtian age, overlying the Djadokhta Formation, Gradziński and Jerzykiewicz, 1974a; 1974b). *Khaan* occurs with *Citipati* but seems to have a different

cranial function as shown by FEA results here and the different relative jaw adductor muscle strengths and lines of action of Chapter 4. This is likely an example of niche partitioning among Oviraptoridae which has previously been suggested to have allowed a high diversity of oviraptorids coexist (Funston *et al.*, 2018; Ma *et al.*, 2020a).

The incisor-like elongated front teeth of *Incisivosaurus* bear prominent wear facets on their lingual surface. This was interpreted by Xu *et al.* (2002) as a possible indicator of herbivory. The smooth, rounded form of the wear facets may imply they are the product of grinding or wear from repetitive contact, rather than the more traumatic spalling that can occur on the teeth of carnivorous forms from feeding (Schubert and Ungar, 2005). However, it is unclear what exactly the prominent teeth of *Incisivosaurus* were wearing against; the anterior of the mandible is edentulous and appears correctly positioned with the dentary tip posterior to the front cranial teeth, in order for the maxillary and dentary tooth rows to occlude properly. It is possible the mandible terminated with a beak-like keratinous covering, as the edentulous jaws of later diverging oviraptorids would have (Xu *et al.*, 2002; Balanoff *et al.*, 2009). The contact of softer keratin producing wear facets on the harder enamel of the front teeth seems unlikely.

The comparatively good performance of the *Incisivosaurus* cranium under the head-twisting scenario may somewhat suggest the elongate front teeth were used robustly as a tool, in such a way to create these wear facets, against foodstuffs and the environment. The still relatively elongate skull (for an oviraptorosaurian), terminating in the prominent front teeth, may have functioned as an adaptation for *Incisivosaurus* to manipulate its environment more keenly than other species. Rather than utilising jaw musculature, more powerful neck musculature could have driven the front teeth as a tool for twisting away bark, stripping through plant material, or digging, as part of an effective system for acquiring a variety of food in ways other animals were not equipped to be able to. Wearing facets forming on the lingual surface of the front teeth seems reasonable under these circumstances. The relatively long roots of the teeth may be related to this — superficially similar long rooted mandibular teeth in rodent mammals

do not reduce stress distribution across mandible but are driven by factors such as rapid incisor wear (Morris *et al.*, 2022), though tooth replacement is a factor in *Incisivosaurus* and replacement teeth for both front teeth are present within the premaxilla (Balanoff *et al.*, 2009) (and included in the FEA models here). Nevertheless, the models here suggest pulling these front teeth against material/substrate with posteriorly directed movement of the head would create more stresses (chiefly in the teeth themselves and the palate and pterygoids) than a twisting motion of the same force, though less than comparatively experienced by the crania of *Erlikosaurus* and *Ornithomimus*. In still retaining small maxillary teeth, *Incisivosaurus* may have had more capacity than some of the oviraptorids for orally processing food. Experiencing the lowest stresses of any bite position when modelling a mid-palate bite on this toothrow further suggest that its cranium was adapted for biting/chewing in this way, either bilaterally or unilaterally.

Reconstructing a keratinous covering on the beak of the oviraptorids reiterates the findings of other studies; that a rhamphotheca reduces mechanical stresses directly under the areas it covers (Lautenschlager *et al.*, 2013; Cuff *et al.*, 2015; Bestwick *et al.*, 2021). However, unlike in *Erlikosaurus* and *Ornithomimus*, in which the premaxillae and nasal arch experience high stresses in anterior biting scenarios (Lautenschlager, 2013; Bestwick *et al.*, 2021), in *Conchoraptor*, *Citipati*, and *Khaan* the regions presumably covered by a rhamphotheca do not broadly experience high stress, other than the immediate position of the bite point constraints themselves, especially compared to the posterior half of the cranium. Stress reduction may, therefore, be less of a driving factor in the evolution of the rhamphotheca in Oviraptoridae, compared with these other groups. My results show the more ornamented oviraptorid crania (*Citipati* most, *Conchoraptor* least), though not elaborate by the standard of some other oviraptorids, are experiencing the most cranial stress when biting. Though there is no evidence the keratinous covering of the beak extended up the vertical premaxilla onto the crest-like nasals of *Citipati* (and these areas actually experience relatively little cranial stress in all biting tests), in elaborately crested species where keratin may have been more

extensive (e.g. *Corythoraptor jacobsi*, Lü *et al.*, 2017; *Rinchenia mongoliensis*, Osmólska *et al.*, 2004), it is unclear whether stress reduction from overlying keratin may have occurred across more of the cranial bone.

The elevated cranial stress under biting in oviraptorids, compared with the other theropods, results from the comparatively strong jaw adductor muscles and high mechanical advantage of their jaws, somewhat overtaking their adaptation towards cranial strength. However, there is no reason this would necessarily be the case in caenagnathid oviraptorosaurians. From what little we know of their jaws, they were more characterised by a longer rostrum and lower mechanical advantage, interpreted as adaption towards jaw closing velocity for prey capture as part of an omnivorous diet with more carnivory than oviraptorids (Funston and Currie, 2016; Ma *et al.*, 2020b). On this theme, the thin rod-like jugal of the oviraptorids was one of the most highly stressed regions of their cranium during both the biting FEA tests and also the extrinsic head-shake scenario, the latter of which may replicate the capture and despatch of struggling prey. The jugal is one of the few preserved cranial elements of the relatively large North American caenagnathid *Anzu wyliei* and is more robust and of a conventional theropod shape (Lamanna *et al.*, 2014) compared to those seen in Oviraptoridae (Clark *et al.*, 2002; Funston *et al.*, 2018). Perhaps this is indicative of cranial morphologies existing among Caenagnathidae with plesiomorphic adaptations to deal with struggling prey as part of a more carnivorous diet.

Initial selection for tooth loss in oviraptorosaurians was likely not related to weight reduction (the effect is small: Lautenschlager *et al.*, 2013; Zhou *et al.*, 2019) and may have been a side effect of selection for fast embryo growth and thus shorter incubation (Yang and Sander, 2018). This would have been particularly advantageous for clades like oviraptorosaurians which are known to have brooded nests of eggs (Norell *et al.*, 1995a; Norell *et al.*, 2018; Bi *et al.*, 2021; Yang and Sander, 2022); reducing the time before embryo hatching would make this less energetically costly behaviour. Although influences of developmental biology and dietary ecology are not

mutually exclusive, selection towards a toothless beak purely linked with a dietary shift or specialism seems unlikely. The subsequent lack of a mechanical benefit from a keratinous rhamphotheca to cranial strength broadly (Fig. 5.9 and 5.10) in oviraptorids may leave its morphology more readily adapted by other factors. Indeed, the diversity of beak shapes in modern birds has been largely contingent on trade-offs and constraints (Navalón *et al.*, 2018) rather than dominated by dietary effects. Functional influences on the rhamphotheca in addition to those linked to diet in oviraptorosaurians may include roles as a possible sensory organ (Crole and Stoley, 2017) or thermoregulatory organ (Tattersall *et al.*, 2017; Eastick *et al.*, 2019). This latter factor may apply particularly in forms that possessed high vascularised crests (e.g. *Corythoraptor jacobsi*, Lü *et al.*, 2017; *Rinchenia mongoliensis*, Osmólska *et al.*, 2004), which may have functioned as structures to offload heat at high temperatures or restrict heat loss at lower temperatures.

5.5 Conclusion

Oviraptorosaurian taxa display greater cranial stress when modelling muscle driven biting than other theropods indicating that, despite the increased comparative strength of the oviraptorid cranial morphology, the strengthening is outweighed by the greatly increased relative force of their jaw adductor musculature and may function closer to structural safety limits. This situation is likely the product of competing functional requirements on the cranium, to be strong but lightweight, beyond a purely food processing function (e.g. locomotion, vision etc.). The oviraptorosaurian crania (oviraptorids especially) perform better than other herbivorous theropods (and similarly to overengineered carnivorous *Allosaurus*) in extrinsic modelling of neck muscle driven head-pulling, head-shaking, head-twisting scenarios, indicating the increased relative strength of their crania apply to these other scenarios.

Citipati appears adapted for symmetrical rostrally positioned bites, an interpretation of which could include a cropping use of its wider, blunter snout in a herbiv-

orous diet. This differs in cranial function to *Khaan*, which appears suited for biting in variable positions, perhaps as a more generalist herbivore with more inclination to crush material and undertake durophagy. Differences in cranial function between *Citipati* and *Khaan* may indicate niche partitioning in oviraptorids from the same ecosystem. *Conchoraptor* appears to have a very similar cranial function to *Khaan* and occurred in a different time and place. The prominent front teeth of *Incisivosaurus* may represent an adaptive tool, useful not only in biting but for manipulating environment in actions more driven with neck musculature.

A keratinous beak covering in oviraptorids mainly reduces stress in areas it directly overlays, an important effect at immediate bite points, but less needed over the premaxilla and area of the nares generally as stresses from biting are not particularly high. Other herbivorous theropods (therizinosaurian *Erlikosaurus* and ornithomimosaurian *Ornithomimus*) experience high stresses throughout the premaxilla and narial arch when biting. This suggests different functional driving factors in rhamphotheca morphology in oviraptorids (with less need for structural support), compared with these other groups.

6 | Summary and future directions

6.1 Summary

In this thesis, I created high quality digital 3D models of oviraptorosaurian dinosaur crania. I employed digital functional analysis methods on these models to quantitatively test hypotheses on oviraptorosaurian cranial functional morphology for the first time. Results have implications on oviraptorosaurian diet and functional morphology, niche partitioning among oviraptorids and with other herbivores, and functional trade offs in the oviraptorosaurian cranial and body plan.

Through conducting this research, I developed an understanding of the tools the freeware package Blender has to offer for the digital restoration of fossils along with a sense of best practices to maximise accuracy and precision throughout the process. I cover this briefly in Chapter 2 and at more length in my contribution to Herbst *et al.* (2022) — I hope these may be of use to others.

Chapter 3 focused on investigating the assertion that the oviraptorosaurian cranium was adapted for strength. I tested the hypothesis that the oviraptorosaurian cranial morphology would undergo lower stress magnitudes and therefore perform better and stronger under a comparable extrinsic bending load compared with other herbivorous theropod dinosaurs. Using FEA with directly comparable scaled extrinsic loads, I found oviraptorid crania were stronger (experienced lower stresses) and more efficient (lower total strain energy) in the bending test compared with other herbivorous theropods (therizinosaurian *Erlikosaurus*, and ornithomimosaurian *Orthinomimus*). The

oviraptorid crania also performed equally well or better compared with a large carnivorous theropod (*Allosaurus*) in a number of scenarios. Cranial adaptations that provide this comparative strength are primarily the shortening of their rostrum, and a robust premaxilla with strong connections through its posterior processes and to the palate via the maxilla connection the longitudinally rearranged palatine and ectopterygoid. Cranial strength to resist bending did vary among oviraptorids (with *Citipati* being weakest). The intermediate cranial morphology of the early diverging oviraptorosaurian *Incisivosaurus* performed more like the crania of the oviraptorids than the non-oviraptorosaurian theropods tested.

Chapter 4 addressed the related question, did the oviraptorosaurian cranium have the space and arrangement to support greater jaw adductor musculature and generate powerful bite forces compared with other herbivorous theropods. Given previous suggestions (e.g. Barsbold, 1976a; Currie *et al.*, 1993; Funston *et al.*, 2018; Ma et al. 2020b; 2022) and the findings of cranial strengthening in Chapter 3, I hypothesised this to be the case. Estimates of bite force were much greater in the oviraptorosaurians compared with other herbivorous theropods (therizinosaurian *Erlikosaurus*, and ornithomimosaurians *Garudimimus*, *Struthiomimus*, and *Ornithomimus*) both relative to body mass and in some cases absolutely. Bite forces are increased in oviraptorids compared with the early diverging *Incisivosaurus* primarily through cranial shortening and expanded space for musculature, not more efficient muscular arrangement. Reconstructed muscular arrangement remained fairly conservative from early diverging *Incisivosaurus* to the later diverging Oviraptoridae, and differed more within Oviraptoridae itself (*Citipati* differed more from its fellow oviraptorids in the relative contribution of different muscles to bite force than it did *Incisivosaurus*). Differences in relative jaw adductor muscular strengths and angles may hint at differing cranial function in oviraptorids, with some better adapted for palinal jaw motion than others (less so in *Citipati*; more vertical muscle orientations). Reconstructed angles of maximum jaw gape are relatively small in oviraptorids, further suggesting a predominately herbivorous diet.

Chapter 5 extended the work of Chapters 3 and 4 by assessing how the relative strengthening of the oviraptorid cranial structure and and their powerful bite forces. My results show that despite the increased comparative strength of oviraptorid cranial structure, this is outweighed by the increased relative force of their bite and experiences higher stresses than other theropod dinosaurs tested. This suggests the oviraptorid cranium may have functioned closer to structural safety limits when using its maximal bite force and the cranial structure was product of competing functional requirements, to be strong but lightweight, beyond a purely food processing function. However, oviraptorosaurian crania (oviraptorids especially) do perform better than other herbivorous theropods (therizinosaurian *Erlikosaurus*, and ornithomimosaurian *Orthinomimus*) and similarly to overengineered carnivorous *Allosaurus* under scaled extrinsic loading representing head-pulling, head-shaking, head-twisting scenarios — the relative strength of oviraptorid crania is more diverse than just the bending tested in Chapter 3.

Results presented in this thesis suggest that members of Oviraptoridae were adapted for powerful bites (though with the caveat of competing functional requirements in the cranium) as part of a predominately herbivorous diet. Cranial function differed in co-occuring oviraptorids like *Citipati* and *Khaan*. The two species differed in size (and therefore bite force) and in muscular arrangement (better for palinal jaw movement in *Khaan* than *Citipati*). The muscle driven FEA suggests *Citipati* was adapted for symmetrical application of high forces at front of beak for a cropping style function, while *Khaan* (and the functionally similar *Conchoraptor*) were more equally well adapted for multiple bite points and a more generalised function that may have included crushing behaviours. These results better define the kind of niche partitioning that may have allowed for high diversity of oviraptorosaurians in ecosystems (Funston *et al.*, 2018; *Ma et al.*, 2020a. The early diverging *Incisivosaurus* may have retained more plesiomorpic adaptations for incorporating a degree of dietary omnivory (lower jaw mechanical advantage, higher jaw gape) and had a cranial functional morphology that performed intermediately between oviraptorids and other theropods in a number

of circumstances. The elongate front teeth of *Incisivosaurus* may represent an effective tool for both biting and manipulating its environment in movements more driven by neck musculature.

Different adaptive factors may have shaped the keratinous covering of the beak in Oviraptoridae compared with other herbivorous beaked theropods. Unlike other groups (therizinosaurians and ornithomimosaurians), the majority of the premaxilla and the nasal arch do not experience elevated stress under feeding in oviraptorids and require structural support of the rhamphotheca; elevated stress only occurs at the immediate bite point.

It is difficult to extend these findings away from the oviraptorids towards their sister group Caenagnathidae. Previous work on caenagnathid mandibles suggest a longer rostrum and lower jaw mechanical advantage, interpreted as adaption towards jaw closing velocity for prey capture as part of an omnivorous diet with more carnivory than oviraptorids (Funston and Currie, 2016; Ma *et al.*, 2020b). Chapter 5 of this thesis may somewhat suggest the more robust jugal preserved of some caenagnathids (*Anzu wyliei*; Lamanna *et al.*, 2014) may be indicative of cranial morphologies existing among Caenagnathidae with plesiomorphic adaptations to deal with struggling prey. Better insight into the functional morphology of the caenagnathid cranium will have to wait for more complete fossil material to come to light.

6.2 Future directions

This thesis has provided valuable insight into the palaeoecology of several key oviraptorosaurians through 3D biomechanical analyses. Further investigations of diet on the same species studied may include assessment of geochemical proxies for diet (Zhao *et al.*, 2022) or the serendipitous discovery of new informative fossil material (e.g. stomach contents). Ideally, a better understanding of floral components of the palaeoenvironments represented by the Nemegt and Djadokhta Formations could give a more complete insight into the ecosystems that supported the oviraptorids studied

here (Fastovsky *et al.*, 1997) and their diet.

Chapter 4 has shown that, though time consuming and user intensive, useful information can be gleaned through the reconstruction of musculature in studying extinct taxa. I am hopeful that recently developed methods focussing on free software like Blender (Herbst *et al.*, 2022) will improve the accessibility and speed of volumetric muscle reconstruction in extant and fossil models, without compromising accuracy and reproducibility (as examined in Broyde *et al.*, 2021; Bates *et al.*, 2021). Emerging work has focussed on alternative approaches to predict functionally relevant parameters (such as muscle physiological cross-sectional area) from measurements of fossil specimens and phylogeny (Sakamoto, 2022), and may represent a powerful and expansive tool to investigate any relevant single continuous variable correlated with osteological measurements. An untested example may perhaps include predicting mean von Mises stress (in response to some specific functional load), using a training set of data from FEA studies, to broadly assess structural competence over a phylogenetic framework.

Time, effort, and breadth of study are also at odds when it comes to detailed 3D FEA on biological structures. Finite element analysis is no longer the newest technique in palaeontology. There is an emerging suite of work concerning what level of simplification is acceptable (e.g. Herbst *et al.*, 2021) and whether as much care needs to be taken to derive digital models from CT-data (Rowe and Rayfield, 2022) that may facilitate broader and more expansive studies. Nevertheless, one of the best possibilities to use FEA to study aspects of morphology comparatively across larger biological groups is using theoretical models to test the functional significance and variance of specific parts of an anatomical structure (Rayfield and Milner, 2008; Lautenschlager, 2022) – more studies of this sort or novel set-ups that begin to leverage non-linear FEA models (see Marcé-Nogué (2022) and suggestions therein) are avenues for FEA studies with a lot of potential promise.

References

ADAMS, L. A. 1919. A memoir on the phylogeny of the jaw muscles in recent and fossil vertebrates. *Annals of the New York Academy of Sciences*, **28**, 51–166.

ARBOUR, V. M. and CURRIE, P. J. 2012. Analyzing taphonomic deformation of ankylosaur skulls using retrodeformation and finite element analysis. *PloS One*, **7**, e39323.

BALANOFF, A. M., XU, X., KOBAYASHI, Y., MATSUFUNE, Y. and NORELL, M. A. 2009. Cranial osteology of the theropod dinosaur *Incisivosaurus gauthieri* (Theropoda: Oviraptorosauria). *American Museum Novitates*, **3651**, 1–35.

BALANOFF, A. 2011. Oviraptorosauria: morphology, phylogeny, and endocranial evolution. Doctoral dissertation, Columbia University.

BALANOFF, A. M. and NORELL, M. A. 2012. Osteology of *Khaan mckennai* (Oviraptorosauria: Theropoda). *Bulletin of the American Museum of Natural History*, **372**, 1–77.

BALANOFF, A. M., BEVER, G. S., ROWE, T. B. and NORELL, M. A. 2013. Evolutionary origins of the avian brain. *Nature*, **501**, 93–96.

BALANOFF, A. M., BEVER, G. S. and NORELL, M. A. 2014. Reconsidering the avian nature of the oviraptorosaur brain (Dinosauria: Theropoda). *PLoS One*,

9, e113559.

BALANOFF, A. M., BEVER, G. S., COLBERT, M. W., CLARKE, J. A., FIELD, D. J., GIGNAC, P. M., KSEPKA, D. T., RIDGELY, R. C., SMITH, N. A., TORRES, C. R. and WALSH, S. 2016. Best practices for digitally constructing endocranial casts: examples from birds and their dinosaurian relatives. *Journal of Anatomy*, **229**, 173–190.

BALANOFF, A. M., NORELL, M. A., HOGAN, A. V. and BEVER, G. S. 2018. The endocranial cavity of oviraptorosaur dinosaurs and the increasingly complex, deep history of the avian brain. *Brain, Behavior and Evolution*, **91**, 125–135.

BARGHUSEN, H. R. 1973. The adductor jaw musculature of *Dimetrodon* (Reptilia, Pelycosauria). *Journal of Paleontology*, **47**, 823–834.

BARRETT, P. M. and RAYFIELD, E. J. 2006. Ecological and evolutionary implications of dinosaur feeding behaviour. *Trends in Ecology & Evolution*, **21**, 217–224.

BARSBOLD, R. 1976a. [On a new Late Cretaceous family of small theropods (Oviraptoridae fam. n.) of Mongolia.] *Dokladi Akademii Nauk S.S.S.R.*, **226**, 685–688. [In Russian.]

BARSBOLD, R. 1976b. [On the evolution and systematics of the late Mesozoic dinosaurs.] *Sovmestnaia Sovetsko-Mongol'skaia Paleontologicheskaia Ekspeditsiia Trudy*, **3**, 68–75. [In Russian with English summary.]

BARSBOLD, R. 1977. Kinetism and specialty of the jaw apparatus of oviraptors (Theropoda, Saurischia). *Transactions of the Joint Soviet-Mongolian Palaeontological Expedition*, **4**, 34–47.

BARSBOLD, R. and PERLE, A. 1980. Segnosauria, a new infraorder of carnivorous

dinosaurs. *Acta Palaeontologica Polonica*, **25**, 185–195.

BARSBOLD, R. 1986. The predatory dinosaurs - Oviraptors; pp. 210–223 in *Herpetologische Untersuchungen in der Mongolischen Volksrepublik*. Academia Nauk SSSR.

BARSBOLD, R. 1988. The bony crest and helmet on the skull of predatory dinosaurs—oviraptors. *Transactions of the Joint Soviet Mongolian Paleontological Expedition*, **34**, 77–80.

BARSBOLD, R., MARYAŃSKA, T. and OSMÓLSKA, H. 1990. Oviraptorosauria. In Weishampel, D. B., Dodson, P. and Osmólska, H. (eds.) *The Dinosauria*. University of California Press, Berkeley, 249–258 pp.

BARSBOLD, R., OSMÓLSKA, H., WATABE, M., CURRIE, P. J. and TSOGTBAATAR, K. 2000a. A new oviraptorosaur (Dinosauria, Theropoda) from Mongolia: the first dinosaur with a pygostyle. *Acta Palaeontologica Polonica*, **45**, 97–106.

BARSBOLD, R., CURRIE, P. J., MYHRVOLD, N. P., OSMÓLSKA, H., TSOGTBAATAR, K. and WATABE, M. 2000b. A pygostyle from a non-avian theropod. *Nature*, **403**, 155–156.

BATES, K. T. and FALKINGHAM, P. L. 2012. Estimating maximum bite performance in *Tyrannosaurus rex* using multi-body dynamics. *Biology Letters*, **8**, 660–664.

BATES, K. T. and FALKINGHAM, P. L. 2018. The importance of muscle architecture in biomechanical reconstructions of extinct animals: a case study using *Tyrannosaurus rex*. *Journal of Anatomy*, **233**, 625–635.

BATES, K. T., WANG, L., DEMPSEY, M., BROYDE, S., FAGAN, M. J. and COX, P. G. 2021. Back to the bones: do muscle area assessment techniques predict

functional evolution across a macroevolutionary radiation? *Journal of the Royal Society Interface*, **18**, 20210324.

BENAVIDEZ, A., PALACIO, F. X., RIVERA, L. O., ECHEVARRIA, A. L. and POLITI, N. 2018. Diet of Neotropical parrots is independent of phylogeny but correlates with body size and geographical range. *Ibis*, **160**, 742–754.

BESTWICK, J., JONES, A. S., NESBITT, S. J., LAUTENSCHLAGER, S., RAYFIELD, E. J., CUFF, A. R., BUTTON, D. J., BARRETT, P. M., PORRO, L. B. and BUTLER, R. J. 2021. Cranial functional morphology of the pseudosuchian *Effigia* and implications for its ecological role in the Triassic. *The Anatomical Record*, 1–28.

BI, S., AMIOT, R., DE FABRÈGUES, C. P., PITTMAN, M., LAMANNA, M. C., YU, Y., YU, C., YANG, T., ZHANG, S., ZHAO, Q. and XU, X. 2021. An oviraptorid preserved atop an embryo-bearing egg clutch sheds light on the reproductive biology of non-avialan theropod dinosaurs. *Science Bulletin*, **66**, 947–954.

BOUT, R. G. and ZWEERS, G. A. 2001. The role of cranial kinesis in birds. *Comparative Biochemistry and Physiology Part A: Molecular & Integrative Physiology*, **131**, 197–205.

BRIGHT, J. A. and RAYFIELD, E. J. 2011. The response of cranial biomechanical finite element models to variations in mesh density. *The Anatomical Record*, **294**, 610–620.

BROYDE, S., DEMPSEY, M., WANG, L., COX, P. G., FAGAN, M. and BATES, K. T. 2021. Evolutionary biomechanics: hard tissues and soft evidence? *Proceedings of the Royal Society B: Biological Sciences*, **288**, 20202809.

BRUSATTE, S. L., LLOYD, G. T., WANG, S. C. and NORELL, M. A. 2014. Gradual assembly of avian body plan culminated in rapid rates of evolution across the

dinosaur-bird transition. *Current Biology*, **24**, 2386–2392.

BUTTON, D. J., RAYFIELD, E. J. and BARRETT, P. M. 2014. Cranial biomechanics underpins high sauropod diversity in resource-poor environments. *Proceedings of the Royal Society B: Biological Sciences*, **281**, 20142114.

BUTTON, D. J., BARRETT, P. M. and RAYFIELD, E. J. 2016. Comparative cranial myology and biomechanics of *Plateosaurus* and *Camarasaurus* and evolution of the sauropod feeding apparatus. *Palaeontology*, **59**, 887–913.

BUTTON, D. J. and ZANNO, L. E. 2020. Repeated evolution of divergent modes of herbivory in non-avian dinosaurs. *Current Biology*, **30**, 158–168.

CARRIL, J., DEGRANGE, F. J. and TAMBUSSI, C. P. 2015. Jaw myology and bite force of the monk parakeet (Aves, Psittaciformes). *Journal of Anatomy*, **227**, 34–44.

CHANG, S. C., GAO, K. Q., ZHOU, C. F. and JOURDAN, F. 2017. New chronostratigraphic constraints on the Yixian Formation with implications for the Jehol Biota. *Palaeogeography, Palaeoclimatology, Palaeoecology*, **487**, 399–406.

CHEN, P. Y., LIN, A. Y. M., LIN, Y. S., SEKI, Y., STOKES, A. G., PEYRAS, J., OLEVSKY, E. A., MEYERS, M. A. and MCKITTRICK, J. 2008. Structure and mechanical properties of selected biological materials. *Journal of the Mechanical Behavior of Biomedical Materials*, **1**, 208–226.

CHRISTIANSEN, P. 1998. Strength indicator values of theropod long bones, with comments on limb proportions and cursorial potential. *Gaia*, **15**, 241–255.

CHRISTIANSEN, P. and BONDE, N. 2002. Limb proportions and avian terrestrial locomotion. *Journal für Ornithologie*, **143**, 356–371.

CLARK, J. M., NORELL, M. A. and CHIAPPE L. M. 1999. An oviraptorid skeleton from the Late Cretaceous of Ukhaa Tolgod, Mongolia, preserved in an avianlike brooding position over an oviraptorid nest. *American Museum Novitates*, **3265**, 1–36.

CLARK, J. M., NORELL, M. A. and BARSBOLD, R. 2001. Two new oviraptorids (Theropoda: Oviraptorosauria), Upper Cretaceous Djadokhta Formation, Ukhaa Tolgod, Mongolia. *Journal of Vertebrate Paleontology*, **21**, 209–213.

CLARK, J. M., NORELL, M. A. and ROWE, T. 2002. Cranial anatomy of *Citipati osmolskae* (Theropoda, Oviraptorosauria), and a reinterpretation of the holotype of *Oviraptor philoceratops*. *American Museum Novitates*, **3364**, 1–24.

COATES, P. S., CONNELLY, J. W. and DELEHANTY, D. J. 2008. Predators of greater sage-grouse nests identified by video monitoring. *Journal of Field Ornithology*, **79**, 421–428.

COST, I. N., MIDDLETON, K. M., SELLERS, K. C., ECHOLS, M. S., WITMER, L. M., DAVIS, J. L. and HOLLIDAY, C. M. 2020. Palatal biomechanics and its significance for cranial kinesis in *Tyrannosaurus rex*. *The Anatomical Record*, **303**, 999–1017.

CRACRAFT, J. 1971 Caenagnathiformes: Cretaceous birds convergent in jaw mechanism to dicynodont reptiles. *Journal of Paleontology*, **45**, 805–809.

CREECH, J. E. 2004. Phylogenetic character analysis of crocodylian enamel microstructure and its relevance to biomechanical performance. MS thesis, Florida State University, Tallahassee, FL.

CROLE, M. R. and SOLEY, J. T. 2017. Bony pits in the ostrich (*Struthio camelus*) and emu (*Dromaius novaehollandiae*) bill tip. *The Anatomical Record*, **300**, 1705–1715.

CUFF, A. R. and RAYFIELD, E. J. 2015 Retrodeformation and muscular reconstruction of ornithomimosaurian dinosaur crania. PeerJ, **3**, e1093.

CUNNINGHAM, J. A., RAHMAN, I. A., LAUTENSCHLAGER, S., RAYFIELD, E. J. and DONOGHUE, P. C. 2014. A virtual world of paleontology. *Trends in Ecology & Evolution*, **29**, 347–357.

CURRIE, P. J. and RUSSELL, D. A. 1988 Osteology and relationships of *Chirostenotes pergracilis* (Saurischia, Theropoda) from the Judith River (Oldman) Formation of Alberta, Canada. *Canadian Journal of Earth Sciences*, **25**, 972–986.

CURRIE, P. J., GODFREY, S. J. and NESSOV, L. 1993. New caenagnathid (Dinosauria: Theropoda) specimens from the Upper Cretaceous of north America and Asia. *Canadian Journal of Earth Sciences*, **30**, 2255–2272.

DASHZEVEG, D., DINGUS, L., LOOPE, D. B., SWISHER, C. C., DULAM, T. and SWEENEY, M. R. 2005. New stratigraphic subdivision, depositional environment, and age estimate for the Upper Cretaceous Djadokhta Formation, southern Ulan Nur Basin, Mongolia. *American Museum Novitates*, **3498**, 1–31.

DEVRIES, R. P., SERENO, P. C., VIDAL, D. and BAUMGART, S. L. 2022. Reproducible Digital Restoration of Fossils Using Blender. *Frontiers in Earth Science*, **10**.

DÍEZ DÍAZ, V., MALLISON, H., ASBACH, P., SCHWARZ, D. and BLANCO, A. 2021. Comparing surface digitization techniques in palaeontology using visual perceptual metrics and distance computations between 3D meshes. *Palaeontology*, **64**, 179–202.

DINGUS, L., LOOPE, D. B., DASHZEVEG, D., SWISHER, C. C., MINJIN, C., NOVACEK, M. J. and NORELL, M. A. 2008. The geology of Ukhaa Tolgod (Djadokhta Formation, Upper Cretaceous, Nemegt Basin, Mongolia). *American Museum*

Novitates, **3616**, 1–40.

DONG, Z.-M., CURRIE, P. J. 1996. On the discovery of an oviraptorid skeleton on a nest of eggs at Bayan Mandahu, Inner Mongolia, People's Republic of China. *Canadian Journal of Earth Sciences*, **33**, 631–636.

DUMONT, E. R., PICCIRILLO, J. and GROSSE, I. R. 2005. Finite-element analysis of biting behavior and bone stress in the facial skeletons of bats. *The Anatomical Record*, **283A**, 319–330.

DUMONT, E. R., GROSSE, I. R. and SLATER, G. J. 2009. Requirements for comparing the performance of finite element models of biological structures. *Journal of Theoretical Biology*, **256**, 96–103.

EASTICK, D. L., TATTERSALL, G. J., WATSON, S. J., LESKU, J. A. and ROBERT, K. A. 2019. Cassowary casques act as thermal windows. *Scientific reports*, **9**, 1–7.

ELZANOWSKI, A. 1999. A comparison of the jaw skeleton in theropods and birds, with a description of the palate in the Oviraptoridae. *Smithsonian Contributions to Paleobiology*, **89**, 311–323.

EWER, R. F. 1965. The anatomy of the thecodont reptile *Euparkeria capensis* Broom. Philosophical Transactions of the Royal Society of London B, **248**, 379–435.

FALKINGHAM, P. L. 2012. Acquisition of high resolution three-dimensional models using free, open-source, photogrammetric software. *Palaeontologia electronica*, **15**, 15.

FANTI, F., CURRIE, P. J. and BADAMGARAV, D. 2012. New specimens of *Nemegtomaia* from the Baruungoyot and Nemegt Formations (Late Cretaceous) of Mongolia. *PLoS One*, **7**, e31330.

FASTOVSKY, D. E., BADAMGARAV, D., ISHIMOTO, H., WATABE, M. and WEISHAMPEL, D. B. 1997. The paleoenvironments of Tugrikin-Shireh (Gobi Desert, Mongolia) and aspects of the taphonomy and paleoecology of *Protoceratops* (Dinosauria: Ornithishichia). *Palaios*, **12**, 59–70.

FOTH, C., TISCHLINGER, H. and RAUHUT, O. W. M. 2014. New specimen of *Archaeopteryx* provides insights into the evolution of pennaceous feathers. *Nature*, **511**, 79–82.

FECCHIO, R. S., SEKI, Y., BODDE, S. G., GOMES, M. S., KOLOSOSKI, J., ROSSI Jr, J. L., GIOSO, M. A. and MEYERS, M. A. 2010. Mechanical behavior of prosthesis in Toucan beak (*Ramphastos toco*). *Materials Science and Engineering: C*, **30**, 460–464.

FUNSTON, G. F. and CURRIE, P. J. 2014. A previously undescribed caenagnathid mandible from the late Campanian of Alberta, and insights into the diet of *Chirostenotes pergracilis* (Dinosauria: Oviraptorosauria). *Canadian Journal of Earth Sciences*, **51**, 156–165.

FUNSTON, G.F. and CURRIE, P. J. 2016. A new caenagnathid (Dinosauria: Oviraptorosauria) from the Horseshoe Canyon Formation of Alberta, Canada, and a reevaluation of the relationships of Caenagnathidae. *Journal of Vertebrate Paleontology*, **36**, e1160910.

FUNSTON, G. F., CURRIE, P. J., EBERTH, D. A., RYAN, M. J., CHINZORIG, T., BADAMGARAV, D. and LONGRICH, N. R. 2016. The first oviraptorosaur (Dinosauria: Theropoda) bonebed: evidence of gregarious behaviour in a maniraptoran theropod. *Scientific Reports*, **6**, 35782.

FUNSTON, G. F., MENDONCA, S. E., CURRIE, P. J. and BARSBOLD, R. 2018. Ovi-

raptorosaur anatomy, diversity and ecology in the Nemegt Basin. *Palaeogeography, Palaeoclimatology, Palaeoecology*, **494**, 101–120.

FUNSTON, G. F. 2019. Anatomy, systematics, and evolution of Oviraptorosauria (Dinosauria, Theropoda). Doctoral dissertation, University of Alberta.

FUNSTON, G. F., CURRIE, P. J., RYAN, M. J. and DONG, Z. M. 2019. Birdlike growth and mixed-age flocks in avimimids (Theropoda, Oviraptorosauria). *Scientific Reports*, **9**, 1–21.

FUNSTON, G. F., WILKINSON, R. D., SIMON, D. J., LEBLANC, A. H., WOSIK, M. and CURRIE, P. J. 2020a. Histology of caenagnathid (Theropoda, Oviraptorosauria) dentaries and implications for development, ontogenetic edentulism, and taxonomy. *The Anatomical Record*, **303**, 918–934.

FUNSTON, G. F., CHINZORIG, T., TSOGTBAATAR, K., KOBAYASHI, Y., SULLIVAN, C. and CURRIE, P. J. 2020b. A new two-fingered dinosaur sheds light on the radiation of Oviraptorosauria. *Royal Society Open Science*, **7**, 201184.

FUNSTON, G. F., CURRIE, P. J., TSOGTBAATAR, C. and KHISHIGJAV, T. 2021. A partial oviraptorosaur skeleton suggests low caenagnathid diversity in the Late Cretaceous Nemegt Formation of Mongolia. *PloS one*, **16**, e0254564.

GANS, C. and OSHIMA, M. 1952. Adaptations for egg eating in the snake *Elaphe climacophora* (Boie). *American Museum Novitates*, **1571**, 1–16.

GARWOOD, R. and DUNLOP, J. 2014. The walking dead: Blender as a tool for paleontologists with a case study on extinct arachnids. *Journal of Paleontology*, **88**, 735–746.

GIGNAC, P. M. and ERICKSON, G. M. 2016. Ontogenetic bite-force modeling of *Alli-*

gator mississippiensis: implications for dietary transitions in a large-bodied vertebrate and the evolution of crocodylian feeding. *Journal of Zoology*, **299**, 229–238.

GIGNAC, P. M. and ERICKSON, G. M. 2017. The biomechanics behind extreme osteophagy in *Tyrannosaurus rex*. *Scientific Reports*, **7**, 1–10.

GILMORE, C. W. 1924. A new coelurid dinosaur from the Belly River Cretaceous of Alberta. *Canada Geological Survey Bulletin*, **38**, 1–12.

GRADZIŃSKI, R. and JERZYKIEWICZ, T. 1974a. Dinosaur- and mammal-bearing aeolian and associated deposits of the Upper Cretaceous in the Gobi Desert (Mongolia). *Sedimentary Geology*, **12**, 249–278.

GRADZIŃSKI, R. and JERZYKIEWICZ, T. 1974b Sedimentation of the Bayan Goryot Formation. In JAWOROWSKA, K. (ed.) *Results of the Polish-Mongolian Palaeontological Expeditions*, Palaeontologia Polonica, Warsaw, 111–146 pp.

HAAS, G. 1955. The jaw musculature in *Protoceratops* and in other ceratopsians. *American Museum Novitates*, **1729**, 1–24.

HAMMER, Ø., HARPER, D. A. and RYAN, P. D. 2001. PAST: Paleontological statistics software package for education and data analysis. *Palaeontologia electronica*, **4**, 1–9.

HASEGAWA, H., TADA, R., ICHINNOROV, N. and MINJIN, C. 2009. Lithostratigraphy and depositional environments of the Upper Cretaceous Djadokhta Formation, Ulan Nuur basin, southern Mongolia, and its paleoclimatic implication. *Journal of Asian Earth Sciences*, **35**, 13–26.

HERBST, E. C., LAUTENSCHLAGER, S., BASTIAANS, D., MIEDEMA, F. and SCHEYER, T. M. 2021. Modeling tooth enamel in FEA comparisons of skulls: Comparing com-

mon simplifications with biologically realistic models. *Iscience*, **24**, 103182.

HERBST E. C., MEADE L. E., LAUTENSCHLAGER S., FIORITTI N. and SCHEYER T. M. 2022. A toolbox for the retrodeformation and muscle reconstruction of fossil specimens in Blender. *Royal Society Open Science*, **9**, 220519.

HERRING, S. W. and HERRING, S. E. 1974. The superficial masseter and gape in mammals. *The American Naturalist*, **108**, 561–576.

HOESE, W.J. and WESTNEAT, M.W. 1996. Biomechanics of cranial kinesis in birds: Testing linkage models in the white-throated sparrow (*Zonotrichia albicollis*). *Journal of Morphology*, **227**, 305–320.

HOFER, H. 1950 Zur Morphologie der Kiefermuskulatur der Vögel. *Zoologische Jahrbücher, Abteilung für Anatomie und Ontogenie der Tiere*, **70**, 427–556.

HOLLIDAY, C. M. and WITMER, L. M. 2007. Archosaur adductor chamber evolution: integration of musculoskeletal and topological criteria in jaw muscle homology. *Journal of Morphology*, **268**, 457–484.

HOLLIDAY, C. M. 2009. New insights into dinosaur jaw muscle anatomy. *The Anatomical* Record, **292**, 1246–1265.

HOLLIDAY, C. M., PORTER, W. R., VLIET, K. A. and WITMER, L. M. 2020. The frontoparietal fossa and dorsotemporal fenestra of archosaurs and their significance for interpretations of vascular and muscular anatomy in dinosaurs. *The Anatomical Record*, **303**, 1060–1074.

HOUNSOME, T. and DELAHAY, R. 2005. Birds in the diet of the Eurasian badger *Meles meles*: a review and meta-analysis. *Mammal Review*, **35**, 199–209.

HUISKES, R. 2000. If bone is the answer, then what is the question? *The Journal of Anatomy*, **197**, 145–156.

JERZYKIEWICZ, T., CURRIE, P. J., FANTI, F. and LEFELD, J. 2021. Lithobiotopes of the Nemegt Gobi Basin[1]. *Canadian Journal of Earth Sciences*, **58**, 829–851.

JI, Q., CURRIE, P. J., NORELL, M. A. and JI, S.-A. 1998. Two feathered dinosaurs from northeastern China. *Nature*, **393**, 753–761.

KING, G. M. 1981. The functional anatomy of a Permian dicynodont. *Philosophical Transactions of the Royal Society of London B*, **291**, 243–322.

KING, G. M., OELOFSEN, B. W. and RUBIDGE, B. S. 1989. The evolution of the dicynodont feeding system. *Zoological Journal of the Linnean Society*, **96**, 185–211.

KUNDRÁT, M. 2007 Avian-like attributes of a virtual brain model of the oviraptorid theropod *Conchoraptor gracilis*. *Naturwissenschaften*, **94**, 499–504.

KUNDRÁT, M. and JANÁČEK, J. 2007. Cranial pneumatization and auditory perceptions of the oviraptorid dinosaur *Conchoraptor gracilis* (Theropoda, Maniraptora) from the Late Cretaceous of Mongolia. *Naturwissenschaften*, **94**, 769–778.

KURZANOV, S. M. 1981. An unusual theropod from the Upper Cretaceous of Mongolia. *Joint Soviet Mongolian Paleontological Expedition*, **15**, 39–49.

LAMANNA, M. C., SUES, H. D., SCHACHNER, E. R. and LYSON, T. R. 2014. A new large-bodied oviraptorosaurian theropod dinosaur from the latest Cretaceous of western North America. *PLoS One*, **9**, e92022.

LAUTENSCHLAGER, S. 2013. Cranial myology and bite force performance of *Erlikosaurus andrewsi*: a novel approach for digital muscle reconstructions. *Journal*

of Anatomy, **222**, 260–272.

LAUTENSCHLAGER, S., WITMER, L. M., ALTANGEREL, P. and RAYFIELD, E. J. 2013. Edentulism, beaks, and biomechanical innovations in the evolution of theropod dinosaurs. *Proceedings of the National Academy of Sciences*, **110**, 20657–20662.

LAUTENSCHLAGER, S. 2015. Estimating cranial musculoskeletal constraints in theropod dinosaurs. *Royal Society Open Science*, **2**, 150495.

LAUTENSCHLAGER, S. 2016a. Digital reconstruction of soft-tissue structures in fossils. *The Paleontological Society Papers*, **22**, 101–117.

LAUTENSCHLAGER, S. 2016b. Reconstructing the past: methods and techniques for the digital restoration of fossils. *Royal Society Open Science*, **3**, 160342.

LAUTENSCHLAGER, S., BRASSEY, C. A., BUTTON, D. J. and BARRETT, P. M. 2016. Decoupled form and function in disparate herbivorous dinosaur clades. *Scientific Reports*, **6**, 1–10.

LAUTENSCHLAGER, S., GILL, P. G., LUO, Z. X., FAGAN, M. J. and RAYFIELD, E. J. 2018. The role of miniaturization in the evolution of the mammalian jaw and middle ear. *Nature*, **561**, 533–537.

LAUTENSCHLAGER, S. 2020. Multibody dynamics analysis (MDA) as a numerical modelling tool to reconstruct the function and palaeobiology of extinct organisms. *Palaeontology*, **63**, 703–715.

LAUTENSCHLAGER, S. 2021. True colours or red herrings?: colour maps for finite-element analysis in palaeontological studies to enhance interpretation and accessibility. *Royal Society Open Science*, **8**, 211357.

LAUTENSCHLAGER, S. 2022. Functional and ecomorphological evolution of orbit shape in mesozoic archosaurs is driven by body size and diet. *Communications Biology*, **5**, 1–11.

LEDERER, R. J. 1975. Bill size, food size, and jaw forces of insectivorous birds. *The Auk*, **92**, 385–387.

LEFÈVRE, U., CAU, A., CINCOTTA, A., HU, D., CHINSAMY, A., ESCUILLIÉ, F. and GODEFROIT, P. 2017. A new Jurassic theropod from China documents a transitional step in the macrostructure of feathers. *The Science of Nature*, **104**, 1–13.

LIEBER, R. L. 2022. Can we just forget about pennation angle? *Journal of Biomechanics*, **132**, 110954.

LONGRICH, N. R., CURRIE, P. J. and ZHI-MING, D. 2010. A new oviraptorid (Dinosauria: Theropoda) from the Upper Cretaceous of Bayan Mandahu, Inner Mongolia. *Palaeontology*, **53**, 945–960.

LONGRICH, N. R., BARNES, K., CLARK, S. and MILLAR, L. 2013. Caenagnathidae from the Upper Campanian Aguja Formation of West Texas, and a revision of the Caenagnathinae. *Bulletin of the Peabody Museum of Natural History*, **54**, 23–49.

LÜ, J. 2003. A new oviraptorosaurid (Theropoda: Oviraptorosauria) from the Late Cretaceous of southern China. *Journal of Vertebrate Paleontology*, **22**, 871–875.

LÜ, J. C. and ZHANG, B. K. 2005. A new oviraptorid (Theropod: Oviraptorosauria) from the Upper Cretaceous of the Nanxiong Basin, Guangdong Province of southern China. *Acta Palaeontologica Sinica*, **44**, 412–422.

LÜ, J., CURRIE, P.J., XU, L., ZHANG, X., PU, H. and JIA, S. 2013a. Chicken-sized oviraptorid dinosaurs from central China and their ontogenetic implications. *Natur-*

wissenschaften, **100**, 165–175.

LÜ, J., YI, L., ZHONG, H. and WEI, X. 2013b. A new oviraptorosaur (Dinosauria: Oviraptorosauria) from the Late Cretaceous of southern China and its paleoecological implications. *PLoS One*, **8**, e80557.

LÜ, J., CHEN, R., BRUSATTE, S. L., ZHU, Y. and SHEN, C. 2016. A Late Cretaceous diversification of Asian oviraptorid dinosaurs: evidence from a new species preserved in an unusual posture. *Scientific Reports*, **6**, 1–12.

LÜ, J., LI, G., KUNDRÁT, M., LEE, Y. N., SUN, Z., KOBAYASHI, Y., SHEN, C., TENG, F. and LIU, H. 2017. High diversity of the Ganzhou Oviraptorid Fauna increased by a new "cassowary-like" crested species. *Scientific Reports*, **7**, 1–13.

MA, W., WANG, J., PITTMAN, M., TAN, Q., TAN, L., GUO, B. and XU, X. 2017. Functional anatomy of a giant toothless mandible from a bird-like dinosaur: *Gigantoraptor* and the evolution of the oviraptorosaurian jaw. *Scientific reports*, **7**, 1–15.

MA, W., BRUSATTE, S. L., LÜ, J. and SAKAMOTO, M. 2020a. The skull evolution of oviraptorosaurian dinosaurs: the role of niche partitioning in diversification. *Journal of Evolutionary Biology*, **33**, 178–188.

MA, W., PITTMAN, M., LAUTENSCHLAGER, S., MEADE, L. E. and XU, X. 2020b. Functional morphology of the Oviraptorosaurian and Scansoriopterygid skull. *Bulletin of the American Museum of Natural History*, **440**, 229–249.

MA, W., PITTMAN, M., BUTLER, R. J. and LAUTENSCHLAGER, S. 2022. Macroevolutionary trends in theropod dinosaur feeding mechanics. *Current Biology*, ***32***, 677–686.

MALLISON, H. 2011. Digitizing methods for paleontology: applications, benefits and

limitations. In *Computational paleontology*. Springer, Berlin, Heidelberg, 7–43 pp.

MANNING, A. 2021. A new approach for landmarking fossil specimens. Unpublished BSc thesis, University of Birmingham.

MARCÉ NOGUÉ, J., DE ESTEBAN-TRIVIGNO, S., ESCRIG, C. and GIL, L. 2016. Accounting for differences in element size and homogeneity when comparing finite element models: armadillos as a case study. *Palaeontologia Electronica*, **19**, 1–22.

MARCÉ-NOGUÉ, J. 2022. One step further in biomechanical models in palaeontology: a nonlinear finite element analysis review. *PeerJ*, **10**, e13890

MARSH, O. C. 1877. Notice of new dinosaurian reptiles from the Jurassic formation. *American Journal of Science and Arts*, **14**, 514–516.

MARYAŃSKA, T., OSMÓLSKA, H. and WOLSAN, M. 2002. Avialan status for Oviraptorosauria. *Acta Palaeontologica Polonica*, **47**, 97–116.

MAZZETTA, G. V., CISILINO, A. P., BLANCO, R. E. and CALVO, N. 2009. Cranial mechanics and functional interpretation of the horned carnivorous dinosaur *Carnotaurus sastrei*. *Journal of Vertebrate Paleontology*, **29**, 822–830.

MCCURRY, M. R., MAHONY, M., CLAUSEN, P. D., QUAYLE, M. R., WALMSLEY, C. W., JESSOP, T. S., WROE, S., RICHARDS, H. and MCHENRY, C. R. 2015. The relationship between cranial structure, biomechanical performance and ecological diversity in varanoid lizards. *PLoS One*, 10, e0130625.

MEADE, L. E. and MA, W. 2022. Cranial muscle reconstructions quantify adaptation for high bite forces in Oviraptorosauria. *Scientific Reports*, **12**, 1–15.

MIEDEMA, F., SPIEKMAN, S. N., FERNANDEZ, V., REUMER, J. W. and SCHEYER, T. M. 2020. Cranial morphology of the tanystropheid *Macrocnemus bassanii* unveiled using synchrotron microtomography. *Scientific Reports*, **10**, 1–19.

MOAZEN, M., CURTIS, N., O'HIGGINS, P., JONES, M. E., EVANS, S. E. and FAGAN, M. J. 2009. Assessment of the role of sutures in a lizard skull: a computer modelling study. *Proceedings of the Royal Society B*, **276**, 39–46.

MOLNAR, J. L., PIERCE, S. E., CLACK, J. A. and HUTCHINSON, J. R. 2012. Idealized landmark-based geometric reconstructions of poorly preserved fossil material: a case study of an early tetrapod vertebra. *Palaeontologia Electronica*, **15**, 1–18.

MONTEFELTRO, F. C., LAUTENSCHLAGER, S., GODOY, P. L., FERREIRA, G. S. and BUTLER, R. J. 2020. A unique predator in a unique ecosystem: modelling the apex predator within a Late Cretaceous crocodyliform-dominated fauna from Brazil. *Journal of Anatomy*, **237**, 323–333.

MORRIS, P. J., COX, P. G. and COBB, S. N. 2022. The biomechanical significance of the elongated rodent incisor root in the mandible during incision. *Scientific reports*, **12**, 1–11.

NABAVIZADEH, A. 2020a New reconstruction of cranial musculature in ornithischian dinosaurs: implications for feeding mechanisms and buccal anatomy. *The Anatomical Record*, **303**, 347–362.

NABAVIZADEH, A. 2020b Cranial musculature in herbivorous dinosaurs: A survey of reconstructed anatomical diversity and feeding mechanisms. *The Anatomical Record,* **303**, 1104–1145.

NALLA, R. K., KINNEY, J. H. and RITCHIE, R. O. 2003. Mechanistic fracture criteria for the failure of human cortical bone. *Nature Materials*, **2**, 164–168.

NAVALÓN, G., BRIGHT, J. A., MARUGÁN-LOBÓN, J. and RAYFIELD, E. J. 2019. The evolutionary relationship among beak shape, mechanical advantage, and feeding ecology in modern birds. *Evolution*, **73**, 422–435.

NIGG, B. M. and HERZOG, W. 2007. *Biomechanics of the Musculo-Skeletal System*. Wiley, New York.

NORELL, M. A., CLARK, J. M., DEMBERELYIN, D., RHINCHEN, B., CHIAPPE, L. M., DAVIDSON, A. R., MCKENNA, M. C., ALTANGEREL, P. and NOVACEK, M. J. 1994. A theropod dinosaur embryo and the affinities of the Flaming Cliffs dinosaur eggs. *Science*, **266**, 779–782.

NORELL, M. A., CLARK, J. M., CHIAPPE, L. M. and DASHZEVEG, D. 1995a. A nesting dinosaur. *Nature*, **378**, 774–776.

NORELL, M. A., GAFFNEY, E. S. and DINGUS, L. 1995b. *Discovering Dinosaurs in the American Museum of Natural History*. Knopf Inc., 225 p.

NORELL, M. A., BALANOFF, A. M., BARTA, D. E. and ERICKSON, G. M. 2018. A second specimen of *Citipati osmolskae* associated with a nest of eggs from Ukhaa Tolgod, Omnogov Aimag, Mongolia. *American Museum Novitates*, **3899**, 1–44.

OSBORN, H. F. 1924 Three new Theropoda, *Protoceratops* zone, central Mongolia. *American Museum Novitates*, **144**, 1–12.

OSMÓLSKA, H. 1976. New light on the skull anatomy and systematic position of *Oviraptor philoceratops*. *Nature*, **262**, 683–684.

OSMÓLSKA, H., CURRIE, P. J. and BARSBOLD, R. 2004. Oviraptorosauria. In WEISHAMPEL, D. B., DODSON, P. and OSMÓLSKA, H. (eds.) *The Dinosauria, Second Edition*. California University Press, 165–183 pp.

OSTROM, J. H. 1961. Cranial morphology of the hadrosaurian dinosaurs of North America. *Bulletin of the American Museum of Natural History*, **122**, 39–186.

PERSONS, W. S., CURRIE, P. J. and NORELL, M. A. 2013. Oviraptorosaur tail forms and functions. *Acta Palaeontologica Polonica*, **59**, 553–567.

PITTMAN, M., O'CONNOR, J., FIELD, D. J., TURNER, A. H., MA, W., MAKOVICKY, P. and XU, X. 2020. Pennaraptoran systematics. *Bulletin of the American Museum of Natural History*, **440**, 7–36.

PORRO, L. B., HOLLIDAY, C. M., ANAPOL, F., ONTIVEROS, L. C., ONTIVEROS, L. T. and ROSS, C. F. 2011. Free body analysis, beam mechanics, and finite element modeling of the mandible of *Alligator mississippiensis*. *Journal of morphology*, **272**, 910–937.

RAHMAN, I. A. and LAUTENSCHLAGER, S. 2016. Applications of three-dimensional box modeling to paleontological functional analysis. *The Paleontological Society Papers*, **22**, 119–132.

RAYFIELD, E. J., NORMAN, D. B., HORNER, C. C., HORNER, J. R., SMITH, P. M., THOMASON, J. J. and UPCHURCH, P. 2001. Cranial design and function in a large theropod dinosaur. *Nature*, **409**, 1033–1037.

RAYFIELD, E. J. 2007. Finite element analysis and understanding the biomechanics and evolution of living and fossil organisms. *Annual Review of Earth and Planetary Sciences*, **35**, 541–576.

RAYFIELD, E. J. and MILNER, A. C. 2008. Establishing a framework for archosaur cranial mechanics. *Paleobiology*, **34**, 494–515.

RAYFIELD, E. J. 2011. Structural performance of tetanuran theropod skulls, with em-

phasis on the Megalosauridae, Spinosauridae and Carcharodontosauridae. *Special Papers in Palaeontology*, **86**, 241–253.

REICHEL, M. 2010. A model for the bite mechanics in the herbivorous dinosaur *Stegosaurus* (Ornithischia, Stegosauridae). *Swiss Journal of Geosciences*, **103**, 235–240.

RHODES, M. M., FUNSTON, G. F. and CURRIE, P. J. 2020. New material reveals the pelvic morphology of Caenagnathidae (Theropoda, Oviraptorosauria). *Cretaceous Research*, **114**, 104521.

RICHARDS, H. L, BISHOP, P. J, HOCKING, D. P, ADAMS, J. W. and EVANS, A. R. 2021. Low elbow mobility indicates unique forelimb posture and function in a giant extinct marsupial. *Journal of Anatomy*, **238**, 1425–1441.

RICHMOND, B. G., WRIGHT, B. W., GROSSE, I., DECHOW, P. C., ROSS, C. F., SPENCER, M. A. and Strait, D. S. 2005. Finite element analysis in functional morphology. *The Anatomical Record*, **283A**, 259–274.

ROESLER, H. 1987. The history of some fundamental concepts in bone biomechanics. *Journal of Biomechanics*, **20**, 1025–1034.

ROSS, C. F. 2005. Finite element analysis in vertebrate biomechanics. *The Anatomical Record*, **283A**, 253–258.

RUFF, C., HOLT, B. and TRINKAUS, E. 2006. Who's afraid of the big bad Wolff?: "Wolff's law" and bone functional adaptation. *American Journal of Physical Anthropology*, **129**, 484–498.

SAKAMOTO, M. 2010. Jaw biomechanics and the evolution of biting performance in theropod dinosaurs. *Proceedings of the Royal Society B: Biological Sciences*, **277**,

3327–3333.

SAKAMOTO, M. 2022. Estimating bite force in extinct dinosaurs using phylogenetically predicted physiological cross-sectional areas of jaw adductor muscles. PeerJ, **10**, e13731.

SATO, T., CHANG, Y.-N., WU, X.-C., ZELENITSKY, D. A., HSIAO, Y.-F. 2005. A pair of shelled eggs inside a female dinosaur. *Science*, **308**, 375.

SCHUBERT, B. W. and UNGAR, P. S. 2005. Wear facets and enamel spalling in tyrannosaurid dinosaurs. *Acta Palaeontologica Polonica*, **50**, 93–99.

SENTER, P. 2007. A new look at the phylogeny of Coelurosauria (Dinosauria: Theropoda). *Journal of Systematic Palaeontology*, **5**, 429–463

SENTER, P. and PARRISH J. M. 2005. Functional analysis of the hands of the theropod dinosaur *Chirostenotes pergracilis*: evidence for an unusual paleoecological role. *PaleoBios*, **25**, 9–19.

SENTER, P., KIRKLAND, J. I., DEBLIEUX, D. D., MADSEN, S. and TOTH, N. 2012. New dromaeosaurids (Dinosauria: Theropoda) from the Lower Cretaceous of Utah, and the evolution of the dromaeosaurid tail. *PLoS One*, **7**, e36790.

SHERWOOD, L, KLANDORF, H. and YANCEY, P. 2005. *Animal Physiology: From Genes to Organisms.* Brooks/Cole, Belmont, California, 335–384 pp.

SMITH, D. 1992. The type specimen of *Oviraptor philoceratops*, a theropod dinosaur from the Upper Cretaceous of Mongolia. *Neues Jahrbuch für Geologie und Paläontologie. Abhandlungen*, **186**, 365–388.

SNIVELY, E., RUSSELL, A. P. and POWELL, G. L. 2004. Evolutionary morphology of

the coelurosaurian arctometatarsus: descriptive, morphometric and phylogenetic approaches. *Zoological Journal of the Linnean Society*, **142**, 525–553.

SNIVELY, E., COTTON, J. R., RIDGELY, R. and WITMER, L. M. 2013. Multibody dynamics model of head and neck function in *Allosaurus* (Dinosauria, Theropoda). *Palaeontologia Electronica*, **16**, 11A.

STERNBERG C. M. 1933. A new *Ornithomimus* with complete abdominal cuirass. *The Canadian Field Naturalist*, **47**, 79–83.

STERNBERG R. M. 1940. A toothless bird from the Cretaceous of Alberta. *Journal of Paleontology*, **14**, 81–85.

SUES. H. D. 1997. On *Chirostenotes*, a Late Cretaceous oviraptorosaur (Dinosauria: Theropoda) from western North America. *Journal of Vertebrate Paleontology*, **17**, 698–716.

SULLIVAN, R. M., JASINSKI, S. E. and VAN TOMME, M. P. A. 2011. A new caenagnathid *Ojoraptorsaurus boerei*, n. gen., n. sp. (Dinosauria, Oviraptorosauria), from the Upper Cretaceous Ojo Alamo Formation (Naashoibito member), San Juan basin, New Mexico. *Bulletin of the New Mexico Museum of Natural History and Science*, **53**, 418–428.

SULLIVAN, C. and XU, X. 2017. Morphological diversity and evolution of the jugal in dinosaurs. *The Anatomical Record*, **300**, 30–48.

SWISHER, C. C., WANG, X., ZHOU, Z., WANG, Y., JIN, F., ZHANG, J., XU, X., ZHANG, F. and WANG, Y. 2002. Further support for a Cretaceous age for the feathered-dinosaur beds of Liaoning, China: New $^{40}Ar \div ^{39}Ar$ dating of the Yixian and Tuchengzi Formations. *Chinese Science Bulletin*, **47**, 136–139.

TATTERSALL, G. J., ARNAOUT, B. and SYMONDS, M. R. 2017. The evolution of the avian bill as a thermoregulatory organ. *Biological Reviews*, **92**, 1630–1656.

TAYLOR, A. C., LAUTENSCHLAGER, S., QI, Z. and RAYFIELD, E. J. 2017. Biomechanical evaluation of different musculoskeletal arrangements in *Psittacosaurus* and implications for cranial function. *The Anatomical Record*, **300**, 49–61.

TAYLOR, M. P., WEDEL, M. J. and NAISH, D. 2009. Head and neck posture in sauropod dinosaurs inferred from extant animals. *Acta Palaeontologica Polonica*, **54**, 213–220.

THOMASON, J. J. 1991. Cranial strength in relation to estimated biting forces in some mammals. *Canadian Journal of Zoology*, **69**, 2326–2333.

TURNER, A. H., MAKOVICKY P. J. and NORELL M. A. 2012. A review of dromaeosaurid systematics and paravian phylogeny. *Bulletin of the American Museum of Natural History*, **371**, 1–206.

TSCHOPP, E., RUSSO, J. and DZEMSKI, G. 2013. Retrodeformation as a test for the validity of phylogenetic characters: An example from diplodocid sauropod vertebrae. *Palaeontologia Electronica*, **16**, 1–23.

TSENG, Z. J. and FLYNN, J. J. 2018. Structure-function covariation with nonfeeding ecological variables influences evolution of feeding specialization in Carnivora. *Science Advances*, **4**, eaao5441.

TSUIHIJI, T., WITMER, L. M., WATABE, M., BARSBOLD, R., TSOGTBAATAR, K., SUZUKI, S. and KHATANBAATAR, P. 2017. New information on the cranial morphology of *Avimimus* (Theropoda: Oviraptorosauria). *Journal of Vertebrate* Paleontology, e1347177.

VARRICCHIO, D. J., MOORE, J. R., ERICKSON, G. M., NORELL, M. A., JACKSON, F. D. and BORKOWSKI, J. J. 2008. Avian paternal care had dinosaur origin. *Science*, **322**, 1826–1828.

WALMSLEY, C. W., SMITS, P. D., QUAYLE, M. R., MCCURRY, M. R., RICHARDS, H. S., OLDFIELD, C. C., WROE, S., CLAUSEN, P. D. and MCHENRY, C. R. 2013. Why the long face? The mechanics of mandibular symphysis proportions in crocodiles. *PLoS One*, **8**, p.e53873.

WANG, M. and HU, H. 2017. A comparative morphological study of the jugal and quadratojugal in early birds and their dinosaurian relatives. *The Anatomical Record*, **300**, 62–75.

WEI, X., KUNDRÁT, M., XU, L., MA, W., WU, Y., CHANG, H., ZHANG, J. and ZHOU, X. 2022. A new subadult specimen of oviraptorid *Yulong mini* (Theropoda: Oviraptorosauria) from the Upper Cretaceous Qiupa Formation of Luanchuan, central China. *Cretaceous Research*, **138**, 105261.

WEIJS, W. A. and HILLEN, B. 1985. Cross-sectional areas and estimated intrinsic strength of the human jaw muscles. *Acta Morphologica Neerlando-Scandinavica*, **23**, 267–274.

WIEMANN, J., YANG, T. R., SANDER, P. N., SCHNEIDER, M., ENGESER, M., KATHSCHORR, S., MÜLLER, C. E. and Sander, P. M. 2017. Dinosaur origin of egg color: oviraptors laid blue-green eggs. *PeerJ*, **5**, e3706.

WINGS, O. and SANDER, P. M. 2007. No gastric mill in sauropod dinosaurs: new evidence from analysis of gastrolith mass and function in ostriches. *Proceedings of the Royal Society B: Biological Sciences*, **274**, 635–640.

WOLFF, J. 1892. Das Gesetz der Transformation der Knochen. (Transl. The Law of

Bone Remodelling). Springer-Verlag, Berlin.

WROE, S., MCHENRY, C. and THOMASON, J. 2005. Bite club: comparative bite force in big biting mammals and the prediction of predatory behaviour in fossil taxa. *Proceedings of the Royal Society B: Biological Sciences*, **272**, 619–625.

XU, X., CHENG, Y. N., WANG, X. L. and CHANG, C. H. 2002. An unusual oviraptorosaurian dinosaur from China. *Nature*, **419**, 291–293.

XU, X., TAN, Q., WANG, J., ZHAO, X. and TAN, L. 2007. A gigantic bird-like dinosaur from the Late Cretaceous of China. *Nature*, **447**, 844–847.

XU, X., ZHENG X. and YOU, H. 2010. Exceptional dinosaur fossils show ontogenetic development of early feathers. *Nature*, **464**, 1338–1341.

XU, X., TAN, Q., WANG, S., SULLIVAN, C., HONE, D. W. E., HAN, F., MA, Q., TAN, L. and XIAO, D. 2013. A new oviraptorid from the Upper Cretaceous of Nei Mongol, China, and its stratigraphic implications. *Vertebrata PalAsiatica*, **51**, 85–101.

XU, X., ZHENG, X., SULLIVAN, C., WANG, X., XING, L., WANG, Y., ZHANG, X., O'CONNOR, J. K., ZHANG, F. and PAN, Y. 2015. A bizarre Jurassic maniraptoran theropod with preserved evidence of membranous wings. *Nature*, **521**, 70–73.

XU, X., CURRIE, P., PITTMAN, M., XING, L., MENG, Q., LÜ, J., HU, D. and YU, C. 2017. Mosaic evolution in an asymmetrically feathered troodontid dinosaur with transitional features. *Nature communications*, **8**, 1–12.

XU, X. 2020. Filamentous integuments in nonavialan theropods and their kin: advances and future perspectives for understanding the evolution of feathers. In FOTH, C. and RAUHUT, O. W. M. (eds.) *The Evolution of Feathers*, Springer, 67–78 pp.

YANG, T. R. and SANDER, P. M. 2018. The origin of the bird's beak: new insights from dinosaur incubation periods. *Biology Letters*, **14**, 20180090.

YANG, T. R., WIEMANN, J., XU, L., CHENG, Y. N., WU, X. C. and SANDER, P. M. 2019. Reconstruction of oviraptorid clutches illuminates their unique nesting biology. *Acta Palaeontologica Polonica*, **64**, 581–596.

YANG, T. R. and SANDER, P. M. 2022. The reproductive biology of oviraptorosaurs: a synthesis. *Geological Society, London, Special Publications*, **521**, 19–34.

YOUNG, M. T., RAYFIELD, E. J., HOLLIDAY, C. M., WITMER, L. M., BUTTON, D. J., UPCHURCH, P. and BARRETT, P. M. 2012. Cranial biomechanics of *Diplodocus* (Dinosauria, Sauropoda): testing hypotheses of feeding behaviour in an extinct megaherbivore. *Naturwissenschaften*, **99**, 637–643.

YU, Y., WANG, K., CHEN, S., SULLIVAN, C., WANG, S., WANG, P. and XU, X. 2018. A new caenagnathid dinosaur from the Upper Cretaceous Wangshi Group of Shandong, China, with comments on size variation among oviraptorosaurs. *Scientific Reports*, **8**, 1–10.

ZANNO, L. E. and SAMPSON, S. D. 2005. A new oviraptorosaur (Theropoda, Maniraptora) from the Late Cretaceous (Campanian) of Utah. *Journal of Vertebrate Paleontology*, **25**, 897–904.

ZANNO, L. E. 2010. A taxonomic and phylogenetic reevaluation of Therizinosauria (Dinosauria: Maniraptora). *Journal of Systematic Palaeontology*, **8**, 503–543.

ZANNO, L. E. and MAKOVICKY, P. J. 2011. Herbivorous ecomorphology and specialization patterns in theropod dinosaur evolution. *Proceedings of the National Academy of Sciences*, **108**, 232–237.

ZANNO, L. E. and MAKOVICKY, P. J. 2013. No evidence for directional evolution of body mass in herbivorous theropod dinosaurs. *Proceedings of the Royal Society B: Biological Sciences*, **280**, 20122526.

ZAPATA, U., METZGER, K., WANG, Q., ELSEY, R. M., ROSS, C. F. and DECHOW, P. C. 2010. Material properties of mandibular cortical bone in the American alligator, *Alligator mississippiensis*. *Bone*, **46**, 860–867.

ZHAO, Y., YANG, Y. B., GUO, Y., REN, G. Y. and ZHANG, F.C. 2021. Stable carbon isotope composition of bone hydroxylapatite: significance in paleodietary analysis. *Palaeoworld*, **31**, 169–184.

ZHOU, Y. C., SULLIVAN, C. and ZHANG, F. C. 2019. Negligible effect of tooth reduction on body mass in Mesozoic birds. *Vertebrata PalAsiatica*, **57**, 38–50.

ZHOU Z.-H. and WANG X.-L 2000. A new species of *Caudipteryx* from the Yixian Formation of Liaoning, northeast China. *Vertebrata PalAsiatica*, **38**, 111–127.

ZIENKIEWICZ O. C., TAYLOR R. L. and Zhu J. Z. 2005. *The Finite Element Method: Its Basis and Fundamentals*. Elsevier Butterworth-Heinemann, Oxford, UK.

ZUSI, R. L. 1967. The role of the depressor mandibulae muscle in kinesis of the avian skull. *Proceedings of the United States National Museum*, **123**, 1–28.

Appendices

A | Bending test sensitivity tests and stress data

The figures and tables in this appendix are supplementary to Chapter 3: "Strength and comparative performance of the oviraptorid cranium in response to bending".

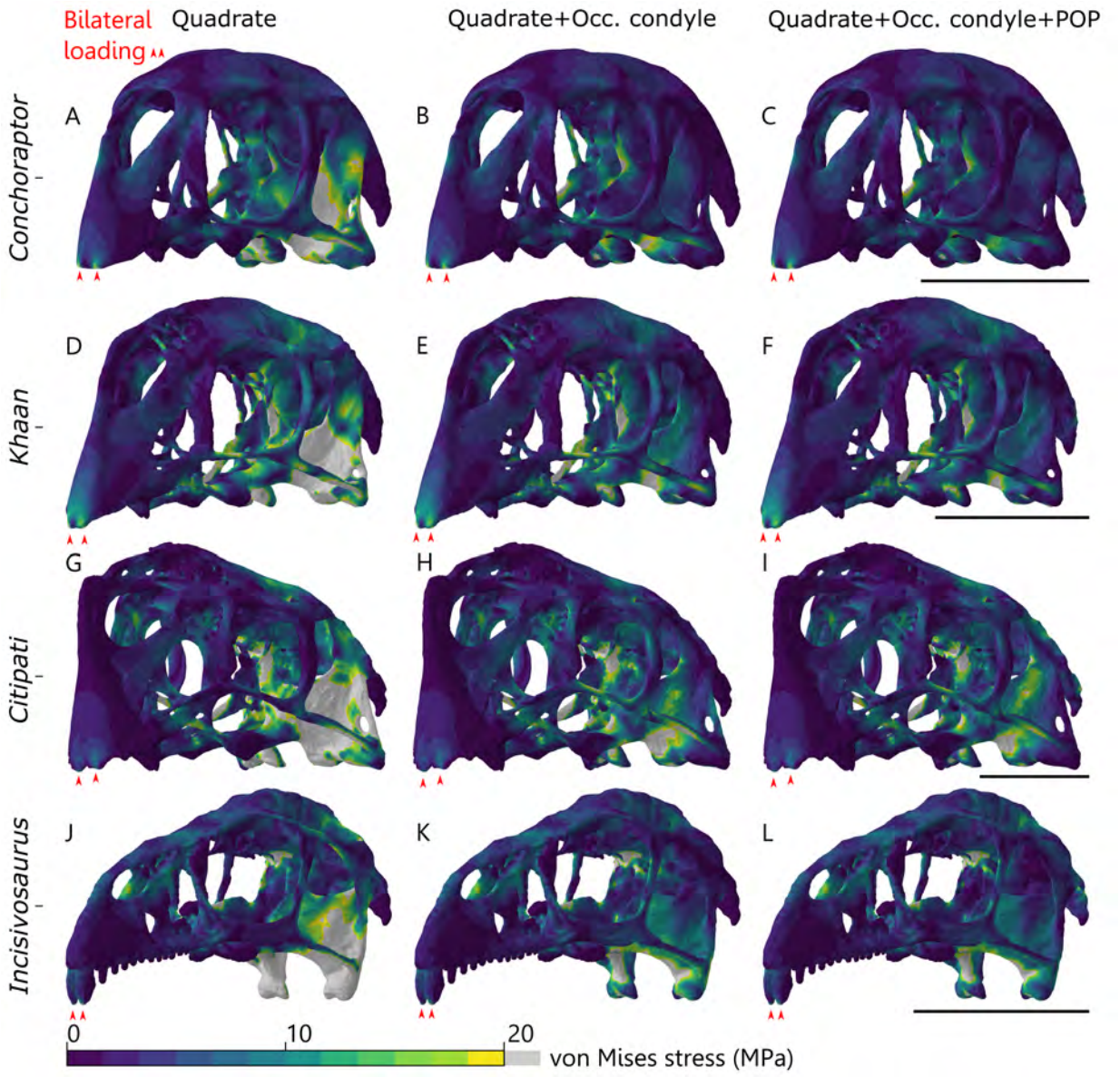

Figure A.1: Comparison of von Mises stress contour plots for different constraint points on the FEA scenarios modelling bilateral loading in *Conchoraptor* (A–C), *Khaan* (D–F), *Citipati* (G–I), and *Incisivosaurus* (J–L). Note constraining only the quadrate (A,D,G,J) produces vast stress hotspots on the quadrate and pterygoid, and there is comparatively little stress difference when the paroccipital processes (POP) are constrained (C,F,I,L; minor increase in cranial roof, minor decrease in quadrate) in addition to the occipital condyle and quadrate (B,E,H,K). Scale bars 50 mm

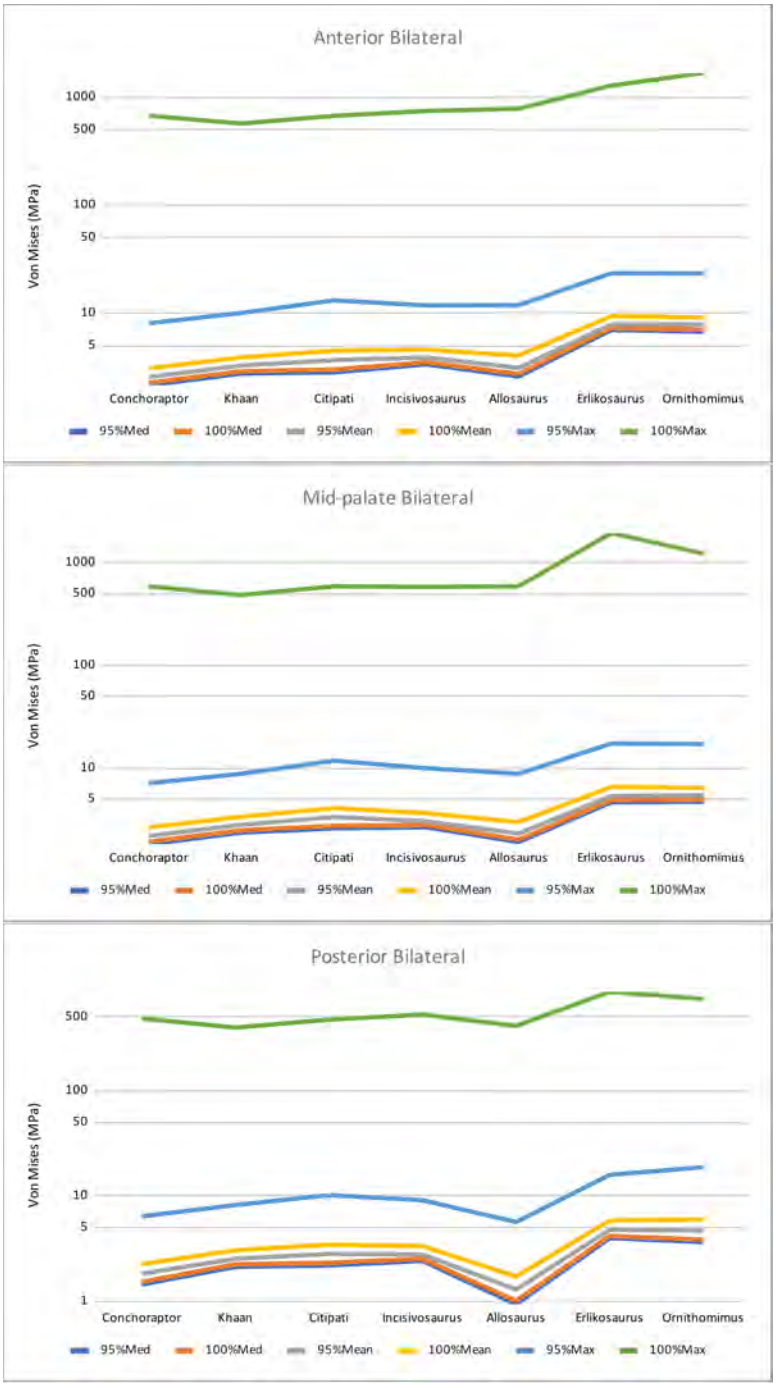

Figure A.2: Calculated means and medians, and maximum values of stress (during bilateral loading) from both 95% and 100% of data produce a very similar pattern but are dissimilar to the to 100% values, due to artificially high stresses from point loads/constraints, justifying using the 95% quantile for data analysis.

Table A.1: Table of mean, median, and maximum values of stress (MPa) (during bilateral loading) from both 95% and 100% of von Mises stress data.

	Anterior bilateral					
	95%Med	100%Med	95%Mean	100%Mean	95%Max	100%Max
Conchoraptor	2.15	2.27	2.56	3.08	8.05	672.71
Khaan	2.76	2.90	3.27	3.89	10.04	569.86
Citipati	2.82	3.00	3.67	4.49	13.14	672.00
Incisivosaurus	3.35	3.51	3.88	4.59	11.78	745.36
Allosaurus	2.59	2.74	3.11	4.04	11.84	781.74
Erlikosaurus	6.97	7.28	7.87	9.36	23.36	1280.00
Ornithomimus	6.74	7.06	7.86	9.11	23.33	1678.28
	Mid-palate bilateral					
	95%Med	100%Med	95%Mean	100%Mean	95%Max	100%Max
Conchoraptor	1.82	1.92	2.19	2.65	7.13	586.64
Khaan	2.36	2.49	2.81	3.36	8.81	483.56
Citipati	2.59	2.75	3.35	4.09	11.82	588.40
Incisivosaurus	2.66	2.80	3.04	3.65	9.98	579.94
Allosaurus	1.91	2.01	2.31	2.99	8.83	588.71
Erlikosaurus	4.65	4.89	5.36	6.57	17.33	1939.00
Ornithomimus	4.71	4.94	5.44	6.43	17.18	1221.29
	Posterior bilateral					
	95%Med	100%Med	95%Mean	100%Mean	95%Max	100%Max
Conchoraptor	1.44	1.52	1.82	2.25	6.39	484.47
Khaan	2.12	2.24	2.53	3.04	8.19	396.57
Citipati	2.19	2.32	2.81	3.45	10.17	472.11
Incisivosaurus	2.41	2.54	2.78	3.33	9.10	527.69
Allosaurus	0.93	1.01	1.29	1.72	5.65	411.65
Erlikosaurus	3.97	4.17	4.76	5.82	15.84	866.47
Ornithomimus	3.64	3.84	4.67	5.98	18.74	742.48

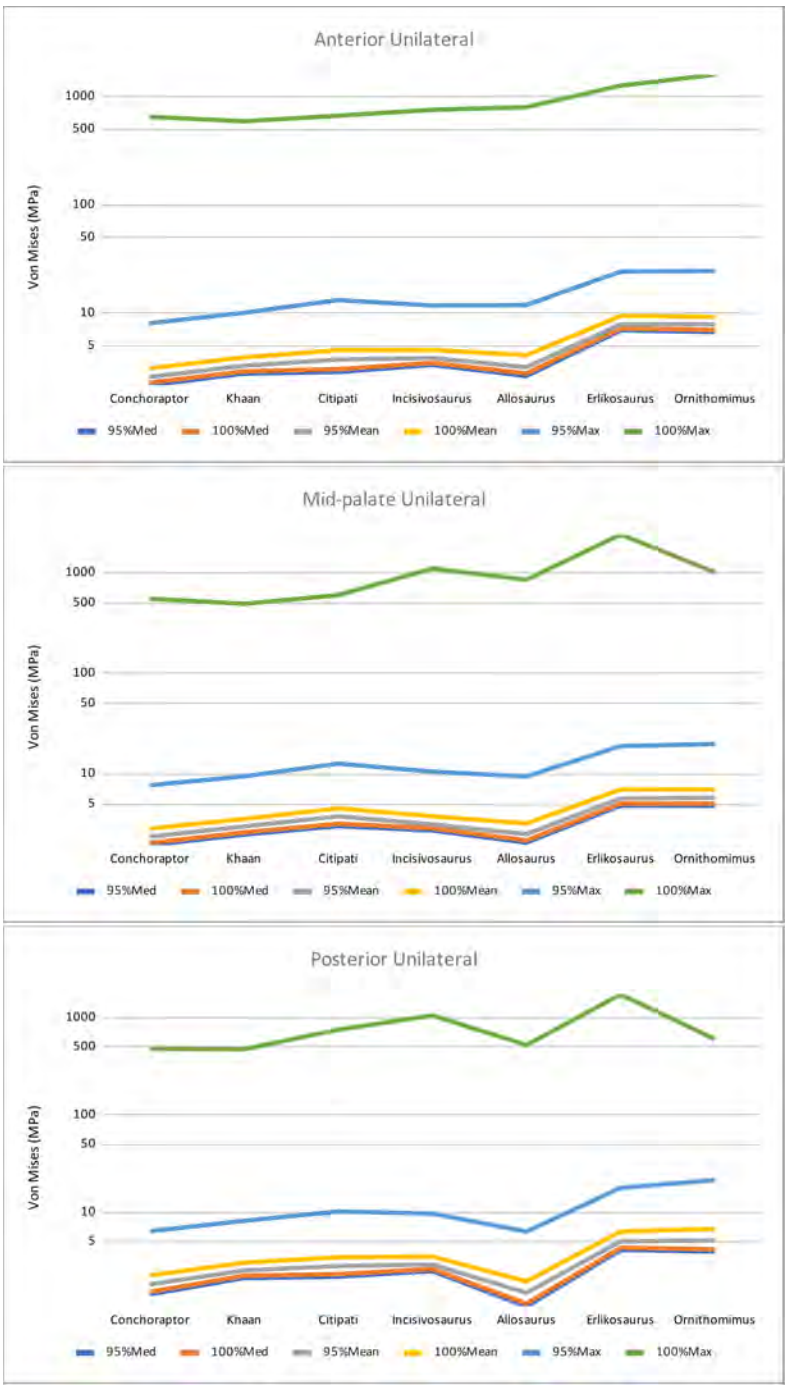

Figure A.3: Calculated means and medians, and maximum values of stress (during bilateral loading) from both 95% and 100% of data produce a very similar pattern but are dissimilar to the to 100% values, due to artificially high stresses from point loads/constraints, justifying using the 95% quantile for data analysis. justifying this approach in the FEA scenarios modelling bilateral loading.

Table A.2: Table of mean, median, and maximum values of stress (during unilateral loading) from both 95% and 100% of von Mises stress data.

	Anterior unilateral					
	95%Med	100%Med	95%Mean	100%Mean	95%Max	100%Max
Conchoraptor	2.16	2.28	2.58	3.10	8.08	650.87
Khaan	2.77	2.91	3.28	3.91	10.09	592.39
Citipati	2.86	3.05	3.73	4.55	13.24	666.50
Incisivosaurus	3.34	3.49	3.87	4.58	11.79	755.27
Allosaurus	2.63	2.78	3.17	4.10	11.92	800.01
Erlikosaurus	6.93	7.24	7.92	9.45	24.26	1263.00
Ornithomimus	6.71	7.02	7.91	9.25	24.56	1593.28
	Mid-palate unilateral					
	95%Med	100%Med	95%Mean	100%Mean	95%Max	100%Max
Conchoraptor	1.95	2.05	2.37	2.84	7.70	552.69
Khaan	2.48	2.61	2.99	3.55	9.43	491.42
Citipati	3.02	3.19	3.78	4.53	12.64	598.40
Incisivosaurus	2.73	2.87	3.14	3.78	10.49	1103.00
Allosaurus	2.07	2.18	2.51	3.20	9.41	853.43
Erlikosaurus	4.83	5.07	5.70	6.98	18.89	2403.00
Ornithomimus	4.81	5.06	5.78	6.98	19.79	1014.08
	Posterior unilateral					
	95%Med	100%Med	95%Mean	100%Mean	95%Max	100%Max
Conchoraptor	1.44	1.53	1.82	2.25	6.40	478.97
Khaan	2.12	2.24	2.54	3.05	8.20	473.98
Citipati	2.19	2.32	2.81	3.46	10.22	753.55
Incisivosaurus	2.49	2.62	2.92	3.53	9.73	1055.00
Allosaurus	1.08	1.16	1.49	1.96	6.35	524.74
Erlikosaurus	4.12	4.34	5.05	6.37	17.88	1733.00
Ornithomimus	3.96	4.18	5.15	6.77	21.47	603.56

B | Muscle reconstruction calculation tables

The tables in this appendix are supplementary to Chapter 4: "Cranial muscle reconstructions quantify adaptation for high bite forces in Oviraptorosauria".

Original Excel files can be found in Supplementary Information 2 of the published manuscript.

Meade, L. E. and Ma, W. 2020. Cranial muscle reconstructions quantify adaptation for high bite forces in Oviraptorosauria. *Scientific Reports*, **12**, 3010.

https://doi.org/10.1038/s41598-022-06910-4

The datasets, including 3D models in the format of Blender projects for the retrodeformations, muscular reconstructions, and gape analyses, along with associated python scripts, generated and analysed during the current study are available from the Zenodo data repository and available for download at: https://doi.org/10.5281/zenodo.5585305.

Table B.1: Full values for the calculation of bite force in *Citipati* and *Incisivosaurus*.

Citipati														**Anterior**					**Mid**					**Posterior**				
	Muscle	Volume (mm^3)	Length (mm)	CSA (mm^2)	Fmus (N)	Fmus (N)x1.5	Contribution (%)	Angle a	Angle b	Fres (N)	Fres (N)x1.5	Contribution (%)		Inlever (mm)	Outlever (mm)	Fbite (N)	Fbite (N)x1.5		Inlever (mm)	Outlever (mm)	Fbite (N)	Fbite (N)x1.5		Inlever (mm)	Outlever (mm)	Fbite (N)	Fbite (N)x1.5	Contribution (%)
Left	AMEM	16490.0	69.1	238.6	71.6	107.4	15.9	23.1	5.1	65.6	98.4	17.0		32.9	142.0	15.2	22.8		32.9	122.0	17.7	26.5		32.9	99.4	21.7	32.6	13.5
	AMEP	9936.0	59.7	166.4	49.9	74.9	11.1	32.4	6.9	41.9	62.8	10.9		59.3	142.0	17.5	26.2		59.3	122.0	20.3	30.5		59.3	99.4	25.0	37.5	15.6
	AMES	20149.0	60.5	333.0	99.9	149.9	22.1	15.1	6.5	95.8	143.8	24.9		45.7	142.0	30.8	46.3		45.7	122.0	35.9	53.9		45.7	99.4	44.1	66.1	27.5
	AMP	7189.0	43.7	164.5	49.4	74.0	10.9	46.1	15.5	33.0	49.5	8.6		44.7	142.0	10.4	15.6		44.7	122.0	12.1	18.1		44.7	99.4	14.8	22.2	9.3
	PSTp	4906.0	51.0	96.2	28.9	43.3	6.4	34.8	29.1	20.7	31.1	5.4		55.3	142.0	8.1	12.1		55.3	122.0	9.4	14.1		55.3	99.4	11.5	17.3	7.2
	PSTs	6870.0	64.1	107.2	32.2	48.2	7.1	26.2	7.2	28.6	42.9	7.4		63.7	142.0	12.8	19.3		63.7	122.0	14.9	22.4		63.7	99.4	18.3	27.5	11.4
	PTd	3763.0	42.0	89.6	26.9	40.3	6.0	37.8	14.3	20.6	30.9	5.3		16.7	142.0	2.4	3.6		16.7	122.0	2.8	4.2		16.7	99.4	3.5	5.2	2.2
	PTv	10911.0	35.4	308.2	92.5	138.7	20.5	20.1	23.7	79.5	119.3	20.6		26.7	142.0	15.0	22.4		26.7	122.0	17.4	26.1		26.7	99.4	21.4	32.0	13.3
				Sum	451.1	676.7			Sum	385.7	578.5				Sum	112.2	168.3			Sum	130.6	195.8			Sum	160.2	240.4	
Right	AMEM	15770.0	69.2	227.9	68.4	102.6	15.2	24.5	2.8	62.1	93.2	16.1		37.1	142.0	16.2	24.4		37.1	122.0	18.9	28.3		37.1	99.4	23.2	34.8	13.5
	AMEP	10309.0	60.1	171.5	51.5	77.2	11.5	32.3	9.9	42.8	64.3	11.1		61.9	142.0	18.7	28.0		61.9	122.0	21.7	32.6		61.9	99.4	26.7	40.0	15.5
	AMES	19012.0	56.9	334.1	100.2	150.4	22.3	17.4	7.0	94.9	142.4	24.7		48.0	142.0	32.1	48.1		48.0	122.0	37.4	56.0		48.0	99.4	45.8	68.8	26.6
	AMP	7254.0	43.9	165.2	49.6	74.4	11.0	43.2	13.8	35.1	52.6	9.1		47.2	142.0	11.7	17.5		47.2	122.0	13.6	20.4		47.2	99.4	16.7	25.0	9.7
	PSTp	4846.0	50.8	95.4	28.6	42.9	6.4	32.4	25.3	21.8	32.8	5.7		56.8	142.0	8.7	13.1		56.8	122.0	10.2	15.3		56.8	99.4	12.5	18.7	7.2
	PSTs	7055.0	65.6	107.5	32.3	48.4	7.2	25.5	4.5	29.0	43.5	7.5		66.7	142.0	13.6	20.5		66.7	122.0	15.9	23.8		66.7	99.4	19.5	29.2	11.3
	PTd	3514.0	42.4	82.9	24.9	37.3	5.5	37.1	12.3	19.4	29.1	5.0		18.1	142.0	2.5	3.7		18.1	122.0	2.9	4.3		18.1	99.4	3.5	5.3	2.0
	PTv	10805.0	34.7	311.4	93.4	140.1	20.8	17.8	26.4	79.7	119.5	20.7		30.6	142.0	17.2	25.8		30.6	122.0	20.0	30.0		30.6	99.4	24.5	36.8	14.2
				Sum	448.8	673.2			Sum	384.9	577.4				Sum	120.7	181.0			Sum	140.5	210.7			Sum	172.4	258.6	
Both sides	AMEM	16130.0	69.2	233.3	140.0	209.9	15.6	23.8	4.0	127.7	191.6	16.6				31.4	47.1				36.6	54.9				44.9	67.4	13.5
	AMEP	10122.5	59.9	169.0	101.4	152.1	11.3	32.3	8.4	84.7	127.1	11.0				36.2	54.2				42.1	63.1				51.7	77.5	15.5
	AMES	19580.5	58.7	333.6	200.2	300.2	22.2	16.3	6.8	190.8	286.2	24.8				62.9	94.4				73.3	109.9				89.9	134.9	27.0
	AMP	7221.5	43.8	164.9	98.9	148.4	11.0	44.7	14.7	68.1	102.1	8.8				22.0	33.1				25.7	38.5				31.5	47.2	9.5
	PSTp	4876.0	50.9	95.8	57.5	86.2	6.4	33.6	27.2	42.6	63.8	5.5				16.8	25.2				19.6	29.3				24.0	36.0	7.2
	PSTs	6962.5	64.9	107.4	64.4	96.6	7.2	25.9	5.9	57.7	86.5	7.5				26.5	39.7				30.8	46.2				37.8	56.7	11.4
	PTd	3638.5	42.2	86.2	51.7	77.6	5.7	37.5	13.3	40.0	59.9	5.2				4.9	7.3				5.7	8.5				7.0	10.5	2.1
	PTv	10858.0	35.1	309.8	185.9	278.8	20.7	19.0	25.0	159.2	238.8	20.7				32.1	48.2				37.4	56.1				45.9	68.8	13.8
				Sum	899.9	1349.9			Sum	770.6	1155.9				Sum	232.9	349.3			Sum	271.0	406.5			Sum	332.7	499.0	

Incisivosaurus														**Anterior**					**Mid**					**Posterior**				
	Muscle	Volume (mm^3)	Length (mm)	CSA (mm^2)	Fmus (N)	Fmus (N)x1.5	Contribution (%)	Angle a	Angle b	Fres (N)	Fres (N)x1.5	Contribution (%)		Inlever (mm)	Outlever (mm)	Fbite (N)	Fbite (N)x1.5		Inlever (mm)	Outlever (mm)	Fbite (N)	Fbite (N)x1.5		Inlever (mm)	Outlever (mm)	Fbite (N)	Fbite (N)x1.5	Contribution (%)
Left	AMEM	1535.4	43.2	35.5	10.7	16.0	12.7	28.6	5.4	9.3	14.0	12.4		19.7	90.4	2.0	3.0		19.7	71.6	2.6	3.8		19.7	58.1	3.2	4.7	11.6
	AMEP	1441.9	45.4	31.8	9.5	14.3	11.3	30.7	4.9	8.2	12.2	10.9		29.8	90.4	2.7	4.0		29.8	71.6	3.4	5.1		29.8	58.1	4.2	6.3	15.3
	AMES	2226.3	41.3	53.9	16.2	24.3	19.2	23.0	1.7	14.9	22.3	19.8		22.8	90.4	3.8	5.6		22.8	71.6	4.7	7.1		22.8	58.1	5.8	8.8	21.4
	AMP	655.2	21.3	30.8	9.2	13.8	11.0	27.1	2.1	8.2	12.3	10.9		19.7	90.4	1.8	2.7		19.7	71.6	2.3	3.4		19.7	58.1	2.8	4.2	10.2
	PSTp	378.8	31.1	12.2	3.7	5.5	4.3	25.7	5.3	3.3	4.9	4.4		25.3	90.4	0.9	1.4		25.3	71.6	1.2	1.7		25.3	58.1	1.4	2.1	5.2
	PSTs	759.0	46.9	16.2	4.9	7.3	5.8	18.7	1.8	4.6	6.9	6.1		30.8	90.4	1.6	2.3		30.8	71.6	2.0	3.0		30.8	58.1	2.4	3.7	8.9
	PTd	575.3	29.8	19.3	5.8	8.7	6.9	45.0	10.9	4.0	6.0	5.4		8.9	90.4	0.4	0.6		8.9	71.6	0.5	0.7		8.9	58.1	0.6	0.9	2.3
	PTv	1691.4	20.9	80.9	24.3	36.4	28.8	13.1	16.6	22.7	34.0	30.2		17.6	90.4	4.4	6.6		17.6	71.6	5.6	8.4		17.6	58.1	6.9	10.3	25.1
				Sum	84.2	126.3			Sum	75.1	112.7				Sum	17.6	26.3			Sum	22.2	33.2			Sum	27.3	41.0	
Right	AMEM	1448.7	43.6	33.2	10.0	15.0	11.9	26.5	3.3	8.9	13.4	11.9		19.8	90.4	2.0	2.9		19.8	71.6	2.5	3.7		19.8	58.1	3.0	4.6	11.0
	AMEP	1345.7	43.4	31.0	9.3	14.0	11.1	29.3	3.4	8.1	12.1	10.8		30.7	90.4	2.8	4.1		30.7	71.6	3.5	5.2		30.7	58.1	4.3	6.4	15.4
	AMES	2258.3	42.1	53.6	16.1	24.1	19.3	25.3	1.3	14.5	21.8	19.5		24.1	90.4	3.9	5.8		24.1	71.6	4.9	7.3		24.1	58.1	6.0	9.0	21.7
	AMP	687.8	22.4	30.7	9.2	13.8	11.0	27.6	2.1	8.2	12.2	10.9		20.0	90.4	1.8	2.7		20.0	71.6	2.3	3.4		20.0	58.1	2.8	4.2	10.1
	PSTp	379.1	31.0	12.2	3.7	5.5	4.4	27.5	5.2	3.2	4.9	4.3		26.7	90.4	1.0	1.4		26.7	71.6	1.2	1.8		26.7	58.1	1.5	2.2	5.4
	PSTs	637.1	44.4	14.3	4.3	6.5	5.2	20.1	1.1	4.0	6.1	5.4		32.2	90.4	1.4	2.2		32.2	71.6	1.8	2.7		32.2	58.1	2.2	3.4	8.1
	PTd	603.2	29.8	20.2	6.1	9.1	7.3	43.7	12.6	4.3	6.4	5.7		10.0	90.4	0.5	0.7		10.0	71.6	0.6	0.9		10.0	58.1	0.7	1.1	2.7
	PTv	1700.1	20.5	82.9	24.9	37.3	29.8	13.4	14.6	23.4	35.1	31.4		17.6	90.4	4.6	6.8		17.6	71.6	5.8	8.6		17.6	58.1	7.1	10.6	25.6
				Sum	83.5	125.2			Sum	74.7	112.0				Sum	17.8	26.7			Sum	22.5	33.7			Sum	27.7	41.6	
Both sides	AMEM	1492.1	43.4	34.4	20.6	30.9	12.3	27.6	4.4	18.2	27.3	12.2				4.0	6.0				5.0	7.5				6.2	9.3	11.3
	AMEP	1393.8	44.4	31.4	18.8	28.2	11.2	30.0	4.2	16.3	24.4	10.9				5.4	8.2				6.9	10.3				8.5	12.7	15.4
	AMES	2242.3	41.7	53.8	32.3	48.4	19.2	24.2	1.5	29.4	44.1	19.6				7.6	11.4				9.6	14.4				11.9	17.8	21.6
	AMP	671.5	21.9	30.7	18.4	27.7	11.0	27.4	2.1	16.4	24.6	10.9				3.6	5.4				4.5	6.8				5.6	8.4	10.2
	PSTp	379.0	31.1	12.2	7.3	11.0	4.4	26.6	5.3	6.5	9.8	4.4				1.9	2.8				2.4	3.6				2.9	4.4	5.3
	PSTs	698.1	45.7	15.3	9.2	13.7	5.5	19.4	1.5	8.6	13.0	5.8				3.0	4.5				3.8	5.7				4.7	7.0	8.5
	PTd	589.3	29.8	19.8	11.9	17.8	7.1	44.4	11.8	8.3	12.5	5.5				0.9	1.3				1.1	1.6				1.4	2.0	2.5
	PTv	1695.8	20.7	81.9	49.2	73.7	29.3	13.3	15.6	46.1	69.1	30.8				9.0	13.5				11.3	17.0				14.0	20.9	25.4
				Sum	167.7	251.5			Sum	149.8	224.7				Sum	35.4	53.0			Sum	44.6	67.0			Sum	55.0	82.5	

Table B.2: Full values for the calculation of bite force in *Khaan* and *Conchoraptor*.

Khaan																**Anterior**					**Mid**					**Posterior**				
	Muscle	Volume (mm^3)	Length (mm)	CSA (mm^2)	Fmus (N)	Fmus (N)x1.5	Contribution (%)	Angle a	Angle b	Fres (N)	Fres (N)x1.5	Contribution (%)	Inlever (mm)	Outlever (mm)	Fbite (N)	Fbite (N)x1.5	Inlever (mm)	Outlever (mm)	Fbite (N)	Fbite (N)x1.5	Inlever (mm)	Outlever (mm)	Fbite (N)	Fbite (N)x1.5	Contribution (%)
Left	AMEM	4080.0	48.2	84.6	25.4	38.1	12.3	27.8	1.1	22.5	33.7	12.8	18.4	103.6	4.0	6.0	18.4	88.7	4.6	7.0	18.4	72.0	5.7	8.6	8.6
	AMEP	4507.0	46.7	96.5	29.0	43.4	14.0	36.3	7.3	23.1	34.7	13.2	34.6	103.6	7.7	11.6	34.6	88.7	9.0	13.5	34.6	72.0	11.1	16.7	16.7
	AMES	6320.0	45.9	137.7	41.3	62.0	20.0	18.2	10.1	38.6	57.9	22.0	27.3	103.6	10.2	15.3	27.3	88.7	11.9	17.8	27.3	72.0	14.6	22.0	21.9
	AMP	1748.0	27.6	63.3	19.0	28.5	9.2	38.7	8.5	14.7	22.0	8.4	25.0	103.6	3.5	5.3	25.0	88.7	4.1	6.2	25.0	72.0	5.1	7.6	7.6
	PSTp	1443.0	35.2	41.0	12.3	18.4	6.0	38.5	22.2	8.9	13.4	5.1	37.2	103.6	3.2	4.8	37.2	88.7	3.7	5.6	37.2	72.0	4.6	6.9	6.9
	PSTs	2336.0	48.8	47.9	14.4	21.5	7.0	26.8	2.5	12.8	19.2	7.3	41.2	103.6	5.1	7.6	41.2	88.7	5.9	8.9	41.2	72.0	7.3	11.0	11.0
	PTd	1679.0	30.8	54.5	16.4	24.5	7.9	46.0	11.7	11.1	16.7	6.3	14.4	103.6	1.5	2.3	14.4	88.7	1.8	2.7	14.4	72.0	2.2	3.3	3.3
	PTv	4007.0	24.7	162.2	48.7	73.0	23.6	16.7	20.8	43.6	65.4	24.9	26.5	103.6	11.1	16.7	26.5	88.7	13.0	19.5	26.5	72.0	16.0	24.1	24.0
				Sum	206.3	309.5			Sum	175.3	263.0			Sum	46.4	69.6		Sum	54.2	81.3		Sum	66.8	100.2	
Right	AMEM	3984.0	48.7	81.8	24.5	36.8	11.8	30.0	1.3	21.2	31.9	12.0	18.8	103.6	3.9	5.8	18.8	88.7	4.5	6.8	18.8	72.0	5.5	8.3	8.5
	AMEP	4289.0	44.8	95.7	28.7	43.1	13.8	34.6	6.8	23.5	35.2	13.3	34.0	103.6	7.7	11.6	34.0	88.7	9.0	13.5	34.0	72.0	11.1	16.6	17.1
	AMES	6423.0	46.7	137.5	41.3	61.9	19.9	17.2	8.5	39.0	58.5	22.1	27.5	103.6	10.3	15.5	27.5	88.7	12.1	18.1	27.5	72.0	14.9	22.3	22.9
	AMP	1817.0	27.4	66.3	19.9	29.8	9.6	42.1	6.9	14.7	22.0	8.3	27.1	103.6	3.8	5.7	27.1	88.7	4.5	6.7	27.1	72.0	5.5	8.3	8.5
	PSTp	1437.0	34.4	41.8	12.5	18.8	6.0	40.4	22.7	8.8	13.2	5.0	35.7	103.6	3.0	4.6	35.7	88.7	3.5	5.3	35.7	72.0	4.4	6.5	6.7
	PSTs	2185.0	49.8	43.9	13.2	19.7	6.3	27.1	2.9	11.7	17.6	6.6	41.5	103.6	4.7	7.0	41.5	88.7	5.5	8.2	41.5	72.0	6.7	10.1	10.4
	PTd	1680.0	30.0	56.0	16.8	25.2	8.1	48.3	13.6	10.9	16.3	6.1	12.3	103.6	1.3	1.9	12.3	88.7	1.5	2.3	12.3	72.0	1.9	2.8	2.9
	PTv	3793.0	22.5	168.6	50.6	75.9	24.4	13.1	17.5	47.0	70.5	26.6	22.9	103.6	10.4	15.6	22.9	88.7	12.1	18.2	22.9	72.0	14.9	22.4	23.0
				Sum	207.5	311.2			Sum	176.7	265.1			Sum	45.1	67.7		Sum	52.7	79.1		Sum	64.9	97.4	
Both sides	AMEM	4032.0	48.5	83.2	49.9	74.9	12.1	28.9	1.2	43.7	65.6	12.4			7.8	11.8			9.1	13.7			11.3	16.9	8.6
	AMEP	4398.0	45.8	96.1	57.7	86.5	13.9	35.5	7.1	46.6	69.9	13.2			15.4	23.2			18.0	27.0			22.2	33.3	16.9
	AMES	6371.5	46.3	137.6	82.6	123.9	20.0	17.7	9.3	77.6	116.4	22.0			20.5	30.8			24.0	36.0			29.5	44.3	22.4
	AMP	1782.5	27.5	64.8	38.9	58.3	9.4	40.4	7.7	29.3	44.0	8.3			7.4	11.1			8.6	12.9			10.6	15.9	8.1
	PSTp	1440.0	34.8	41.4	24.8	37.2	6.0	39.5	22.5	17.7	26.6	5.0			6.2	9.4			7.3	10.9			9.0	13.5	6.8
	PSTs	2260.5	49.3	45.9	27.5	41.3	6.7	27.0	2.7	24.5	36.8	7.0			9.8	14.7			11.4	17.1			14.1	21.1	10.7
	PTd	1679.5	30.4	55.3	33.2	49.7	8.0	47.2	12.6	22.0	33.0	6.2			2.8	4.3			3.3	5.0			4.1	6.1	3.1
	PTv	3900.0	23.6	165.4	99.2	148.9	24.0	14.9	19.2	90.6	135.8	25.7			21.5	32.3			25.1	37.7			31.0	46.5	23.5
				Sum	413.8	620.7			Sum	352.0	528.0			Sum	91.5	137.3		Sum	106.9	160.4		Sum	131.7	197.6	

Conchoraptor																**Anterior**					**Mid**					**Posterior**				
	Muscle	Volume (mm^3)	Length (mm)	CSA (mm^2)	Fmus (N)	Fmus (N)x1.5	Contribution (%)	Angle a	Angle b	Fres (N)	Fres (N)x1.5	Contribution (%)	Inlever (mm)	Outlever (mm)	Fbite (N)	Fbite (N)x1.5	Inlever (mm)	Outlever (mm)	Fbite (N)	Fbite (N)x1.5	Inlever (mm)	Outlever (mm)	Fbite (N)	Fbite (N)x1.5	Contribution (%)
Left	AMEM	2372.0	47.1	50.4	15.1	22.7	10.2	26.7	1.2	13.5	20.2	10.1	17.6	85.8	2.8	4.2	17.6	76.9	3.1	4.6	17.6	58.3	4.1	6.1	7.4
	AMEP	3076.0	44.3	69.4	20.8	31.2	14.0	33.2	6.1	17.3	26.0	13.0	31.1	85.8	6.3	9.4	31.1	76.9	7.0	10.5	31.1	58.3	9.2	13.9	16.8
	AMES	4030.0	45.6	88.4	26.5	39.8	17.8	18.2	6.5	25.0	37.5	18.8	25.0	85.8	7.3	10.9	25.0	76.9	8.1	12.2	25.0	58.3	10.7	16.1	19.5
	AMP	1593.0	28.9	55.1	16.5	24.8	11.1	26.2	1.4	14.8	22.2	11.1	22.2	85.8	3.8	5.8	22.2	76.9	4.3	6.4	22.2	58.3	5.6	8.5	10.3
	PSTp	814.0	32.2	25.3	7.6	11.4	5.1	16.5	11.3	7.1	10.7	5.3	27.6	85.8	2.3	3.4	27.6	76.9	2.6	3.8	27.6	58.3	3.4	5.1	6.1
	PSTs	1749.0	47.4	36.9	11.1	16.6	7.4	22.9	4.4	10.2	15.3	7.6	32.2	85.8	3.8	5.7	32.2	76.9	4.3	6.4	32.2	58.3	5.6	8.4	10.2
	PTd	1161.0	34.9	33.3	10.0	15.0	6.7	37.9	8.7	7.8	11.7	5.8	14.1	85.8	1.3	1.9	14.1	76.9	1.4	2.1	14.1	58.3	1.9	2.8	3.4
	PTv	3568.0	26.1	136.7	41.0	61.5	27.6	14.6	19.0	37.5	56.3	28.2	22.4	85.8	9.8	14.7	22.4	76.9	10.9	16.4	22.4	58.3	14.4	21.6	26.2
				Sum	148.6	223.0			Sum	133.3	199.9			Sum	37.4	56.0		Sum	41.7	62.5		Sum	55.0	82.5	
Right	AMEM	1911.0	46.7	40.9	12.3	18.4	8.7	27.0	2.7	10.9	16.4	8.6	16.0	85.8	2.0	3.1	16.0	76.9	2.3	3.4	16.0	58.3	3.0	4.5	6.0
	AMEP	2825.0	44.6	63.3	19.0	28.5	13.5	33.6	7.9	15.7	23.5	12.3	28.4	85.8	5.2	7.8	28.4	76.9	5.8	8.7	28.4	58.3	7.6	11.5	15.4
	AMES	4112.0	46.5	88.4	26.5	39.8	18.8	19.4	6.6	24.9	37.3	19.5	24.3	85.8	7.0	10.6	24.3	76.9	7.9	11.8	24.3	58.3	10.4	15.5	20.9
	AMP	1553.0	26.9	57.7	17.3	26.0	12.3	23.6	1.8	15.9	23.8	12.4	19.9	85.8	3.7	5.5	19.9	76.9	4.1	6.2	19.9	58.3	5.4	8.1	10.9
	PSTp	758.0	30.0	25.3	7.6	11.4	5.4	17.6	8.2	7.2	10.7	5.6	25.4	85.8	2.1	3.2	25.4	76.9	2.4	3.5	25.4	58.3	3.1	4.7	6.3
	PSTs	1608.0	47.6	33.8	10.1	15.2	7.2	22.3	3.8	9.4	14.0	7.3	30.9	85.8	3.4	5.1	30.9	76.9	3.8	5.6	30.9	58.3	5.0	7.4	10.0
	PTd	1032.0	33.5	30.8	9.2	13.9	6.5	39.2	7.3	7.1	10.7	5.6	13.1	85.8	1.1	1.6	13.1	76.9	1.2	1.8	13.1	58.3	1.6	2.4	3.2
	PTv	3488.0	26.7	130.6	39.2	58.8	27.7	13.3	16.7	36.5	54.8	28.7	21.7	85.8	9.2	13.9	21.7	76.9	10.3	15.5	21.7	58.3	13.6	20.4	27.4
					141.3	211.9			Sum	127.5	191.2			Sum	33.8	50.6		Sum	37.7	56.5		Sum	49.7	74.5	
Both sides	AMEM	2141.5	46.9	45.6	27.4	41.1	9.4	26.9	2.0	24.4	36.6	9.3			4.8	7.2			5.4	8.0			7.1	10.6	6.7
	AMEP	2950.5	44.5	66.4	39.8	59.7	13.7	33.4	7.0	33.0	49.5	12.7			11.5	17.2			12.8	19.2			16.9	25.3	16.1
	AMES	4071.0	46.1	88.4	53.0	79.6	18.3	18.8	6.6	49.9	74.8	19.1			14.3	21.5			16.0	24.0			21.1	31.6	20.2
	AMP	1573.0	27.9	56.4	33.9	50.8	11.7	24.9	1.6	30.7	46.0	11.8			7.5	11.3			8.4	12.6			11.1	16.6	10.6
	PSTp	786.0	31.1	25.3	15.2	22.7	5.2	17.1	9.8	14.3	21.4	5.5			4.4	6.6			4.9	7.4			6.5	9.7	6.2
	PSTs	1678.5	47.5	35.3	21.2	31.8	7.3	22.6	4.1	19.5	29.3	7.5			7.2	10.8			8.0	12.0			10.6	15.9	10.1
	PTd	1096.5	34.2	32.0	19.2	28.8	6.6	38.6	8.0	14.9	22.3	5.7			2.4	3.5			2.6	4.0			3.5	5.2	3.3
	PTv	3528.0	26.4	133.7	80.2	120.3	27.7	14.0	17.9	74.1	111.1	28.4			19.0	28.6			21.2	31.9			28.0	42.0	26.8
				Sum	289.9	434.9			Sum	260.8	391.1			Sum	71.1	106.7		Sum	79.4	119.0		Sum	104.7	157.0	

C | Additional FEA figures

The figures in this appendix are supplementary to Chapter 5: "Diversity of cranial function in Oviraptorosauria as revealed by biomechanical analyses".

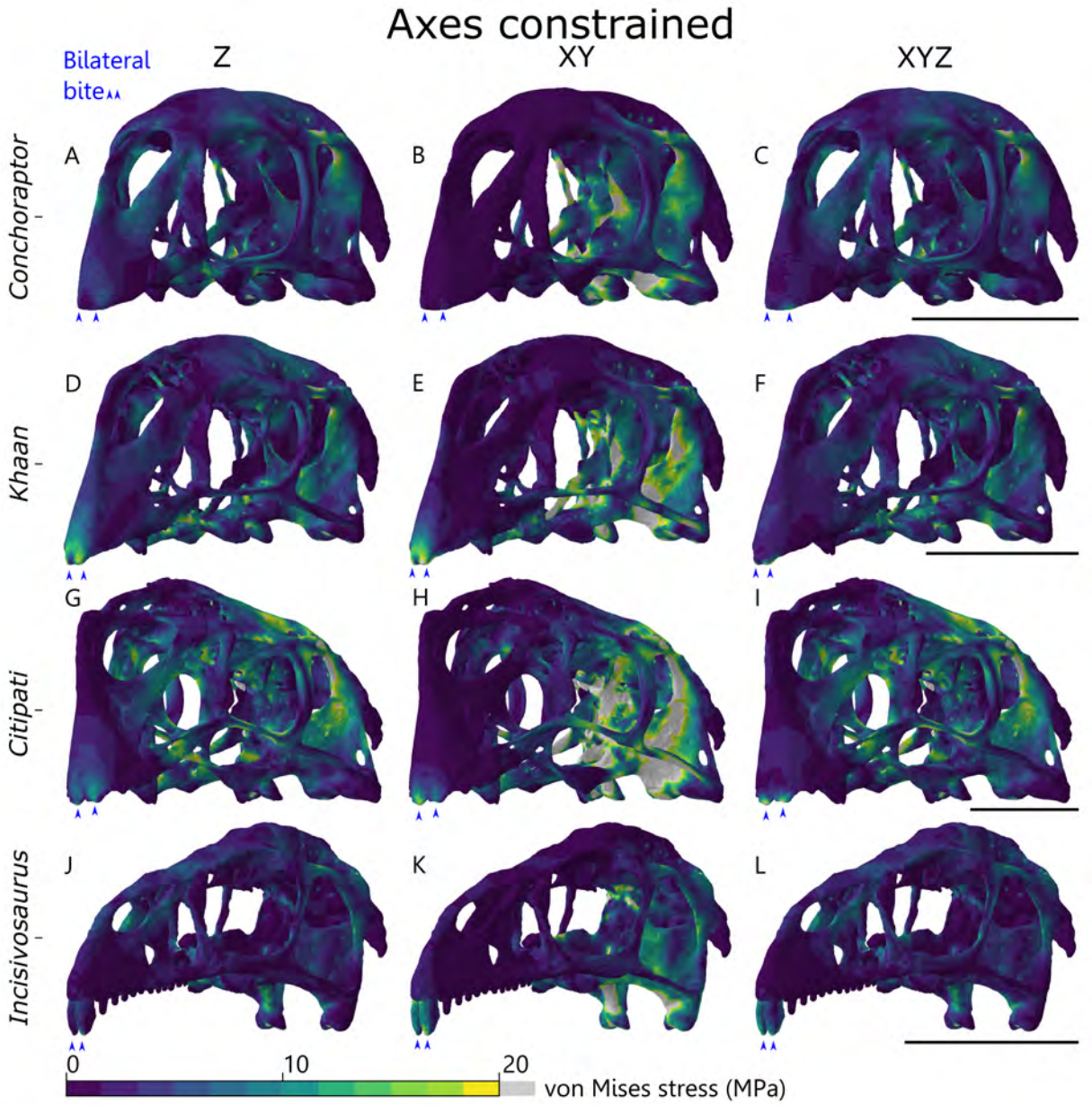

Figure C.1: Comparison of von Mises stress contour plots when different axes are limited at constraint points in FEA scenarios modelling anterior bilateral biting for *Conchoraptor* (A–C), *Khaan* (D–F), *Citipati* (G–I), and *Incisivosaurus* (J–L). Note constraining the bite point in the X and Y axes (B,E,H,K) produces eleveated stress hotspots on the quadrate, pterygoid, and squamosal. There is comparatively little stress difference when all three axes are constrained (C,F,I,L; minor stress decrease in premaxilla) as opposed to just the Z axis (vertical) (A,D,G,J). Scale bars 50 mm.

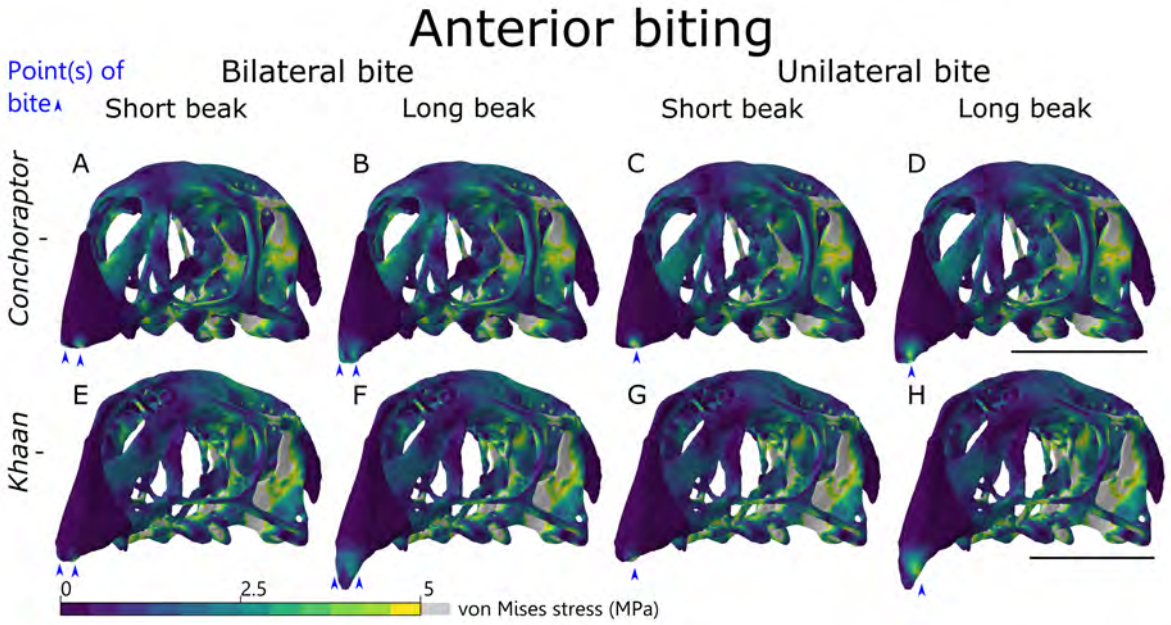

Figure C.2: FEA using anterior bilateral bite point constraints and intrinsic muscle forces in cranial models of oviraptorosaurians *Conchoraptor* (A–D) and *Khaan* (E–H) with a shorter (A,C,E,G) or longer (B,D,F,H) modelled keratinous beak coverings. Note very little difference in cranial von Mises stress between the morphologies. Constraints at bite points shown by small blue arrows at the anterior of the beak/teeth. Scale bars 50 mm.

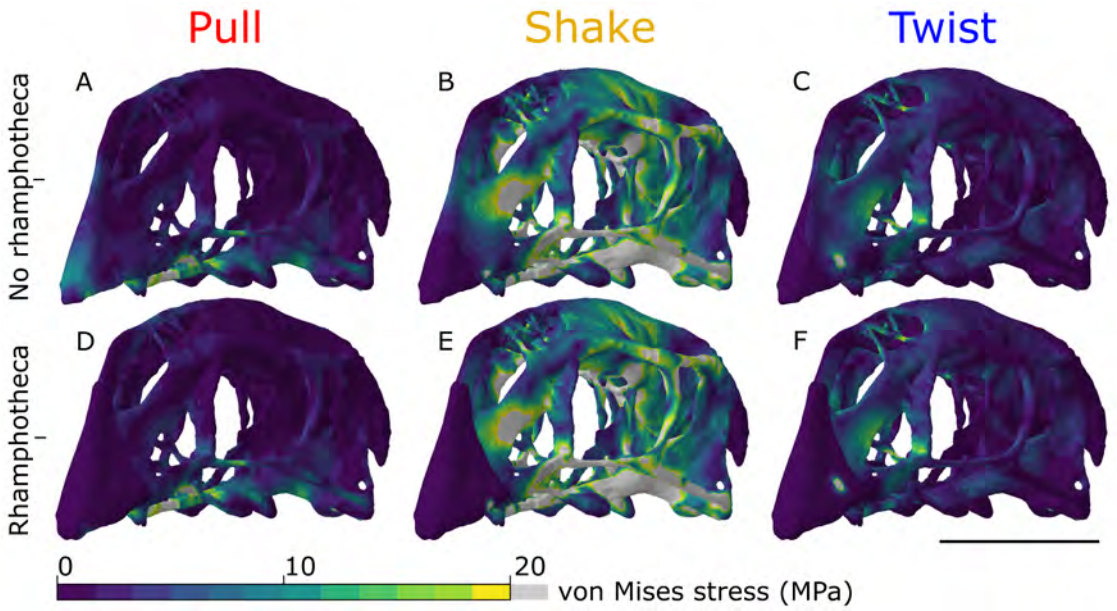

Figure C.3: Von Mises stress (MPa) contour plots from FEA modelling head pull-back (A,D), head shaking (B,E), and head twisting (C,F) feeding scenarios using extrinsic applied loads on the cranial models of oviraptorid *Khaan*. Note the effect on von Mises is essentially identical whether the cranial model has a modelled keratinous rhamphotheca (D–F) or not (A–C). Scale bars 50 mm.

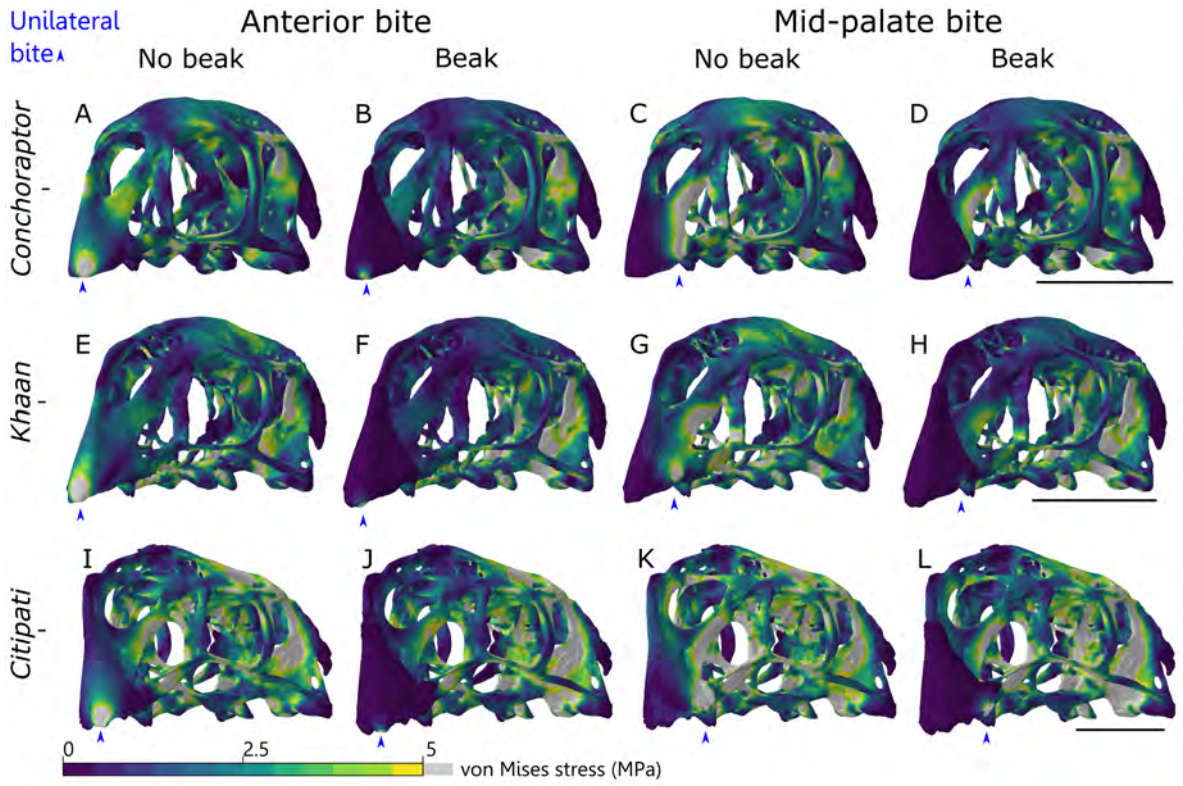

Figure C.4: Von Mises stress (MPa) contour plots from FEA using unilateral bite point constraints and intrinsic muscle forces in cranial models of oviraptorosaurians *Conchoraptor* (A–D), *Khaan* (E–H), and *Citipati* (I–L) modelled without (A,C,E,G,I,K) and with (B,D,F,H,J,L) a keratinous rhamphotheca covering the beak. Constraints at bite points shown by small blue arrows at the anterior of the beak (A,B,E,F,I,J) and the lateral edge of beak (C,D,G,H,K,L).